



Università degli Studi di Pavia  
Dipartimento di Fisica



DOTTORATO DI RICERCA IN FISICA – XXXI CICLO

A new path to combine III-V and IV elements for  
high-efficiency and low-cost multi-junction solar  
cells

Gianluca Timò

Submitted to the Graduate School of Physics in partial

fulfilment of the requirements for the degree of

DOTTORE DI RICERCA IN FISICA

DOCTOR OF PHILOSOPHY IN PHYSICS

at the

University of Pavia

Supervisor: Prof. Lucio Claudio Andreani



# Contents

<b>Abstract</b> .....	vii
<b>Acknowledgements</b> .....	ix
<b>Introduction</b> .....	1
<b>1. Efficiency limit of single-Junction solar cells and the multi-junction solar cell concept</b> .....	7
1.1. The “give and take” balance of single junction solar cells.....	7
1.2. The multi-junction (MJ) solar cell concept.....	8
<b>2. Modelling Multi-junction solar cells</b> .....	9
2.1. General assumptions .....	11
2.2. Transport and continuity equation .....	11
2.3. Hovel model .....	13
2.4. The transfer matrix method .....	14
2.4.1. Matrix elements for TM polarization .....	20
2.4.2. Determination of the Poynting vector for TM polarization .....	24
2.4.3. Matrix elements for TE polarization.....	27
2.4.4. Determination of the Poynting vector for TE polarization .....	30
<b>3. A new mathematical approach for MJ solar cells performance simulation</b> .....	33
3.1. Simplifying the generation function.....	33
3.2. The triple junction InGaP/InGaAs/Ge benchmark case study .....	35
3.3. Scattering matrix method.....	39
3.4. Analytic solution of the continuity equation .....	46
3.4.1. Determination of $j_p$ .....	49
3.4.2. Determination of $j_n$ .....	51
3.5. Hovel model, TMM and SMM applied on thick InGaP/InGaAs/Ge TJ cells.....	54
3.6. TMM and SMM applied on MJ solar cells with improved voltage (thin substrate) .....	56
3.6.1. Numerical instability of TMM on MJ solar cells with improved voltage (thin substrate) ....	56
3.6.2. Validation of the SSM on thin 3J InGaP/InGaAs/Ge solar cells .....	57
<b>4. State-of-the-art integration of SiGeSn in III-V based heterostructures</b> .....	61
4.1. Motivation and challenges .....	61
4.2. Literature survey .....	63
4.2.1. The problem of tin incorporation in SiGeSn and related challenges .....	63
4.2.2. Structural properties of SiGeSn .....	66
4.2.3. Optical properties of SiGeSn .....	68

4.2.4.	Some significant growth experiments on Ge, GeSn and SiGeSn .....	70
4.2.5.	SiGeSn devices .....	73
<b>5.</b>	<b>Advancement on the MOVPE technology to expand the band gap engineering possibilities with the combined growth of III-V and group-IV materials .....</b>	<b>75</b>
5.1.	MOVPE equipment and basic growth background .....	77
5.1.1.	The MOVPE equipment.....	77
5.1.2.	Basic MOVPE growth background.....	79
5.2.	Criteria for precursor selections .....	82
5.3.	MOVPE Growth of SiGe and SiGeSn by IBuGe, Si <sub>2</sub> H <sub>6</sub> and SnCl <sub>4</sub> .....	83
5.3.1.	Preliminary SiGe deposition by IBuGe and Si <sub>2</sub> H <sub>6</sub> .....	83
5.3.2.	SiGe deposition optimization by IBuGe and Si <sub>2</sub> H <sub>6</sub> .....	86
5.3.3.	SiGeSn deposition by IBuGe, Si <sub>2</sub> H <sub>6</sub> and SnCl <sub>4</sub> .....	88
5.4.	MOVPE Growth of Ge, SiGe and SiGeSn with GeH <sub>4</sub> , Si <sub>2</sub> H <sub>6</sub> and SnCl <sub>4</sub> .....	95
5.4.1.	MOVPE Growth of Ge with GeH <sub>4</sub> .....	96
5.4.2.	MOVPE Growth of SiGe with GeH <sub>4</sub> and Si <sub>2</sub> H <sub>6</sub> .....	98
5.4.3.	MOVPE Growth of SiGeSn with GeH <sub>4</sub> , Si <sub>2</sub> H <sub>6</sub> and SnCl <sub>4</sub> .....	101
5.5.	Study of the cross-influence between III-V and IV elements deposited in the same MOVPE growth chamber .....	115
5.5.1.	Control of As carry over and back ground carrier concentration in Ge.....	116
5.5.2.	Back ground carrier concentration in SiGeSn.....	120
5.5.3.	Back ground carrier concentration in III-V compounds .....	123
5.5.4.	Morphological aspects.....	127
<b>6.</b>	<b>Towards the realization of all MOVPE grown 4J InGaP/InGaAs/SiGeSn/Ge solar cells....</b>	<b>129</b>
6.1.	Realization and characterization of GaAs(n-type)/InGaP(n-type)/SiGeSn(n-type)/Ge(p-type) heterojunction.....	129
6.2.	Efficiency prediction of InGaP/InGaAs/SiGeSn/Ge solar cells in two and three terminal configurations .....	136
<b>7.</b>	<b>Conclusions and perspectives.....</b>	<b>145</b>
<b>Appendix 1.</b>	<b>Determination of the electric field at the beginning of each layer by applying TMM and SMM .....</b>	<b>165</b>
<b>List of publications promoted by the thesis.....</b>	<b>169</b>	

*"This thesis work has been carried out in the framework of an Executive PhD agreement between the University of Pavia and RSE SpA. Supervision within RSE by Ing. Luigi Mazzocchi is gratefully acknowledged."*

*Questo lavoro di tesi si è svolto nell'ambito di una convenzione per un percorso di formazione dottorale in cotutela università-impresa fra l'Università di Pavia e RSE SpA. Si ringrazia il tutor aziendale in RSE, Ing. Luigi Mazzocchi."*



*The awareness of my ignorance, instead of putting an end to my research work, is rather the genuine cause of its awakening.*

*La coscienza della mia ignoranza, in luogo di metter fine alle mie ricerche, costituisce piuttosto la genuina causa del loro risveglio.*

*Immanuel Kant*

I dedicate this work to Angela, who encouraged my PHD and to my sons who patiently understood the many long hours of work.



## Abstract

This thesis assesses the potential of a new technological path for the monolithic integration of III-V and IV based materials in view of the realization of high efficiency - low cost – InGaP/InGaAs/SiGeSn/Ge quadruple junction (QJ) solar cells.

A new mathematical approach is first proposed for evaluating the performance of a Multi-junction (MJ) devices with reduced substrate thickness (and improved voltage), in order to overcome the limit that the Hovel model and the transfer matrix method (TMM) showed for this application. Then, an in depth growth analysis has been addressed in order to advance in the deposition of III-V and IV elements in the same Metalorganic Vapour Phase Epitaxy (MOVPE) growth chamber, trying to overcome the problems that hindered so far this approach.

The new mathematical approach has been developed by considering the scattering matrix method (SMM) and building a simplified generation function that allows describing with good accuracy the propagation of electromagnetic waves in the solar cell device, preserving, at the same time, the possibility of getting simple analytical solutions of the continuity equations. The robustness of the new mathematical approach is validated by considering as a case study a triple junction InGaP/InGaAs/Ge solar cell, in which the Ge substrate is considered as the last layer (layer N) and then as the N-1 layer (i.e. by also considering the substrate in the calculation of the reflection coefficient).

In order to accomplish a step ahead towards the realization of - all MOVPE grown - III-V and IV-based monolithic architectures, the experimental work has been addressed to tackle four key challenges: i) to identify a growth approach suitable for an industrial scale-up of the SiGeSn MOVPE process, by adopting only commercially available sources (IBuGe, GeH<sub>4</sub>, Si<sub>2</sub>H<sub>6</sub> and SnCl<sub>4</sub>), ii) to grow SiGeSn layers tin precipitation/segregation free by keeping the temperature as high as possible, to allow controlling the temperature profile over the wafer during the MOVPE deposition, iii) to reduce the As “carry-over” to avoid growth rate penalization in the deposition of IV-based materials, and iv) to adopt proper growth conditions in order to control the III-V and IV elements *cross influence*, so that the conductivities of both III-V and IV-based semiconductors could be modulated and the morphology controlled.

The study allows bringing insights on several aspects of the MOVPE SiGeSn growth in order to get a better control of SiGeSn composition and to obtain epitaxial layers with improved morphology. In this first stage, diluted SiGeSn (i.e., layer with Si and Sn content <5%) have been deposited and extensively characterized by several structural, optical and electrical techniques.

In particular, when SiGeSn is grown in the kinetic growth regime, it is shown that the gas source Si<sub>2</sub>H<sub>6</sub> is more influenced by the growth temperature compared to GeH<sub>4</sub> and SnCl<sub>4</sub>, moreover, its competition with SnCl<sub>4</sub> makes it difficult to incorporate Si in SiGeSn, as SnCl<sub>4</sub> partial pressure is increased. SiGeSn morphology is shown to be strongly dependent on temperature, As carry-over and growth rate. It has been discovered that this last parameter can be increased (up to 40%) by the use of DEZn, exploiting its radicals. A new growth model has been introduced in order to explain the importance of the adatom bond lengths in inhibiting tin segregation when SiGeSn is grown at relatively high growth temperature (>480 °C).

Concerning the cross influence between III-V and IV elements, it is shown that by adopting an innovative proper design of the MOVPE growth chamber and proper growth condition, the IV elements growth rate penalization due to As “carry over” can be eliminated and the background doping level in both IV and III-V semiconductors can be drastically reduced. The possibility to control the layers conductivity is considered a key achievement for the monolithic integration of the III-V and IV elements in the same MOVPE growth chamber.

In the temperature range 748 K - 888 K, Ge and SiGe morphologies do not degrade when the semiconductors are grown in a III-V-contaminated MOVPE growth chamber. On other hand, critical morphology aspects have been identified III-Vs, when the MOVPE deposition takes place, in a Sn-contaminated MOVPE growth chamber. In particular, III-Vs morphologies are influenced by substrate type and orientation.

A GaAs/InGaP/SiGeSn/Ge functional device has then been manufactured in order to finally investigate the PV properties of SiGeSn realized in the same MOVPE chamber used for III-V deposition. For this purpose, external quantum efficiency (EQE) and current-voltage measurements in the concentration range 1-170 X, under AM1.5D spectrum, have been carried out.

The experimental data and the performed simulations show that the quality of SiGeSn n-type layers realized in this study are already sufficient to be integrated in triple-junction structures (InGaP/InGaAs/SiGeSn). In particular, owing to the remarkably higher absorption coefficient of SiGeSn with respect to Ge, we show that it is possible to use SiGeSn layers with a thickness three times lower than Ge to produce the same photovoltaic current. This suggests that SiGeSn solar cells could be more radiation resistance than Ge ones and, apart CPV and TPV applications, SiGeSn solar cells could be profitably used also for space application. On the other hand, further MOVPE growth optimizations are envisaged for getting SiGeSn p-type layers Sn-precipitation free.

In conclusion, an assessment of the potential of the InGaP/InGaAs/SiGeSn/Ge solar cell technology has been carried out by using the experimentally determined optical properties of SiGeSn and by applying the new developed mathematical method to simulate the performance of thin QJ InGaP/InGaAs/SiGeSn/Ge solar cells, in two and three terminal configuration. For these devices, efficiency values up to 45.1% and 44.9%, have been respectively simulated at  $1000\times$  concentration. Eventually, we estimated that InGaP/InGaAs/SiGeSn/Ge solar cells have the potential to reach efficiencies over 50% by assuming proper antireflective coatings and by considering the QJ device limited by the InGaAs sub-cell.

## Acknowledgements

The realization of this thesis has required the collaboration and contribution of several people. First of all I would like to extend a sincere acknowledgment to Stefano Bessegini (ex CEO of RSE), Romano Ambrogi (Staff DG of RSE) and Luigi Mazzocchi (Material and Generation Technologies Department Head of RSE) who trusted in this research work and gave me the opportunity to follow the courses and seminars foreseen in the academic path. By all means, this thesis allowed strengthening the link and the knowledge transfer between the University and RSE. A special acknowledgment has to be addressed to prof. Lucio Andreani, my thesis tutor, who supported the modelling work and allowed me a deeper understanding of the mathematical methods for the simulation of the MJ solar cells performance. I have to express my sincere thanks to the researchers of the RSE CPV lab, who greatly supported this research work. In particular to Giovanni Abagnale and Marco Calicchio who shared with me the development on the MOVPE growth, Armani Nicola e Elisabetta Achilli who characterized and analysed by HRXRD and ECV a considerable amount of samples, Marina Cornelli, Filippo Farina and Filippo Annoni who took care to manufacture the devices and carried out the SEM characterisation work, Franco Trespidi, Emanuele Malvisi, Alessandro Minuto and Nicola Castagnetti who performed the important EQE and IV characterization of the solar cells. I also have to address a particular thank to Alessio Martinelli whose fundamental work constituted a preliminary and strong mathematical base for applying the TMM and SMM to the MJ modelling. The important characterization efforts also required the collaboration with Institutions outside RSE: I thank Lucia Nasi of IMEM-CNR for the TEM ad EDX characterization, Maddelena Patrini of the University of Pavia for the AFM and Ellipsometry characterization, Peter Helm of RTG Mikroanalyse GmbH Berlin for the SIMS measurements and analysis.

A particular thanks to D.Schmitz and B.Shineller for the fruitful discussions and for the collaboration of AIXTRON that allowed implementing the MOVPE hardware modifications necessary to optimize the SiGeSn growth and reduce the cross doping.

This research activity has been partially supported by the European H2020 project CPVMatch, “*Concentrating Photovoltaic modules using advanced technologies and cells for highest efficiencies*”<sup>1</sup>. The project started in May 2016 and ended in October 2018.

I also gratefully acknowledge the funding support of the Research Fund for the Italian Electrical System under the Contract Agreement between RSE (formerly known as ERSE), by the Ministry of Economic Development - General Directorate for Nuclear Energy, Renewable Energy and Energy Efficiency- stipulated on July 29, 2009 in compliance with the Decree of March 19, 2009.

---

<sup>1</sup> During the CPVMatch project I led the WP named “Frontier multi-junction solar cells” whose main objective was to develop frontier lattice multi-junction solar cell with high efficiency potential and low process cost, comprising nanostructured coatings and innovative lattice-matched materials, obtained by combining III-V and IV elements.



## Introduction

World electricity generation has been constantly increasing from 1971 to 2018, for example, it raised of a factor five (from 5000 TWh to 26000 TWh). The increase of the world electricity generation has followed the trend in the electricity needs. A recent study still foresees a 30% rise in global energy demand to 2040 [1]. The high energy consumptions brought our Country to become a *net importer* of electricity: from 2014 to 2018, Italy imported around 44-46 TWh/year [2],[3],[4].

Having in mind the well-known fundamental statement: "*No foreign cartel can set the price of sun power; no one can embargo it*"<sup>2</sup>, we could better and safer fulfil our electricity needs, by reducing and even by eliminating the amount of imported electricity, throughout a wider exploitation of the solar resources.

Photovoltaic (PV) technology offers a renewable-energy source of electricity at a cost that has become more and more competitive with respect to fossil-fuel power generation and it allows reducing the greenhouse-gas emissions as well [5]. In particular, Italy has abundant solar resources, not always fully recognised.

From Milan to Catania the available global solar energy (GHI) changes from 1400 kWh/m<sup>2</sup>year to 1851 kWh/m<sup>2</sup>year<sup>3</sup>. By considering an average amount of solar energy of 1625 kWh/m<sup>2</sup>year and by exploiting just 0,1% of the area of our Country ( $\sim 3 \times 10^8 \text{ m}^2$ ), even with 10% efficient PV systems, we could generate an amount of energy per year of 48.9 TWh, which is higher than the energy Italy imported in 2018. Therefore, our Country could stop importing electricity whether, for example, each of its 20 regions covered just 15 Km<sup>2</sup> of their surface with PV systems. This goal could be accomplished just by exploiting the house's roofs. The city of Piacenza, for instance, has a surface of 118 km<sup>2</sup>, if 10% of this surface were covered by PV roofs, we would be already near to fulfil the regional contribution.

These calculations are more conservative than optimistic, since nowadays Si flat plate technology already reached PV system efficiencies that easily overcome 15% and there is room for developing new PV technologies which promise efficiency values even twice times higher. So far, the PV technology that more than others can fulfil this efficiency target is the *concentrator photovoltaic* (CPV) one, which uses lenses or mirrors to concentrate the direct solar light on tiny, very efficient, multi-junction (MJ) solar cells, firstly developed for space application.

The CPV technology is still in earlier stage of development if compared with the PV technology based on silicon, but it has a great potential to reduce the environmental impact and the cost of the energy generation, since nowadays the CPV solar cell conversion efficiency is more than 40% and the area of the costly semiconductors (i.e. the area of the solar cells materials) is very much reduced and replaced with cheaper mirrors or lens [6].

---

<sup>2</sup> By President Jimmy Carter, Solar Energy Message to the Congress. June 20, 1979  
<http://www.presidency.ucsb.edu/ws/?pid=32503>

<sup>3</sup> <http://globalsolaratlas.info/?c=37.335224,27.333984,4&s=45.02695,9.839357>

## INTRODUCTION

Another advantage of the CPV technology is that it *fully* exploits the *direct* component of the solar light. It has to be considered that the maximum amount of energy that is possible to extract from the sun is not the same for direct and diffused radiation, since the loss of directivity is evidently an irreversible process. Willian H. Press has calculated that till 93% of the sun energy can be utilized if the sun direct component is considered, while the utilization drops to 70% for the diffused component [7]. Therefore, in location characterized by a high level of direct normal solar irradiation (DNI), a fixed PV system is penalized with respect to a CPV one, since for the former, the more exploitable component of the sun, the direct light, is diluted by a factor  $\cos\theta$  (where  $\theta$  is the angle between the sun rays and the normal to the PV module surface) and the diffused component, which is present in a much lower percentage, can be 20 % less exploited.

As a matter of fact, a recent study conducted by Sumitomo Electric has shown that in regions with direct radiation of 6.8 kWh/m<sup>2</sup> per day, 33% efficient CPV modules are able to produce twice the energy that can be produced by 18% efficient fixed Si-based modules with the same area [8]. In locations characterized by a high level of DNI, like, for example, the south of Italy and its island, and where the footprint of the PV technology has to be minimized, it appears more convenient to install photovoltaic systems that fully exploit the high energetic content of the DNI, like CPV systems, than to use any other PV technology.

From an energetic point of view, still considering location characterized by a high level of DNI and the same occupied surface, the advantage in the utilization of a CPV system is even preserved over a Si-based one with sun tracking, thanks to the much higher efficiency conversion of the former. For example, in Madrid the average direct and diffused radiation components are, respectively, 2000 kWh/m<sup>2</sup>y and 500 kWh/m<sup>2</sup>y [9]; a 33% efficient CPV module would be able to produce 660 kWh/m<sup>2</sup>y, while a 18% efficient Si-based PV module with sun tracking would be able to produce only 450 kWh/m<sup>2</sup>y.

Two further important factors make CPV a very attractive renewable technology from the performances point of view: i) by increasing the concentration factor, the PV conversion entropy losses are decreased [10], therefore the efficiency values of the CPV system can be nearer the PV conversion theoretical limits, ii) the performance are less sensitive to temperature variation [11].

In spite of the all mentioned advantages, nowadays the CPV market is still a niche market owing to the production cost of the components, which, although it has decreased in recent years, is not yet competitive with the costs of Si-based photovoltaics. If the cost of the land is not of importance and larger area can be occupied to get the same power, the PV silicon-based technology installations are preferred over CPV ones, since the cost/W of the Si-based photovoltaic is lower the cost/W of CPV technology.

The plant size, the efficiency, the standardization, the ability to raise capital and to take on the risk of large investments have been the main driving factors that helped the PV silicon technology to reduce its costs [12]. The CPV technology has to follow the same path to see its wide-spread deployment. First, CPV technology has to arrive developing a *standard* module type that can be produced everywhere on large scale, while nowadays too many technological solutions are still proposed in the CPV community. On the 14<sup>th</sup> CPV conference hold in Puertollano in 2018, for

## INTRODUCTION

example, I have been able to identify at least 15 different CPV system types<sup>4</sup>. In the future, a clearer convergence towards less “academic” solutions, with real potentiality to drive down the cost will be of crucial importance for the success of the CPV technology.

In particular, the research has to be addressed towards smarter and cheaper solar tracking solutions, as well as towards the development of more efficient optics and *solar cells*. By all means, the photovoltaic device is the “*heart*” of the CPV system and the success of the CPV technology has been so far mainly due to the constant improvement in the multi-junction solar cell performances [13].

Among 2000 and 2019 the MJ solar cell efficiency has increased from 32%, with the Spectrolab triple junction solar cell, to 47%, with the NREL *inverted metamorphic six-junction solar cell* [14], whose design has even the potential to exceed 50% efficiency [15].

In parallel, trying to reduce the cost, it is also worthwhile to mention the experimentation in the combination of the Si technology with III/V semiconductors, which in a tandem or TJ configuration, reached, respectively efficiency around 30 and 35.9% [16], [17], [18].

It has to be pointed out, that ultra-highly efficient devices have not been transferred from the lab to the market yet. Most of the CPV systems are still using triple junction (TJ) InGaP/InGaA/Ge solar cells. This is due to practical and economic challenges that must still be overcome.

Therefore, it seems that in order to bring solar cells performances closer to theoretical limits, without a penalty cost and/or complicated manufacturing processes, novel multi-junction (MJ) solar cell architectures using advanced materials and deposition processes for an optimal solar energy harvesting have to be conceived.

One promising path for a progress in MJ technology, both from an efficiency and cost point of view, concerns the utilization of 1 eV SiGeSn semiconductor material, lattice-matched to Germanium [19]. In fact, first theoretical calculations have showed that a 1.0 eV sub-cell placed in between a Ga<sub>0.99</sub>In<sub>0.01</sub>As middle cell and a Ge bottom cell of a lattice-matched In<sub>0.49</sub>Ga<sub>0.51</sub>P/Ga<sub>0.99</sub>In<sub>0.01</sub>As/Ge triple-junction device would lead to a nearly optimal 45 % efficient solar cell [20]. SiGeSn alloys have then been proposed both for MJ and thermo-photovoltaic applications, as well as an intermediate buffer layers to realize monolithic III-V structure on silicon substrate, paving the path for next generation low cost MJ devices [21].

Even if the efficiency value predicted for the *InGaP/InGaAs/SiGeSn/Ge* device is lower than the actual world record (47%) obtained with a metamorphic structure [14], this multi-junction solar cell would offer the remarkable advantage to present a monolithic configuration - *all lattice matched* - with the same *front-end* of the most common *InGaP/InGaAs/Ge TJ* cell. Therefore, adopting this solution, the CPV technology could indeed make a jump ahead in the market, as we

---

<sup>4</sup> High concentration (HC) point focus modules with achromatic doublet on glass (i), CPV modules with Fresnel lenses (ii), or mirrors (iii), with hybrid PV/thermal receiver and linear tracking (iv), CPV systems with parabolic mirrors (v), and with central receiver (CPV/T) (vi), with Dense array (vii), CPV/T with Trough-Lens-Cone (three stage optic) (viii), with Hybrid Dense array/Point focus, HC (500 X) (ix), with Hybrid Lens Arrays, Static LC (3 X and 4 X) (x), with Hybrid Concentrator III-V/Planar Thin-Film Modules (HC) (xi), CPV/T, with Hybrid Photovoltaic and Thermoelectric Module (with Cassegrain-type concentrator) (xii), hybrid concentrator photovoltaic module III/and Si MC (226 X) (xiii). CPV with passive tracking (xiv), CPV with Spectrum splitting systems (xv).

## INTRODUCTION

could get higher performances keeping down, at the same time, the “post growth” manufacturing cost.

So far, the main problem that still hindered the take-off of the InGaP/InGaAs/SiGeSn/Ge solar cell technology has been the difficulty of growing the SiGeSn semiconductor and properly integrating it in III-V MJ structures.

The very low solubility of Sn in the Ge matrix [22] introduces a severe challenge for tin incorporation. The pioneering work of M.Bauer [23] and J.Kouvetakis [24] on the binary GeSn already showed the necessity to set up very low deposition temperature in order to avoid Sn segregation. For the same reason, the ternary SiGeSn has also been grown in the temperature range 300-350°C [25]. The requirement of an unprecedented very low temperature growth process has earlier stimulated the necessity to develop new gas sources [26], and it has introduced a challenge for the deposition control, since in most commercial MOVPE systems, the pyrometers used to control the temperature profile over the wafer surface during the MOVPE growth start working over 400 °C.

The “*cross contamination*” among the III-V elements and the IV elements of the periodic table [27] has been the other barrier to be overcome for a low cost integration of SiGeSn in the III-V MJ structure. As a matter of fact, the most recent integration of SiGeSn with III-V for MJ solar cells applications has been accomplished by using two different growth equipment: a CVD reactor for the growth of SiGeSn and a MOVPE growth chamber for the deposition of the remaining part of the cell structure [28], [29]. The utilization of twofold growth equipment, however, reduces the economic advantage of the monolithic architecture, owing to the related higher capital expenditure required.

Last but not least, the realization of the first SiGeSn solar devices manufactured by using two different growth equipment did not bring to the expected results yet: the open circuit voltage value of the SiGeSn SJ cells was even lower than that obtained by Ge solar cells [30].

From these considerations it appears that for a scale up and an industrial take off of the MJ technology based on the combination of III-V and SiGeSn alloys, new advanced MOVPE deposition solutions have to be searched that address both the reduction of the manufacturing cost and the increase of the MJ device performance.

The goal of this thesis is to assess the potential of combining III-V and IV elements *in the same MOVPE equipment* in order to fulfil the above reported requirements, and therefore exploit the band gap engineering possibilities which this integration offers, with the final objective, to realize *monolithic*, low cost, high efficiency, - *fully MOVPE grown* - InGaP/InGaAs/SiGeSn/Ge solar cells.

The first chapter of the thesis motivates the use of the MJ technology. Chapter 2 describes the different mathematical methods so far developed for simulating the electromagnetic radiation distribution inside the cell structure. In particular, I introduce the Hovel model (HM) and the Transfer Matrix method (TMM) as well as their limits.

## INTRODUCTION

In chapter 3, I describe a new mathematical approach based on the scattering matrix method (SMM) and on a simplified generation function. This method overcomes the limit presented by the previous models, in order to get a very good trade-off between computing time and accuracy. The experimental work is introduced by a literature survey in chapter 4. The challenges to be faced for the MOVPE growth of SiGeSn and for its integration in a III-V based MJ structure are explained in detail.

Then, in chapter 5, I present a new approach to MOVPE material deposition, with the final aim to successfully integrate, at low cost, SiGeSn in III-V structures. The criteria for the precursor's selection are indicated, the growth condition to deposit SiGeSn - Sn precipitation free - and to reduce the cross-contamination effects between III-V and IV base materials are identified. The growth data are supported by an extensive material characterizations work. To understand the critical issues related to the low temperature growth necessary for the deposition of SiGeSn, several Ge and SiGe MOVPE runs have been preliminary carried out. Afterwards, SiGeSn layers have been grown with different solid composition, both on Ge and GaAs, 4- and 6-inch substrates, testing different precursors. An in-depth investigation on the effect of the cross influence between groups IV and III-V elements on the growth rate, background doping and morphology is finally carried out, to show the feasibility of the new proposed path.

In order to investigate the PV properties of SiGeSn realized in the same MOVPE chamber used for III-V deposition, in chapter 6, the external quantum efficiency and I-V characterizations of a single junction InGaP/SiGeSn/Ge *functional device* filtered by a GaAs layer are presented. For a final assessment of the potential of the InGaP/InGaAs/SiGeSn/Ge solar cell technology, the PV performances of the MJ device have been calculated, in two and three terminal configuration, by using the SMM implemented in chapter 3 and the optical properties of SiGeSn measured and reported in chapter 5. The results of the modelling are compared with previous theoretical calculations.

In the Conclusions, I discuss the open problems to be solved and the perspectives for developing next-generation, high efficiency, and cost-effective MJ devices.

## INTRODUCTION

# 1. Efficiency limit of single-Junction solar cells and the multi-junction solar cell concept

*The “give and take” balance limits the photovoltaic conversion efficiency in single-junction solar cells. To overcome this limit, the multi-junction solar cell concept is introduced.*

## 1.1. The “give and take” balance of single junction solar cells

A fundamental limitation related to single junction solar cells is the “give and take” balance between the current and the voltage. Once the energy gap ( $E_g$ ) value is decreased for improving the photovoltaic current, the output voltage of the solar cell is reduced. We must *take* less voltage to *give* more current. Another way to see this limitation is the “give and take balance” between the absorption coefficient and the density of states. It has to be taken into account that when an electron and a hole are produced by a photon with a proper energy, an average entropy per electron and per hole,  $\sigma_{e,h}$ , is also produced. This term reduces the electrochemical energy terms for each electron and hole and then, the solar cell’s voltage. The entropy produced per electron and hole is given by the following expression [31]:

$$\sigma_{e,h} = k \left( \frac{5}{2} + \ln \frac{N_{c,v}}{n_{e,h}} \right) \quad 1.1$$

The entropy contribution is higher for the semiconductors that have higher value of the effective conduction band or valance band density of states,  $N_{c,v}$ . In fact, while carriers distribute macroscopically in the conduction and valence band with a certain probability of occupying the different energetic levels, that is, by following the Fermi-Dirac or Boltzmann statistics, there are different microscopic distributions of the electron and holes in the possible available states. Therefore, at room temperature, the carriers are preferably distributed near the edge of the conduction (valence) band, however, the higher the values of the conduction (valence) band density of states, the higher the number of microscopic distribution of the electrons (holes) within these permitted energy levels, hence, according to the Boltzmann formula, the higher the entropy value. Since the absorption coefficient is proportional to the product of the densities of the initial and final states, it results that if we decrease the density of states in order to decrease the entropy contribution produced per electron and hole and *give* more voltage to the device, we also *take* less photovoltaic current. By considering that the solar cell conversion efficiency is proportional to the product of the voltage and the current, we can understand why in the efficiency versus  $E_g$  curve of single junction solar cells we can always find a maximum.

## 1.2. *The multi-junction (MJ) solar cell concept*

One way to overcome the “give and take” balance limitation is to consider the multi-junction solar cell concept. The monolithic, series-connected, multijunction (MJ) solar cell is an optoelectronic device formed by a stack of p-n (or n-p) junctions interconnected with tunnel junctions, whose bandgaps values is usually decreased from the top to the bottom of the device, resulting, in the simplest case, in a two-terminal electrical output device (see Figure 1).

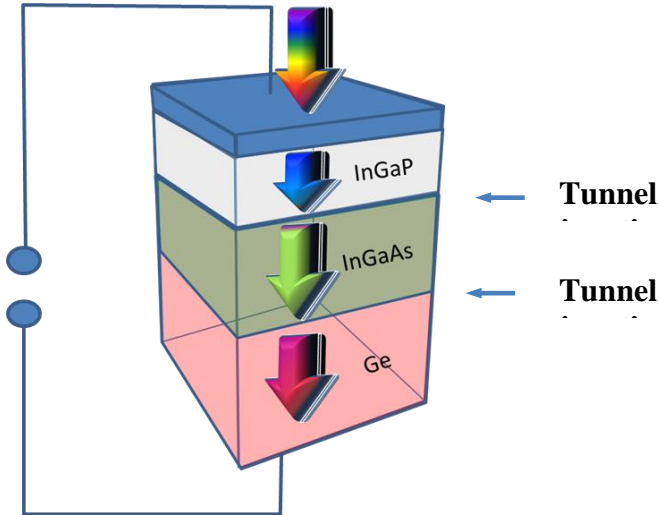


**Figure 1. Structure of a two terminal MJ solar cell composed of InGaP ( $E_g = 1.9$  eV), InGaAs ( $E_g = 1.39$  eV) and Ge ( $E_g = 0.67$  eV) junctions connected in series through two tunnel junctions.**

In a MJ solar cell, the “give and take” balance limitation between the current and the voltage can be overcome, as it is possible to collect photons in a wide wavelength region and, at the same time, get a voltage which is the sum of the voltages produced by the series-connected junctions.

It is quite seldom recognized that one of the successful proof of the quantum mechanics is the MJ solar cell device, since its working principle is based on the utilization of “Esaki tunnel diodes”[32]. The Esaki tunnel diodes are p-n (n-p) junctions formed between degenerate p-type materials and degenerate n-type materials. The variation of current with voltage for the diodes is controlled by quantum mechanical tunneling between the two sides of the diodes. The MJ solar cell works on the positive resistive part of the tunnel diode IV characteristic, so that the different junctions of the MJ device can be connected by “resistances”.

It is worthwhile to point out that the tunnel junctions are both the strength and weakness of the MJ device, since during the growth of the MJ layers, the temperature activates atoms diffusion, therefore the high doping level in the two sides of the diodes required for the tunnel effect can be reduced and the good functioning of the tunnel diode compromised.

This means that the higher the number of junctions, the more critical is the operation of the MJ device (especially at high concentration) and the temperature of the MOVPE growth process must be properly selected.

## 2. Modelling Multi-junction solar cells

*The determination of the “generation function” i.e. of photon flux in each layer of the MJ structure, is of paramount importance for the computation of the photovoltaic performance of a MJ solar cell. For this purpose, several mathematical methods have been developed. Among them, I describe the Hovel model and the transfer matrix method (TMM), as well as their limits. The TMM is developed in detail, starting from the Maxwell equation formulation till to determine the energy flux in each solar cell layer. The transfer matrix elements will then be used for the construction of the scattering matrix elements, at the base of the new mathematical approach that will be presented in chapter 3.*

The performances of a MJ solar cell can be determined in the following main steps: i) preliminary design of the solar cell structure, suitable for a certain solar spectrum, with the calculation of the related band diagram and the solution of the Poisson equation, ii) calculation of the EQE and the generated current in the active parts of the solar device, through the solution of the continuity equation, which allows checking the currents balance among the sub-cells and optimize the cell structure, iii) identification of the cell equivalent electrical model to establish a relationship between the current and the voltage, which eventually allows the fine tuning of the cell structure and designing the solar cell front contact (see Figure 2).

In order to solve the continuity equation, the generation rates of holes/electrons in excess with respect to the thermal equilibrium value have to be determined. For this purpose, according to the structures to be simulated, different mathematical models have been applied: from the most complex ones, based on Finite Element Analysis (FEA) which take into account 2D effects [33], or based on Rigorous Coupled-Wave Analysis (RCWA), for solar cells with nano-photonic designs [34], to the simpler and most popular ones, like the Hovel [35] and the Transfer Matrix Method (TMM) [36], [37], [38]. In particular, the Hovel model has been successfully applied to simulate the performance of optical thick single junction solar cells [39], while TMM has been widely applied for analysing the propagation of electromagnetic waves through planar stratified media, like the MJ structures [40], [41], [42] and through some organic thin films [43], where interference effects are more important.

As it can be expected, the more complex is the mathematical model for the calculation of the generation function, the more difficult is to find analytical solutions for the continuity equation, and when they are found, they are usually quite complicated [44], [45].

However, it will be shown that the generation function calculated by applying the TMM can be notably simplified and the continuity equation solved with simpler analytical solutions once the counter propagating waves in the active layers of the solar cell can be omitted.

This approximation is justified by the fact that the counter propagating waves introduce a very negligible variation in the Poynting vector. This was already reported by Deparis for a Si-based thin-film tandem solar cell structure [46] and here it will be also confirmed for a III-V-based MJ cell structure.

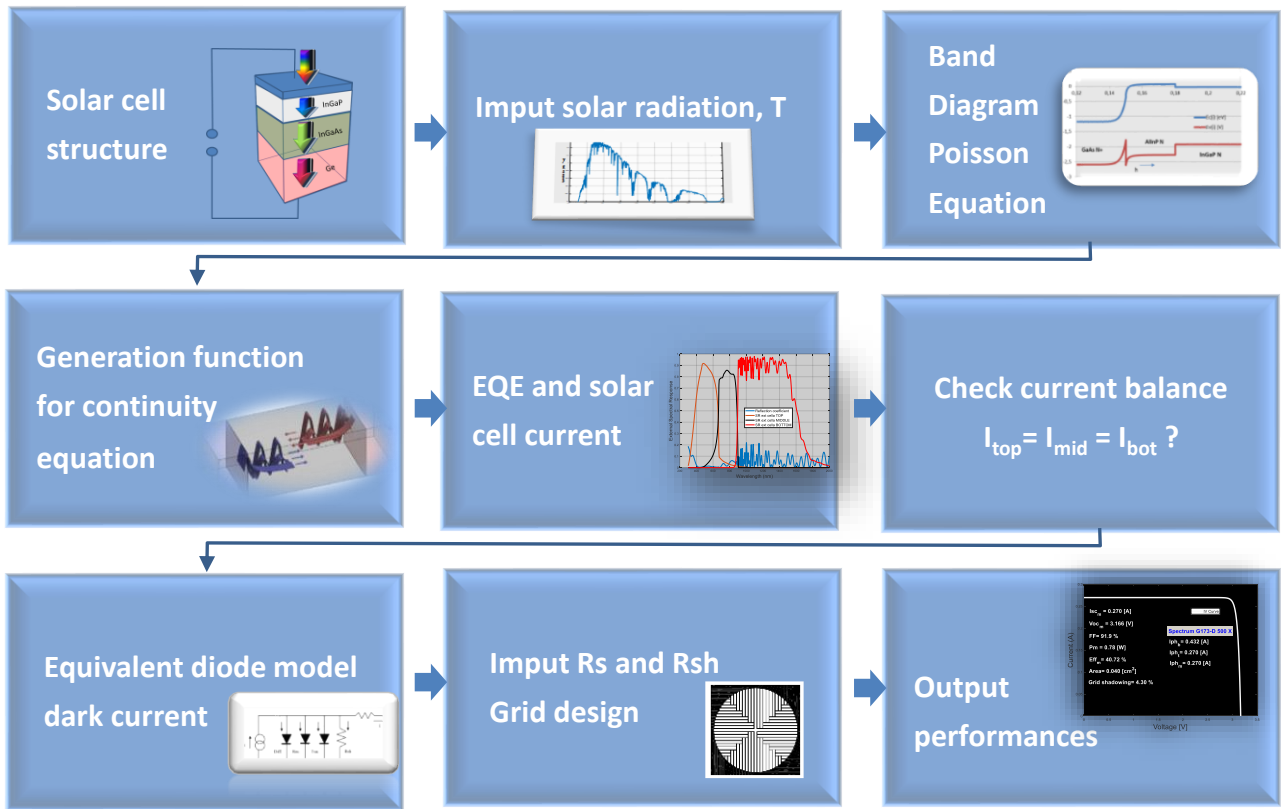


**Figure 2. Main steps for the calculation of the output performance of a MJ solar cell (as a particular case a triple junction solar cell is considered).**

Applying TMM, it can be discovered that this method can fail in the determination of the reflection coefficient in the short wavelength range for a MJ designed for improving the device voltage (obtained by thinning the solar cell and depositing on the back side a perfect mirror). For this reason in chapter 3, the numerical instability has been overcome by replacing TMM with a simplified Scattering Matrix Method (SMM) implemented from [47] with proper precaution.

For sake of completeness, the general assumptions adopted in the mathematical modelling and a brief description of the transport and continuity equation as well as a short retrieval of the Hovel model are introduced. The TMM, as introductory to the SMM, is described in detail.

## 2.1. General assumptions

The different mathematical methods here after presented have all in common the following assumptions:

1. One Dimension (edge effects are neglected).
2. Boltzmann approximation for the calculation of the carriers distribution. Non-degenerate semiconductors.
3. Low injection conditions.
4. All parameters, mobility, diffusion coefficient, lifetimes are assumed constant within each semiconductor material. Since the concentrations of dopant atoms in the base and emitter<sup>5</sup> are assumed uniform (quasi neutral region) the electric field value is zero outside the depletion region.
5. The mobility of minority carriers is supposed to depend on the doping of the side where majority carries are located. In reality, scattering by donors is different from that by acceptors, because repulsive potentials scatter less than attractive potentials of the same strength [48]. In other words, the minority carrier mobility is not equal to the majority carrier mobility, but it is higher. If the majority carrier mobility values obtained by Hall measurements are assumed for minority carriers, the related minority diffusion length values will be lower than the actual ones. Therefore, this assumption brings to a more conservative computation of the PV performances.
6. The solar cell window absorbs the solar light, however the carriers here produced by absorption are neglected for the computation of the photovoltaic current. This assumption can bring to underestimate the photovoltaic current, as reported in [49]. The same assumption is applied for the back-surface field (BSF) layers. The reason behind these assumptions is that such layers are usually very thin compared with base and emitter layers of the solar cell.
7. In the depletion region, owing to the strong electric field, it is assumed that all the generated carries are swept in opposite direction and collected. Instead of assuming a 100 % probability that the carries are swept in opposite direction and collected, it is also possible to introduce a “loss factor” by reducing the percentage of the collection probability.
8. The tunnel current peak value of each tunnel diode (TD) is supposed to be higher than the solar cell short circuit current value. Therefore, TD layers are considered only with respect to light absorption. The series resistance of the TD can be included in the total series resistance of the MJ device
9. For each absorbed photon an electron-hole pair is produced,, that is, the photon absorption rate [ $n \cdot ph \cdot s^{-1} \cdot m^{-3} \cdot nm^{-1}$ ] is equal to the carriers generation rate [ $n \cdot e^-/h^+ \cdot s^{-1} \cdot m^{-3} \cdot nm^{-1}$ ].

## 2.2. Transport and continuity equation

Transport and continuity equation are reported in several text books (see for example [50]). Hereafter a brief description is considered. In compositional homogeneous semiconductor, with no thermal gradient, the current densities can be determined by considering the drift and diffusion components.

---

<sup>5</sup> The term “emitter” comes from the fact that in a N-P junction, the N- type semiconductor emits or produces electrons that are transferred to the base, as in a transistor.

For the 1D case, the values of the holes and electron current densities are given respectively by:

$$J_p = q\mu_p p_n E - qD_p \frac{dp_n}{dx} \quad 2.1$$

$$J_n = q\mu_n n_p E + qD_n \frac{dn_p}{dx} \quad 2.2$$

Where:

$J_{p,n}$  = hole/electron current density in N-type/P-type semiconductor.

$\mu_{p,n}$  = mobility on holes/electrons.

$p_n$  = hole density in the N-type semiconductor.

$n_p$  = electron density in the P-type semiconductor.

$E$  = electric field

$D_{p,n}$  = holes/electron diffusion coefficient

The balance of electrons and holes in P-type and N-type regions are described by the continuity equations:

$$\frac{\partial n_p}{\partial t} = \frac{1}{q} \frac{dJ_n}{dx} + G_n - U_n \quad 2.3$$

$$\frac{\partial p_n}{\partial t} = -\frac{1}{q} \frac{dJ_p}{dx} + G_p - U_p \quad 2.4$$

Where,  $J_p$  and  $J_n$  are given by Eq.2.1 and Eq.2.2,  $G_{p,n}$  is the volume generation rate of holes/electrons in excess with respect to the thermal equilibrium,  $U_{n,p}$  is the volume recombination rate of holes/electrons in excess with respect to the thermal equilibrium, which can be expressed by [51]:

$$U_n = \frac{\Delta n}{\tau_n} ; U_p = \frac{\Delta p}{\tau_p} \quad 2.5$$

where  $\Delta n$  and  $\Delta p$  are the excess of minority carriers in P-type and N-type material repetitively and  $\tau_n$  and  $\tau_p$  are the electron and holes lifetime. For each sub-junction, the continuity equations are solved in the two *quasi-neutral regions* of the emitter and the base (where the electric fields are assumed equal to zero), by considering proper boundary conditions. (see Figure 3).

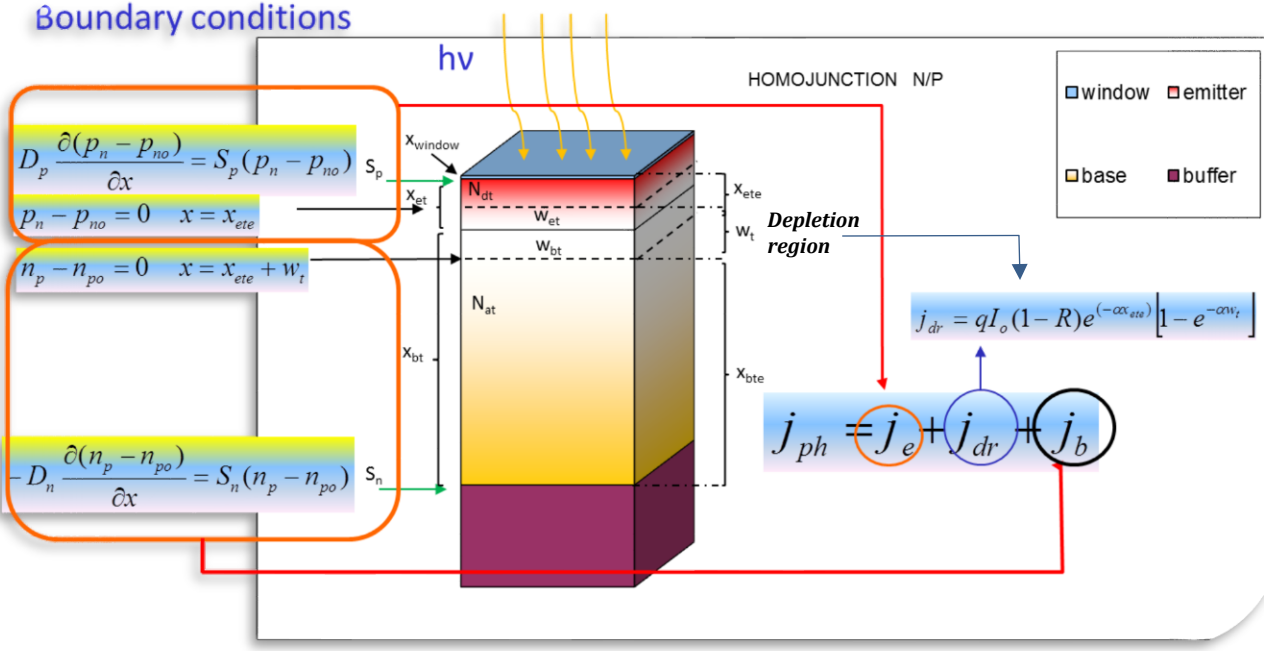


**Figure 3.** Schematic of each single junction sub cell and boundary conditions considered to solve the continuity equation in the emitter and base in order to get the short circuit current. The expression of the current generated in the depletion region ( $J_{dr}$ ) is also explicitly shown considering the Hovel model.

The equations from Eq.2.1 to Eq.2.4 are thus solved for each sub cell of the MJ device, identifying for each sub cell the proper incident flux. In all cases which will follow, in first approximation, the generation terms owing to *self-excitation* [52] and *photon coupling effects* [53] are not explicitly considered. Self-excitation can be easily encompassed by introducing an effective lifetime, while photon coupling effects will be considered in a future work.

### 2.3. Hovel model

In the Hovel mathematical model [35] the multiple light reflections inside the MJ structure are neglected, therefore, the generation term,  $G$ , is calculated only considering positive light flux,  $F(\lambda, x)$ , absorbed according to the Beer–Lambert law. The reflection coefficient,  $R(\lambda)$ , which takes into account the solar light reflected at the solar cells surface, is computed only considering the interference effects produced inside the coating and the solar cell window layer. By considering the assumption 9 of chapter 2.1, it holds:

$$F(\lambda, x) = [1 - R(\lambda)]F(\lambda, 0)e^{-\alpha(x)x} \quad 2.6$$

$$G(\lambda, x) = -\frac{dF(x, \lambda)}{dx} = \alpha(\lambda)F(\lambda)[1 - R(\lambda)]e^{-\alpha(x)x} \quad 2.7$$

Where “ $\lambda$ ” and “ $x$ ” are respectively the wavelength and the path travelled by light. The continuity equations are then solved by replacing in the Eq.2.3 and Eq.2.4 the generation term given by Eq.2.7. The electron and hole density distributions in excess with respect to the equilibrium value are then introduced in Eq.2.1 and Eq.2.2 to get the electron and hole currents.

## 2.4. The transfer matrix method

In MJ solar cells, several layers with different refraction index and thicknesses comparable with light wavelength are present. This means that multiple reflections and interference phenomena take place inside the MJ structure and they can strongly modify the light distribution in the photovoltaic active layers of the solar cells. The transfer matrix method (TMM) is a suitable mathematical method which considers the complex nature of the wave vector and is able to consider multiple reflections and interference phenomena of the forward and backward travelling waves. The calculated electromagnetic radiation by TMM can then be inserted in the semiconductor continuity equations to determine the photo-carrier generation, replacing the flux term used by Hovel. It has been pointed out that the utilization of TMM to describe the position dependent flux in the solar cells can become prohibitively complicated even for relatively few layers [45]. In Chapter 3, the generation function will be simplified, and the continuity equation solved with simple analytical expressions even by applying the TMM. Despite TMM is very popular, rarely the method has been explained in detail. Hereafter the formalism of the TMM is then developed step by step, from the contribution of Yuffa and Scales [47].

Let's consider the structure reported in Figure 4. The following starting general assumptions are considered:

1. Solar Radiation propagates like plane waves coming from the #0 layer (air)
2. The solar intensity is not polarized, and it can be thought as equally distributed in the transvers magnetic (TM) and transvers electric (TE) polarization modes.
3. Without loss of generality, we can set null the component of the wave vector along the z direction,  $k_z = 0$ , because we can always rotate the coordinate system so that the incidence plane is the x-y plane.
4. The substrate, or more generally, the last layer, (#N layer) is very thick and the reflected radiation at its back can be neglected; this means that for convenience of calculus, the N# layer thickness can be set to zero.
5. Each layer is homogeneous and isotropic.
6. lateral dimensions of the MJ solar cell are much greater than the thickness (1D problem)
7. Source-free layers and interfaces (current density,  $J$ , and charge density,  $\varrho$ , are set to zero).

The starting equations for determining the electromagnetic radiation inside the MJ structure are the source-free macroscopic Maxwell equations, which in the SI Unit are given by:

$$\nabla \times \mathbf{H} = \frac{\partial \mathbf{D}}{\partial t} \quad 2.8$$

$$\nabla \times \mathbf{E} = -\frac{\partial \mathbf{B}}{\partial t} \quad 2.9$$

$$\nabla \cdot \mathbf{D} = 0 \quad 2.10$$

$$\nabla \cdot \mathbf{B} = 0 \quad 2.11$$

$$\mathbf{D} = \epsilon \mathbf{E} \quad 2.12$$

$$\mathbf{B} = \mu \mathbf{H}$$

2.13

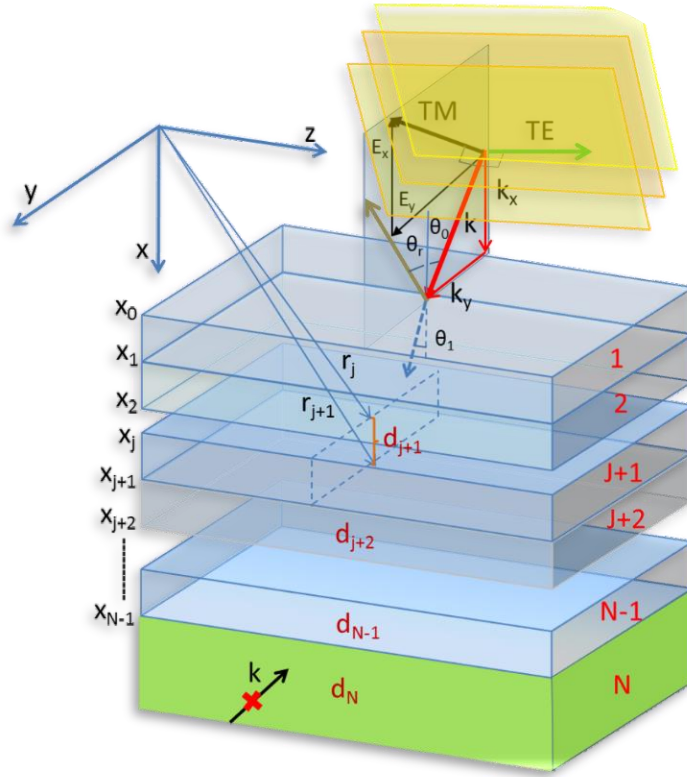


**Figure 4.** Schematic of a MJ structure. Solar Radiation propagates like plane waves coming from the #0 layer (air). The solar intensity is not polarized, and it can be thought as equally distributed in the TM and TE polarization modes. When the substrate is very thick, the backward propagating wave coming from the substrate-air interface can be neglected.

Where,  $\mathbf{E}$  is the electric field,  $\mathbf{D}$  is the displacement field,  $\mathbf{B}$  is the magnetic field,  $\mathbf{H}$  is the magnetic intensity,  $\varepsilon$  and  $\mu$  are, respectively, the complex permittivity and complex permeability. The bold character has been used to indicate the vector notation. The solar radiation propagates like plane waves coming from the #0 layer (air). Plane waves can be generally described by:

$$\mathbf{E}(\mathbf{r}, t) = \mathbf{E}(\mathbf{r}) e^{i(\mathbf{k} \cdot \mathbf{r} - \omega t)} \quad 2.14$$

$$\mathbf{H}(\mathbf{r}, t) = \mathbf{H}(\mathbf{r}) e^{i(\mathbf{k} \cdot \mathbf{r} - \omega t)} \quad 2.15$$

Where  $\mathbf{k}$  is the complex wavenumber,  $\omega$  is the angular frequency,  $\mathbf{r}$  is the position vector.

By considering Eq.2.12 and Eq. 2.13 and by replacing Eq.2.14 in Eq.2.8, and Eq.2.15 in Eq.2.9 it holds:

$$\nabla \times \mathbf{H}(\mathbf{r}, t) = -i\omega\varepsilon\mathbf{E}(\mathbf{r}, t) \quad 2.16$$

$$\nabla \times \mathbf{E}(\mathbf{r}, t) = i\omega\mu\mathbf{H}(\mathbf{r}, t) \quad 2.17$$

By applying the curl to Eq.2.16 and by considering Eq.2.17, we can write:

$$\nabla \times \nabla \times \mathbf{H}(\mathbf{r}, t) = \omega^2\mu\varepsilon\mathbf{H}(\mathbf{r}, t) \quad 2.18$$

Similarly, by applying the curl to the Eq.2.17 and by considering the Eq.2.16, we can get:

$$\nabla \times \nabla \times \mathbf{E}(\mathbf{r}, t) = \omega^2 \mu \epsilon \mathbf{E}(\mathbf{r}, t) \quad 2.19$$

By remembering that for a generic vector  $\mathbf{T}$ , it holds:

$$\nabla \times \nabla \times \mathbf{T} = \nabla(\nabla \cdot \mathbf{T}) - \nabla^2 \mathbf{T} \quad 2.20$$

and by considering that  $\nabla \cdot \mathbf{E} = 0$  and  $\nabla \cdot \mathbf{H} = 0$ , Eq.2.18 and Eq.2.19 become:

$$\nabla \times \nabla \times \mathbf{H}(\mathbf{r}, t) = -\nabla^2 \mathbf{H}(\mathbf{r}, t) \quad 2.21$$

$$\nabla \times \nabla \times \mathbf{E}(\mathbf{r}, t) = -\nabla^2 \mathbf{E}(\mathbf{r}, t) \quad 2.22$$

Eq.2.21 and Eq.2.22 along with Eq.2.18 and Eq.2.19 allow showing that the electric field and the magnetic intensity satisfy the Helmholtz wave equations:

$$\nabla^2 \mathbf{H}(\mathbf{r}, t) + k^2 \mathbf{H}(\mathbf{r}, t) = \mathbf{0} \quad 2.23$$

$$\nabla^2 \mathbf{E}(\mathbf{r}, t) + k^2 \mathbf{E}(\mathbf{r}, t) = \mathbf{0} \quad 2.24$$

With:

$$k^2 = \omega^2 \mu \epsilon \quad 2.25$$

and:

$$k^2 = \frac{\omega^2}{v^2} \quad 2.26$$

where  $v$  is the wave propagation velocity, and according to Figure 4:

$$k^2 = k_x^2 + k_y^2 \rightarrow k_x = \sqrt{\frac{\omega^2}{v^2} - k_y^2} \quad 2.27$$

The boundary conditions for a source-free interface separating two adjacent layers  $j$  and  $j+1$  can be obtained by applying the divergence and Stokes theorems (see Figure 5).

$$\mathbf{n} \cdot (\mathbf{B}_j - \mathbf{B}_{j+1}) = \mathbf{0} \quad 2.28$$

$$\mathbf{n} \times (\mathbf{E}_j - \mathbf{E}_{j+1}) = \mathbf{0} \quad 2.29$$

$$\mathbf{n} \cdot (\mathbf{D}_j - \mathbf{D}_{j+1}) = \mathbf{0} \quad 2.30$$

$$\mathbf{n} \times (\mathbf{H}_j - \mathbf{H}_{j+1}) = \mathbf{0} \quad 2.31$$

Eq.2.28 and Eq.2.30 show that the components of the magnetic field and displacement field *normal* to interface are conserved, while Eq.2.29 and Eq.2.31 show that the components of the electric field and magnetic intensity *tangent* to interface are conserved.

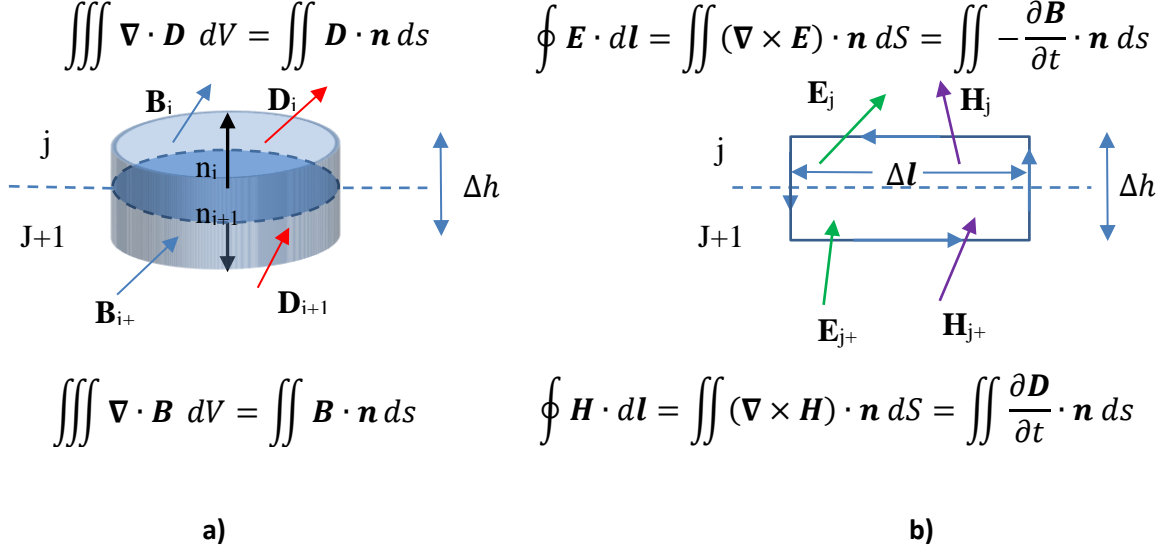


**Figure 5. Boundary condition for  $B$ ,  $D$ ,  $E$  and  $H$ .** a) Divergence theorem applied to  $B$  and  $D$ .  $B$  and  $D$  are thought uniform inside the infinitesimal volume of the cylinder. The height  $\Delta h$  of the cylinder volume is reduced to zero so that the flux of  $B$  and  $D$  has to be calculated only through the top and bottom base of the cylinder; b) Stokes theorem applied to  $H$  and  $E$ .  $H$  and  $E$  are thought uniform along the infinitesimal path  $\Delta l$  of the circuit. The height  $\Delta h$  of the circuit is reduced to zero so that the contribution of  $H$  and  $E$  is different from zero only along the horizontal part of the circuit and the surface integrals become zero, while  $\frac{\partial B}{\partial t}$  and  $\frac{\partial D}{\partial t}$  are finite.

A useful relationship between  $\mathbf{E}$  and  $\mathbf{H}$  can be determined considering the following relationship between a scalar quantity  $\beta$  and a vector  $\mathbf{T}$ :

$$\nabla \times (\beta \mathbf{T}) = \beta(\nabla \times \mathbf{T}) + (\nabla \beta) \times \mathbf{T} \quad 2.32$$

From Eq.2.14 and Eq.2.15, and setting:

$$\beta = e^{i(k \cdot r - \omega t)}$$

and

$$\mathbf{T} = \mathbf{E}(r), \mathbf{H}(r)$$

It holds:

$$\nabla \times \mathbf{E}(r, t) = \{\nabla \times \mathbf{E}(r) + ik \times \mathbf{E}(r)\}e^{i(k \cdot r - \omega t)} \quad 2.33$$

$$\nabla \times \mathbf{H}(r, t) = \{\nabla \times \mathbf{H}(r) + ik \times \mathbf{H}(r)\}e^{i(k \cdot r - \omega t)} \quad 2.34$$

By considering Eq.2.16 and Eq.2.17, we get:

$$\mathbf{H}(r) = \frac{\nabla \times \mathbf{E}(r)}{i\omega\mu} + \frac{\mathbf{k} \times \mathbf{E}(r)}{\omega\mu} \quad 2.35$$

$$\mathbf{E}(\mathbf{r}) = - \left[ \frac{\nabla \times \mathbf{H}(\mathbf{r})}{i\omega\varepsilon} + \frac{\mathbf{k} \times \mathbf{H}(\mathbf{r})}{\omega\varepsilon} \right] \quad 2.36$$

It is possible to show that the first right terms of Eq.2.35 and Eq.2.36 are null. Let's start considering  $\nabla \times \mathbf{E}(\mathbf{r})$ :

$$\begin{aligned} \nabla \times \mathbf{E}(\mathbf{r}) &= \begin{bmatrix} \hat{\mathbf{x}} & \hat{\mathbf{y}} & \hat{\mathbf{z}} \\ \frac{\partial}{\partial x} & \frac{\partial}{\partial y} & \frac{\partial}{\partial z} \\ E_x(\mathbf{r}) & E_y(\mathbf{r}) & E_z(\mathbf{r}) \end{bmatrix} = \\ &= \hat{\mathbf{x}} \left( \frac{\partial E_z(\mathbf{r})}{\partial y} - \frac{\partial E_y(\mathbf{r})}{\partial z} \right) - \hat{\mathbf{y}} \left( \frac{\partial E_z(\mathbf{r})}{\partial x} - \frac{\partial E_x(\mathbf{r})}{\partial z} \right) + \hat{\mathbf{z}} \left( \frac{\partial E_y(\mathbf{r})}{\partial x} - \frac{\partial E_x(\mathbf{r})}{\partial y} \right) \end{aligned}$$

As we have assumed each layer homogeneous and isotropic, all the partials derivate along y and z are null, therefore:

$$\nabla \times \mathbf{E}(\mathbf{r}) = -\hat{\mathbf{y}} \left( \frac{\partial E_z(\mathbf{r})}{\partial x} \right) + \hat{\mathbf{z}} \left( \frac{\partial E_y(\mathbf{r})}{\partial x} \right)$$

However, as the components of the electric field tangent to interface are conserved, also the last expression has to be null. The same procedure can be applied for the magnetic intensity. We can then write:

$$\mathbf{H}(\mathbf{r}) = \frac{\mathbf{k} \times \mathbf{E}(\mathbf{r})}{\omega\mu} \quad 2.37$$

$$\mathbf{E}(\mathbf{r}) = -\frac{\mathbf{k} \times \mathbf{H}(\mathbf{r})}{\omega\varepsilon} \quad 2.38$$

and multiplying by  $e^{i(\mathbf{k} \cdot \mathbf{r} - \omega t)}$ :

$$\mathbf{H}(\mathbf{r}, t) = \frac{\mathbf{k} \times \mathbf{E}(\mathbf{r}, t)}{\omega\mu} \quad 2.39$$

$$\mathbf{E}(\mathbf{r}, t) = -\frac{\mathbf{k} \times \mathbf{H}(\mathbf{r}, t)}{\omega\varepsilon} \quad 2.40$$

The fact that the factors  $\frac{\nabla \times \mathbf{E}(\mathbf{r})}{i\omega\mu}$  and  $\frac{\nabla \times \mathbf{H}(\mathbf{r})}{i\omega\varepsilon}$  can be neglected means that both  $\mathbf{E}(\mathbf{r})$  and  $\mathbf{H}(\mathbf{r})$  in reality are not dependent by  $\mathbf{r}$ , that is, they do not change when the wave propagates in each layer. Therefore, the spatial dependence of  $\mathbf{E}$  and  $\mathbf{H}$  is only contained in the term  $e^{i(\mathbf{k} \cdot \mathbf{r} - \omega t)}$ .

By using the Eq.2.39 and considering the boundary condition given by Eq.2.28 and Eq.2.29, it is possible to arrive to an important expression for the wave vector.

According to Figure 4, the normal to the interfaces is along the  $\hat{\mathbf{x}}$ , therefore the Eq.2.28 becomes:

$$\mu_j H_{j,x} e^{i(k_j \cdot r_j - \omega t)} = \mu_{j+1} H_{j+1,x} e^{i(k_{j+1} \cdot r_j - \omega t)} \quad 2.41$$

The “x” component of the magnetic intensity can be obtained from Eq.2.39, by pointing out that the plane of incidence is defined by  $\hat{x}$  and  $\hat{y}$  and therefore,  $k_z=0$ :

$$H_x = \frac{\mathbf{k}_y \cdot \mathbf{E}_z}{\omega \mu} \quad 2.42$$

By replacing  $H_{j,x}$  and  $H_{j+1,x}$  in Eq.2.41 with the expression given by Eq.2.42:

$$k_{j,y} E_{j,z}(\mathbf{r}_j, t) = k_{j+1,y} E_{j+1,z}(\mathbf{r}_j, t) \quad 2.43$$

Where it has been assumed  $\mu_j = \mu_{j+1}$ . From Eq.2.29:

$$\begin{aligned} \mathbf{n} \times [\mathbf{E}_j(\mathbf{r}_j, t) - \mathbf{E}_{j+1}(\mathbf{r}_j, t)] &= \\ &= \begin{bmatrix} \hat{x} & \hat{y} & \hat{z} \\ 1 & 0 & 0 \\ \mathbf{E}_{j,x}(\mathbf{r}_j, t) - \mathbf{E}_{j+1,x}(\mathbf{r}_j, t) & \mathbf{E}_{j,y}(\mathbf{r}_j, t) - \mathbf{E}_{j+1,y}(\mathbf{r}_j, t) & \mathbf{E}_{j,z}(\mathbf{r}_j, t) - \mathbf{E}_{j+1,z}(\mathbf{r}_j, t) \end{bmatrix} \\ &= -\hat{y} [\mathbf{E}_{j,z}(\mathbf{r}_j, t) - \mathbf{E}_{j+1,z}(\mathbf{r}_j, t)] + \hat{z} [\mathbf{E}_{j,y}(\mathbf{r}_j, t) - \mathbf{E}_{j+1,y}(\mathbf{r}_j, t)] = 0 \end{aligned}$$

Therefore:

$$E_{j,z}(\mathbf{r}_j, t) = E_{j+1,z}(\mathbf{r}_j, t) \quad 2.44$$

$$E_{j,y}(\mathbf{r}_j, t) = E_{j+1,y}(\mathbf{r}_j, t) \quad 2.45$$

Considering Eq.2.43 and Eq.2.44, it must be:

$$k_{j,y} = k_{j+1,y} = k_{0,y} \quad 2.46$$

The wave vector is conserved along  $\hat{y}$  (that is, along the direction parallel to the interfaces) and its value is real. In the following, the electric field and magnetic intensity will be calculated for TM and TE polarization and then the boundary condition will be applied in the two cases.

### 2.4.1. Matrix elements for TM polarization

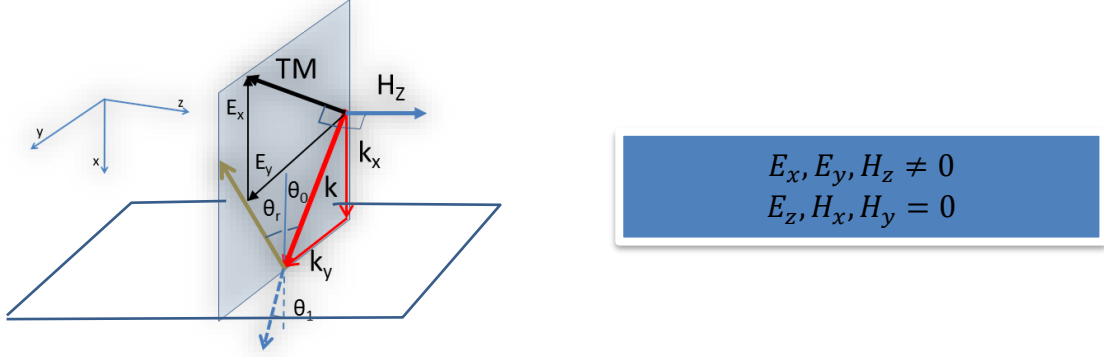


**Figure 6. TM polarization representation: the electric field is in the plane of incidence while the magnetic intensity is perpendicular to the plane on incidence.**

The wave vector can be written as:

$$\mathbf{k}^\pm = \pm \hat{\mathbf{x}}k_x + \hat{\mathbf{y}}k_y \quad 2.47$$

The sign “+” indicates a transmitted wave propagating in the  $+x$  direction, while the sign “-“ indicates a reflected wave propagating in the  $-x$  direction; there is no reflection along  $y$  direction, as the side dimension of the solar cells is assumed much bigger than the solar cell thickness (therefore in  $y$  direction the cell is optically thick). By introducing the Eq.2.14 and Eq.2.47 in Eq.2.39 we get:

$$\mathbf{H}^\pm(\mathbf{r}, t) = \frac{1}{\omega\mu} \begin{bmatrix} \hat{\mathbf{x}} & \hat{\mathbf{y}} & \hat{\mathbf{z}} \\ \pm k_x & k_y & 0 \\ E_x(\mathbf{r}, t) & E_y(\mathbf{r}, t) & 0 \end{bmatrix} = \frac{1}{\omega\mu} \hat{\mathbf{z}} [\pm k_x E_y(\mathbf{r}, t) - k_y E_x(\mathbf{r}, t)] \quad 2.48$$

Setting:

$$E^\pm = \frac{[\pm k_x E_y - k_y E_x]}{\epsilon\mu\omega^2} \quad 2.49$$

It holds:

$$\mathbf{H}^\pm(\mathbf{r}, t) = \hat{\mathbf{z}} E^\pm \epsilon\omega e^{i(\mathbf{k}^\pm \cdot \mathbf{r} - \omega t)} \quad 2.50$$

$\mathbf{H}^\pm$  has the dimension of  $[\text{Cs}^{-1}\text{m}^{-1}]$ , while the dimension of  $E^\pm$  is [V]. By introducing in the Eq.2.40, the expression  $\mathbf{k}$  and  $\mathbf{H}$  given, respectively by Eq.2.47 in Eq.2.50, we get:

$$\mathbf{E}^\pm(\mathbf{r}, t) = [\pm \hat{\mathbf{y}}k_x - \hat{\mathbf{x}}k_y] E^\pm e^{i(\mathbf{k}^\pm \cdot \mathbf{r} - \omega t)} \quad 2.51$$

The total magnetic intensity and electric field are the sum of the two components propagating in opposite direction along “x”. For each layer “j“, as  $e^{i(\mathbf{k}^\pm_j \cdot \mathbf{r} - \omega t)} = e^{i(\pm k_{j,x}x + k_{j,y}y)} e^{-i\omega t}$ , it holds:

$$\mathbf{H}_j(\mathbf{r}, t) = \hat{\mathbf{z}} \epsilon_j \omega [E_j^+ e^{ik_{j,x}x} + E_j^- e^{-ik_{j,x}x}] e^{i(k_{j,y}y - \omega t)} \quad 2.52$$

$$\mathbf{E}_j(\mathbf{r}, t) = [E_j^+ (\hat{\mathbf{y}}k_{j,x} - \hat{\mathbf{x}}k_{j,y}) e^{ik_{j,x}x} - E_j^- (\hat{\mathbf{y}}k_{j,x} + \hat{\mathbf{x}}k_{j,y}) e^{-ik_{j,x}x}] e^{i(k_{j,y}y - \omega t)} \quad 2.53$$

Once the expressions for the magnetic intensity and electric field for TM polarization have been determined, it is possible to apply the boundary condition at  $\mathbf{r}_j$  by using Eq.2.29 and Eq.2.31 (see Figure 7).

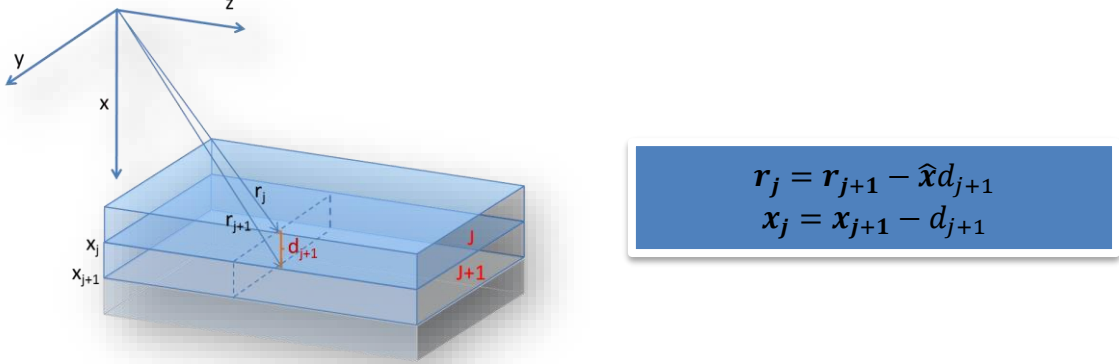


**Figure 7.** Geometrical representation of the interface between layer  $j$  and  $j+1$ . The coordinate  $x_j$  identifies the end of the layer  $j$ .

$$\begin{aligned} \mathbf{n} \times \mathbf{E}_j(\mathbf{r}_j, t) &= \\ e^{i(k_{j,y}y_j - \omega t)} \begin{bmatrix} \hat{x} & \hat{y} & \hat{z} \\ 1 & 0 & 0 \\ -E_j^+ k_{j,y} e^{ik_{j,x}x_j} - E_j^- k_{j,y} e^{-ik_{j,x}x_j} & E_j^+ k_{j,x} e^{ik_{j,x}x_j} - E_j^- k_{j,x} e^{-ik_{j,x}x_j} & 0 \end{bmatrix} & 2.54 \\ &= \hat{\mathbf{z}} [E_j^+ k_{j,x} e^{ik_{j,x}x_j} - E_j^- k_{j,x} e^{-ik_{j,x}x_j}] e^{i(k_{j,y}y_j - \omega t)} \end{aligned}$$

Therefore:

$$\begin{aligned} \mathbf{n} \times \mathbf{E}_{j+1}(\mathbf{r}_j, t) &= \\ -\hat{\mathbf{z}} [E_{j+1}^+ k_{j+1,x} e^{ik_{j+1,x}x_j} - E_{j+1}^- k_{j+1,x} e^{-ik_{j+1,x}x_j}] e^{i(k_{j+1,y}y_j - \omega t)} & 2.55 \end{aligned}$$

By remembering the conservation of the wave vector along “y”, it holds:

$$E_j^+ k_{j,x} e^{ik_{j,x}x_j} - E_j^- k_{j,x} e^{-ik_{j,x}x_j} = E_{j+1}^+ k_{j+1,x} e^{ik_{j+1,x}x_j} - E_{j+1}^- k_{j+1,x} e^{-ik_{j+1,x}x_j} \quad 2.56$$

$$\begin{aligned} \mathbf{n} \times \mathbf{H}_j(\mathbf{r}_j, t) &= e^{i(k_{j,y}y_j - \omega t)} \begin{bmatrix} \hat{x} & \hat{y} & \hat{z} \\ 1 & 0 & 0 \\ 0 & 0 & \varepsilon_j \omega [E_j^+ e^{ik_{j,x}x_j} + E_j^- e^{-ik_{j,x}x_j}] \end{bmatrix} \\ &= \hat{\mathbf{y}} \varepsilon_j \omega [E_j^+ e^{ik_{j,x}x_j} + E_j^- e^{-ik_{j,x}x_j}] e^{i(k_{j,y}y_j - \omega t)} \end{aligned} \quad 2.57$$

In the same way, since  $\omega$  does not change at the boundary between layers:

$$\mathbf{n} \times \mathbf{H}_{j+1}(\mathbf{r}_j, t) = \hat{\mathbf{y}} \varepsilon_{j+1} \omega [E_{j+1}^+ e^{ik_{j+1,x}x_j} + E_{j+1}^- e^{-ik_{j+1,x}x_j}] e^{i(k_{j+1,y}y_j - \omega t)} \quad 2.58$$

Hence:

$$\varepsilon_j E_j^+ e^{ik_{j,x}x_j} + \varepsilon_j E_j^- e^{-ik_{j,x}x_j} = \varepsilon_{j+1} E_{j+1}^+ e^{ik_{j+1,x}x_j} + \varepsilon_{j+1} E_{j+1}^- e^{-ik_{j+1,x}x_j} \quad 2.59$$

Eq.2.56 and Eq.2.59 can be written in a more compact form by setting:

$$N_j^\pm = \pm k_{j,x} E_j^\pm e^{\pm ik_{j,x}x_j} \quad 2.60$$

where,  $N_j^\pm$  denotes the y-component of the electric field at the end of the layer j. Defining  $w_j$  as:

$$w_j = \frac{\varepsilon_j}{k_{j,x}} \quad 2.61$$

and referring to Figure 7,

$$e^{\pm ik_{j+1,x}x_j} = e^{\pm ik_{j+1,x}(x_{j+1} - d_{j+1})} \quad 2.62$$

By considering Eq.2.60 in Eq.2.56 and in Eq.2.59, we get:

$$N_j^+ + N_j^- = N_{j+1}^+ e^{-ik_{j+1,x}d_{j+1}} + N_{j+1}^- e^{ik_{j+1,x}d_{j+1}} \quad 2.63$$

$$w_j(N_j^+ - N_j^-) = w_{j+1}(N_{j+1}^+ e^{-ik_{j+1,x}d_{j+1}} - N_{j+1}^- e^{ik_{j+1,x}d_{j+1}}) \quad 2.64$$

Since we have N interfaces (at  $x_0, x_1, \dots, x_{N-1}$ ), Eq.2.63 and Eq.2.64 form a system of 2N equations with  $N_1^+, N_2^+, \dots, N_N^+$ ,  $N_1^-, N_2^-, \dots, N_{N-1}^- = 2N$  unknowns. In fact,  $N_0^+$  is known, as it can be shown related, through the Poynting vector, to the input electromagnetic field (i.e. to the incident solar radiation, see Eq.2.101), while  $N_N^- = 0$ , since there is no electromagnetic radiation coming back from the last layer (very thick).

As far as the wave vectors are concerned, recalling Eq.2.25, Eq.2.26 and Eq.2.27, and the Snell's law it can be easily shown that:

$$k_{j,x} = \frac{2\pi}{\lambda_0} n_j \cos \vartheta_j \quad 2.65$$

Where  $n_j$  and  $\vartheta_j$  are respectively the complex refractive index and refractive angle related to the layer j and  $\lambda_0$  is the wavelength of the plane wave propagating in the layer.

By setting:

$$\Psi_j^\pm = e^{\pm ik_{j,x}d_j} \quad 2.66$$

Eq.2.63 and Eq.2.64 can be further simplified and written as:

$$N_j^+ + N_j^- = N_j^+ \Psi_{j+1}^- + N_j^- \Psi_{j+1}^+ \quad 2.67$$

$$w_j(N_j^+ - N_j^-) = w_{j+1}(N_{j+1}^+ \Psi_{j+1}^- - N_{j+1}^- \Psi_{j+1}^+) \quad 2.68$$

It is possible to express the above equations by solving with respect to  $N_j^+$  and  $N_j^-$ :

$$\mathbf{x}_j^+ = \frac{1}{2} \left[ \mathbf{x}_{j+1}^- \Psi_{j+1}^- \left( 1 + \frac{w_{j+1}}{w_j} \right) + \mathbf{x}_{j+1}^+ \Psi_{j+1}^+ \left( 1 - \frac{w_{j+1}}{w_j} \right) \right] \quad 2.69$$

$$\mathbf{x}_j^- = \frac{1}{2} \left[ \mathbf{x}_{j+1}^- \Psi_{j+1}^- \left( 1 - \frac{w_{j+1}}{w_j} \right) + \mathbf{x}_{j+1}^+ \Psi_{j+1}^+ \left( 1 + \frac{w_{j+1}}{w_j} \right) \right] \quad 2.70$$

By using the matrix notation:

$$\begin{bmatrix} \mathbf{x}_j^+ \\ \mathbf{x}_j^- \end{bmatrix} = \frac{1}{2w_j} \begin{bmatrix} \Psi_{j+1}^- (w_j + w_{j+1}) & \Psi_{j+1}^+ (w_j - w_{j+1}) \\ \Psi_{j+1}^- (w_j - w_{j+1}) & \Psi_{j+1}^+ (w_j + w_{j+1}) \end{bmatrix} \begin{bmatrix} \mathbf{x}_{j+1}^+ \\ \mathbf{x}_{j+1}^- \end{bmatrix} \quad 2.71$$

Therefore, for each layer we can define a matrix  $M_j$ :

$$M_j = \frac{1}{2w_{j-1}} \begin{bmatrix} \Psi_j^- (w_{j-1} + w_j) & \Psi_j^+ (w_{j-1} - w_j) \\ \Psi_j^- (w_{j-1} - w_j) & \Psi_j^+ (w_{j-1} + w_j) \end{bmatrix} \quad 2.72$$

Eq.2.71 becomes:

$$\begin{bmatrix} \mathbf{x}_j^+ \\ \mathbf{x}_j^- \end{bmatrix} = M_{j+1} \begin{bmatrix} \mathbf{x}_{j+1}^+ \\ \mathbf{x}_{j+1}^- \end{bmatrix} \quad 2.73$$

It is straightforward to see that the matrix  $M_{j+1}$  can be expressed as a product of an “interface” and “propagation” matrix, which describe the reflection of the electric field at the interface  $j, j+1$  and the propagation of the electric field inside the layer  $j+1$ :

$$M_{j+1} = \frac{w_j + w_{j+1}}{2w_j} \underbrace{\begin{bmatrix} 1 & \frac{w_j - w_{j+1}}{w_j + w_{j+1}} \\ \frac{w_j - w_{j+1}}{w_j + w_{j+1}} & 1 \end{bmatrix}}_{\text{Interface}} \underbrace{\begin{bmatrix} \Psi_{j+1}^- & 0 \\ 0 & \Psi_{j+1}^+ \end{bmatrix}}_{\text{Propagation}} \quad 2.74$$

Where:

$$\frac{w_j + w_{j+1}}{2w_j} \begin{bmatrix} 1 & \frac{w_j - w_{j+1}}{w_j + w_{j+1}} \\ \frac{w_j - w_{j+1}}{w_j + w_{j+1}} & 1 \end{bmatrix} = \frac{1}{t_{j,j+1}} \begin{bmatrix} 1 & r_{j,j+1} \\ r_{j,j+1} & 1 \end{bmatrix} \quad 2.75$$

$t_{j,j+1}$  and  $r_{j,j+1}$ , are, respectively, the Fresnel transmission and reflection coefficient for TM polarization

The solution of the linear system expressed by Eq.2.71 or Eq.2.73 is easily obtained pointing out that:

$$\begin{bmatrix} \mathbf{x}_0^+ \\ \mathbf{x}_0^- \end{bmatrix} = M_1 \begin{bmatrix} \mathbf{x}_1^+ \\ \mathbf{x}_1^- \end{bmatrix}, \quad \begin{bmatrix} \mathbf{x}_1^+ \\ \mathbf{x}_1^- \end{bmatrix} = M_2 \begin{bmatrix} \mathbf{x}_2^+ \\ \mathbf{x}_2^- \end{bmatrix} \rightarrow \begin{bmatrix} \mathbf{x}_0^+ \\ \mathbf{x}_0^- \end{bmatrix} = M_1 M_2 \begin{bmatrix} \mathbf{x}_2^+ \\ \mathbf{x}_2^- \end{bmatrix} \quad 2.76$$

Therefore.

$$\begin{bmatrix} \mathbf{x}_0^+ \\ \mathbf{x}_0^- \end{bmatrix} = M_1 M_2 \dots M_N \begin{bmatrix} \mathbf{x}_N^+ \\ \mathbf{x}_N^- \end{bmatrix} \quad 2.77$$

Since  $\mathbf{x}_N^- = 0$ , it holds:

$$\begin{bmatrix} \mathbf{x}_0^+ \\ \frac{\mathbf{x}_N^+}{\mathbf{x}_N^-} \\ \mathbf{x}_0^- \\ \frac{\mathbf{x}_N^+}{\mathbf{x}_N^-} \end{bmatrix} = M \begin{bmatrix} 1 \\ 0 \end{bmatrix} \quad 2.78$$

Where:

$$M = M_1 M_2 \dots M_N \rightarrow M = \begin{bmatrix} M_{11} & M_{12} \\ M_{21} & M_{22} \end{bmatrix} \quad 2.79$$

From Eq.2.78 and Eq.2.79 it follows:

$$\frac{\mathbf{x}_0^+}{\mathbf{x}_N^+} = M_{11}, \rightarrow \mathbf{x}_N^+ = \frac{\mathbf{x}_0^+}{M_{11}}, \quad \frac{\mathbf{x}_0^-}{\mathbf{x}_N^+} = M_{21} \rightarrow \mathbf{x}_0^- = \mathbf{x}_N^+ M_{21} \quad 2.80$$

hence, we can calculate with the following procedure:

$$\begin{bmatrix} \mathbf{x}_{N-1}^+ \\ \frac{\mathbf{x}_N^+}{\mathbf{x}_N^-} \\ \mathbf{x}_{N-1}^- \\ \frac{\mathbf{x}_N^+}{\mathbf{x}_N^-} \end{bmatrix} = M_N \begin{bmatrix} 1 \\ 0 \end{bmatrix}, \rightarrow \begin{bmatrix} \mathbf{x}_{N-2}^+ \\ \frac{\mathbf{x}_N^+}{\mathbf{x}_N^-} \\ \mathbf{x}_{N-2}^- \\ \frac{\mathbf{x}_N^+}{\mathbf{x}_N^-} \end{bmatrix} = M_{N-1} \begin{bmatrix} \mathbf{x}_{N-1}^+ \\ \frac{\mathbf{x}_N^+}{\mathbf{x}_N^-} \\ \mathbf{x}_{N-1}^- \\ \frac{\mathbf{x}_N^+}{\mathbf{x}_N^-} \end{bmatrix} \dots \rightarrow \begin{bmatrix} \mathbf{x}_1^+ \\ \frac{\mathbf{x}_N^+}{\mathbf{x}_N^-} \\ \mathbf{x}_1^- \\ \frac{\mathbf{x}_N^+}{\mathbf{x}_N^-} \end{bmatrix} = M_2 \begin{bmatrix} \mathbf{x}_2^+ \\ \frac{\mathbf{x}_N^+}{\mathbf{x}_N^-} \\ \mathbf{x}_2^- \\ \frac{\mathbf{x}_N^+}{\mathbf{x}_N^-} \end{bmatrix} \quad 2.81$$

all the ratios:  $\frac{\mathbf{x}_{N-1}^+}{\mathbf{x}_N^+}$ ,  $\frac{\mathbf{x}_{N-2}^+}{\mathbf{x}_N^+}$ , ...,  $\frac{\mathbf{x}_1^+}{\mathbf{x}_N^+}$  and  $\frac{\mathbf{x}_{N-1}^-}{\mathbf{x}_N^+}$ ,  $\frac{\mathbf{x}_{N-2}^-}{\mathbf{x}_N^+}$ , ...,  $\frac{\mathbf{x}_1^-}{\mathbf{x}_N^+}$ . that is, the electric field at the end of each solar cell layer for TM polarization.

#### 2.4.2. Determination of the Poynting vector for TM polarization

The energy flux through a surface can be calculated by means of the Poynting vector:

$$\tilde{\mathbf{S}} = \tilde{\mathbf{E}} \times \tilde{\mathbf{H}} \quad 2.82$$

Where  $\tilde{\mathbf{E}}$  and  $\tilde{\mathbf{H}}$  are the real part of the complex vectors  $\mathbf{E}$  and  $\mathbf{H}$  given by Eq.2.14 and Eq.2.15.

By recalling that for a complex vector  $\mathbf{T}$ , it holds:

$$Re[\mathbf{T}] = \frac{1}{2} [\mathbf{T} + \mathbf{T}^*] \quad 2.83$$

where  $\mathbf{T}^*$  is the complex conjugate of  $\mathbf{T}$ , it follows:

$$\tilde{\mathbf{S}} = \frac{1}{4} [\mathbf{E} + \mathbf{E}^*] \times [\mathbf{H} + \mathbf{H}^*] \quad 2.84$$

Introducing Eq.2.14 and Eq.2.15 in Eq.2.84 :

$$\begin{aligned} \tilde{\mathbf{S}} = \frac{1}{4} & \{ \mathbf{E}(\mathbf{r}) \times \mathbf{H}(\mathbf{r}) e^{2i(\mathbf{k} \cdot \mathbf{r} - \omega t)} + \mathbf{E}(\mathbf{r}) e^{i\mathbf{k} \cdot \mathbf{r}} \times [\mathbf{H}(\mathbf{r}) e^{i\mathbf{k} \cdot \mathbf{r}}]^* \\ & + [\mathbf{E}(\mathbf{r}) e^{i\mathbf{k} \cdot \mathbf{r}}]^* \times \mathbf{H}(\mathbf{r}) e^{i\mathbf{k} \cdot \mathbf{r}} + [\mathbf{E}(\mathbf{r})]^* \times [\mathbf{H}(\mathbf{r})]^* [e^{2i\mathbf{k} \cdot \mathbf{r}}]^* e^{-2i\omega t} \} \end{aligned} \quad 2.85$$

We can now argue that the integration time of the measurement of the electromagnetic radiation is much longer than the period of the wave associated to the electromagnetic radiation itself. For example, if we consider  $\lambda = 500$  nm, the related oscillation period is  $1.6 \cdot 10^{-15}$  sec, while the measurement time can be of the order of msec. This means that we can consider the average of the above expression. The average of the oscillatory terms containing  $e^{-2i\omega t}$  are null. Therefore, the Eq.2.85 becomes:

$$\langle \tilde{\mathbf{S}} \rangle = \frac{1}{4} \{ \mathbf{E}(\mathbf{r}) e^{i\mathbf{k} \cdot \mathbf{r}} \times [\mathbf{H}(\mathbf{r}) e^{i\mathbf{k} \cdot \mathbf{r}}]^* + [\mathbf{E}(\mathbf{r}) e^{i\mathbf{k} \cdot \mathbf{r}}]^* \times \mathbf{H}(\mathbf{r}) e^{i\mathbf{k} \cdot \mathbf{r}} \} \quad 2.86$$

which recalling the Eq.2.83 simplifies to:

$$\langle \tilde{\mathbf{S}} \rangle = \frac{1}{2} Re \{ \mathbf{E}(\mathbf{r}) e^{i\mathbf{k} \cdot \mathbf{r}} \times [\mathbf{H}(\mathbf{r}) e^{i\mathbf{k} \cdot \mathbf{r}}]^* \} \quad 2.87$$

By multiplying and dividing for  $e^{i\omega t}$  :

$$\langle \tilde{\mathbf{S}} \rangle = \frac{1}{2} Re \{ \mathbf{E}(\mathbf{r}) e^{i(\mathbf{k} \cdot \mathbf{r} - \omega t)} \times [\mathbf{H}(\mathbf{r}) e^{i(\mathbf{k} \cdot \mathbf{r} - \omega t)}]^* \} = \frac{1}{2} Re \{ \mathbf{E}(\mathbf{r}, t) \times \mathbf{H}(\mathbf{r}, t)^* \} \quad 2.88$$

The energy that in unit time crosses a surface is given by the flux of the Poynting vector:

$$\mathbf{q}(S) = \iint S \cdot \mathbf{n} da \quad 2.89$$

where  $\mathbf{n}$  is the normal to the surface. Considering that the Poynting vector does not change on the plane  $yz$ , the energy that in unit time and unit surface crosses a surface at the end of layer  $j$  is given by  $\langle \tilde{\mathbf{S}}_j(\mathbf{r}_j) \rangle \cdot \hat{\mathbf{x}}$ .

In order to determine  $\langle \tilde{\mathbf{S}}_j(\mathbf{r}_j) \rangle_{TM} \cdot \hat{\mathbf{x}}$ , let's start writing the expression of  $\mathbf{E}(\mathbf{r}, t)$  and  $\mathbf{H}(\mathbf{r}, t)$  given by Eq.2.52 and Eq.2.53 by considering Eq.2.60::

$$\mathbf{H}_j(\mathbf{r}, t) = \hat{\mathbf{z}} \frac{\epsilon_j \omega}{k_{j,x}} [\mathbf{x}_j^+ - \mathbf{x}_j^-] e^{i(k_{j,y} y - \omega t)} \quad 2.90$$

$$\mathbf{E}_j(\mathbf{r}, t) = \left\{ \hat{\mathbf{x}} \frac{k_{j,y}}{k_{j,x}} [-\mathbf{n}_j^+ + \mathbf{n}_j^-] + \hat{\mathbf{y}} [\mathbf{n}_j^+ + \mathbf{n}_j^-] \right\} e^{i(k_{j,y}y - \omega t)} \quad 2.91$$

$$\begin{aligned} & \mathbf{E}_j(\mathbf{r}_j, t) \times \mathbf{H}_j(\mathbf{r}_j, t)^* = \\ &= \begin{bmatrix} \hat{\mathbf{x}} & \hat{\mathbf{y}} & \hat{\mathbf{z}} \\ \frac{k_{j,y}}{k_{j,x}} \{-\mathbf{n}_j^+ + \mathbf{n}_j^-\} e^{i(k_{j,y}y_j - \omega t)} & [\mathbf{n}_j^+ + \mathbf{n}_j^-] e^{i(k_{j,y}y_j - \omega t)} & 0 \\ 0 & 0 & \left\{ \frac{\varepsilon_j \omega}{k_{j,x}} [\mathbf{n}_j^+ - \mathbf{n}_j^-] e^{i(k_{j,y}y_j - \omega t)} \right\}^* \end{bmatrix} \end{aligned} \quad 2.92$$

Since we only need the projection of the Poynting vector along  $\hat{\mathbf{x}}$ , we can just consider<sup>6</sup>

$$\{\mathbf{E}_j(\mathbf{r}_j, t) \times \mathbf{H}_j(\mathbf{r}_j, t)^*\}_x = [\mathbf{n}_j^+ + \mathbf{n}_j^-] e^{i(k_{j,y}y_j)} \left\{ \frac{\varepsilon_j \omega}{k_{j,x}} [\mathbf{n}_j^+ - \mathbf{n}_j^-] e^{i(k_{j,y}y_j)} \right\}^* \quad 2.93$$

Therefore, since  $k_{j,y}$  is real,  $|e^{i(k_{j,y}y_j)}|^2 = 1$ , then it follows:

$$\{\mathbf{E}_j(\mathbf{r}, t) \times \mathbf{H}_j(\mathbf{r}, t)^*\}_x = \frac{\varepsilon_j^* k_{j,x}}{|k_{j,x}|^2} \omega \left\{ |\mathbf{n}_j^+|^2 - |\mathbf{n}_j^-|^2 - \mathbf{n}_j^+ \mathbf{n}_j^{-*} + \mathbf{n}_j^- \mathbf{n}_j^{+*} \right\} \quad 2.94$$

$$\begin{aligned} \langle \tilde{\mathbf{S}}_j(\mathbf{r}_j) \rangle_{TM} \cdot \hat{\mathbf{x}} &= \frac{1}{2} \operatorname{Re} \{\mathbf{E}_j(\mathbf{r}, t) \times \mathbf{H}_j(\mathbf{r}, t)^*\}_x \\ &= \frac{1}{2} \operatorname{Re} \left\{ \frac{\varepsilon_j^* k_{j,x}}{|k_{j,x}|^2} \omega \left[ |\mathbf{n}_j^+|^2 - |\mathbf{n}_j^-|^2 - \mathbf{n}_j^+ \mathbf{n}_j^{-*} + \mathbf{n}_j^- \mathbf{n}_j^{+*} \right] \right\} \end{aligned} \quad 2.95$$

The Eq.2.95 can be written as:

$$\langle \tilde{\mathbf{S}}_j(\mathbf{r}_j) \rangle_{TM} \cdot \hat{\mathbf{x}} = \langle \tilde{S}_j(x_j) \rangle_{TM}^+ + \langle \tilde{S}_j(x_j) \rangle_{TM}^- + \langle \tilde{S}_j(x_j) \rangle_{TM}^\pm \quad 2.96$$

$$\langle \tilde{S}_j(x_j) \rangle_{TM}^+ = \frac{1}{2} \operatorname{Re} [\varepsilon_j^* k_{j,x}] \omega \frac{|\mathbf{n}_j^+|^2}{|k_{j,x}|^2} \quad 2.97$$

$$\langle \tilde{S}_j(x_j) \rangle_{TM}^- = -\frac{1}{2} \operatorname{Re} [\varepsilon_j^* k_{j,x}] \omega \frac{|\mathbf{n}_j^-|^2}{|k_{j,x}|^2} \quad 2.98$$

$$\langle \tilde{S}_j(x_j) \rangle_{TM}^\pm = \frac{1}{2} \frac{\omega}{|k_{j,x}|^2} \operatorname{Re} \{ \varepsilon_j^* k_{j,x} [\mathbf{n}_j^- \mathbf{n}_j^{+*} - \mathbf{n}_j^+ \mathbf{n}_j^{-*}] \} \quad 2.99$$

$\langle \tilde{S}_j(x_j) \rangle_{TM}^+$  represents the TM energy current density<sup>7</sup> at the end of layer  $j$ , owing to the electric field propagating in the x positive direction,  $\langle \tilde{S}_j(x_j) \rangle_{TM}^-$  represents the TM energy current density at the end of layer  $j$ , owing to the electric field propagating in the x negative direction, while

<sup>6</sup> It holds:  $\frac{1}{2} \operatorname{Re} \{\mathbf{E}_j(\mathbf{r}_j, t) \times \mathbf{H}_j(\mathbf{r}_j, t)^*\} \cdot \hat{\mathbf{x}} = \frac{1}{2} \operatorname{Re} \{[\mathbf{E}_j(\mathbf{r}_j, t) \times \mathbf{H}_j(\mathbf{r}_j, t)^*] \cdot \hat{\mathbf{x}}\}$

<sup>7</sup> The energy current density is expressed in W/m<sup>2</sup>.

$\langle \tilde{S}_j(x_j) \rangle_{TM}^{\pm}$  represents the TM energy current density at the end of layer  $j$ , due to the interference between the counter propagating waves. Since:

$$[\mathbf{x}_j^- \mathbf{x}_j^{+*} - \mathbf{x}_j^+ \mathbf{x}_j^{-*}] = 2i[Im(\mathbf{x}_j^-)Re(\mathbf{x}_j^+) - Im(\mathbf{x}_j^+)Re(\mathbf{x}_j^-)] \quad 2.100$$

the third term vanishes when  $k_{j,x}$  and  $\varepsilon_j$  are real (not absorbing material). As the solar radiation comes from layer #0, by recalling the assumption 2) of section 2.4, it holds:

$$\langle \tilde{S}_0(x_0) \rangle_{TM}^+ = \frac{1}{2} I_0 \rightarrow |\mathbf{x}_0^+| = \sqrt{\frac{I_0 k_{0,x}}{\omega \varepsilon_0}} \quad 2.101$$

Where  $I_0$  is the solar energy current density.

The transmittance and reflectance are given by:

$$T_{TM} = \frac{\langle \tilde{S}_N(x_N) \rangle_{TM}^+}{\langle \tilde{S}_0(x_0) \rangle_{TM}^+} = \frac{Re[\varepsilon_N^* k_{N,x}] |k_{0,x}|^2 |\mathbf{x}_N^+|^2}{Re[\varepsilon_0^* k_{0,x}] |k_{N,x}|^2 |\mathbf{x}_0^+|^2} \quad 2.102$$

$$R_{TM} = \frac{\langle \tilde{S}_0(x_0) \rangle_{TM}^-}{\langle \tilde{S}_0(x_0) \rangle_{TM}^+} = \frac{|\mathbf{x}_0^-|^2}{|\mathbf{x}_0^+|^2} \quad 2.103$$

By considering Eq.2.80, Eq.2.102 and Eq.2.103 can be written as:

$$T_{TM} = \frac{k_{0,x} Re[\varepsilon_N^* k_{N,x}]}{\varepsilon_0 |k_{N,x}|^2 |M_{11}|^2} \quad 2.104$$

$$R_{TM} = \frac{|M_{21}|^2}{|M_{11}|^2} \quad 2.105$$

### 2.4.3. Matrix elements for TE polarization

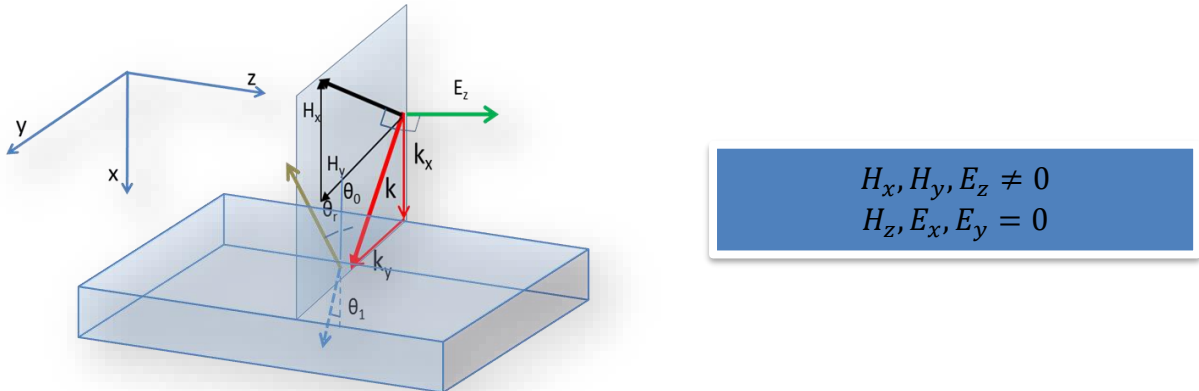


**Figure 8. TE polarization representation: the magnetic intensity is in the plane of incidence while the electric field is perpendicular to the plane on incidence.**

By introducing Eq.2.15 and Eq.2.47 in Eq.2.38 we get:

$$\mathbf{E}^{\pm}(\mathbf{r}, t) = -\frac{1}{\omega\varepsilon} \begin{bmatrix} \hat{\mathbf{x}} & \hat{\mathbf{y}} & \hat{\mathbf{z}} \\ \pm k_x & k_y & 0 \\ H_x(\mathbf{r}, t) & H_y(\mathbf{r}, t) & 0 \end{bmatrix} = \frac{1}{\omega\varepsilon} \hat{\mathbf{z}} [\pm k_x H_y(\mathbf{r}, t) - k_y H_x(\mathbf{r}, t)] \quad 2.106$$

Setting:

$$E^{\pm} = \frac{[\pm k_x H_y - k_y H_x]}{\omega\varepsilon} \quad 2.107$$

where  $\mathbf{E}_j^{\pm}$  has the dimension of [V/m], while in Eq.2.49 it had the dimension of [V] and the superscripts “ $\pm$ ” have the same meaning as in given in the previous chapter, it is possible to write:

$$\mathbf{E}_j^{\pm}(\mathbf{r}, t) = \hat{\mathbf{z}} E_j^{\pm} e^{i(\mathbf{k}_j^{\pm} \cdot \mathbf{r} - \omega t)} \quad 2.108$$

By introducing Eq.2.108 and Eq.2.47 in Eq.2.39, it holds for the generic layer j

$$\mathbf{H}_j^{\pm}(\mathbf{r}, t) = [\hat{x} k_{j,y} \mp \hat{y} k_{j,x}] \frac{E_j^{\pm} e^{i(\mathbf{k}_j^{\pm} \cdot \mathbf{r} - \omega t)}}{\mu_j \omega} \quad 2.109$$

Applying the boundary condition in  $\mathbf{r}_j$ , Eq.2.29 and Eq.2.31:

$$\mathbf{n} \times \mathbf{E}_j^{\pm}(\mathbf{r}_j, t) = E_j^{\pm} e^{i(\mathbf{k}_j \cdot \mathbf{r} - \omega t)} \begin{bmatrix} \hat{\mathbf{x}} & \hat{\mathbf{y}} & \hat{\mathbf{z}} \\ 1 & 0 & 0 \\ 0 & 0 & 1 \end{bmatrix} = -\hat{\mathbf{y}} E_j^{\pm} e^{i(\mathbf{k}_j^{\pm} \cdot \mathbf{r} - \omega t)} \quad 2.110$$

$$E_j^+ e^{i(\mathbf{k}_j^+ \cdot \mathbf{r}_j)} + E_j^- e^{-i(\mathbf{k}_j^- \cdot \mathbf{r}_j)} = E_{j+1}^+ e^{i(\mathbf{k}_{j+1}^+ \cdot \mathbf{r}_j)} + E_{j+1}^- e^{-i(\mathbf{k}_{j+1}^- \cdot \mathbf{r}_j)} \quad 2.111$$

Since  $e^{i(\mathbf{k}_j^{\pm} \cdot \mathbf{r}_j)} = e^{i(\pm k_{j,x} x_j + k_{j,y} y_j)}$ , and remembering Eq.2.46, it holds

$$E_j^+ e^{i(k_{j,x} x_j)} + E_j^- e^{-i(k_{j,x} x_j)} = E_{j+1}^+ e^{i(k_{j+1,x} x_j)} + E_{j+1}^- e^{-i(k_{j+1,x} x_j)} \quad 2.112$$

By setting:

$$\Omega_j^{\pm} = E_j^{\pm} e^{\pm i k_{j,x} x_j} \quad 2.113$$

and considering Eq.2.62:

$$\Omega_j^+ + \Omega_j^- = \Omega_{j+1}^+ e^{-i k_{j+1,x} d_{j+1}} + \Omega_{j+1}^- e^{i k_{j+1,x} d_{j+1}} \quad 2.114$$

$$\mathbf{n} \times \mathbf{H}_j^{\pm}(\mathbf{r}_j, t) = \frac{E_j^{\pm} e^{i(\mathbf{k}_j \cdot \mathbf{r} - \omega t)}}{\mu_j \omega} \begin{bmatrix} \hat{\mathbf{x}} & \hat{\mathbf{y}} & \hat{\mathbf{z}} \\ 1 & 0 & 0 \\ k_{j,y} & \mp k_{j,x} & 0 \end{bmatrix} = \mp \hat{\mathbf{z}} k_{j,x} \frac{E_j^{\pm} e^{i(\mathbf{k}_j \cdot \mathbf{r} - \omega t)}}{\mu_j \omega} \quad 2.115$$

$$\begin{aligned}
 & -\frac{k_{j,x}}{\mu_j} E_j^+ e^{i(k_{j,x} \cdot x_j)} + \frac{k_{j,x}}{\mu_j} E_j^- e^{-i(k_{j,x} \cdot x_j)} \\
 & = -\frac{k_{j+1,x}}{\mu_{j+1}} E_{j+1}^+ e^{i(k_{j+1,x} \cdot x_j)} + \frac{k_{j+1,x}}{\mu_{j+1}} E_{j+1}^- e^{-i(k_{j+1,x} \cdot x_j)}
 \end{aligned} \tag{2.116}$$

By considering Eq.2.113 and setting:

$$\eta_j = \frac{k_{j,x}}{\mu_j} \tag{2.117}$$

Eq.2.116 becomes (changing the sign to all terms):

$$\eta_j (\Omega_j^+ - \Omega_j^-) = \eta_{j+1} (\Omega_{j+1}^+ e^{-ik_{j+1,x} d_{j+1}} - \Omega_{j+1}^- e^{ik_{j+1,x} d_{j+1}}) \tag{2.118}$$

Solving Eq.2.114 and Eq.2.118 with respect to  $\Omega_j^+, \Omega_j^-$ :

$$\Omega_j^+ = \frac{1}{2} \left[ \left( 1 + \frac{\eta_{j+1}}{\eta_j} \right) \Omega_{j+1}^+ e^{-ik_{j+1,x} d_{j+1}} + \left( 1 - \frac{\eta_{j+1}}{\eta_j} \right) \Omega_{j+1}^- e^{ik_{j+1,x} d_{j+1}} \right] \tag{2.119}$$

$$\Omega_j^- = \frac{1}{2} \left[ \left( 1 - \frac{\eta_{j+1}}{\eta_j} \right) \Omega_{j+1}^+ e^{-ik_{j+1,x} d_{j+1}} + \left( 1 + \frac{\eta_{j+1}}{\eta_j} \right) \Omega_{j+1}^- e^{ik_{j+1,x} d_{j+1}} \right] \tag{2.120}$$

Eq.2.119 and Eq.2.120 , by considering Eq.2.66 can be written in matrix form as:

$$\begin{bmatrix} \Omega_j^+ \\ \Omega_j^- \end{bmatrix} = \frac{1}{2\eta_j} \begin{bmatrix} \Psi_{j+1}^- (\eta_j + \eta_{j+1}) & \Psi_{j+1}^+ (\eta_j - \eta_{j+1}) \\ \Psi_{j+1}^- (\eta_j - \eta_{j+1}) & \Psi_{j+1}^+ (\eta_j + \eta_{j+1}) \end{bmatrix} \begin{bmatrix} \Omega_{j+1}^+ \\ \Omega_{j+1}^- \end{bmatrix} \tag{2.121}$$

We can define, for each layer a matrix:

$$\tilde{M}_j = \frac{1}{2\eta_{j-1}} \begin{bmatrix} \Psi_j^- (\eta_{j-1} + \eta_j) & \Psi_j^+ (\eta_{j-1} - \eta_j) \\ \Psi_j^- (\eta_{j-1} - \eta_j) & \Psi_j^+ (\eta_{j-1} + \eta_j) \end{bmatrix} \tag{2.122}$$

It is straightforward to see that the matrix  $\tilde{M}_{j+1}$  can be expressed as a product of an “interface” and “propagation” matrix, which describe the reflection of the electric field at the interface j, j+1 and the propagation of the electric field inside the layer j+1:

$$\begin{aligned}
 \tilde{M}_{j+1} &= \frac{\eta_j + \eta_{j+1}}{2\eta_j} \underbrace{\begin{bmatrix} 1 & \frac{\eta_j - \eta_{j+1}}{\eta_j + \eta_{j+1}} \\ \frac{\eta_j - \eta_{j+1}}{\eta_j + \eta_{j+1}} & 1 \end{bmatrix}}_{\text{Interface}} \underbrace{\begin{bmatrix} \Psi_{j+1}^- & 0 \\ 0 & \Psi_{j+1}^+ \end{bmatrix}}_{\text{Propagation}}
 \end{aligned} \tag{2.123}$$

Where:

$$\frac{\eta_j + \eta_{j+1}}{2\eta_j} \begin{bmatrix} 1 & \frac{\eta_j - \eta_{j+1}}{\eta_j + \eta_{j+1}} \\ \frac{\eta_j - \eta_{j+1}}{\eta_j + \eta_{j+1}} & 1 \end{bmatrix} = \frac{1}{t_{j,j+1}} \begin{bmatrix} 1 & r_{j,j+1} \\ r_{j,j+1} & 1 \end{bmatrix} \quad 2.124$$

$t_{j,j+1}$  and  $r_{j,j+1}$ , are, respectively, the Fresnel transmission and reflection coefficient for TE polarization.

Following the same procedure shown for TM, Since  $\Omega_N^- = 0$ . It holds:

$$\begin{bmatrix} \frac{\Omega_0^+}{\Omega_N^+} \\ \frac{\Omega_N^-}{\Omega_0^-} \\ \frac{\Omega_0^+}{\Omega_N^+} \\ \frac{\Omega_N^-}{\Omega_0^-} \end{bmatrix} = \tilde{M} \begin{bmatrix} 1 \\ 0 \end{bmatrix} \quad 2.125$$

$$\tilde{M} = \tilde{M}_1 \tilde{M}_2 \dots \tilde{M}_N \rightarrow \tilde{M} = \begin{bmatrix} \tilde{M}_{11} & \tilde{M}_{12} \\ \tilde{M}_{21} & \tilde{M}_{22} \end{bmatrix} \quad 2.126$$

From Eq.2.125 and Eq.2.126 it follows:

$$\frac{\Omega_0^+}{\Omega_N^+} = \tilde{M}_{11}, \rightarrow \Omega_N^+ = \frac{\Omega_0^+}{\tilde{M}_{11}}, \quad \frac{\Omega_0^-}{\Omega_N^-} = \tilde{M}_{21} \rightarrow \Omega_0^- = \Omega_N^+ \tilde{M}_{21} \quad 2.127$$

Hence, we can calculate with the following procedure:

$$\begin{bmatrix} \frac{\Omega_{N-1}^+}{\Omega_N^+} \\ \frac{\Omega_N^-}{\Omega_{N-1}^-} \\ \frac{\Omega_{N-1}^+}{\Omega_N^+} \\ \frac{\Omega_N^-}{\Omega_{N-1}^-} \end{bmatrix} = \tilde{M}_N \begin{bmatrix} 1 \\ 0 \end{bmatrix}, \rightarrow \begin{bmatrix} \frac{\Omega_{N-2}^+}{\Omega_N^+} \\ \frac{\Omega_N^-}{\Omega_{N-2}^-} \\ \frac{\Omega_{N-2}^+}{\Omega_N^+} \\ \frac{\Omega_N^-}{\Omega_{N-2}^-} \end{bmatrix} = \tilde{M}_{N-1} \begin{bmatrix} \frac{\Omega_{N-1}^+}{\Omega_N^+} \\ \frac{\Omega_N^-}{\Omega_{N-1}^-} \\ \frac{\Omega_{N-1}^+}{\Omega_N^+} \\ \frac{\Omega_N^-}{\Omega_{N-1}^-} \end{bmatrix} \dots \rightarrow \begin{bmatrix} \frac{\Omega_1^+}{\Omega_N^+} \\ \frac{\Omega_N^-}{\Omega_1^-} \\ \frac{\Omega_1^+}{\Omega_N^+} \\ \frac{\Omega_N^-}{\Omega_1^-} \end{bmatrix} = \tilde{M}_2 \begin{bmatrix} \frac{\Omega_2^+}{\Omega_N^+} \\ \frac{\Omega_N^-}{\Omega_2^-} \\ \frac{\Omega_2^+}{\Omega_N^+} \\ \frac{\Omega_N^-}{\Omega_2^-} \end{bmatrix} \quad 2.128$$

all the ratios:  $\frac{\Omega_{N-1}^+}{\Omega_N^+}, \frac{\Omega_{N-2}^+}{\Omega_N^+}, \dots, \frac{\Omega_1^+}{\Omega_N^+}$  and  $\frac{\Omega_{N-1}^-}{\Omega_N^+}, \frac{\Omega_{N-2}^-}{\Omega_N^+}, \dots, \frac{\Omega_1^-}{\Omega_N^+}$ . that is, the electric field at the end of each solar cell layer for TE polarization.

#### 2.4.4. Determination of the Poynting vector for TE polarization

We have to determine:

$$\langle \tilde{S}_j(\mathbf{r}_j) \rangle_{TE} \cdot \hat{x} = \frac{1}{2} \operatorname{Re} \left\{ \mathbf{E}_j(\mathbf{r}, t) \times \mathbf{H}_j(\mathbf{r}, t)^* \right\}_x \quad 2.129$$

Let's start writing the Eq.2.108 and Eq.2.109 by using Eq.2.113:

$$\mathbf{E}_j(\mathbf{r}_j, t) = \hat{\mathbf{z}} [\Omega_j^+ + \Omega_j^-] e^{i(k_{j,y} y_j - \omega t)} \quad 2.130$$

$$\mathbf{H}_j(\mathbf{r}, t) = \left\{ \hat{\mathbf{x}} \left[ \frac{k_{j,y}}{\mu_j \omega} (\Omega_j^+ + \Omega_j^-) \right] - \hat{\mathbf{y}} \left[ \frac{k_{j,x}}{\mu_j \omega} (\Omega_j^+ - \Omega_j^-) \right] \right\} e^{i(k_{j,y} y_j - \omega t)} \quad 2.131$$

It holds:

$$\begin{aligned} & \mathbf{E}_j(\mathbf{r}_j, t) \times \mathbf{H}_j(\mathbf{r}_j, t)^* = \\ &= \begin{bmatrix} \hat{\mathbf{x}} & \hat{\mathbf{y}} & \hat{\mathbf{z}} \\ 0 & 0 & [\Omega_j^+ + \Omega_j^-] e^{i(k_{j,y} y_j - \omega t)} \\ \left\{ \frac{k_{j,x}}{\mu_j \omega} (\Omega_j^+ + \Omega_j^-) e^{i(k_{j,y} y_j - \omega t)} \right\}^* & -\left\{ \frac{k_{j,x}}{\mu_j \omega} (\Omega_j^+ - \Omega_j^-) e^{i(k_{j,y} y_j - \omega t)} \right\}^* & 0 \end{bmatrix} \end{aligned}$$

Since we only need the projection of the Poynting vector along  $\hat{\mathbf{x}}$ , we get:

$$\{\mathbf{E}_j(\mathbf{r}_j, t) \times \mathbf{H}_j(\mathbf{r}_j, t)^*\}_x = [\Omega_j^+ + \Omega_j^-] e^{i(k_{j,y} y_j - \omega t)} \left\{ \frac{k_{j,x}}{\mu_j \omega} (\Omega_j^+ - \Omega_j^-) e^{i(k_{j,y} y_j - \omega t)} \right\}^* \quad 2.132$$

$$\{\mathbf{E}_j(\mathbf{r}, t) \times \mathbf{H}_j(\mathbf{r}, t)^*\}_x = \frac{k_{j,x}^*}{\mu_j^*} \frac{1}{\omega} \left[ |\Omega_j^+|^2 - |\Omega_j^-|^2 - \Omega_j^+ \Omega_j^{-*} + \Omega^- \Omega_j^{+*} \right] \quad 2.133$$

$$\begin{aligned} \langle \tilde{\mathbf{S}}_j(\mathbf{r}_j) \rangle_{TE} \cdot \hat{\mathbf{x}} &= \frac{1}{2} \operatorname{Re} \{\mathbf{E}_j(\mathbf{r}, t) \times \mathbf{H}_j(\mathbf{r}, t)^*\}_x \\ &= \frac{1}{2\omega} \operatorname{Re} \left\{ \frac{k_{j,x}^*}{\mu_j^*} \left[ |\Omega_j^+|^2 - |\Omega_j^-|^2 - \Omega_j^+ \Omega_j^{-*} + \Omega^- \Omega_j^{+*} \right] \right\} \end{aligned} \quad 2.134$$

Eq.2.134 can be written as:

$$\langle \tilde{\mathbf{S}}_j(\mathbf{r}_j) \rangle_{TE} \cdot \hat{\mathbf{x}} = \langle \tilde{S}_j(x_j) \rangle_{TE}^+ + \langle \tilde{S}_j(x_j) \rangle_{TE}^- + \langle \tilde{S}_j(x_j) \rangle_{TE}^\pm \quad 2.135$$

$$\langle \tilde{S}_j(x_j) \rangle_{TE}^+ = \frac{1}{2\omega} \operatorname{Re} \left[ \frac{k_{j,x}^*}{\mu_j^*} \right] |\Omega_j^+|^2 \quad 2.136$$

$$\langle \tilde{S}_j(x_j) \rangle_{TE}^- = -\frac{1}{2\omega} \operatorname{Re} \left[ \frac{k_{j,x}^*}{\mu_j^*} \right] |\Omega_j^-|^2 \quad 2.137$$

$$\langle \tilde{S}_j(x_j) \rangle_{TE}^\pm = \frac{1}{2\omega} \operatorname{Re} \left\{ \frac{k_{j,x}^*}{\mu_j^*} [\Omega_j^- \Omega_j^{+*} - \Omega_j^+ \Omega_j^{-*}] \right\} \quad 2.138$$

$\langle \tilde{S}_j(x_j) \rangle_{TE}^+$  represents the TE energy current density at the end of layer  $j$ , owing to the electric field propagating in the x positive direction,  $\langle \tilde{S}_j(x_j) \rangle_{TE}^-$  represents the TE energy current density at the end of layer  $j$ , owing to electric field propagating in the x negative direction, while  $\langle \tilde{S}_j(x_j) \rangle_{TE}^\pm$  represents the TE energy current density at the end of layer  $j$ , owing to interference term between the counter propagating waves. Since:

$$[\Omega_j^- \Omega_j^{+*} - \Omega_j^+ \Omega_j^{-*}] = 2i[Im(\Omega_j^-)Re(\Omega_j^+) - Im(\Omega_j^+)Re(\Omega_j^-)] \quad 2.139$$

the third term vanishes when  $k_{j,x}$  and  $\mu_j$  are real (not absorbing material). As the solar radiation comes from layer #0, it holds:

$$\langle \tilde{S}_0(x_0) \rangle^+_{TE} = \frac{1}{2} I_0 \rightarrow |\Omega_0^+| = \sqrt{\frac{l_0 \omega}{k_{0,x}}} \quad 2.140$$

Considering Eq.2.127, the transmittance and reflectance are given by:

$$T_{TE} = \frac{\langle \tilde{S}_N(x_N) \rangle^+_{TE}}{\langle \tilde{S}_0(x_0) \rangle^+_{TE}} = \frac{Re\left[\frac{k_{N,x}^*}{\mu_N^*}\right] |\Omega_N^+|^2}{Re\left[\frac{k_{0,x}^*}{\mu_0^*}\right] |\Omega_0^+|^2} = \frac{1}{|\tilde{M}_{11}|^2 k_{0,x}} Re\left[\frac{k_{N,x}^*}{\mu_N^*}\right] \quad 2.141$$

$$R_{TE} = \frac{\langle \tilde{S}_0(x_0) \rangle^-_{TE}}{\langle \tilde{S}_0(x_0) \rangle^+_{TE}} = \frac{|\tilde{M}_{21}|^2}{|\tilde{M}_{11}|^2} \quad 2.142$$

Since the solar intensity can be thought as equally distributed in the TM and TE polarization modes, the total transmission and reflection coefficient are given by:

$$T = \frac{T_{TM} + T_{TE}}{2}; \quad R = \frac{R_{TM} + R_{TE}}{2} \quad 2.143$$

In conclusion, by solving the linear systems expressed by Eq.2.81 and Eq.2.128, respectively for TM and TE propagation, we can compute the related Poynting vectors given by Eq.2.96 and Eq.2.135, from which we can get the photon flux inside each layer of the MJ device. The photon flux can be finally inserted in the continuity equations for the determination of the minority carriers distribution.

The solution of the continuity equation, however, is complicated by the presence of the interference terms between the counter propagating waves. In the next chapter a simplification will be introduced, that will allow solving the continuity equation analytically.

### 3. A new mathematical approach for MJ solar cells performance simulation

The “generation function” to be used to solve the continuity equation is simplified by showing that it is possible to neglect the interference terms between the counter propagating waves. For this purpose, as a case study, a triple junction (TJ) InGaP/InGaAs/Ge solar cell is introduced. The three different terms of the Poynting vector are computed and compared for the emitter and the base of the top and middle cells. I show explicitly that, for certain MJ structures, TMM can be numerically unstable, therefore, I develop the scattering matrix method (SMM), as an alternative solution for the determination of the photon flux inside each solar cell layer. As an example, the continuity equation is solved for the TJ case study, obtaining simple analytical solutions. Eventually, I compare the Hovel model, the TMM and SMM. The robustness of the new mathematical approach is validated on thin TJ cells, while showing its advantage in offering a very good trade-off between computing time and accuracy.

#### 3.1. Simplifying the generation function

In the previous analysis, the Poynting vector has been determined at the end of each layer. It is very useful to show how the Poynting vector is changing within each layer, since this helps determining the generation function to be used to solve the continuity equation.

Let's start considering the propagation of the energy flux in the positive and negative direction for TM and TE polarization.

Setting:

$$\delta = \frac{\frac{1}{2} \operatorname{Re}[\varepsilon_j^* k_{j,x}] \omega}{|k_{j,x}|^2} \quad 3.1$$

Eq. 2.97 and Eq. 2.98, calculated in  $x_j - x$ , by considering Eq. 2.60, become:

$$\begin{aligned} \langle \tilde{S}_j(x_j - x) \rangle^+_{TM} &= \delta |\mathbf{n}_j^+|^2 = \delta |k_{j,x} E_j^+ e^{ik_{j,x}(x_j - x)}|^2 = \langle \tilde{S}_j(x_j) \rangle^+_{TM} |e^{-ik_{j,x}x}|^2 \\ &= \langle \tilde{S}_j(x_j) \rangle^+_{TM} e^{2\operatorname{Im}(k_{j,x})x} \end{aligned} \quad 3.2$$

$$\begin{aligned} \langle \tilde{S}_j(x_j - x) \rangle^-_{TM} &= -\delta |\mathbf{n}_j^-|^2 = \delta |k_{j,x} E_j^- e^{-ik_{j,x}(x_j - x)}|^2 = \langle \tilde{S}_j(x_j) \rangle^-_{TM} |e^{ik_{j,x}x}|^2 \\ &= \langle \tilde{S}_j(x_j) \rangle^-_{TM} e^{-2\operatorname{Im}(k_{j,x})x} \end{aligned} \quad 3.3$$

In similar way, setting:

$$\gamma = \frac{1}{2\omega} Re \left[ \frac{k_{j,x}^*}{\mu_j^*} \right] \quad 3.4$$

Eq. 2.136 and Eq. 2.137, calculated in  $x_j-x$ , by considering Eq.2.113, become:

$$\begin{aligned} \langle \tilde{S}_j(x_j - x) \rangle^+_{TE} &= \gamma |\Omega_j^+|^2 = \gamma |E_j^+ e^{ik_{j,x}(x_j - x)}|^2 = \langle \tilde{S}_j(x_j) \rangle^+_{TE} |e^{-ik_{j,x}x}|^2 \\ &= \langle \tilde{S}_j(x_j) \rangle^+_{TE} e^{2Im(k_{j,x})x} \end{aligned} \quad 3.5$$

$$\begin{aligned} \langle \tilde{S}_j(x_j - x) \rangle^-_{TE} &= \gamma |\Omega_j^-|^2 = \gamma |E_j^- e^{-ik_{j,x}(x_j - x)}|^2 = \langle \tilde{S}_j(x_j) \rangle^-_{TE} |e^{ik_{j,x}x}|^2 \\ &= \langle \tilde{S}_j(x_j) \rangle^-_{TE} e^{-2Im(k_{j,x})x} \end{aligned} \quad 3.6$$

Eq.3.2, Eq.3.3, Eq.3.5 and Eq.3.6 tell us that the energy flux propagates inside each layer by following a “generalized” Beer-Lambert law<sup>8</sup>. The factor  $2Im(k_{j,x})$  is exactly equal to the absorption coefficient in case of perpendicular incidence. Therefore, the generation rate,  $G^\pm(\lambda, x)$ , can be computed by:

$$G^\pm(\lambda, x) = \mp \frac{dF^\pm(x, \lambda)}{dx} \quad 3.7$$

where,  $F^\pm(x, \lambda)$  is the photon flux propagating in positive and negative x direction, determined by the Poynting vector, as the following. If we could neglect the interference terms between the counter propagating waves, the *generation function* in each layer, j, which starts at coordinate  $x_0$  and ends at coordinate  $x_N$ , (*therefore with  $x_0 < x < x_N$* ) could be written as:

$$G_j(x, \lambda) = 2Im[k_{j,x}(\lambda)] [F_j^+(x_0, \lambda)e^{2Im[k_{j,x}(\lambda)](x_0 - x)} + F_j^-(x_N, \lambda)e^{2Im[k_{j,x}(\lambda)](x - x_N)}] \quad 3.8$$

$F_j^+(x_0, \lambda)$  is the photon flux propagating in the positive x direction, present at the beginning of the layer in  $x_0$ ,  $F_j^-(x_N, \lambda)$  is the photon flux propagating in the negative x direction, present at the end of the layer, in  $x_N$ , given by:

$$F_j^+(x_0, \lambda) = \frac{\{\langle \tilde{S}_j(x_0) \rangle^+_{TE} + \langle \tilde{S}_j(x_0) \rangle^+_{TM}\} \lambda}{hc} \quad 3.9$$

$$F_j^-(x_N, \lambda) = \frac{\{\langle \tilde{S}_j(x_N) \rangle^-_{TE} + \langle \tilde{S}_j(x_N) \rangle^-_{TM}\} \lambda}{hc} \quad 3.10$$

Where:  $h$ = Plank constant.

Let's now consider the counter propagating waves contribution.

---

<sup>8</sup> Increasing x means to go from the end to the beginning of the layer, therefore the energy flux increases exponentially.

For TM polarization, by considering that for two complex numbers  $A$  and  $B$  it holds:

$$Re[A \cdot B] = Re[A] \cdot Re[B]$$

$$\begin{aligned} \langle \tilde{S}_j(x_j) \rangle_{TM}^{\pm} &= \frac{1}{2} \frac{\omega}{|k_{j,x}|^2} Re\{\varepsilon_j^* k_{j,x} [\mathbf{n}_j^- \mathbf{n}_j^{+*} - \mathbf{n}_j^+ \mathbf{n}_j^{-*}]\} \\ &= \frac{1}{2} \frac{\omega}{|k_{j,x}|^2} Re\{\varepsilon_j^* k_{j,x} [\mathbf{n}_j^- \mathbf{n}_j^{+*}]\} - \frac{1}{2} \frac{\omega}{|k_{j,x}|^2} Re\{\varepsilon_j^* k_{j,x} [\mathbf{n}_j^+ \mathbf{n}_j^{-*}]\} \end{aligned} \quad 3.11$$

Therefore:

$$\begin{aligned} \langle \tilde{S}_j(x_j - x) \rangle_{TM}^{\pm} &= \\ &= \frac{1}{2} \frac{\omega}{|k_{j,x}|^2} Re\{\varepsilon_j^* k_{j,x} [\mathbf{n}_j^- \mathbf{n}_j^{+*}] e^{i2Re(k_{j,x})x}\} \\ &\quad - \frac{1}{2} \frac{\omega}{|k_{j,x}|^2} Re\{\varepsilon_j^* k_{j,x} [\mathbf{n}_j^+ \mathbf{n}_j^{-*}] e^{-i2Re(k_{j,x})x}\} \end{aligned} \quad 3.12$$

A similar expression is found for TE polarization:

$$\langle \tilde{S}_j(x_j) \rangle_{TE}^{\pm} = \frac{1}{2\omega} Re\left\{ \frac{k_{j,x}}{\mu_j^*} [\Omega_j^- \Omega_j^{+*} - \Omega_j^+ \Omega_j^{-*}] \right\} \quad 3.13$$

$$\begin{aligned} \langle \tilde{S}_j(x_j - x) \rangle_{TE}^{\pm} &= \\ &= \frac{1}{2\omega} Re\left\{ \frac{k_{j,x}}{\mu_j^*} [\Omega_j^- \Omega_j^{+*}] e^{i2Re(k_{j,x})x} \right\} - \frac{1}{2\omega} Re\left\{ \frac{k_{j,x}}{\mu_j^*} [\Omega_j^+ \Omega_j^{-*}] e^{-i2Re(k_{j,x})x} \right\} \end{aligned} \quad 3.14$$

Both  $\langle \tilde{S}_j(x_j - x) \rangle_{TM}^{\pm}$  and  $\langle \tilde{S}_j(x_j - x) \rangle_{TE}^{\pm}$  are oscillatory terms whose values will be shown (in the next section), negligible with respect to the energy density fluxes in positive and negative direction, therefore the photon flux owing to the interference between the counter propagating waves given by Eq.3.12 and Eq.3.14 will be ignored in the continuity equation and the following expression will be used:

$$F_j^{\pm}(x_j - x, \lambda) = \frac{\{\langle \tilde{S}_j(x_j - x) \rangle_{TE}^{\pm} + \langle \tilde{S}_j(x_j - x) \rangle_{TM}^{\pm}\} \lambda}{hc} \quad 3.15$$

Where with  $\langle \tilde{S}_j(x_j - x) \rangle_{TE}^{\pm}$  in Eq.3.15 have the same expression of the oscillatory terms, but in this case, they mean the positive or negative pointing vectors given respectively by Eq.3.5 and Eq.3.6. The same meaning is used for TM polarization.

### 3.2. The triple junction InGaP/InGaAs/Ge benchmark case study

In order to demonstrate that the photon flux oscillatory terms are negligible with respect to the photon flux in positive and negative direction, the TMM is applied to study the electromagnetic

radiation distribution inside a “conventional” InGaP/InGaAs/Ge triple junction solar cell structure (benchmark structure).

As far as the optical properties are concerned, in first approximation, the difference introduced by doping levels are not considered. This means that for the InGaP top cell, for example, all the layers, namely: the emitter, the base, the spacer and the BSF layer have all the same value of the complex refractive index.

The structure of the InGaP/InGaAs/Ge TJ solar cell is reported in Table 1. For this structure, the photon fluxes for the layers #6, #9 and #10, are computed and compared. For improving the comparison, the negative and interference components of the photon flux are multiplied respectively by 10. It is also assumed to concentrate the solar light of a factor 500 X.

**Table 1. InGaP/InGaAs/Ge TJ optical layers.**

#	Layer	Thickness (nm)
1	SiO <sub>2</sub>	88
	Ta <sub>2</sub> O <sub>5</sub>	52
5	AllnP (window top)	36
6	InGaP (emitter+ spacer+ base + BSF)	456
7	AlGaAs TD2	30
8	InGaP TD2 + Window mid	45.7
9	AllnGaAs (emitter)	100
10	InGaAs (base +spacer)	3800
11	GaAs BSF	290
12	AlGaAs - barrier TD1	50
13	AlGaAs TD1	72
14	GaAs TD1	70.6
15	AlGaAs - barrier TD1	50
16	InGaAs buffer	1751
17	InGaP nucleation	114
18	Ge substrate (emitter + base)	150

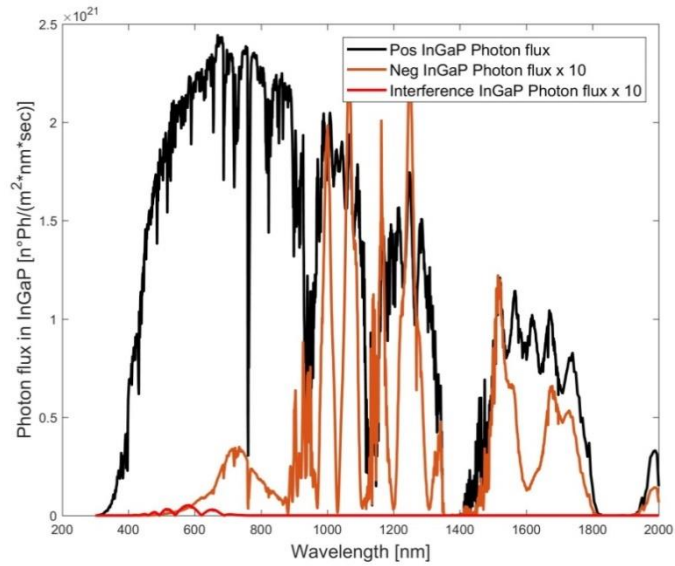


**Figure 9.** Absolute value of the spectral photon fluxes at the end of the layer #6.

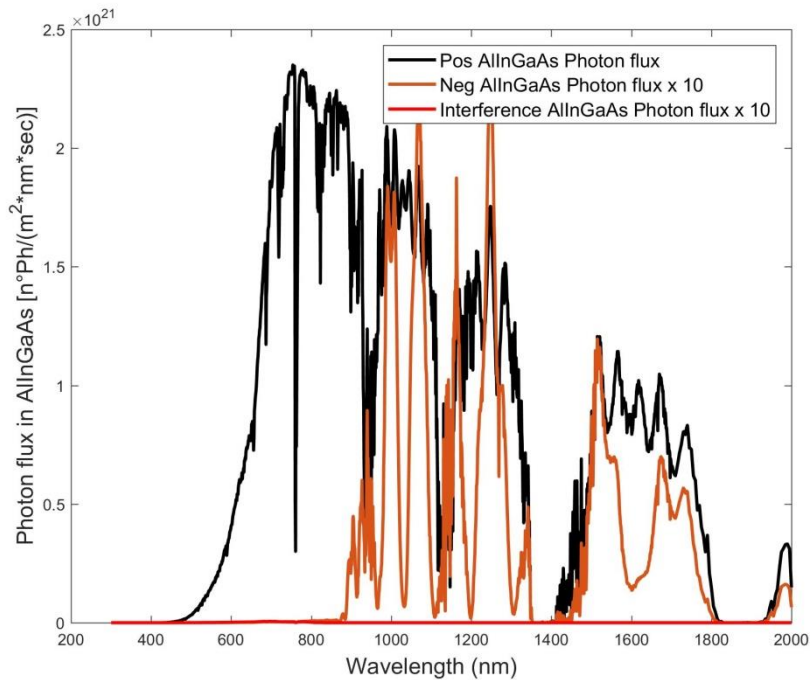


**Figure 10.** Absolute value of the spectral photon fluxes at the end of the layer #9.

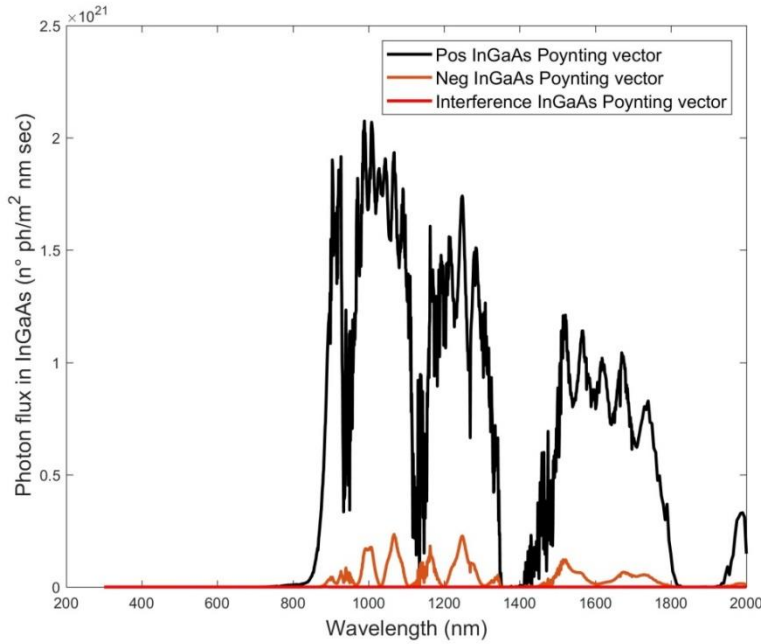


**Figure 11.** Absolute value of the spectral photon fluxes at the end of the layer #10.

Figure 9, Figure 10 and Figure 11 clearly show that the photon flux oscillatory terms are negligible with respect to the photon flux in positive and negative direction. A numerical evaluation of the photon fluxes is also reported in Table 2. In all cases, the photon flow values due to the interference between counter propagating waves are four order of magnitude lower than the values of the positive flow and two order of magnitude lower than the values of the negative flow.

**Table 2. Photon flows values in InGaP, AlInGaAs and InGaAs photovoltaic active layers.**

Flux (ph/m <sup>2</sup> sec)	Layer #6	Layer#9	Layer#10
Positive Flux	$1.3 \cdot 10^{24}$	$1.31 \cdot 10^{24}$	$8.79 \cdot 10^{23}$
Negative Flux	$5.36 \cdot 10^{22}$	$4.85 \cdot 10^{22}$	$4.85 \cdot 10^{22}$
Interference flux between counter propagating waves	$3.00 \cdot 10^{20}$	$7.03 \cdot 10^{19}$	$2.03 \cdot 10^{19}$

In conclusion, it is possible to use a *simplified generation function*, given by Eq.3.8, in which the positive and negative flow at the beginning and at the end of each layer can be calculated by TMM<sup>9</sup>. The simplified generation function will be used to solve the continuity equation in each PV active layer of the MJ structure.

<sup>9</sup> The positive and negative fluxes at the beginning of each layer have been computed by using the matrix elements reported in Appendix 1.

### 3.3. Scattering matrix method

It has been shown that by applying TMM the complex amplitudes of the forward and backward waves of a layer  $j$  are connected to the forward and backward waves of the layer  $j+1$ , so that it is possible to connect the first layer with the last one according to scheme reported in Figure 12.



**Figure 12.** Tracking the complex amplitudes of the forward and backwards waves from the layer “0” to the layer “N” with the transfer matrix  $M$ . The backward propagating wave coming from the last layer-air interface is considered null.

Considering the matrix elements, it is straightforward to assess that the transfer matrix  $M$  can grow exponentially as the number of layers and their thicknesses increase. I discovered that in a MJ structure where the substrate is thinned in order to increase the photo-voltage, and then it is considered as an active layer of the structure, a numerical instability can arise. In fact, for both polarization, each layer matrix contains the propagation matrix term (see Eq.2.74 and Eq.2.123) given by:

$$\begin{bmatrix} \Psi_j^- & \mathbf{0} \\ \mathbf{0} & \Psi_j^+ \end{bmatrix}$$

Considering  $N$  layers, the overall propagation matrix becomes:

$$\begin{bmatrix} \Psi_1^- * \dots * \Psi_{jN}^- & \mathbf{0} \\ \mathbf{0} & \Psi_1^+ * \dots * \Psi_N^+ \end{bmatrix}$$

The left terms of the propagation matrix are:  $\Psi_1^- * \dots * \Psi_{jN}^- = e^{-ik_{1,x}d_1} * \dots * e^{-ik_{N,x}d_N} = e^{-i(n_1 + i k'_{1,x})d_1} * \dots * e^{-i(n_N + i k'_{N,x})d_N} = e^{i(n_1 d_1 + \dots + n_N d_N)} * \dots * e^{(k'_{1,x} d_1 + \dots + k'_{N,x} d_N)}$

It is easy to see that the last exponential term can diverge if the thickness of the layers overcome a certain limit, especially in the wavelength region where the extinction coefficient, ( $k'_{N,x}$ ) are larger. In the simulation of MJ solar cell over a Ge substrate, for example, usually the substrate is considered optically thick and it is not considered in the propagation matrix. However, in the case where the solar cell substrate is thinned (for example, reduced from 150  $\mu\text{m}$  to 10  $\mu\text{m}$ ) and its thickness is considered in the propagation matrix, the numerical instability arises as the computation of the overall propagation matrix goes in overflow (see an example in chapter 3.6).

The simple S-matrix formulation suggested in [47] is a suitable alternative method that can be applied to study the electromagnetic fluxes in MJ solar cells, in order to avoid the numerical instabilities. In this thesis, the S-matrix elements have been calculated considering a different relationship among the outgoing and incoming waves with respect to what has been reported in [47]. The outgoing waves are connected to the incoming waves as reported in Figure 13 and Eq.3.16.

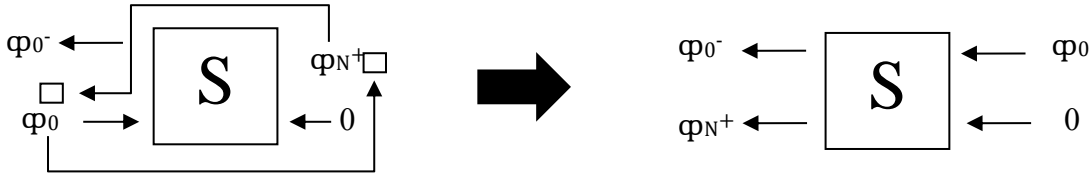


**Figure 13.** Tracking the complex amplitudes of the outgoing waves and incoming waves of the layer “0” and layer “N” connected by the S-matrix. The backward propagating wave coming from the last layer is considered null.

$$\begin{pmatrix} \varphi_0^- \\ \varphi_N^+ \end{pmatrix} = S \begin{pmatrix} \varphi_0^+ \\ 0 \end{pmatrix} \quad 3.16$$

In particular, we can think to build up a scattering matrix which connects the outgoing and incoming waves of the generic  $j$  layer with the outgoing and incoming waves of the last layer (still considering null the backward propagating wave coming from the last layer-air interface):

$$\begin{pmatrix} \varphi_j^- \\ \varphi_N^+ \end{pmatrix} = S_j \begin{pmatrix} \varphi_j^+ \\ 0 \end{pmatrix} = \begin{bmatrix} S_j(1,1) & S_j(1,2) \\ S_j(2,1) & S_j(2,2) \end{bmatrix} \begin{pmatrix} \varphi_j^+ \\ 0 \end{pmatrix} \quad 3.17$$

Therefore  $S_j$ -matrix elements, for example for the TM mode, can be calculated by forcing the compatibility of the system of Eq.2.73 with the system of Eq.3.17, and then considering:

$$F_j^\pm = \varphi_j^\pm \quad 3.18$$

More generically (for TM and TE case), for a layer  $j$ , we can build a characteristic layer matrix, such as:

$$\begin{cases} F_j^+ = M_{j+1}(1,1)F_{j+1}^+ + M_{j+1}(1,2)F_{j+1}^- & (A) \\ F_j^- = M_{j+1}(2,1)F_{j+1}^+ + M_{j+1}(2,2)F_{j+1}^- & (B) \end{cases} \quad 3.19$$

The wave function  $F_j^\pm$  are then equal to  $\chi_j^\pm$  or  $\Omega_j^\pm$ , and the matrix element  $M_{j+1}(i,j)$  are given by Eq 2.74 or Eq.2.123 respectively for TM and TE case. Eq.3.17 can written as:

$$\begin{cases} F_j^- = S_j(1,1)F_j^+ & (C) \\ F_N^+ = S_j(2,1)F_j^+ & (D) \end{cases} \quad 3.20$$

For  $j=N$ , Eq.3.20 becomes:

$$\begin{cases} F_N^- = S_N(1,1)F_N^+ \\ F_N^+ = S_N(2,1)F_N^+ \end{cases} \quad 3.21$$

Since  $F_N^- = 0 \rightarrow S_N(\mathbf{1}, \mathbf{1}) = \mathbf{0}$  and  $S_N(\mathbf{2}, \mathbf{1}) = \mathbf{1}$

Now, let's force the compatibility of the system of Eq.3.19 with the system of Eq.3.20.

For Eq. 3.19 A) and Eq. 3.20 C), it holds:

$$F_j^+ = M_{j+1}(1,1)F_{j+1}^+ + M_{j+1}(1,2)S_{j+1}(1,1)F_{j+1}^+ = F_{j+1}^+ [M_{j+1}(1,1) + M_{j+1}(1,2)S_{j+1}(1,1)] \quad 3.22$$

Since Eq.3.20 holds for every  $j$ , we can also write:

$$F_N^+ = S_{j+1}(2,1)F_{j+1}^+ = S_j(2,1)F_j^+ \quad 3.23$$

From Eq.3.23 Therefore, we get:

$$F_j^+ = F_{j+1}^+ \frac{S_{j+1}(2,1)}{S_j(2,1)} \quad 3.24$$

Considering Eq.3.22 and Eq.3.24, it follows:

$$\frac{S_{j+1}(2,1)}{S_j(2,1)} = M_{j+1}(1,1) + M_{j+1}(1,2)S_{j+1}(1,1) \quad 3.25$$

For Eq.3.19 B) and Eq.3.20 C), it holds:

$$F_j^- = S_j(1,1)F_j^+ = M_{j+1}(2,1)F_{j+1}^+ + M_{j+1}(2,2)S_{j+1}(1,1)F_{j+1}^+ \quad 3.26$$

Therefore:

$$S_j(1,1) = [M_{j+1}(2,1) + M_{j+1}(2,2)S_{j+1}(1,1)] \frac{F_{j+1}^+}{F_j^+} \quad 3.27$$

Eq.3.27 and Eq.3.24 gives:

$$S_j(1,1) = [M_{j+1}(2,1) + M_{j+1}(2,2)S_{j+1}(1,1)] \frac{S_j(2,1)}{S_{j+1}(2,1)} \quad 3.28$$

Then:

$$\frac{S_{j+1}(2,1)}{S_j(2,1)} = \frac{[M_{j+1}(2,1) + M_{j+1}(2,2)S_{j+1}(1,1)]}{S_j(1,1)} \quad 3.29$$

By equalling Eq.3.25 with Eq.3.29:

$$M_{j+1}(1,1) + M_{j+1}(1,2)S_{j+1}(1,1) = \frac{[M_{j+1}(2,1) + M_{j+1}(2,2)S_{j+1}(1,1)]}{S_j(1,1)} \quad 3.30$$

The Eq.3.30 allows calculating the scattering matrix element  $S_j(1,1)$ :

$$S_j(1,1) = \frac{[M_{j+1}(2,1) + M_{j+1}(2,2)S_{j+1}(1,1)]}{M_{j+1}(1,1) + M_{j+1}(1,2)S_{j+1}(1,1)} \quad 3.31$$

by knowing the scattering matrix element  $S_{j+1}(1,1)$  and the transfer matrix elements  $M_{j+1}(1,1)$ ,  $M_{j+1}(1,2)$ ,  $M_{j+1}(2,1)$ ,  $M_{j+1}(2,2)$ .

Let's now introduce in the Eq.3.31 the explicit expression of the matrix elements  $M_{j+1}$ , that we can write for TM and TE polarization with the generic form:

$$M_{j+1} = \frac{1}{2\gamma_j} \begin{bmatrix} \psi_{j+1}^-(\beta_j + \beta_{j+1}) & \psi_{j+1}^+(\beta_j - \beta_{j+1}) \\ \psi_{j+1}^-(\beta_j - \beta_{j+1}) & \psi_{j+1}^+(\beta_j + \beta_{j+1}) \end{bmatrix} \quad 3.32$$

where the terms  $\beta_j$  are given by Eq.2.61 or by Eq.2.117 for TM and TE case respectively. Then it holds:

$$S_j(1,1) = \frac{\psi_{j+1}^-(\beta_j - \beta_{j+1}) + \psi_{j+1}^+(\beta_j + \beta_{j+1})S_{j+1}(1,1)}{\psi_{j+1}^-(\beta_j + \beta_{j+1}) + \psi_{j+1}^+(\beta_j - \beta_{j+1})S_{j+1}(1,1)} \quad 3.33$$

Now, the divergent terms  $\psi_{j+1}^-$  can be easily eliminated by multiplying the numerator and denominator of Eq.3.33 by  $\psi_{j+1}^+$ , thus, we get :

$$S_j(1,1) = \frac{(\beta_j - \beta_{j+1}) + (\psi_{j+1}^+)^2(\beta_j + \beta_{j+1})S_{j+1}(1,1)}{(\beta_j + \beta_{j+1}) + (\psi_{j+1}^+)^2(\beta_j - \beta_{j+1})S_{j+1}(1,1)} \quad 3.34$$

Since  $S_N(1,1) = 0$ , from Eq.3.34 we can calculate  $S_{N-1}(1,1)$ :

$$S_{N-1}(1,1) = \frac{(\beta_{N-1} - \beta_N)}{(\beta_{N-1} + \beta_N)} \quad 3.35$$

By remembering that  $\psi_N^+ = e^{ik_{x,N}d_N} = 1$  because the thickness of the last layer can be considered null, from Eq.3.34 and Eq.3.35 it is then possible to calculate all the  $S_j(1,1)$  terms without numerical instability and utilizing Eq.3.20 C), all the  $F_j^-$  terms from the  $F_j^+$  ones.

By considering Eq.3.29 and Eq.3.31, it holds:

$$S_j(2,1) = \frac{S_{j+1}(2,1)}{M_{j+1}(1,1) + M_{j+1}(1,2)S_{j+1}(1,1)} \quad 3.36$$

Then, by considering the explicit expression of the matrix elements  $M_{j+1}$ :

$$S_j(2,1) = \frac{2\beta_j S_{j+1}(2,1)}{\psi_{j+1}^- (\beta_j + \beta_{j+1}) + \psi_{j+1}^+ (\beta_j - \beta_{j+1}) S_{j+1}(1,1)} \quad 3.37$$

Now, the divergent terms  $\psi_{j+1}^-$  can again be easily eliminated by multiplying the numerator and denominator of Eq.3.37 by  $\psi_{j+1}^+$ , so we get:

$$S_j(2,1) = \frac{2\beta_j \psi_{j+1}^+ S_{j+1}(2,1)}{(\beta_j + \beta_{j+1}) + (\beta_j - \beta_{j+1}) S_{j+1}(1,1) (\psi_{j+1}^+)^2} \quad 3.38$$

Since  $S_N(2,1) = 1$  and  $S_N(1,1) = 0$ , per  $J=N-1$  it holds:

$$S_{N-1}(2,1) = \frac{2\beta_{N-1} \psi_N^+}{(\beta_{N-1} + \beta_N)} \quad 3.39$$

Therefore, from Eq.3.38 and Eq.3.39, we can calculate all the matrix elements  $S_j(2,1)$ .

The outgoing and incoming waves in each layer, for TM and TE polarization, can now be easily calculated.

From Eq.3.20 D), for  $j=0$ , it holds:

$$F_0^+ = \frac{F_N^+}{S_0(2,1)} \quad 3.40$$

The electric field  $F_0^+$  propagating in the layer “0” (air) in the positive direction (toward the solar cell surface) can be calculated from the Poynting vector from Eq.2.140 or Eq.2.101 for TE and TM respectively. Therefore, From Eq.3.40 we can get  $F_N^+$  and therefore from Eq.3.20 all the  $F_j^+$  and  $F_j^-$ . In the following block diagram, the sequence of steps to be followed to calculate the outgoing and incoming waves in each layer with the S-method are summarized.

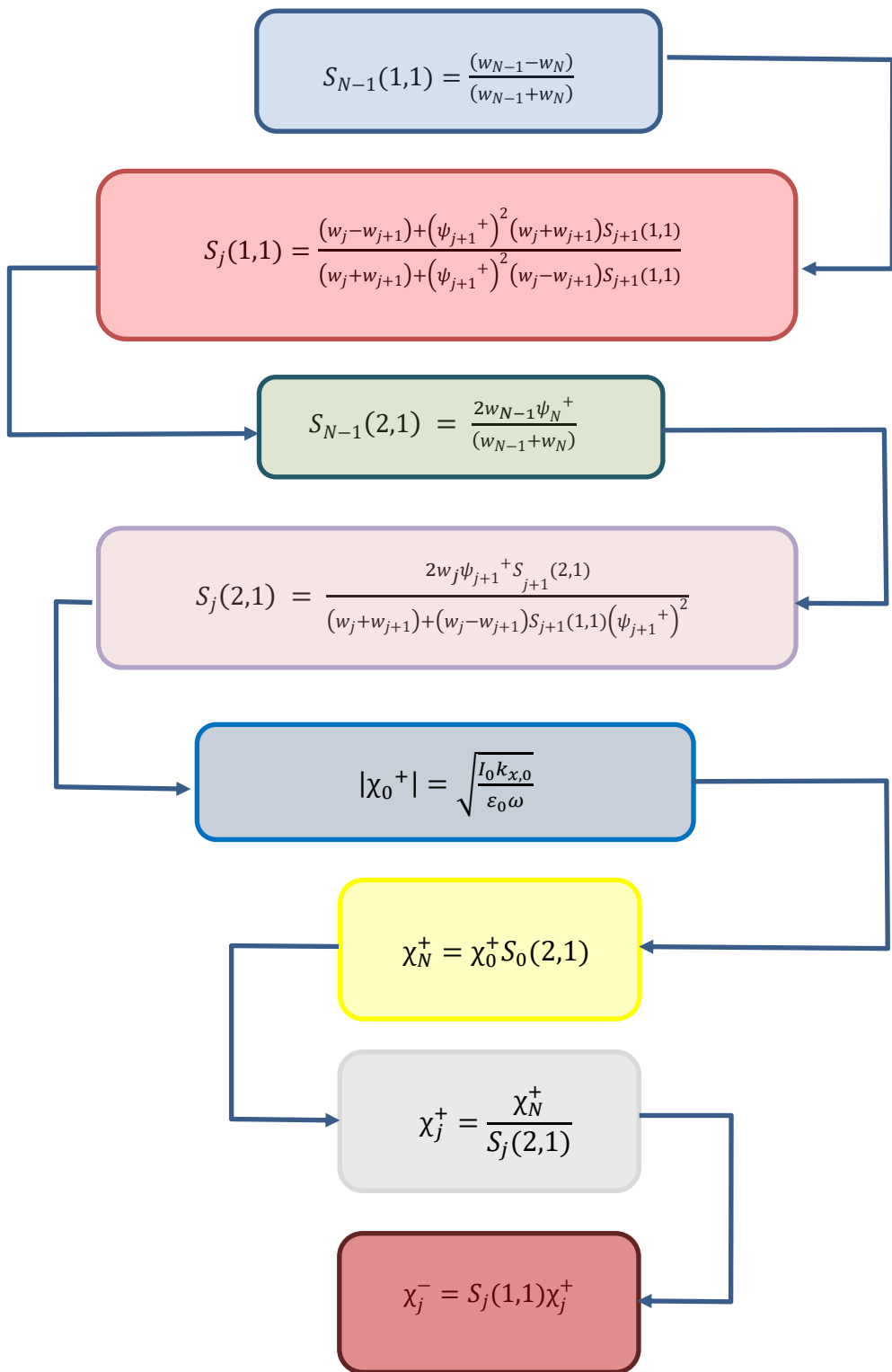


**Figure 14.** Sequence of steps to calculate the outgoing and incoming waves in each layer with the S-method for TM mode.

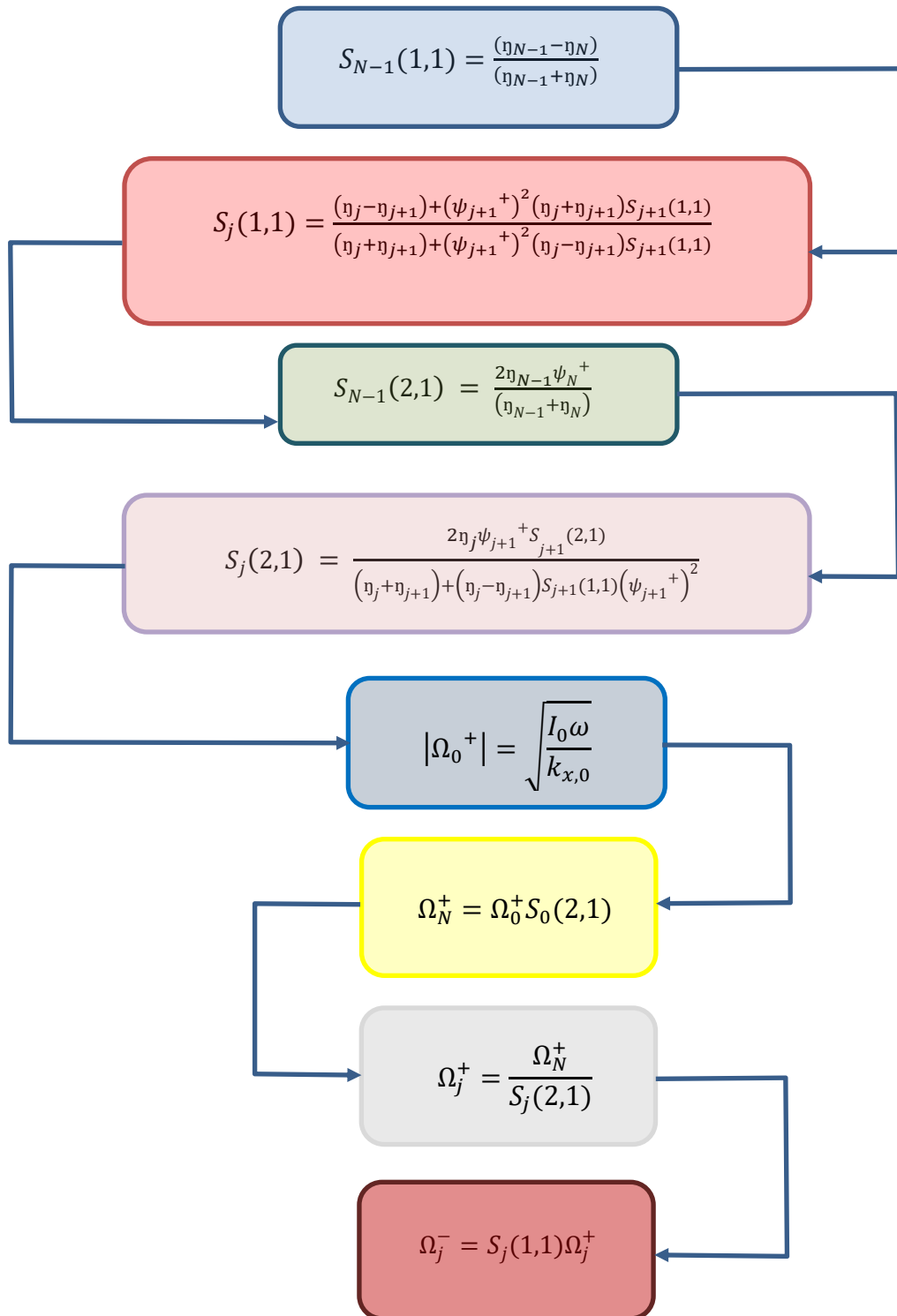


**Figure 15. Sequence of steps to calculate the outgoing and incoming waves in each layer with the S-method, TE case.**

### 3.4. Analytic solution of the continuity equation

Figure 16 shows a generic top-cell structure. Each sub-cell can include heterojunctions, intrinsic materials (or slightly doped materials), called spacer, inserted between the emitter and the base and eventually a BSF layer.

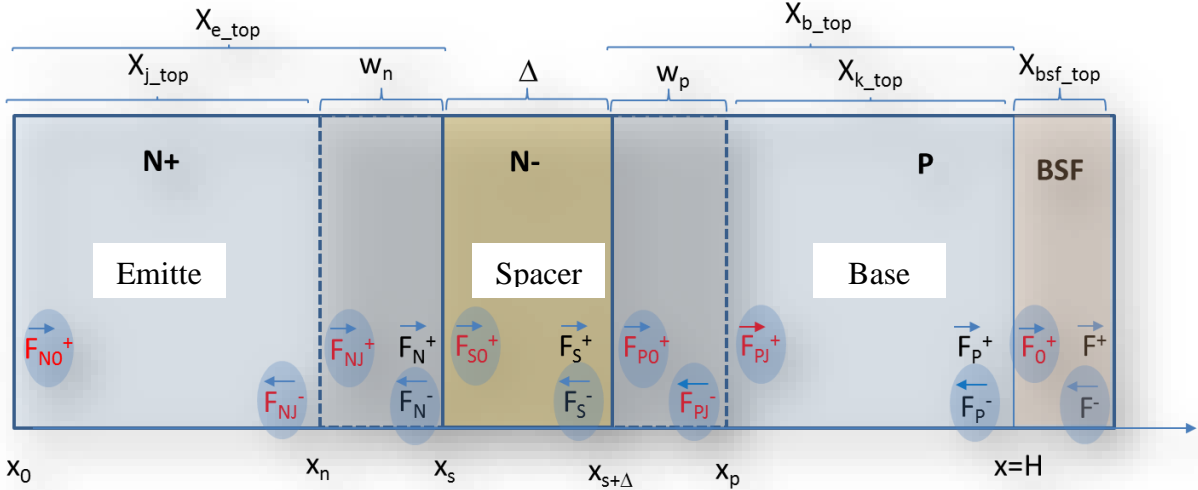


**Figure 16.** Schematic of a top cell structure (without the window layer) having the emitter, the spacer, the base and the BSF realized with different materials. The photon flows,  $F$ , to be calculated by TMM are indicated with the black colour, the photon flows indicated by a red colour can be easily obtained from the formers by using the generalized Lambert-Beer law. In each layer, the fluxes propagating in positive and negative direction to be used in the continuity equation are evidenced.

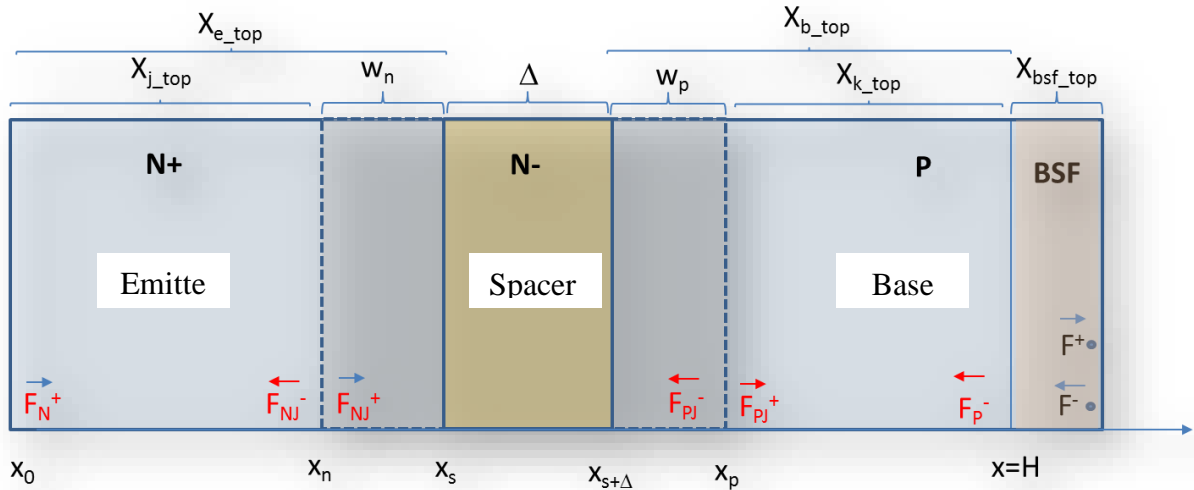


**Figure 17.** Schematic of the top cell homojunction structure (without the window layer) considering the same materials for all the layers. The photon flows calculated by TMM or SMM are indicated with the black colour, the photon flows indicated by a red colour can be easily obtained from the formers by using the generalized Lambert-Beer law.

With  $w_n$  and  $w_p$  are indicated the thickness of the depletion regions extending respectively in the emitter and base. With  $\Delta$  is indicated the thickness of the spacer layer. According to the MJ solar

cell structure reported in Table 1, the emitter, the spacer, the base and the BSF of the top cell are made of the same material (top cell homojunction), therefore the photon flows to be calculated by TMM are those reported in Figure 17. The spacer, with thickness  $\Delta$ , can be considered completed depleted of free carriers, therefore the total thickness of the depletion region is:  $W=W_n+\Delta+W_p$ .

According to Eq. 3.8, the top cell emitter and the base generation rates are respectively given by:

$$G_{p,top}(x, \lambda) = 2\text{Im}[k_{top,x}(\lambda)] [F_N^+(x_0, \lambda)e^{2\text{Im}[k_{top,x}(\lambda)](x_0-x)} + F_{Nj}^-(x_N, \lambda)e^{2\text{Im}[k_{top,x}(\lambda)](x-x_N)}] \quad 3.41$$

$$G_{n,top}(x, \lambda) = 2\text{Im}[k_{top,x}(\lambda)] [F_P^+(x_P, \lambda)e^{2\text{Im}[k_{top,x}(\lambda)](x_P-x)} + F_P^-(H, \lambda)e^{2\text{Im}[k_{top,x}(\lambda)](x-H)}] \quad 3.42$$

Where  $k_{top,x} = k_{InGaP}$ ; and  $(x_0 - x), (x - x_N), (x_P - x), (x - H) \leq 0$ .

In the top cell depletion region, with the assumption that all the generated carries are swept in opposite direction and collected, the generation rate is:

$$G_{dr,top}(x, \lambda) = \{[F_{Nj}^+(x_N, \lambda) + F_P^-(x_P, \lambda)] (1 - e^{-2\text{Im}[k_{top,x}(\lambda)]W})\} \quad 3.43$$

By considering the TJ structure reported in Table 1, for the middle cell, the emitter and the BSF are made of different materials with respect to the spacer and the base, therefore the photon flows to be considered are those reported in Figure 18.

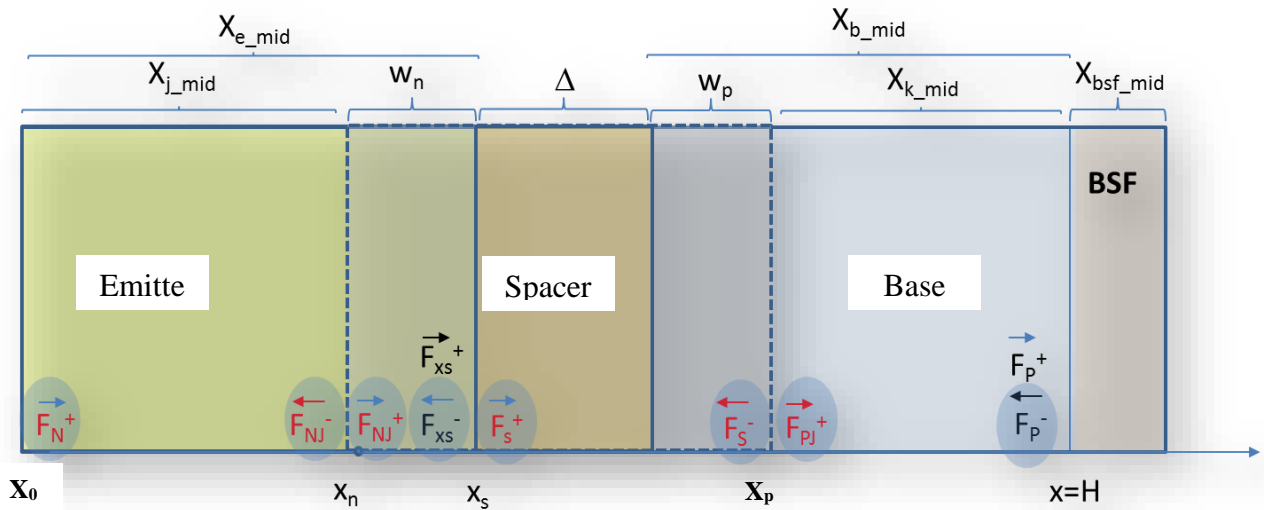


**Figure 18.**Schematic of the middle cell structure (without the window) considering the emitter and the BSF realized with a different material with respect to the spacer and base. The photon flows calculated by TMM or SMM are evidenced with the black colour, the photon flows indicated by the red colour are easily obtained from the former by using the generalized Lambert-Beer law.

The generation rates in emitter and base have the same expression determined for the top cell:

$$G_{p,mid}(x, \lambda) = 2\text{Im}[k_{em}(\lambda)] [F_N^+(x_0, \lambda)e^{2\text{Im}[k_{em}(\lambda)](x_0-x)} + F_{Nj}^-(x_N, \lambda)e^{2\text{Im}[k_{em}(\lambda)](x-x_N)}] \quad 3.44$$

$$G_{n,mid}(x, \lambda) = 2Im[k_{base}(\lambda)][F_P^+(x_p, \lambda)e^{2Im[k_{base}(\lambda)](x_p-x)} + F_P^-(H, \lambda)e^{2Im[k_{base}(\lambda)](x-H)}] \quad 3.45$$

Where  $k_{em} = k_{AlInGaAs}$  and  $k_{base} = k_{InGaAs}$ .

For the middle cell depletion region, we have two contributions:

$$G_{dr1,mid}(x, \lambda) = \{[F_N^+(x_N, \lambda) + F_S^-(x_S, \lambda)](1 - e^{-2Im[k_{em}(\lambda)]w_n})\} \quad 3.46$$

$$G_{dr2,mid}(x, \lambda) = \{[F_S^+(x_S, \lambda) + F_P^-(x_p, \lambda)](1 - e^{-2Im[k_{base}(\lambda)](\Delta+w_p)})\} \quad 3.47$$

For the bottom cell, in this first computation, we can consider the substrate very thick, therefore only the positive flow has to be considered and the generation function is much more simplified (see Figure 19).

The generation rate for the base and the emitter can be written as:

$$G_{p,bot}(x, \lambda) = 2Im[k_{bot}(\lambda)][F_N^+(x_0, \lambda)e^{2Im[k_{bot}(\lambda)](x_0-x)}] \quad 3.48$$

$$G_{n,bot}(x, \lambda) = 2Im[k_{bot}(\lambda)][F_P^+(x_p, \lambda)e^{2Im[k_{bot}(\lambda)](x_p-x)}] \quad 3.49$$

These terms are formally identical to the generation terms of the Hovel model, therefore for the bottom cell, the solution of the set of equations from Eq.2.1 to Eq. 2.4, considering Eq. 2.5, and the boundary condition shown in Figure 3, coincides with the solution obtained by Hovel, simply by replacing the absorption coefficient with  $2Im[k_{bot}(\lambda)]$  and the incident photon flows reported in the Eq.2.6 and Eq.2.7 with the terms  $F_N^+(x_0, \lambda)$  or  $F_P^+(x_p, \lambda)$  for the emitter and base respectively. Here the solution obtained by Hovel is not reported as it can be found in several textbooks and papers (see, for example ref [35]).

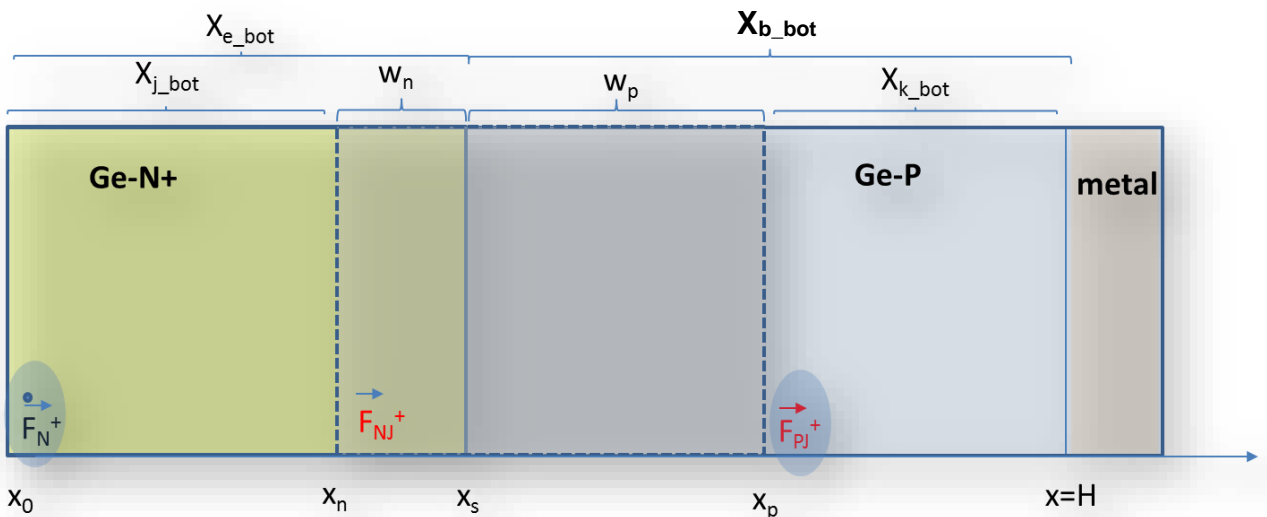


**Figure 19.** Schematic of the bottom cell structure (without the window). The photon flows calculated by TMMor SMM are evidenced with the black colour, the photon flows indicated by the red colour are easily obtained from the formers by using the generalized Lambert-Beer law.

For the bottom depletion region holds:

$$G_{dr,bot}(x, \lambda) = \left\{ F_N^+ e^{-2Imk_{bot}(\lambda)x_j} \left( 1 - e^{-2Im[k_{bot}(\lambda)](w_n+w_p)} \right) \right\} \quad 3.50$$

Since for the top and middle cells the generation terms have the same expression, the solution of the set of equations from Eq.2.1 to Eq.2.4 will be formally identical. Eq.3.41 and Eq. 3.44 can be generically written as:

$$G_p = 2Im(k) [F_N^+ e^{-2Im(k)x} + F_N^- e^{2Im(k)(x-x_N)}] \quad 3.51$$

where it has been assumed,  $x_0 = 0$  and it has been implicitly considered the dependence of  $G_p$  by the wavelength and position.

Similarly Eq.3.42 and Eq.3.45 can be generically written as:

$$G_n = 2Im(k) [F_P^+ e^{2Im(k)(x_P-x)} + F_P^- e^{2Im(k)(x-H)}] \quad 3.52$$

### 3.4.1. Determination of $j_p$

Let's start to solve the set of equations from Eq.2.1 to Eq.2.4 for the emitter.

By considering the assumption 4) of chapter 2.1 and Eq.2.5, the Eq.2.4, in stationary condition, can be written as:

$$-\frac{1}{q} \frac{d}{dx} \left( q D_p \frac{d(p_n - p_{n0})}{dx} \right) - G_p + \frac{p_n - p_{n0}}{\tau_p} = 0 \quad 3.53$$

Where the equilibrium hole concentration in the emitter,  $p_{n0}$ , has been considered position independent.

Multiplying the Eq.3.53 by  $\tau_p L_p^3$  and again, considering  $D_p$  and  $L_p$  position independent, we have:

$$D_p \tau_p \frac{d^2}{dx^2} [(p_n - p_{n0}) L_p^3] + G_p \tau_p L_p^3 - (p_n - p_{n0}) L_p^3 = 0 \quad 3.54$$

Setting:

$$y = (p_n - p_{n0}) L_p^3; \quad L_p = \sqrt{D_p \tau_p}; \quad \mathbb{x} = \frac{x}{L_p} \quad 3.55$$

Eq.3.54 becomes:

$$\frac{d^2 y}{d\mathbb{x}^2} + G_p \tau_p L_p^3 - y = 0 \quad 3.56$$

By considering Eq.3.51 and Eq.3.55, it holds:

$$G_p \tau_p L_p^3 = \tau_p L_p^3 \left\{ 2Im(k) \left[ F_N^+ e^{-2L_p Im(k) \frac{x}{L_p}} + F_N^- e^{2L_p Im(k) \frac{(x-x_N)}{L_p}} \right] \right\} \quad 3.57$$

$$G_p \tau_p L_p^3 = \tau_p L_p^3 \{2Im(k)[F_N^+ e^{-2L_p Im(k)x} + F_N^- e^{2L_p Im(k)(x-x_N)}]\} \quad 3.58$$

By setting:

$$f_N^+ = \tau_p L_p^3 2Im(k) F_N^+; \quad f_N^- = \tau_p L_p^3 2Im(k) F_N^-; \quad \beta_p = 2L_p Im(k) \quad 3.59$$

Eq.3.56 becomes:

$$\frac{d^2y}{dx^2} + f_N^+ e^{-\beta_p x} + f_N^- e^{\beta_p (x-x_N)} - y = 0 \quad 3.60$$

The Eq. 3.60 is a second order nonhomogeneous differential equation.

The general solution of Eq. 3.60 is given by:

$$y = y_c + y_p \quad 3.61$$

where:  $y_c$  is the solution of the associated homogeneous equation:

$$\frac{d^2y}{dx^2} - y = 0 \quad 3.62$$

which can be written as:

$$y_c = A_p \cosh x + B_p \sinh x \quad 3.63$$

and  $y_p$  is a particular solution. As particular solution we can chose:

$$y_p = C_p [f_N^+ e^{-\beta_p x} + f_N^- e^{\beta_p (x-x_N)}] \quad 3.64$$

The constant  $C_p$  can be easily determined by introducing Eq. 3.64 an its second derivate in Eq.3.60.

$$\beta_p^2 y_p + \frac{y_p}{C_p} - y_p = 0 \quad 3.65$$

$$C_p = \frac{1}{1 - \beta_p^2} \quad 3.66$$

The solution of Eq.3.60 is then:

$$y = A_p \cosh x + B_p \sinh x + \frac{f_N^+ e^{-\beta_p x} + f_N^- e^{\beta_p (x-x_N)}}{1 - \beta_p^2} \quad 3.67$$

The constants  $A_n, B_n$  can be determined by applying the two boundary conditions:

$$D_p \frac{d(p_n - p_0)}{dx} = S_p (p_n - p_0) \quad \text{at } x = x_0 = 0 \quad 3.68$$

$$(p_n - p_0) = 0 \quad \text{at } x = x_N \quad 3.69$$

The Eq.3.68 indicates that there is a recombination current towards the surface which, through the recombination velocity  $S_p$ , is proportional to the excess carrier concentration. Eq.3.69 indicates that

at the depletion region boundary, the generated carriers are swept away and the minority carrier concentration is equal to the equilibrium one. By considering Eq.3.55, the boundary conditions can be written as:

$$D_p \frac{d[(p_n - p_0)L_p^3]}{L_p d \frac{x}{L_p}} = S_p [(p_n - p_0)L_p^3] \rightarrow \frac{dy}{dx} = \frac{S_p L_p}{D_p} y \rightarrow \boxed{\frac{dy}{dx} = \eta_p y \quad \text{at } x = 0} \quad 3.70$$

$$(p_n - p_0) = 0 \rightarrow \boxed{y = 0 \quad \text{at } x = x_N = x_e - \frac{w_n}{L_p}} \quad 3.71$$

Where  $x_e$  is the *reduced* emitter thickness, that is the ratio between the emitter thickness and the diffusion length and  $\eta_p = \frac{S_p L_p}{D_p}$ .

From Eq.3.70 it follows:

$$B_p = \eta_p A_p + \frac{f_N^+(\eta_p + \beta_p) + f_N^-(\eta_p - \beta_p)e^{-\beta x_N}}{1 - \beta_p^2} \quad 3.72$$

From Eq.3.71 and considering Eq.3.72 it holds:

$$A_p = \frac{f_N^+[(\eta_p + \beta_p) \sinh x_N + e^{-\beta p x_N}] + f_N^-[(\eta_p - \beta_p)e^{-\beta x_N} \sinh x_N + 1]}{(\beta_p^2 - 1)(\cosh x_N + \eta_p \sinh x_N)} \quad 3.73$$

The emitter current can be calculated in  $x_N$ , by using Eq..1 and remembering the assumption 4) of the chapter 2.1:

$$J_p(x_n) = -q D_p \frac{1}{L_p^3} \frac{d(p_n - p_{n0})L_p^3}{d \frac{x}{L_p} L_p} \Big|_{x_n} = -q D_p \frac{1}{L_p^4} \frac{dy}{dx} \Big|_{x_n} \quad 3.74$$

$$J_p(x_n) = -q D_p \frac{1}{L_p^4} \left[ A_p \sinh x_n + B_p \cosh x_n + \beta \frac{f_N^- - f_N^+ e^{-\beta p x_n}}{1 - \beta_p^2} \right] \quad 3.75$$

Where  $A_p$  and  $B_p$  are given respectively by Eq. 3.73 and Eq.3.72.

### 3.4.2. Determination of $j_n$

Considering Eq.2.2 and Eq. 2.3 with the assumption 4) of chapter 2.1, and that the equilibrium electron concentration in the base,  $n_{p0}$ , is position independent, in stationary condition it holds:

$$\frac{1}{q} \frac{d}{dx} \left( q D_n \frac{d(n_p - n_{p0})}{dx} \right) + G_n - \frac{n_p - n_{p0}}{\tau_n} = 0 \quad 3.76$$

Multiplying Eq. 3.76 by  $\tau_n L_n^3$  and considering, again, both  $L_n$  and  $D_n$  position independent, Eq. 3.76 becomes:

$$D_n \tau_n \frac{d^2}{dx^2} [(n_p - n_{p0}) L_n^3] + G_n \tau_n L_n^3 - (n_p - n_{p0}) L_n^3 = 0 \quad 3.77$$

Setting:

$$y = (n_p - n_{p0}) L_n^3; \quad L_n = \sqrt{D_n \tau_n}; \quad \mathbb{x} = \frac{x - x_p}{L_n} \quad 3.78$$

Eq. 3.77 can be written as:

$$\frac{d^2 y}{d\mathbb{x}^2} + G_n \tau_n L_n^3 - y = 0 \quad 3.79$$

The generation function is given by Eq.3.52, therefore:

$$G_n \tau_n L_n^3 = \tau_n L_n^3 2Imk(\lambda) \left[ F_P^+ e^{2Im(k)L_n \frac{(x_p - x)}{L_n}} + F_P^- e^{2Im(k)L_n \frac{(x - H)}{L_n}} \right] \quad 3.80$$

By considering Eq.3.78 and setting:

$$f_P^+ = \tau_n L_n^3 2Im(k) F_P^+; \quad f_P^- = \tau_n L_n^3 2Im(k) F_P^-; \quad \beta_n = 2L_n Im(k); \quad \mathbb{x}_p = \frac{x_p}{L_n}; \quad h = \frac{H}{L_n} \quad 3.81$$

Eq.3.79 becomes:

$$\frac{d^2 y}{d\mathbb{x}^2} + f_P^+ e^{-\beta_n \mathbb{x}} + f_P^- e^{\beta_n (\mathbb{x} + \mathbb{x}_p - h)} - y = 0 \quad 3.82$$

Eq.3.82 is formally identical to Eq.3.60 in which  $-\mathbb{x}_N$  is replaced by  $\mathbb{x}_p - h$  and  $\beta_p$  is replaced with  $\beta_n$ . The solution of Eq.3.82 is then:

$$y = A_n \cosh \mathbb{x} + B_n \sinh \mathbb{x} + \frac{f_P^+ e^{-\beta_n \mathbb{x}} + f_P^- e^{\beta_n (\mathbb{x} + \mathbb{x}_p - h)}}{1 - \beta_n^2} \quad 3.83$$

The constants  $A_n$ ,  $B_n$  can be determined by applying the two boundary conditions with the same meaning as those written previously in Eq.3.68 and Eq.3.69:

$$(n_p - n_{p0}) = 0 \quad \text{at } x = x_p \quad 3.84$$

$$q D_n \frac{d(n_p - n_{p0})}{dx} = -q S_n (n_p - n_{p0}) \quad \text{at } x = H \quad 3.85$$

By considering Eq.3.78, the boundary conditions of Eq. 3.84 and Eq. 3.85 can be respectively written as:

$y = 0 \quad \text{at } \mathbb{x} = 0$

3.86

$$D_n \frac{d[(n_p - n_{p0})L_n^3]}{L_n d\frac{x}{L_n}} = -S_n [(n_p - n_{p0})L_n^3] \rightarrow \frac{dy}{dx} = -\frac{S_n L_n}{D_n} y \rightarrow \boxed{\frac{dy}{dx} = -\eta_n y \quad \text{at } x = h - x_p} \quad 3.87$$

Where  $\eta_n = \frac{S_n L_n}{D_n}$ .

Considering Eq.3.86, it holds:

$$A_n = \frac{f_p^+ + f_p^- e^{\beta_n(x_p - h)}}{\beta_n^2 - 1} \quad 3.88$$

Considering Eq.3.87, it holds:

$$\begin{aligned} A_n \sinh(h - x_p) + B_n \cosh(h - x_p) &+ \frac{-\beta_n f_p^+ e^{-\beta_n(h - x_p)} + \beta_n f_p^-}{1 - \beta_n^2} \\ &= -\eta_n \left[ A_n \cosh(h - x_p) + B_n \sinh(h - x_p) + \frac{f_p^+ e^{-\beta_n(h - x_p)} + f_p^-}{1 - \beta_n^2} \right] \end{aligned} \quad 3.89$$

Setting:

$$\xi = \frac{f_p^-(\beta_n + \eta_n) - f_p^+ e^{-\beta_n(h - x_p)}(\beta_n - \eta_n)}{\beta_n^2 - 1} \quad 3.90$$

$$\Gamma = [\sinh(h - x_p) + \eta_n \cosh(h - x_p)] \quad 3.91$$

$$\Xi = [\cosh(h - x_p) + \eta_n \sinh(h - x_p)] \quad 3.92$$

The coefficient  $B_n$  is given from Eq. 3.89 by:

$$B_n = \frac{\xi - \Gamma A_n}{\Xi} \quad 3.93$$

The base current can be calculated in  $x = 0$  by using Eq.2.2 and remembering the assumption 4) of the chapter 2.1:

$$J_n(0) = q D_n \frac{1}{L_n^3} \frac{d(n_p - n_{p0})L_n^3}{d\frac{x}{L_n} L_n} \Big|_{x=0} = q D_n \frac{1}{L_p^4} \frac{dy}{dx} \Big|_{x=0} \quad 3.94$$

$$J_n(0) = q D_n \frac{1}{L_n^4} \left[ B_n + \beta_n \frac{f_p^- e^{\beta_n(x_p - h)} - f_p^+}{1 - \beta_n^2} \right] \quad 3.95$$

Where  $B_n$  is given by Eq.3.93.

In conclusion, it has been shown that it is possible to find simple analytical solutions of the continuity equation, expressed by Eq.3.75 and Eq.3.95, which allow calculating the currents in each sub-cell of a MJ device, as a function of the positive and negative flows determined in each layer by TMM model.

### 3.5. Hovel model, TMM and SMM applied on thick InGaP/InGaAs/Ge TJ cells

The Hovel model and the TMM-SMM model have been applied to calculate the external quantum efficiency of the TJ structure reported in Table 1 in which the Ge substrate is 150  $\mu\text{m}$  thick, therefore, is not considered in the computation of the propagation matrix (see Figure 20).

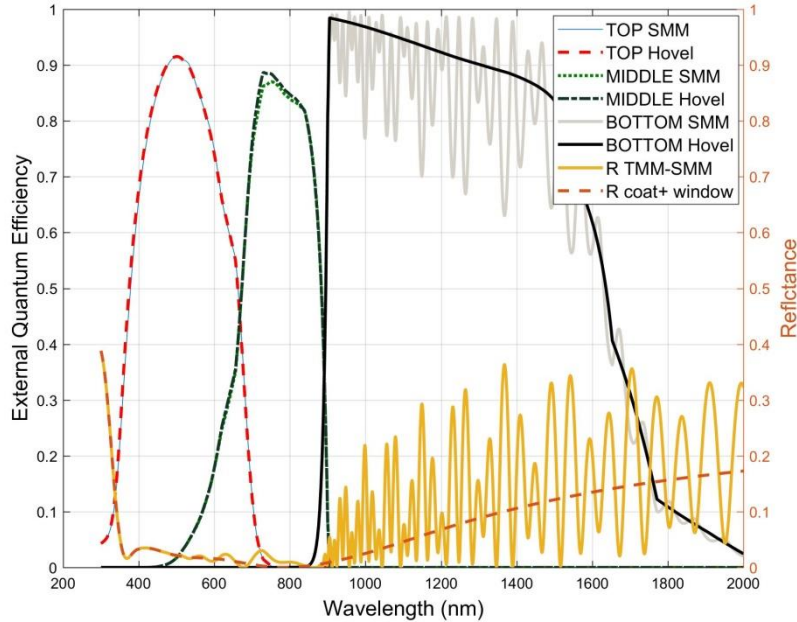


**Figure 20.** External quantum efficiency of the top, middle and bottom cells calculated by TMM, SMM and by the Hovel model. In this TJ structure case, TMM and SMM gives rise to the same results, so only SMM data are shown. In the case of the TMM and SMM models, the reflectance considers all the reflections which take place inside the multi-junction structure. In the case of the Hovel model, the reflectance considers only the reflections which take place inside the coating structure and the top cell window layer.

Once the EQE is integrated with the impinging solar flux, it is possible to calculate the short circuit current density generated in each sub cell, as reported in Table 3. As expected, the results obtained by the Hovel model differs from those obtained by TMM or SMM where the interference effects are more pronounced.

The Hovel model slightly overestimates the short circuit current with respect to SMM-TMM especially for the mid and bottom cell. It should be also considered that the above calculations have been carried out by assuming the light at normal incidence, that is, when the solar rays hit perpendicularly the solar cell's surface. In fact, in the mathematical Hovel model is not included any dependence of the EQE from the incidence angle. As a matter of fact, by changing the incident angle, it can happen that a TJ structure optimized to be middle limited by SMM-TMM can be top limited when the Hovel model is applied (see Table 4).

**Table 3. Short circuit current density calculated by Hovel model and by TMM for the solar spectrum ASTM G173-03.**

<b>Cell</b>	<b>Short circuit current density calculated by using the SMM-TMM model (mA/cm<sup>2</sup>)</b>	<b>Short circuit current density calculated by using the Hovel model (mA/cm<sup>2</sup>)</b>
Top	13.87	13.88
Middle	13.93	14.07
Bottom	22.61	23.89

This difference has to be taken into account when MJ solar cells operate under lenses at high concentration.

**Table 4. Short circuit current density calculated by Hovel model and by TMM for the solar spectrum ASTM G173-03 and considering the solar light impinging the solar cell with an angle of 50°.**

<b>Cell</b>	<b>Short circuit current density calculated by using the SMM-TMM (mA/cm<sup>2</sup>)</b>	<b>Short circuit current density calculated by using the Hovel model (mA/cm<sup>2</sup>)</b>
Top	13.88	13.81
Middle	13.68	13.90
Bottom	21.5	22.72

In conclusion, the Hovel model allows a good estimation of the sub-cells currents values in TJ solar cells, however for a fine tuning of cell's structure in order to reduce the current mismatch, especially for solar cells to be used in concentrator system, TMM and SSM have to be preferred as they give more accurate results.

### 3.6. TMM and SMM applied on MJ solar cells with improved voltage (thin substrate)

In order to improve the MJ cell voltage, the substrate can be thinned and a mirror deposited on the back side of the device [54]. It will be firstly shown that, in such a structure, TMM fails in the determination of the reflection coefficient in the short wavelength range, and, as a consequence, the top cell EQE becomes undetermined. As already reported in chapter 3.3, this failure is due to the intrinsic numerical instability of the TMM, as the number of layer and their thickness overcome a certain threshold. The numerical instability can be overcome by replacing TMM with SMM.

#### 3.6.1. Numerical instability of TMM on MJ solar cells with improved voltage (thin substrate)

Let's start considering the MJ structure of Table 1 in which the substrate has been thinned. In the Ge substrate the third junction is still present. We assume that the back side of the Ge cell is perfectly passivated and, further, a perfect aluminium mirror is deposited. The TMM is applied on such a structure to get the reflectance and then determine the EQE. To better visualize the numerical instability, for all the wavelength in which the calculus based on TMM goes in overflow, the reflectivity values have been set to zero. Figure 21 shows that TMM fails in the determination of the reflectance in the low wave wavelength range. As a benchmark, in the same figure, it is also reported the reflectance calculated by SMM. While the semi-infinite substrate structure allows neglecting the coherent reflections in the substrate, which in turn, it is equivalent to consider a substrate with zero thickness, once the substrate is thinned, the coherent reflections inside this layer have to be taken into account. This means that a further layer has to be included in the TMM calculation for getting the intensity of the forward and backward waves propagating inside the MJ structure. In this situation the TMM becomes numerically unstable and the numerical instability gets worse, that is, the calculus starts going in overflow, at longer wavelength, as the thickness of the substrate is increased.

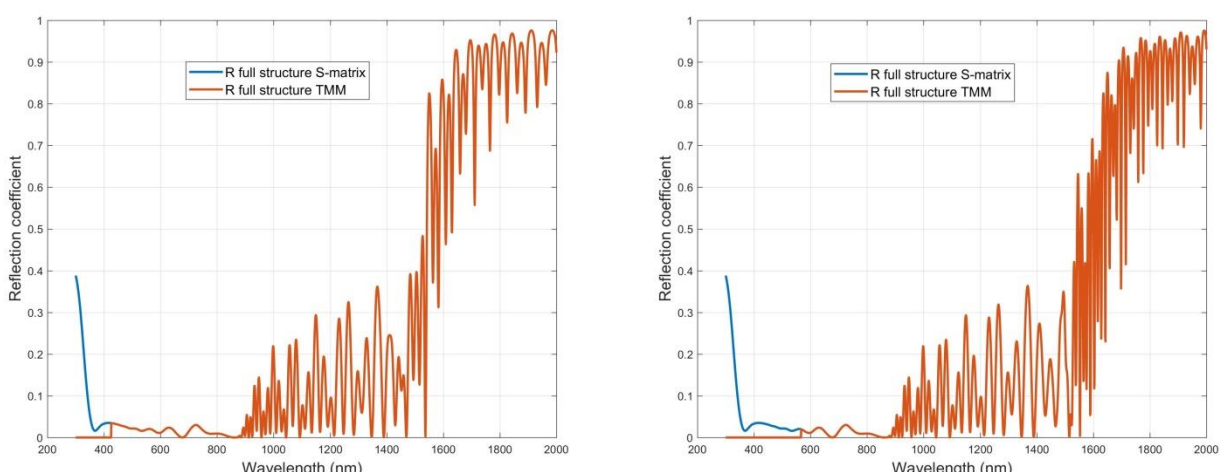


**Figure 21. Reflection coefficient calculated by TMM and S-matrix method for the full InGaP/InGaAs/Ge solar cell structure considering a 6  $\mu\text{m}$  (left) and 15  $\mu\text{m}$  (right) thick Ge substrate. An Al mirror was considered as last layer.**

Since TMM fails in the calculation of the reflectance in the low wavelength region, this means that the top cell EQE cannot be determined. In order to overcome this problem, the TMM can be replaced with SMM which does not become unstable as the number of MJ layers increases. As shown in Figure 21, the SMM fulfils the requirement of the numerical stability.

### 3.6.2. Validation of the SSM on thin 3J InGaP/InGaAs/Ge solar cells

The TMMs and SMMs are hereafter applied to simulate the performance of the 3J InGaP/InGaAs/Ge solar cell whose structure has been reported in tab 2 and in which: i) the substrate has been further thinned with respect to the previous example, ii) the substrate is also included in the computation of the reflection coefficient, i.e., is considered as the N-1 layer. In the simulation the IV curves have been obtained neglecting the series and shunt resistance (ideal IV curves). In all the simulations an Al back contact layer is considered. The IV curves shown in Figure 24 put in evidence that by thinning the Ge substrate, the  $V_{oc}$  of the bottom Ge solar cell improves of 20 mV (because it is possible to reduce the bulk recombination), bringing the  $V_{oc}$  of the TJ from 3.174 V to 3.194 V. It has to point out that the possibility to increase the  $V_{oc}$  value by thinning the Ge substrate is tightly related to the surface recombination velocity value at the base/BSF interface. In the calculation it has been assumed a surface recombination velocity value of  $10^3$  cm/sec. If were possible to decrease the surface recombination velocity to  $10^2$  cm/sec, the  $V_{oc}$  of the TJ would reach 3226 V, with a voltage increase of 52 mV. As a consequence, the TJ efficiency would increase from 38.79% to 39.43%.

It can be pointed out that the SMM simulations carried out by considering a 200  $\mu\text{m}$  thick substrate as the  $N-1$  layer or as the last ( $N$ ) layer give, as expected, the same results (see Figure 23, Figure 24 and Figure 25).

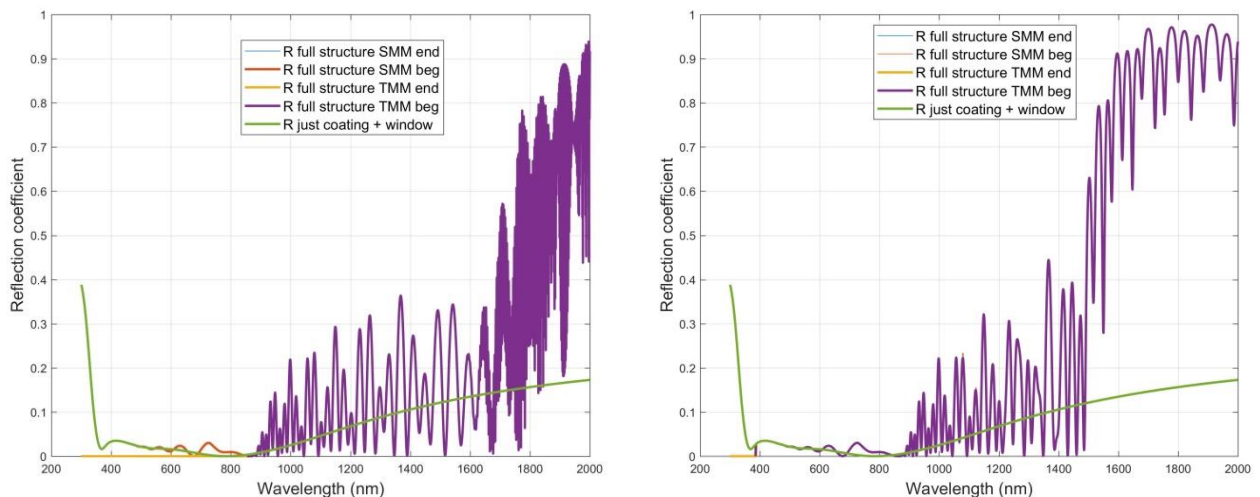


**Figure 22. Reflection coefficient a 3J InGaP/InGaAs/Ge solar cell calculated by applying TMM and SMM and by considering a 200  $\mu\text{m}$  thick (left) and a 3  $\mu\text{m}$  thick (right) Ge substrate with a back Al layer. The calculation has been carried out by considering both the electric fields at the beginning (beg) and at the end of the layers. For comparison, the reflection coefficient calculated only for the coating and the top cell window layer, assuming an underlying thick InGaP layer is also shown.**

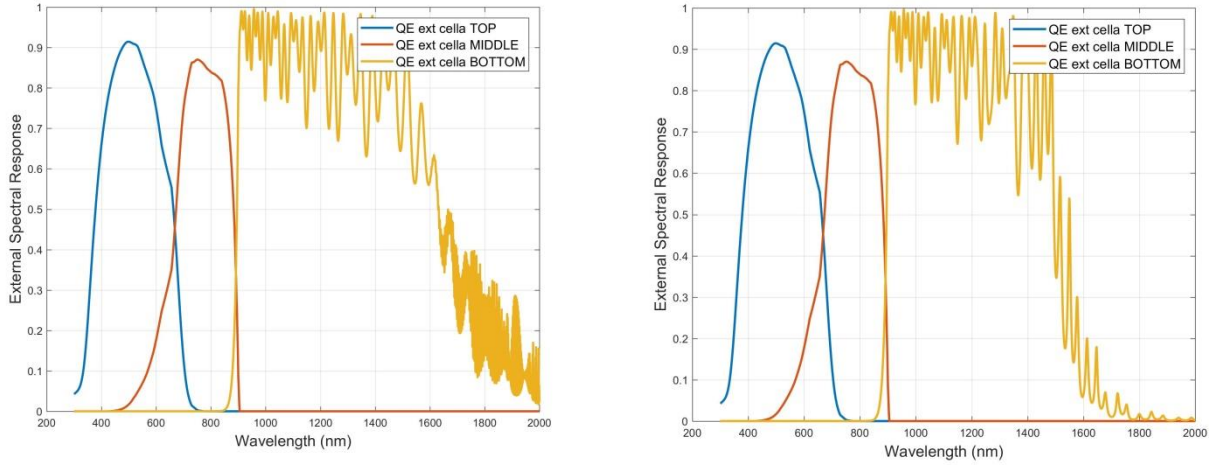


**Figure 23. EQE of a 3J InGaP/InGaAs/Ge solar cell considering a 200  $\mu\text{m}$  thick (left) and a 3  $\mu\text{m}$  thick (right) Ge base.**

This is indeed what we expect, because when the substrate is very thick the negative component of the Poynting vector is negligible.

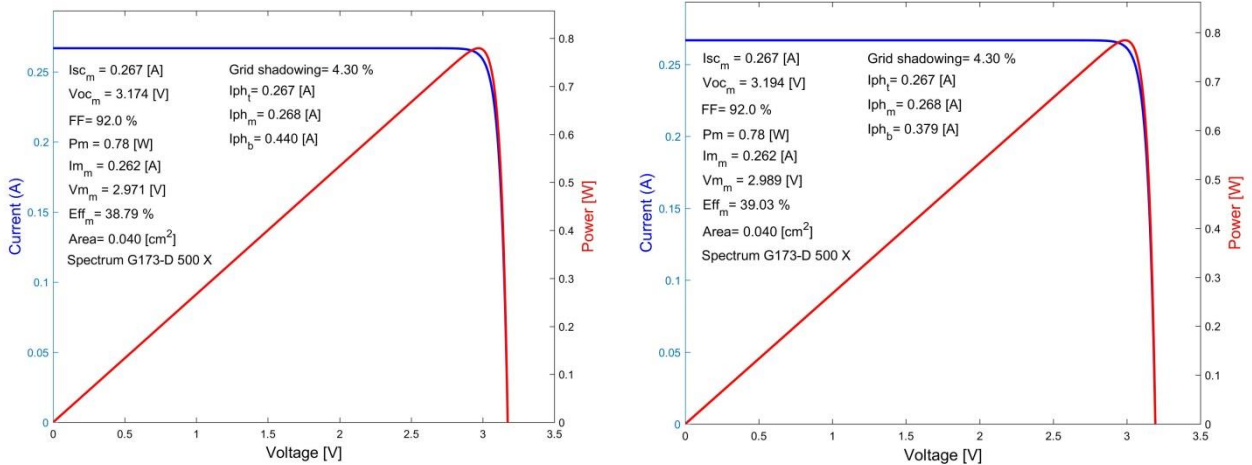


**Figure 24. 500 x- illuminated ideal IV curve of a 3J InGaP/InGaAs/Ge solar cell considering a 200  $\mu\text{m}$  thick (left) and a 3  $\mu\text{m}$  thick (right) Ge base. The subscript  $m$  indicates that the solar cells have a *mask* with a grid shadowing depicted. The surface recombination velocity value for the base/BSF interface was assumed equal to  $10^3 \text{ cm/sec}$ .**

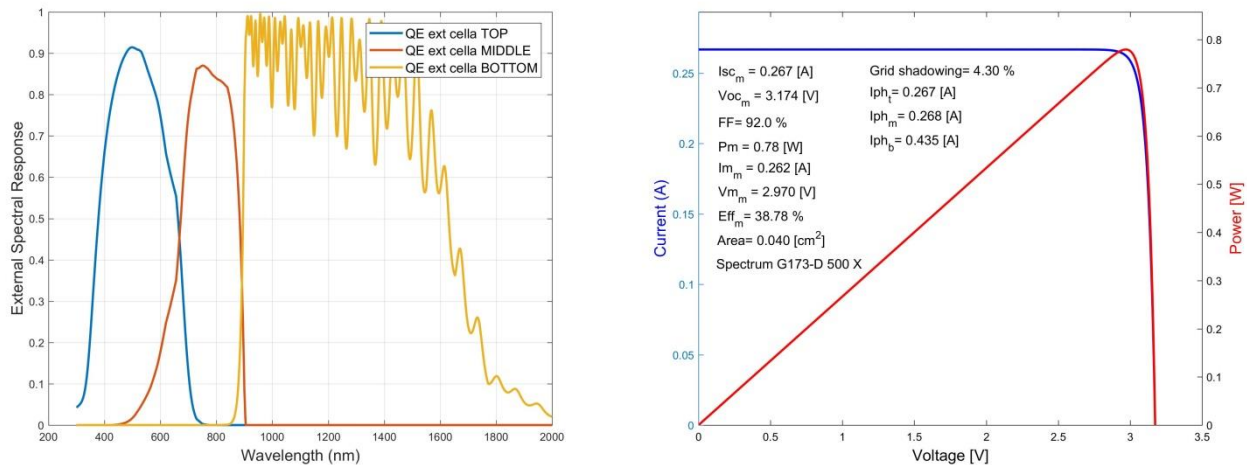


**Figure 25. SMM calculated EQE (left) and ideal IV curve (right) of the 3J InGaP/InGaAs/Ge solar cell considering a 200  $\mu\text{m}$  thick substrate as the last layer.**

The excellent agreement among the data and the numerical stability of the computation demonstrates the robustness of the developed mathematical code based on SMM.



## 4. State-of-the-art integration of SiGeSn in III-V based heterostructures

*This chapter answers to the following questions: why is it convenient to integrate SiGeSn in III-V-based structures? What are the challenges related to the integration of IV and III-V-based semiconductors? What are the results so far related to the photovoltaic devices realized with SiGeSn? A survey of the basic literature concerning the structural and optical properties of SiGeSn, as well as some significant growth experiments are summarized. State-of-the-art performances on SiGeSn-based solar cells are reported.*

### 4.1. Motivation and challenges

The defining characteristics of a semiconductor are mostly related to its fundamental electronic bandgap. The horizon of bandgap engineering was dramatically expanded in the early 1970s with the introduction of epitaxial growth techniques, like the Metalorganic vapour phase epitaxy (MOVPE) one, in which binary, ternary quaternary semiconductor alloys started to be deposited with excellent thickness and composition uniformity [55]. Thus, the new limit imposed in the realization of the heterostructures became the *lattice matching*, that is, the problem of adapting the lattice constants of the film and the substrate. A lattice mismatch, in fact, can generate large stresses in epitaxial films and the epitaxial strain energy can be relieved by dislocations once a characteristic critical film thickness is exceeded [56].

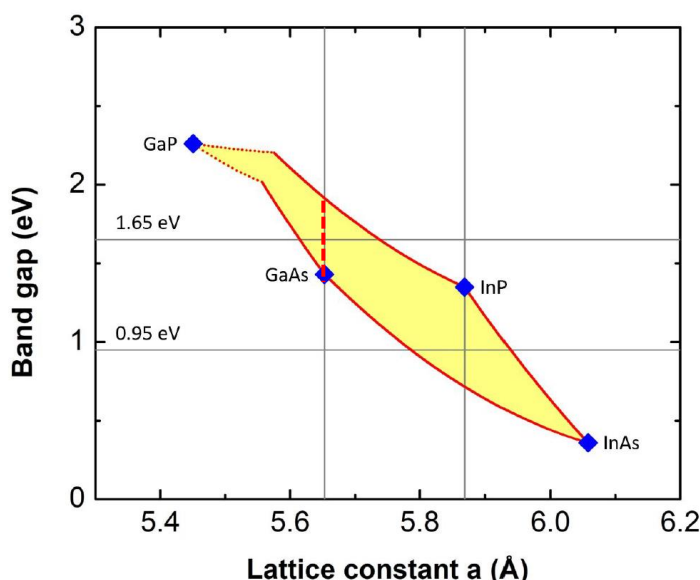


**Figure 26.** Bandgap and lattice constant variation in the InGaAsP alloy. When lattice-matched to GaAs, the band gap of InGaAsP can be tuned from 1.42 to 1.88 eV, by keeping unchanged the lattice constant and by varying the composition following the dashed red line. When lattice matched to InP, the band gap can be tuned from 0.73 to 1.35 eV.

Since dislocations act as recombination centers, lattice matched heterostructures-based devices are the preferred ones to be used. Once the compositional change allows decoupling the strain and band-structure variables, then, it is also possible to expand the band gap engineering possibilities. In the case of III-V materials, for example, the versatility of the InGaAsP quaternary compounds made it possible to control independently the bandgap and the lattice-constant, as shown in Figure 27.

A strong interest on SiGeSn alloy was started when it was reported that, like for the III-V based quaternary material, by changing the composition of the ternary semiconductor in a proper way, it became possible decouple strain and band-structure effects and deposit the ternary alloy lattice matched to Ge [57].

Therefore, it was considered the idea to integrate the ternary SiGeSn in III-V based MJ solar cells, in particular as 1 eV material for replacing InGaAs or InGaNAs in four junction solar cells, or as a buffer layer for growing on the Si platform [58], [59], [60] and [61].

The main question still to be answered is how efficiently integrate the SiGeSn material in a III-V structures without a quality and penalty cost.

Indeed, if we go back to beginning of 80s, we can point out that the integration between III-V and IV elements has always been a subject of great interest for the semiconductor sector. The integration between III-V and silicon, in particular, motivated a lot of research, owing to the high performance of the former compounds and the low cost of the second one. However, the monolithic integration of III-V on Si has been very difficult, not only because of the possible creation of antiphase boundaries, but overall, owing to the lattice and thermal mismatches between the semiconductors, which introduce high threading dislocation density [62]. Therefore, so far, the most successful integrations among III-V and IV elements for PV applications have been accomplished by complex manufacturing process, i.e., by mechanical stacking or by the wafer bonding (see, for example, [17] and [63]). In these cases III-Vs are grown on lattice matched substrates, which are subsequently removed, and replaced by the Si support.

In principle, a cheaper *monolithic* integration of IV and III-V elements can be developed by using the so called “virtual substrate approach”, where, the III-V compounds are grown by MOVPE over a heterostructure, the so called *virtual substrate*, which is composed of a substrate plus a certain number of intermediate layers, which favour the adaptation between the substrate and the III-V compounds [64]. However, so far, in order to accomplish this process, two pieces of equipment have been used: a CVD reactor for the growth of IV elements and a MOVPE growth chamber for the deposition of the remaining III-V part of the cell. GaAsP/SiGe tandem structures, for example, have been realized by growing SiGe epilayers by reduced pressure chemical vapor deposition (RPCVD) and the III-V epilayers by metal organic chemical vapor deposition (MOCVD) [65]. The integration of Ge and III-V for the realization of heterojunction bipolar transistors has been carried out by using a ultrahigh vacuum (UHV) electron-beam evaporation system for the Ge deposition and an organometallic vapour phase epitaxy (OMVPE) system for the growth of GaInP [66]. As reported in the introduction, also the integrations of SiGeSn with III-V for MJ solar cells have been accomplished by using a CVD reactor for the growth of SiGeSn and a MOVPE growth chamber for the deposition of the remaining part of the cell structure [28], [29] and [59].

The utilization of two growth equipment, however, reduces the economic advantage of the multijunction monolithic architecture, owing to the required higher capital expenditure.

The reason behind the utilization of different equipment for the growth of III-V and IV elements is the related “*cross contamination*” problem: III-V elements are dopants for IV-based alloys and vice versa, IV elements are dopants for III-V based compounds. The severe consequence of growing a sequence of III-V ad IV based semiconductors in the same growth environment is the difficulty to control their conductivity, as shown, for example, by E. Welser et al., who measured memory effects of Ge in III-V alloys [27].

Preliminary experiments to integrate III-V and IV element in the same MOVPE growth chamber, have been reported by R. Jakomin in [67], concerning the growth of epitaxial germanium in a reactor utilized for III-V growth. More recently, epitaxial Ge solar cells grown on GaAs (001) substrates have been realized by MOCVD [68]. A much higher level of integration was accomplished in [69], with the manufacturing of InGaP/InGaAs/SiGe/Ge TJ structures. This attempt was based on the results obtained on an earlier study, whose aim was to measure and limit the contamination of IV elements in III-V compounds. In particular, it was measured a background doping level of  $5 \times 10^{17} \text{ cm}^{-3}$  in GaAs layers grown after SiGe layers deposition and III-V coating runs [70]. These results were considered promising and encouraged the research to further reduce the residual contaminations with the final aim to realize high efficiency MJ solar cells. More recently, a contributions related to the integration of III-IV-V elements in the same MOVPE chamber has been reported concerning, in particular the growth of  $(\text{GaAs})_{1-x}(\text{Ge}_2)$  alloy [71]. However, a detailed analysis of the cross doping was not included.

The following experimental work extends and improves these preliminary experiences carried out on integrating IV and III-V elements, in particular, also considering the integration of SiGeSn ternary alloys with III-V-based materials in the same MOVPE apparatus, with the purpose of identifying the MOVPE hardware change, the gas sources and process condition necessary to decrease the residual contamination in the IV and III-V compounds to a level adequate to manufacture high efficiency MJ solar cells.

In order to better understand all the challenges related to integration of SiGeSn with III-V based heterostructures, a critical survey of some significant literature results is preliminary reported.

## 4.2. Literature survey

### 4.2.1. The problem of tin incorporation in SiGeSn and related challenges

The starting point for the semiconductor deposition is the knowledge of the phase stability of the material. We need to know, in particular, how much Sn can be incorporated in the SiGe matrix. The phase stability of a solution can be assessed by evaluating the molar Gibbs free energy of mixing,  $\Delta G_{mix}$ , that for a simple regular solution of a binary compounds is simply given by (see, for example [72] :

$$\Delta G_{mix} = a_o X_1 X_2 + KT(X_1 \ln X_1 + X_2 \ln X_2) \quad 4.1$$

where the first term on the right side of the Eq. 4.1 is the molar *heat of mixing*, while the second one is the molar *entropy of mixing*.  $X_1$  and  $X_2$  are the molar fraction of the elements.

If we restrict our attention to the SiGeSn alloy lattice matched to Ge, in this case, the Si concentration is linked to the tin one according to the following ratio [73]:

$$\frac{X_{Si}}{X_{Sn}} = 4 \quad 4.2$$

Therefore, by setting:

$$X = X_{Sn}, X_{Si} = 4X \text{ and } X_{Ge} = (1 - 5X) \quad 4.3$$

we can then study the alloy,  $Si_{4x}Sn_xGe_{(1-5x)}$ , only as a function of tin concentration. For regular solution, the molar entropy of mixing is equal to the ideal molar entropy of mixing:

$$\Delta S_{mix} = -k \sum_{i=1}^3 X_i \ln X_i = -k[x \ln x + 4x \ln(4x) + (1 - 5x) \ln(1 - 5x)] \quad 4.4$$

The molar enthalpy of mixing has been calculated by Junqi Xie et al., by assuming that for the  $Si_{4x}Sn_xGe_{1-5x}$ , alloy the usual quadratic form can be applied:

$$\Delta H = \Delta U_{mix}(X) = \beta X(1 - X) \quad 4.5$$

where  $\beta = 553.7$  meV [74].

By using the enthalpy and entropy of mixing, the Gibbs free energy of mixing is then calculated, as reported in Figure 27 and Figure 28.

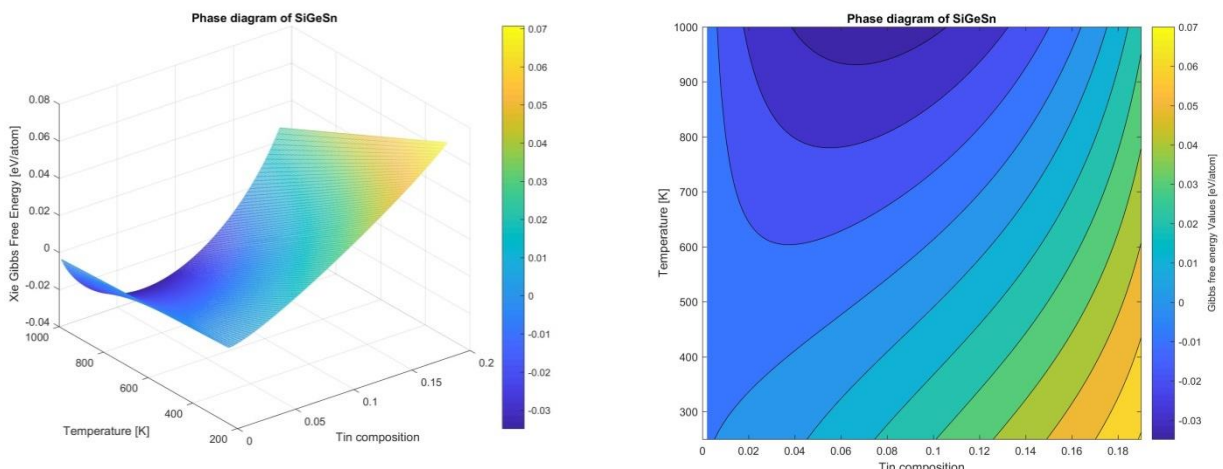


**Figure 27. Gibbs free energy of mixing per atom for the ternary  $Si_{4x}Ge_{1-5x}Sn_x$  as a function of temperature and tin concentration, 3D and 2D representation.**

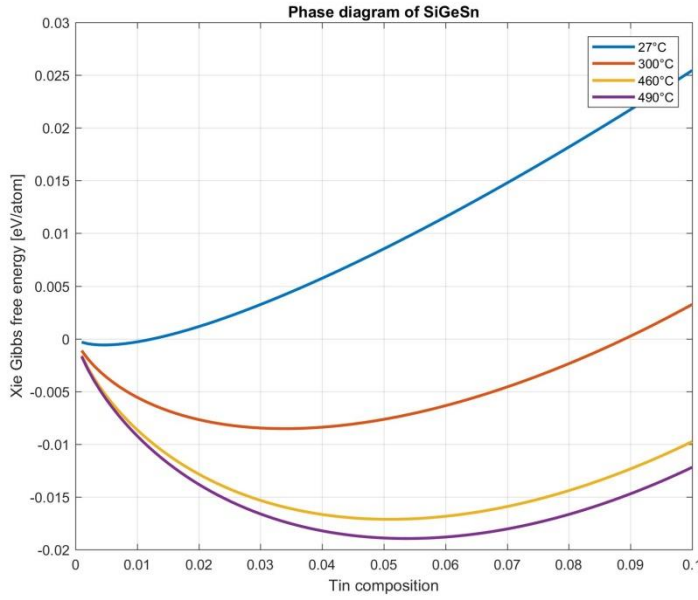


**Figure 28. Gibbs free energy of mixing per atom for the ternary  $\text{Si}_{4x}\text{Ge}_{1-5x}\text{Sn}_x$  for different temperature values.**

Figure 27 and Figure 28 show that in SiGeSn, equilibrium tin concentration around 5% can be obtained at growth temperature around 490°C, however, at room temperature the equilibrium solubility of tin is lower than 1%. The solid solubility of tin in the alloy is very low because of the high value of the lattice constant of the tin (6,489 Å) as compared to that of Ge (5.6579 Å) and Si (5,431 Å). Therefore, tin concentration at room temperature  $\geq 1\%$  can be obtained only by considering growth condition *out of equilibrium* and applying kinetic barriers which do not allow reaching the equilibrium concentration. While Liquid Phase epitaxy (LPE) is an equilibrium process which cannot be used to grow tin-rich SiGeSn alloy, the MOVPE is a non-equilibrium deposition technique and it has been successfully used for growing semiconductors out of equilibrium. Kinetic barriers necessary to stabilize tin concentrations higher than equilibrium value can be created by lowering the growth temperature or by increasing the growth rate. As a matter of fact, the experiments carried out on GeSn showed the necessity to lower the growth temperature to avoid tin precipitation [75], [76]. Low temperature deposition has also been applied for SiGeSn as reported in the next 1 paragraph. However, if for avoiding tin segregation and precipitation is necessary to grow at low temperature, on the other hand, this growth requirement has introduced several challenges:

- 1) Identify suitable gas precursor with low temperature cracking to get reasonable growth rate;
- 2) control the growth in the kinetic regime, where small variation of temperature can cause gradient in the alloy composition;
- 3) obtain mirror like morphologies despite the low diffusivity of the atomic species on the surface.

Furthermore, since in the most MOVPE system, the in-situ temperature control starts working over 400°C, a challenging compromise on the growth temperature should be reached: it should be low enough to avoid tin precipitation/segregation and high enough to allow controlling the temperature

profile over the wafer surface, in order increase the growth uniformity and then the wafer yield. This objective is indeed relevant to pursue un industrial scale up of the growth process.

#### 4.2.2. Structural properties of SiGeSn

Considering the Vegard's law, the lattice constant of SiGeSn can be determined from that of its constituent atoms:

$$a_{SiGeSn} = x a_{Sn} + y a_{Si} + (1 - x - y) a_{Ge} \quad 4.6$$

Therefore considering:  $a_{Si} = 5.431 \text{ \AA}$ ,  $a_{Ge} = 5.6579 \text{ \AA}$ ,  $a_{Sn} = 6.486 \text{ \AA}$ , ( $\alpha$ -Sn), the SiGeSn alloy can be lattice matched with Ge with the following composition:  $Ge_{0.9108}Si_{0.070}Sn_{0.019}$ . It is possible to check that also the alloy with composition  $Ge_{0.9402}Si_{0.047}Sn_{0.0128}$  is lattice matched with Ge. In general, it occurs that by keeping the ratio between the atoms of Si and Sn around 4:1<sup>10</sup>, the SiGeSn alloy can be lattice matched to Ge, while we can get a variation of the energy gap. The decoupling between strain and band-structure effects is showed in Figure 29.

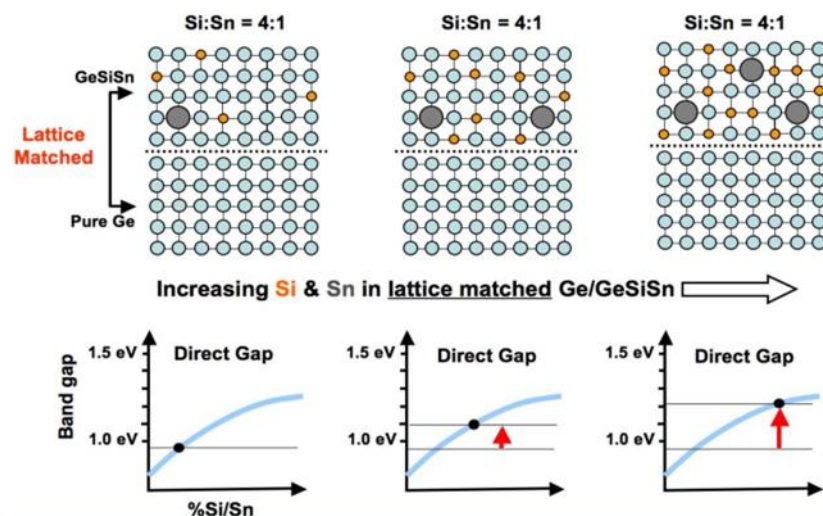


**Figure 29.** In a matrix of Ge atoms (light blue circles), the number of atoms of Si (orange spheres) and Sn (large spheres of grey colour) is increased, maintaining between them a ratio of 4:1. The graphs illustrate the corresponding increase of the energy gap value associated with the increase of Si and Sn atoms concentration in the Ge matrix, while preserving the lattice matching with the substrate. The picture is taken from [26].

Such materials can therefore be considered as pseudo-binary compounds described by the general formula:  $Ge_{1-x}(Si_{0.8}Sn_{0.2})_x$ . Junqui Xie showed by TEM perfect interfaces between the SiGeSn and Ge, with surface morphologies devoid of defects. The measures performed at the atomic force microscope reported surfaces with roughness of 0.5 nm [60]. P.Aella et al., have reported an empirical formula for determining the lattice constant of the SiGeSn alloy that deviates from Vegard's law [77]:

$$a_{SiGeSn}(x, y) = a_{Ge} + \Delta_{SiGe}x + \theta_{SiGe}x(1 - x) + \Delta_{SnGe}y + \theta_{SnGe}y(1 - y) \quad 4.7$$

where:

<sup>10</sup> Exactly at 3.67 by considering the Vegard's law

$$\Delta_{SiGe} = \alpha_{Si} - \alpha_{Ge}$$

$$\Delta_{SnGe} = \alpha_{Sn} - \alpha_{Ge}$$

$$\theta_{SiGe} = -0.026$$

$$\theta_{SnGe} = 0.166$$

According to P.Aella at., SiGeSn is lattice matched with the Ge when the ratio between the atoms of Si and those of Sn is around 3.91, a value a bit larger than the exact value calculated considering the Vegard's law.

Of course, structural integrity is one essential precondition for good devices, therefore it was important to analyse the structural stability of the film SiGeSn when thermally treated.

The structural stability of the film SiGeSn has been studied by Yan-Yan Fang [78], the most significant results are shown in Figure 30.

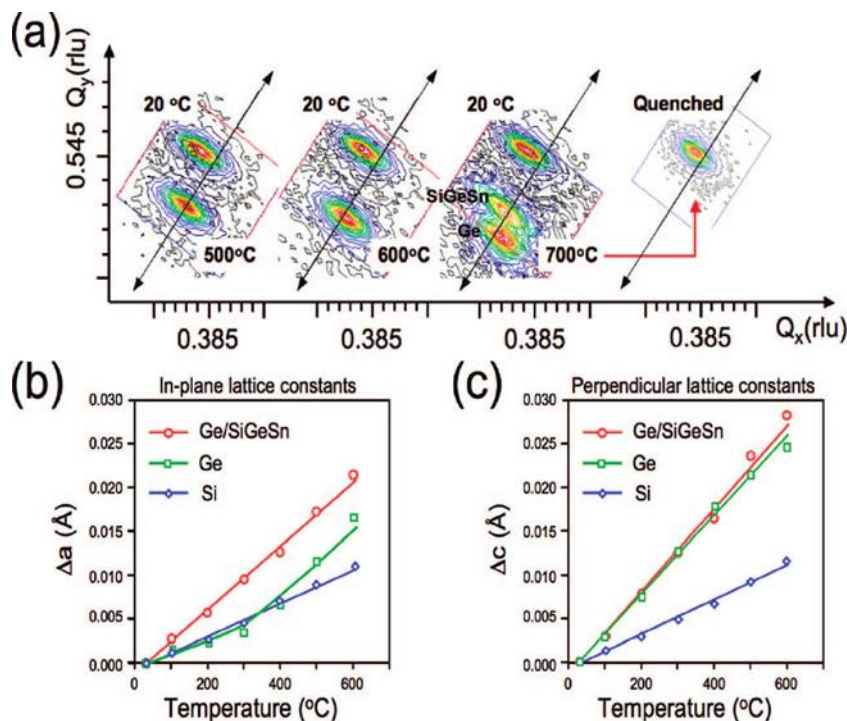


**Figure 30-** HR-XRD reciprocal lattice space maps relating to the reflections (224) for a heterostructure Ge/Ge<sub>0.90</sub>Si<sub>0.08</sub>Sn<sub>0.02</sub> grown on Si at different temperature. The graphs identified with the letters b) and c) show the variation of the value of the lattice constants parallel and perpendicular to the plane of growth as a function of temperature. From [78].

Figure 30 shows the changes in the lattice constants as a function of temperature after heating the SiGeSn alloy in nitrogen up to 700°C and subsequent cooling to ambient temperature. In Figure 30 a), the XRD peaks marked "20°C, 500°C, 600°C and 700°C" correspond to the XRD measurements carried out at different temperatures. It can be pointed out that the heterostructure Ge/Ge<sub>0.90</sub>Si<sub>0.08</sub>Sn<sub>0.02</sub> remains lattice matched to Ge up to 600°C, at temperatures above, the lattice constants perpendicular to the plane of growth differ and a lattice mismatch is set up between SiGeSn and Ge; this lattice mismatch cancels in cooling to ambient temperature.

The thermal stability of the SiGeSn alloy, with tin incorporation up to 9%, was also investigated, more recently, by Bader Alharthi et al, by in situ annealing performed at 650 °C in H<sub>2</sub> ambient, at atmospheric pressure. XRD characterization shown even an improved material quality under thermal treatment [79].

In apparent contradiction with the above presented results, J.-H. Fournier-Lupien et al. found a phase separation in 50 nm thick Ge<sub>0.84</sub>Si<sub>0.04</sub>Sn<sub>0.12</sub> alloy, after annealing above 410°C, with the formation of randomly distributed Sn-rich particles which grown as the annealing temperature was increased [80]. However, the discovered thermal instability of the Ge<sub>0.84</sub>Si<sub>0.04</sub>Sn<sub>0.12</sub> alloy could be due to the high concentration of tin in the alloy. As reported in chapter 4.2.1, a 12% of Sn is strongly far from the equilibrium concentration, therefore the annealing of the sample, at increasing temperature, acts as a mean to overcome the kinetic barrier previously introduced by growing at low temperature, so that the alloy attempts to reach the tin equilibrium concentration with a phase separation. These results suggest that SiGeSn can be subjected to higher temperatures during the MJ junction solar cell growth once the tin concentration in the alloy is lower than 12%.

#### 4.2.3. Optical properties of SiGeSn

First calculations of the energy gap value of the SiGeSn alloy have been reported by R.A Soref and C. Perry [57]. From the calculations performed, it is highlighted the possibility of making an alloy lattice matched with Ge lattice, having different values of the energy gap.

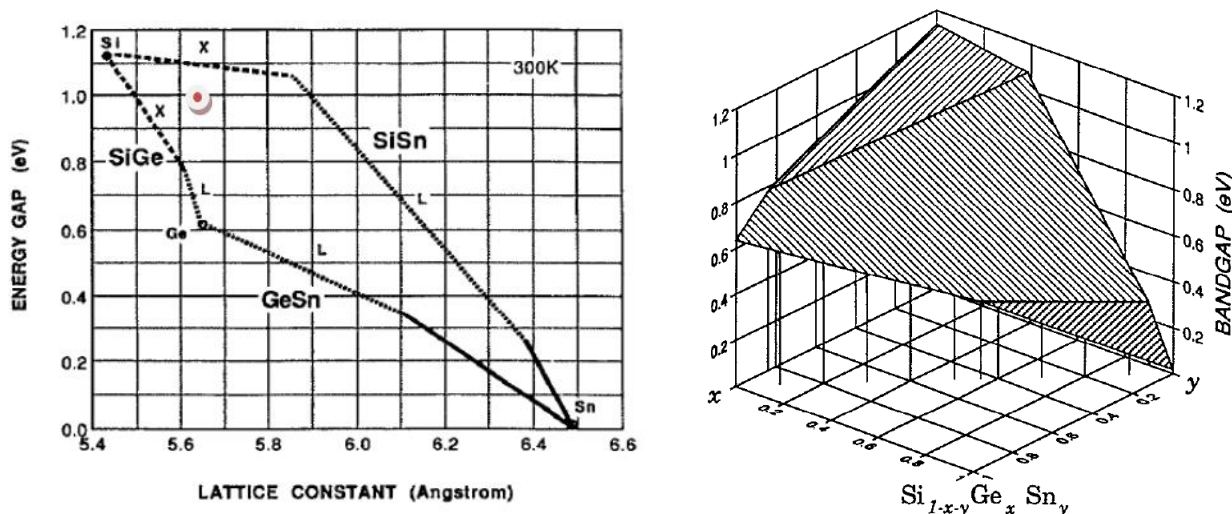


**Figure 31. Energy gap (Eg) diagram of the SiGeSn alloy.** On the left, the dotted line represents the materials with indirect gap. The red dot shows the alloy with a 1 eV value of energy gap lattice matched with Ge. On the right the predicted energy gap of  $\text{Si}_{1-x-y} \text{Ge}_x \text{Sn}_y$  as a function of composition  $x,y$ . The upper and the middle sheet show indirect Eg region, while the bottom one shows a direct Eg region. The vertical lines show Eg along the composition line  $x + y = 1$ . From [57].

According to Figure 31, all possible ternaries found within the triangle bounded by the  $x = 0$  line, the  $y = 0$  line and the  $x + y = 1$  line, present indirect Eg.

The value of the direct energy gap ( $E_g$ ) of SiGeSn lattice matched to Ge has been determined by V.R.D'Costa et al [19],[81], as a function of the alloy composition, by considering SiGeSn as a pseudo-binary compound. It has been found that  $E_g$  varies with composition presenting a highly non-linear behaviour and it can be described by the following equation:

$$E_g[Ge_{1-x}(Si_{0.8}Sn_{0.2})_x] = E_g^0(Ge) + 1.7x - 1.62x^2 \quad 4.8$$

The energy gap initially increases with decreasing Ge concentration but reaches a maximum for a Ge concentration of about 0.55 and then decreases to values lower Ge concentration.

A.V.G Chizmeshya and J. Kouvettakis have reported that the  $E_g$  magnitude and the  $E_g$  character (indirect- direct) can drastically change by Sn clustering [73]. In particular, it has been shown that Sn clustering reduces the gap by 50% and alters the character of the transition from  $\Gamma \rightarrow \Gamma$  to  $\Gamma \rightarrow X$ .

Bader Alharthi et al. evaluated the energy bandgap of  $Si_{0.13}Ge_{0.804}Sn_{0.066}$  and  $Si_{0.19}Ge_{0.783}Sn_{0.027}$  samples by fitting the measured  $(\alpha h\nu)^2 - h\nu$  curves, by considering for the absorption coefficient,  $\alpha$ , the following expression:

$$\alpha(h\nu) = \frac{A(h\nu - E_g^\Gamma)^{\frac{1}{2}}}{h\nu} \quad 4.9$$

The fitted  $E_g^\Gamma$  values were respectively 0.85 eV and 1.05 eV [82]. The low energy side of the absorption curve, however, was not fitted.

Pairot Montragoon et al. have reported the following formulas for indirect (L) and direct transitions ( $\Gamma$ ) in  $Si_x Ge_{1-x-y}Sn_y$  [83]:

$$E_L(x, y) = 0.723 + 0.564x - 2.352y + 0.189xy - 0.074x^2 + 0.068y^2 \quad 4.10$$

$$E_\Gamma(x, y) = 0.880 + 0.929x - 3.807y - 0.16xy - 0.078x^2 + 0.937y^2 \quad 4.11$$

By considering the  $Si_{0.19} Ge_{0.793}Sn_{0.027}$  alloy, the direct energy gap value is 0.95 eV, a bit lower than the value calculated by Bader Alharthi et al.

The data so far shown demonstrate that SiGeSn can be deposited lattice matched to Ge, with an energy gap value around 1 eV; therefore, the alloy can be theoretically integrated to realize high efficiency four junction solar cells InGaP/InGaAs/SiGeSn/Ge.

More recently, Richard Soref has introduced as a possible semiconductor candidate with a “truly direct”  $E_g$ , spanning from 1.5 eV down to 0.41 eV, the quaternary CSiGeSn, however the lattice parameter of this quaternary changes from 0.576 nm to 0.649 nm; these values are out of the range values necessary for getting a lattice matched semiconductor to Ge [84].

#### 4.2.4. Some significant growth experiments on Ge, GeSn and SiGeSn

The phase diagram presented in the previous chapter explains why the growth of the ternary SiGeSn has been performed at very low temperature. For this purpose, at Arizona State University new gas sources for ultra-low-temperature deposition have been proposed [26],[85]. They concerns complex gas sources like  $(\text{GeH}_3)_x\text{SiH}_{4-x}$  (with  $1 < x < 4$ ) that reacting with SnD<sub>4</sub> can form the ternary alloy, at temperatures around 300-350°C. For example, it was used  $\text{GeH}_3\text{SiH}_3$  ( $x=1$ ) which reacts readily with SnD<sub>4</sub>, at a temperature of 300-350 °C, to form Ge-rich alloys, with a content of Si and Sn ranging among ~ 20 to 37 % and 2-12%, respectively. Since in the molecule  $\text{GeH}_3\text{SiH}_3$ , Ge and Si are present with the same concentration, but the Si was found incorporated in the alloy SiGeSn with a concentration lower than 50%, it was assumed the following reaction:



which provides for the formation of silane, which, however, does not decompose at the temperatures considered and therefore explains why part of the silicon is not incorporated in the alloy. It is then the combination of  $(\text{GeH}_3)_2\text{SiH}_2$  with SnD<sub>4</sub> at 350°C that gives rise to the film SiGeSn wherein the ratio of Ge:Si is 2:1, respecting the ratio of atoms present in the gaseous precursors. Through the reaction of  $\text{SiH}_3\text{GeH}_3$  and SnD<sub>4</sub>, at 330°C, it was deposited a film of 80 nm of  $\text{Ge}_{0.745}\text{Si}_{0.20}\text{Sn}_{0.05}$  which is almost the lattice match with the Ge. The growth rate was, however, around 1.5 to 2 nm/min, which can be considered too low for growing films with a few microns of thickness.

In order to have a higher flexibility and control independently the incorporation of Ge and Si, the following gas sources have been also used:  $\text{SiH}_2(\text{SiH}_3)_2$  (trisilane,  $\text{Si}_3\text{H}_8$ , liquid source) and/or  $\text{SiH}_3\text{GeH}_3$  to supply the Si atoms and  $\text{Ge}_2\text{H}_6$ , to supply Ge atoms. With  $\text{SiH}_2(\text{SiH}_3)_2$ , SnD<sub>4</sub> e  $\text{Ge}_2\text{H}_6$ , it has been possible to obtain SiGeSn alloy with 2% of tin, that is, with the following composition:  $\text{Ge}_{0.90}\text{Si}_{0.08}\text{Sn}_{0.02}$ . At 350°C, the  $\text{SiH}_2(\text{SiH}_3)_2$  and  $\text{Ge}_2\text{H}_6$  react according to the following chemical reaction:



which indicates that the two gas sources react completely to give rise to a solid phase that contains the same stoichiometric ratio of the gaseous phase

In the paper of Junqui Xie et al. above cited, besides the structural analysis, a study of dopant incorporation in SiGeSn, deposited on Ge and Si substrates, has also been reported. The gas source utilized were:  $\text{Si}_3\text{H}_8$ , SnD<sub>4</sub> and  $\text{Ge}_2\text{H}_6$ . The samples, not intentionally doped, showed a p-type polarity with dopant levels around  $2-3 \times 10^{17} \text{ cm}^{-3}$ . A heating treatment reduced the level of background impurities at concentrations around  $5 \times 10^{16} \text{ cm}^{-3}$ . Holes mobility was measured around  $250 \text{ cm}^2/\text{Vs}$ . Very high concentration levels of p-type doping, around  $10^{20} \text{ cm}^{-3}$ , have been achieved by using  $\text{B}_2\text{H}_6$  (diborane). Similar results were reported in the work of Yan-Yan Fang et al. who used diborane for the P-type doping and P( $\text{GeH}_3$ )<sub>3</sub> and P( $\text{SiH}_3$ )<sub>3</sub> for N type-doping [78].

All the above reported depositions were performed by low pressure CVD. Deposition of GeSn and SiGeSn has also been reported by MBE technique [86]. Despite the good results obtained on the growth of SiGeSn, the gas sources developed on purpose are not easily commercially available and

they are expensive. The possibility of pursuing the growth of SiGeSn at industrial level is bound to the utilization of more easy-to-buy gas sources to be used by the MOVPE technology

Wirths et al. reported the growth of Ge, GeSn and SiGeSn by the CVD technique, with a showerhead type reactor (AIXTRON TRICENT), using as gas sources  $\text{GeH}_4$ ,  $\text{Ge}_2\text{H}_6$ ,  $\text{Si}_2\text{H}_6$  and  $\text{SnCl}_4$  [76], [87]. The growth rate of Ge as a function of the temperature, the precursors type and the used carrier gases are shown in Figure 32.

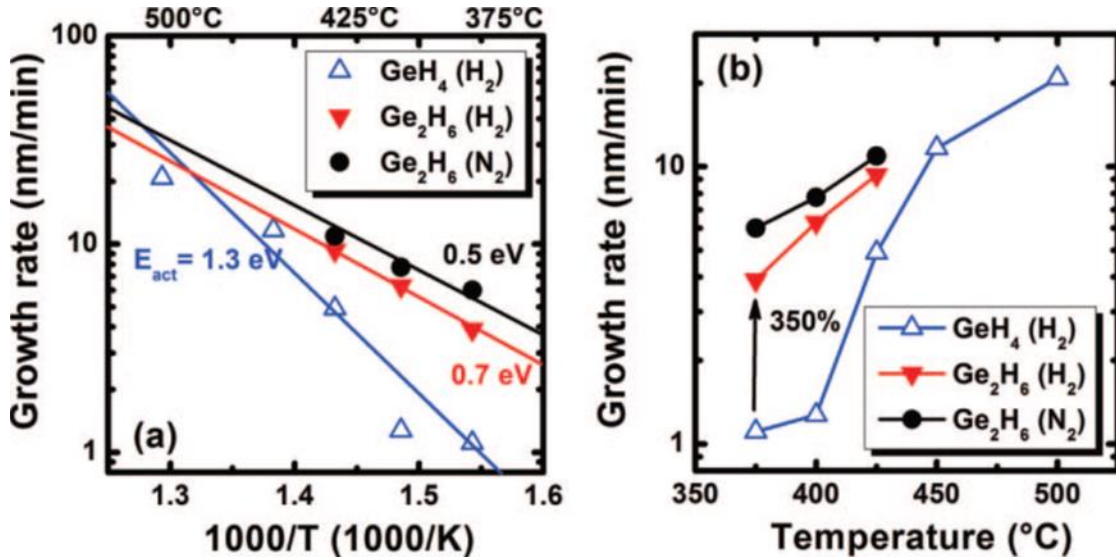


**Figure 32.** Growth rate of the Ge as a function of the inverse value of temperature (Arrhenius plot) by using  $\text{H}_2$  and  $\text{N}_2$  as carrier gasses. Activation energies for  $\text{GeH}_4$  and  $\text{Ge}_2\text{H}_6$  are 1.3 eV and 0.7 eV, respectively, by using  $\text{H}_2$  as carrier gas. The activation energy for  $\text{Ge}_2\text{H}_6$  drops to 0.5 eV by using  $\text{N}_2$  as carrier gas. (b) Growth rate of the Ge versus temperature by considering different Ge precursors;  $\text{Ge}_2\text{H}_6$  and  $\text{GeH}_4$  are used with partial pressure of 15 Pa. From [76].

The growth rate of Ge at 375°C, by using  $\text{Ge}_2\text{H}_6$  and  $\text{N}_2$  as carrier gas was around 0.4  $\mu\text{m}/\text{h}$  (6-7 nm/min). It is evident the advantage of using  $\text{Ge}_2\text{H}_6$  with respect to  $\text{GeH}_4$  for temperature lower than 450°C: the growth rate was increased of 350% at 375°C by using  $\text{Ge}_2\text{H}_6$  instead of  $\text{GeH}_4$ . The drawback of using  $\text{Ge}_2\text{H}_6$  instead of  $\text{GeH}_4$  is the higher source cost. The strong dependence of the growth rate on temperature indicates that the deposition takes place in the kinetic regime and is therefore limited by the surface chemical reactions. The utilization of nitrogen as carrier gas instead of hydrogen allows getting higher growth rate owing to the reduction of the H-surface coverage which inhibits the growth [88].

In order to avoid Sn segregation, the growth of GeSn was carried out at temperatures lower than 450°C, maintaining a ratio between the partial pressure of  $\text{Ge}_2\text{H}_6$  and  $\text{SnCl}_4$  equal to 100. The GeSn deposition took place in the kinetic regime, with an activation energy of 0.4 eV, comparable to the value of 0.5 eV found for the growth of Ge. However, for the growth of GeSn it was used a value of the partial pressure of  $\text{Ge}_2\text{H}_6$  eight times higher than that used for the deposition of Ge. The growth rate of GeSn at 375°C, by using  $\text{N}_2$  as the carrier gas, was much higher than the value found for epitaxial germanium, as it was around 2  $\mu\text{m}/\text{h}$  (33 nm/min).

For the epitaxial growth kinetically controlled, the growth rate should be independent on the partial pressure of the precursor. Since the ratio of partial pressure between the  $\text{Ge}_2\text{H}_6$  and  $\text{SnCl}_4$  was 100,

the increase in the growth rate observed in the GeSn compared to that obtained for the Ge was mainly attributed by the authors to the higher partial pressure of  $\text{Ge}_2\text{H}_6$  used for the grow of GeSn., because they assumed that the dissociation of  $\text{Ge}_2\text{H}_6$  in  $\text{GeH}_3$  radicals accelerated the surface reactions. The high value of the growth rate obtained for GeSn was necessary in order to avoid the segregation of tin during the growth.

SiGeSn layers have been grown both on Si and Ge substrates, by selecting proper partial pressure of the precursors obtaining growth rate as high as  $4.8 \mu\text{m/h}$  ( $80 \text{ nm/min}$ ) at temperature around  $450\text{-}475^\circ\text{C}$  (see Figure 33). The film deposited had thickness of the order of  $200 \text{ nm}$ . The incorporation of Sn decreases as the temperature increases and reaches 1% at  $475^\circ\text{C}$ .

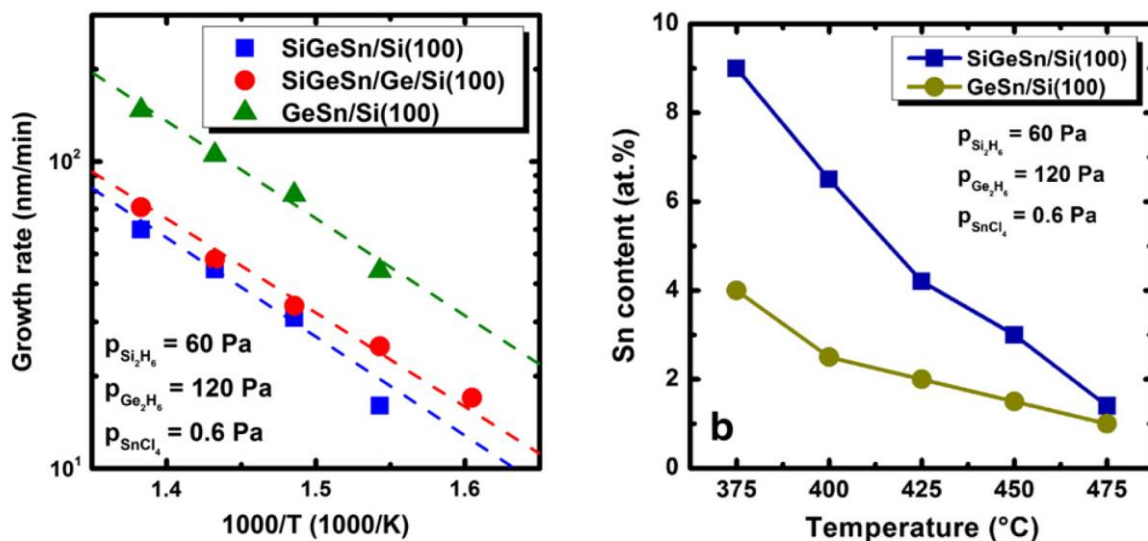


**Figure 33.** On the left, growth rate dependence on the absolute temperature for SiGeSn and GeSn epitaxially grown on Si(100) and Ge buffered Si (ii), on the right, reduction of Sn incorporation in GeSn and SiGeSn as a function of temperature. From [87].

The data of Wirths showed that it is possible to growth SiGeSn - tin precipitation free - at temperature much higher than the temperature reported by J. Kouvettakis.

This could be due to the high growth rate reached for SiGeSn deposition. This hypothesis is supported by the contribution of Noriyuki Taoka at al. In fact, they reported that the possible accumulation of Sn at the surface of SiGeSn could be due to the thermally activated tin migration from the bottom layers, contrasted by the growth rate [86]. Noriyuki Taoka at al. observed an increased accumulation of tin at the surface by increasing the growth temperature from  $200^\circ\text{C}$  to  $350^\circ\text{C}$  with growth rate 50 times lower than the growth rate obtained by Wirths at al.

More recently, Nupur Bhargava at al. reported very interesting results concerning the role of arsine during the (Si)GeSn growth [89]. It was found that diluted  $\text{AsH}_3$  during the (Si)GeSn growth allows inhibiting the formation of unwanted Sn precipitates. The Authors explained this result by considering the possible role of As/ $\text{AsH}_3$  as surfactants in suppressing the islanding and/or Sn segregation during growth with consequent benefit in reducing the surface roughness. It was also observed that during the growth of GeSn when the  $\text{AsH}_3$  flow is increased, *the Sn composition decreases* and a first increase of the growth rate is also observed, followed by a quenching of the

growth at highest AsH<sub>3</sub> flow. The first increase of the growth rate was explained as the catalysing H-desorption action of arsenic. The quenching of the growth rate has been attributed to the blocking role of As in saturating the surface sites: when the surface is completely saturated with As, no adsorption sites are available for GeH<sub>4</sub> and SnCl<sub>4</sub> adsorption. A shift in Bragg angle in the XRD measurement towards more negative values (higher lattice constant) was measured by increasing the arsine flow. As tin incorporation was observed to decrease by increasing arsine concentration in the gas phase, the XRD peak shift was attributed to the lattice expanding action produced by the incorporated arsenic in the layer. In the case of SiGeSn, the role of arsine was found opposite to what discovered for GeSn: an increase of arsine concentration in the gas phase produced a decrease of Si incorporation and an *increase of Sn incorporation*, both resulted in a shift of the Bragg angle in the XRD measurement towards more negative values. Also, for SiGeSn, a quenching of the growth could be reached at high AsH<sub>3</sub> flow. The dramatic consequence of the As incorporation in the layers, owing to the utilization of an arsine flow during the growth, is the strong decrease of the semiconductor resistivity: As-doped SiGeSn alloys were found to have resistivity values as low as 0.6 mΩ cm with arsenic carrier concentration  $2.5 \times 10^{20} \text{ cm}^{-3}$ .

#### 4.2.5. SiGeSn devices

The opportunity offered by the (Si)GeSn technology to expand the energy gap possibilities, opened the path for the realization of different optoelectronic IV-based devices. R.Soref has exhaustively reported how the physical properties of SiGeSn materials can be exploited to create active devices and how those devices can be integrated monolithically in a photonic integrated ‘circuit’ (PIC) or opto-electronic integrated circuit (OEIC) [90]. Hereafter some selected contributions are reported, mostly related to the photovoltaic application.

The first diodes of SiGeSn, with 2% of Sn and 10% of Si, were made on Ge substrates by Richard T. Beeler et al. by applying the CVD technique, with deposition temperature of 390°C and working pressure = 0.53 mbar. As gas sources, Si<sub>3</sub>H<sub>8</sub>, Ge<sub>2</sub>H<sub>6</sub>, and SnD<sub>4</sub> were utilized (growth rate= 0.72 μm/h) [91]. P-type doping was obtained with boron, getting dopant concentration level around  $10^{17} \text{ cm}^{-3}$ , while for the N-type doping, P(GeH<sub>3</sub>)<sub>3</sub> was used and very high doping level around  $8 \times 10^{19} \text{ cm}^{-3}$  was achieved.

Translucents realized a first photovoltaic device of SiGeSn in 2015. The N/P junction was formed by diffusion of arsenic from the solid state [92]. The structure of the device and its electrical characterization are reported in Figure 34 and Table 5, respectively. In spite of the fact that the reported spectral response showed the onset at 1400 nm and it was peaking at 1200 nm, corresponding to the 1.0 eV gap of the Si-Ge-Sn alloy, the open circuit voltage of the device was lower than the typical value measured for Ge cells. This result could be due to the defect density present in the depletion region of the device and/or to a possible further absorption of the photons that could take place at lower energy (not shown in the EQE curve), due to the indirect nature of the semiconductor.

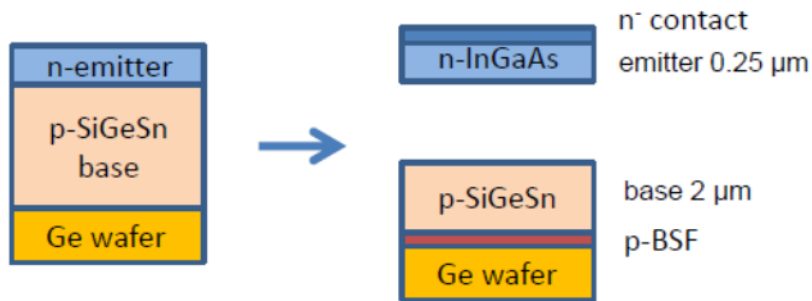


**Figure 34.** Realization of a SiGeSn N/P junction through the solid-state diffusion of As from InGaAs deposited on the top of the p-type SiGeSn/Ge heterostructure. From [92].

**Table 5.** Electrical characterization of the InGaAs filtered SiGeSn N/P junction reported in [92].

Pmax (W)	I <sub>max</sub> (A)	I <sub>sc</sub> (A)	V <sub>max</sub> (V)	V <sub>oc</sub> (V)	FF(%)
<b>1 10<sup>-3</sup></b>	0.75 10 <sup>-2</sup>	9.4 10 <sup>-3</sup>	0.132	0.194	54.7

The indirect nature of SiGeSn was confirmed in the contribution of Phoebe Pearce et al, where an open circuit voltage ( $V_{oc}$ ) lower than expected was measured on a triple junction InGaP/InGaAs/SiGeSn solar cell and this result was attributed to the carriers thermalization to the lowest available conduction band states connected to the upper valence band states by un indirect gap transition. This effect, possibly in combination with high non-radiative recombination, lowered the  $V_{oc}$  [93]. Similar results were reported by Radek Roucka et al.[30].

SiGeSn has been implemented also as barrier material, embedding GeSn active layers, to allow efficient light emission in the resulting device (LED). The SiGeSn/GeSn heterojunction was shown to form a type I alignment, which is advantageous for carrier confinement in the active region [94].

## 5. Advancement on the MOVPE technology to expand the band gap engineering possibilities with the combined growth of III-V and group-IV materials

*I propose a new path for a monolithic integration of III-V and IV elements in MJ solar cells, by growing Ge, SiGe, SiGeSn, InGaP, InGaAs, AlGaAs in the same MOVPE growth chamber. After a preliminary study on SiGe and SiGeSn growth by using IBuGe, the Ge precursor has been replaced by GeH<sub>4</sub> and an in-depth growth analysis is carried out on Ge, SiGe and SiGeSn deposition. In this first stage, diluted SiGeSn layers (i.e., layers with Si and Sn content <5%) have been deposited, searching for adequate growth conditions and suitable commercial gas precursors that can prevent tin segregation. The growth temperature has been kept as high as possible to allow controlling the temperature profile over the wafer surface during the MOVPE growth. This chapter from one side, brings insights on several aspects of the MOVPE SiGeSn growth to get a better control of SiGeSn composition and to obtain epitaxial layers with improved morphology. On the other hand, a study on the effect of the cross influence between groups IV and III-V elements on the growth rate, background doping and morphology is carried out, to show the feasibility of the new prosed path. The MOVPE hardware changes that have been introduced to reduce the cross doping between groups IV and III-V elements are also indicated.*

A new path for combining III-V and IV elements is hereafter proposed in order to exploit the band gap engineering possibilities which this integration offers and set up the basis for realizing, low cost- high efficiency - monolithically thin - InGaP/InGaAs/SiGeSn/Ge solar cells.

While in all previously cited contributions related to SiGeSn, the ternary semiconductor was grown by CVD or MBE and the subsequent integration with III-V elements was carried out by using another CVD or MOVPE growth chamber, for the first time, in this thesis, the results of the investigation concerning the growth of SiGeSn and III-V compounds in the same MOVPE growth chamber are presented.

The growth analysis started by considering the utilization of the following precursors: Si<sub>2</sub>H<sub>6</sub>, (CH<sub>3</sub>)<sub>2</sub>CHCH<sub>2</sub>GeH<sub>3</sub> (IBuGe) and SnCl<sub>4</sub>. To understand the critical issues related to the low temperature growth necessary for the deposition of SiGeSn, several SiGe MOCVD runs have been preliminary carried out.

A more detailed growth analysis has been carried out by replacing IBuGe with GeH<sub>4</sub>. Ge, SiGe and SiGeSn depositions have then been further optimized. The value of the growth temperature has been selected in the attempt to find a compromise between the low temperature growth needed for obtaining Sn precipitation free SiGeSn layer and the minimum temperature required by the MOVPE

pyrometer to measure a suitable radiation signal and make it possible the in-situ temperature monitoring.

In parallel to the study of the SiGeSn growth, an in-depth analysis on the cross influence between III-V and IV element has been carried out.

The grown materials have been characterized with several techniques. The structural characterization have been carried out by high resolution X-Ray diffraction (HRXRD), scanning electron microscope (SEM), transmission electron microscopy (TEM), including selected area electron diffraction (SAED), high angle annular dark field scanning transmission electron microscopy (HAADF-STEM), high energy dispersive X-ray mapping (EDX). The layer morphology has been analysed by optical microscope, SEM planar view and by atomic force microscopy (AFM). The cross-doping evaluation has been accomplished by secondary ion-mass spectroscopy (SIMS) and electrochemical capacitance-voltage (ECV) profiling. Optical properties have been measured by ellipsometry.

An important consideration has to be introduced concerning the SiGeSn composition determination. Since SiGeSn layers with the same lattice constant can be obtained with different Si and Sn concentration [24], the determination of the SiGeSn composition must be accomplished by applying different characterization techniques. In this study, in particular, HRXRD characterization has then been correlated to the secondary ion mass spectrometry (SIMS) analysis. The samples have been sputtered by using Cs<sup>+</sup> ions at 5.5 KeV.

The following methodology has been followed. I started considering that secondary ion emission is dependent by the so called “matrix effects” (therefore the exact quantification of the elements inside a sample requires the utilisation of “standards” whose composition value is near to the composition value of the sample to be analysed). The following hypothesis is then been assumed: when Sn concentration in SiGeSn is very low (around 1%, as measured for the samples of this study) the matrix effects produced by SiGeSn and SiGe are the same<sup>11</sup>. Therefore, SiGe samples, previously characterized by HRXRD, with silicon compositions comparable to the expected values in SiGeSn, have been selected as standards. Once Si concentrations is extracted by SIMS, this value is eventually used as input in the XRD analysis to get Sn concentration, by further assuming fully strained SiGeSn layer. The XRD simulation procedure is based on the dynamic theory of X-rays and was carried out by means of LEPTOS software supplied with the HRXRD Bruker system [95]. The condition of fully strained layers has been double check with reciprocal space map analysis (RSM) in correspondence of -2-24 asymmetrical reflection and TEM cross section. It has been assessed that a variation in simulated Sn content of 0.1 % (in the range 0.6 – 0.8 %) determines a complete disagreement between experimental and simulated HRXRD curves.

---

<sup>11</sup> It is worthwhile to mention that in order to reduce the matrix effect, the SiCs+, GeCs+, and SnCs+ concentrations have been measured. According to Y. Gao (Applied Physics Letters 33, 832 (1978); <https://doi.org/10.1063/1.90546>), by measuring the MCs+ concentration, (where M is the element in the matrix whose concentration has to be measured ) the composition of the matrix element can be determined with an absolute accuracy better than 2%.

## **5.1. MOVPE equipment and basic growth background**

This chapter has the scope to briefly describes the MOVPE apparatus used for the growth of the group IV and III-V elements as well as to introduce a fundamental theoretical background on the MOVPE growth which will be useful to understand the experimental results.

### **5.1.1. The MOVPE equipment**

The growth of IV based materials (Ge, SiGe, SiGeSn) and III-V compounds (GaAs, AlGaAs, InGaP, InGaAs) has been carried out in a AIX 2800G4 MOVPE “planetary” reactor. The original “planetary” reactor design was introduced by Frijlink in 1988 [96], with the purpose of eliminating reactor-induced angular non-uniformity generators through susceptor rotation. Furthermore, a wafer rotation was also added to reduce the intrinsic effect of gas phase reactant decomposition and precursor depletion in the gas phase. The MOVPE growth can be performed from atmospheric pressure to low pressure around 20 mbar, by using a rotary pump. All gas flows are controlled by digital mass flow controllers. A key component of the MOVPE system is the glove box, that allows loading the wafers in a controlled atmosphere of nitrogen: oxygen and H<sub>2</sub>O vapour content are kept under 0.1 ppm. The carrier gasses and gas precursors are purified before to be introduced in the growth chamber. All the precursors used in this study, apart SnCl<sub>4</sub>, had high purity, 99,9999% (6N) or 5N. The MOVPE growth chamber utilized for this research has also been equipped with: i) a multi wavelength reflectometer for the growth rate determination, using three wavelength: 905 nm, 633 nm and 405 nm, ii) an emissivity corrected pyrometer, for the wafer temperature measurement and iii) a deflectometer, for the wafer bowing determination.

For the experimentation here after reported some hardware modification has been introduced in the MOVPE reactor.

- 1) The conventional graphite susceptor has been modified with a special 2 x 4 inch and 6 x 6-inch wafers configuration for an easier process transfer.
- 2) The growth chamber has been equipped with a “double gas foil rotation” (DGFR), which allows injecting in the centre zone and in the edge zone underneath each graphite satellite, where the wafers are set, a different mixture of N<sub>2</sub>/H<sub>2</sub> gases, thus allowing in-situ control of the temperature profile across the wafer with the possibility to change the wafer temperature profile in a few seconds. The in-situ temperature tuning capability allows also countering partial wafer lift-off from the graphite satellite during growth due to strain [70].
- 3) A special triple gas injector has been developed by AIXTRON which allows injecting the elements precursors in the growth chamber trough three independent gas lines, nominally: the top hydride (top hyd), the bottom hydride (bot hyd) and the metalorganic (MO) line. In case of III-V growth, the diffusion of group-III species to the growth surface is impeded by the group-V flow underneath, thereby shifting the peak of depletion profile slightly downstream away from the edge of the injector.
- 4) As the radial position of the initial point of deposition is mainly defined by the injector properties, first and foremost by the injector diameter, in order to enhance precursor

utilisation efficiency over previous generations of the same reactor type, the diameter of the gas injector has been increased [97].

- 5) In addition, a quartz plate, which stays at a substantially lower temperature than the susceptor, is inserted into the centre of the cylindrical graphite susceptor disc itself. In this way, the deposition at the centre zone, upstream of the leading wafer edge, was minimised.

This starting configuration of the MOVPE reactor has been further modified to minimize the parasitic deposition. In particular, un optimization of thermal decoupling between the ceiling and the top reactor cooling plate has been carried out in order to decrease the unwanted parasitic deposition on the ceiling due to condensation (see chapter 5.3.2). Concerning the deposition of group IV elements, in the starting configuration, IBuGe precursor has been injected both thought the top and bottom hydride lines, the silicon precursor trough the top hydride line, while the Sn precursor trough the MO line. Subsequently, the Ge, Si and Sn precursors have been injected through separate gas lines ( $\text{Si}_2\text{H}_6$  on the top hyd,  $\text{GeH}_4$  on the bot hyd,  $\text{SnCl}_4$  in the MO line). An overview of the MOVPE system and of some details of the growth chamber are reported in Figure 35 and Figure 36.



**Figure 35 Overview of the MOVPE system.**

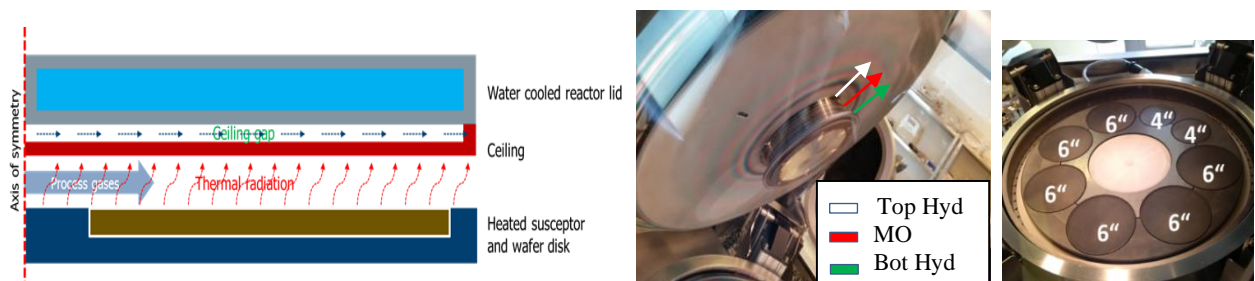


**Figure 36.** A schematic of the MOVPE growth chamber on the left; In the center, the graphite ceiling and the triple gas injector, on the right, the susceptor, the white quartz plate and the special graphite “satellites” for an easier process transfer from 4 inch to 6 inch”. The area of the ceiling and of the susceptor, which are sources of possible contaminations, have been reduced with respect to the standard 2800G4 configuration.

As during the experimentation, IBuGe has been replaced by GeH<sub>4</sub> and the concentration of disilane in hydrogen was increased from 1000 ppm to 10%, proper new gas cabinets had to be installed to guarantee a safe utilization of the precursors. The safety provisions foreseen for the utilization of Si<sub>2</sub>H<sub>6</sub> are shown in Figure 37.



Figure 37. Gas cabinet for disilane 10% diluted in hydrogen. The main safe features are indicated: a flame detector and a hydrogen detector are used to detect any disilane leakage; in case of leakage, a pneumatic valve automatically closes the gas cylinder and activates an aspiration line in order to dilute the leakage.

### 5.1.2. Basic MOVPE growth background

MOVPE since its invention from H.M Manasevit in 1968 has become an important deposition technique for semiconductors alloys, because of the layer thickness and composition controllability, and its suitability for large scale production. An overview of the MOVPE growth technique can be found in several text books and review papers (see, for example: [98], [99], [100]). For the scope of a better comprehension of this thesis work, some basic concepts related to the MOVPE growth are hereafter reported.

The MOVPE growth process is a *cold wall* chemical vapour deposition process mainly based on the pyrolysis reaction of metalorganic sources and hydrides gases which supply the constituent atoms of the semiconductor to be grown. In the best growth condition, the substrate temperature is typically held at a value substantially higher than the pyrolysis temperature of the metal alkyls and hydrides, thus ensuring their rapid decomposition at the growth surface. For III-V growth, for example, since in most cases, a large excess of the group V constituent over the metal alkyl is adopted, the growth rate is limited by the *mass transport* of the group III reactants to the growth

surface and it shows only a weak dependence on temperature. In particular, when a *laminar flow* is fully developed, the mass transport can be described through the formation of a diffusional boundary layer over which the concentration of reactants changes from its initial concentration to the reduced concentration at the growth front. Besides the *mass transport regime*, less favourable growth conditions exist: the *kinetic limited regime*, which is encountered at low deposition temperature, where the rate limiting step is due to the slow decomposition of the molecular species and the *high temperature regime*, where the growth rate decreases as the temperature increases, owing to higher desorption of the adsorbed species and, for example, in the case of GaAs, owing to the higher vapour pressure of Ga which increases the concentration of Ga at the growth front. The three different regimes for the deposition of GaAs are shown, for example, in Figure 38.

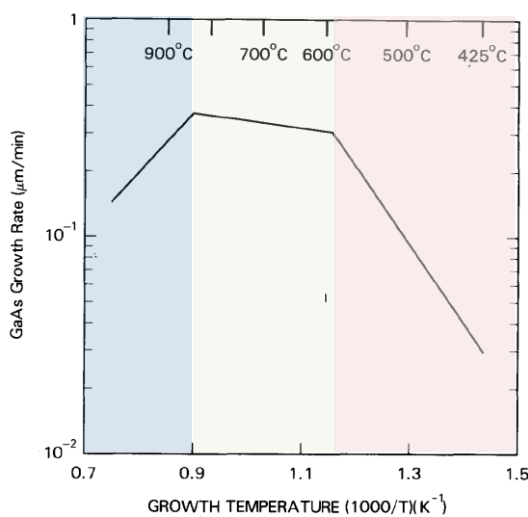


**Figure 38. Growth rate of GaAs as a function of the growth temperature.** Adapted from [99]. The three different growth regimes, as explained in the text, are indicated by different colours.

In the planetary MOCVD reactor (which has been used in this thesis work), the radial flow can be conceptually split up into three distinct regions of reactor operation along the radial direction “ $r$ ”: i) the central region where the reactants heat quickly due to the high reactor temperature required for epitaxial growth, ii) a second reactor region characterized by an increasing deposition rate with respect to  $r$ , where, after sufficient heating, the gas phase reactions commence, and iii) a third and final region which begins after the peak deposition rate; in this region, no gas chemical reactions take place and the species involved in growth are depleted, resulting in a radial deposition profile that tapers off with increasing  $r$  (see Figure 39 a).

The precursor efficiency is maximised by minimising the “entrance length” for deposition, which is defined as the radial distance between the initial point of deposition and the leading wafer edge. In general, it is necessary to find a compromise between the optimization of the precursor utilisation efficiency and thickness and composition uniformity.

The deposition uniformity is governed by the shape of the typically declining growth rate profile over the wafer radius, which is averaged via substrate rotation. If depletion is too steep, rotational averaging will result in a concave, bowl-shaped profile. Uniformity tuning is most effectively carried out by changing the total flowrate of the carrier gas, as the steepness of depletion can be reduced with increasing total flow (see Figure 39 a and Figure 39 b).

The behaviour of the growth rate vs the total carrier gas velocity is, however, dependent on the type of precursors utilized and on the gas injector diameter. If, for example, a precursor with a low pyrolysis temperature is considered, a strong deposition in the entrance zone of the reactor can take place, with a consequent low growth efficiency on the wafer. In this case, the growth efficiency can be increased by increasing the gas velocity, as the decomposition is brought more over the wafer zone. On the other hand, by increasing the injector diameter, the peak of the depletion profile is shift partially or fully onto the wafer area. Therefore, for improving the uniformity, this effect can be compensated by reducing the total flow rate. This explains why for each material and precursor selection a proper carrier gas flow has to be searched.

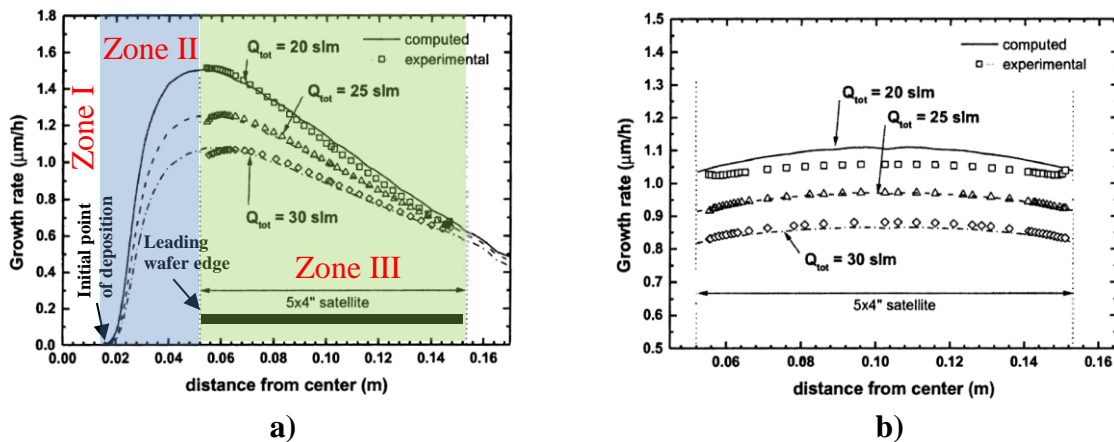


**Figure 39.** Computed (lines) and measured (symbols) growth rate profiles of  $\text{Al}_x\text{Ga}_{1-x}\text{As}$  ( $x=0.28$ ) in the Planetary reactor AIX 2400G3 on static (a) and rotated (b) substrates for various carrier gas flow rates. Growth temperature  $T = 600^\circ\text{C}$  (mass transport regime), process pressure  $P = 100$  mbar. Adapted from [101].

As already mention, in the planetary AIX 2800 reactor, a special triple gas injector has been developed which allows injecting the precursors in the growth chamber trough three independent gas lines. In this way, also the momentum of the group V species entering through the bottom inlet defines the gas entrance length, which acts as an impedance to the supply of growth contributing species (group III) to the growing surface. A larger mass flow entering the bottom inlet results in a longer gas entrance length, and this modifies the position of the depletion curve. The ratio of the hydride gas flows (from the top and from the bottom) is then an additional tuning parameter and can be used to fine-tune the depletion curve position and layer thickness uniformity.

A particular attention has to be payed to avoid *parasitic depositions*, that is, depositions that do not take place on the substrates. Part of the parasitic depositions are unavoidable, i.e the deposition on the graphite susceptor and partially on reactor walls and ceiling. The parasitic deposition on the susceptor can only be minimized by reducing the area of the susceptor out of the area necessary to allocate the substrates. It is very important to minimize the parasitic deposition on the walls and on the ceiling of the reactor chamber to avoid the contamination of the growing layers. This can be done by controlling the heat transfer in the different zones of the reactor, and in particular, since in the MOCVD the chemical reactions are endothermic, the temperature of the ceiling and walls are kept at much lower temperature than the graphite satellites where the substrates are set. The heat transfer between the hot zone of the reactor and the ceiling is mainly due to the emitted radiation from the hot susceptor and wafers and to the carrier gas conduction. The emitted radiation is

governed by the emissivity. Taking into account that the emitted radiation in semiconductors is due to band to band transition, free carrier absorption and lattice vibration, since, in particular, the free carrier absorption and lattice vibration depend on temperature, the emissivity value assumes different values as a function of the temperature. Therefore, the heat transfer between the susceptor (wafers) and the ceiling is not constant during the different depositions. In order to get reproducible growth condition, in the AIX 2800 MOVPE system, the ceiling is thermally coupled, through a mixture of N<sub>2</sub> and H<sub>2</sub> gas to the top reactor ring, which is also water cooled. The temperature of the ceiling can thus be controlled by changing the distance between the ceiling and the reactor top ring and/or by changing the N<sub>2</sub> and H<sub>2</sub> gas mixture. A right ceiling temperature window has to be selected, since if the ceiling temperature were too high, a strong deposition of polycrystalline material would took place on the ceiling; whereas, if it were too low, a strong condensation of material would occur.

Another important concept to be kept in mind is related to the MOVPE in-situ temperature measurement. As already shown, the reactor temperature is a key parameter to be controlled in order to select the wanted growth regime. Nowadays the most used method of controlling the temperature at the wafer surface is to measure the thermal radiation emitted from the wafer itself. However, most of the pyrometers today used for this purpose allow controlling the wafer's temperature starting from 400°C. This means that every deposition process performed a temperature lower than 400°C would not allow monitoring the temperature distribution over the wafer during the growth. In other words, working at wafer temperature lower than 400°C, the deposition processes performed in the kinetical controlled regime would be "thermally blind" for the MOVPE operator. This fact could compromise the wafer yield, and consequently, hinder un industrial scale up of the growth process. This is the reason why for the SiGeSn growth, the efforts have been addressed to find the minimum temperature suitable for obtaining good crystallographic and morphology properties without compromising the possibility to control and tune the temperature profile over the wafer.

## 5.2. *Criteria for precursor selections*

Having in mind the industrial scalability of the growth process, the following main criteria have been identified for the selection of the gas sources to be used for the growth of SiGeSn.

- 1) Since in the MOCVD growth, mostly organometallic and hydrides are used as gas precursors, it has been a priority to identify between these classes of gas sources those precursors that could be appropriate also for the MOCVD growth of SiGeSn. As suggested by Manasevit in one of his first work on the MOCVD growth [102], the use of hydride is recommended if organometallic sources are used as well: in fact, the hydrogen liberated in the decomposition of the hydride source can be combined with the methyl radicals coming from the decomposition of the metalorganic source to give rise methane, which is generally expelled from the growth chamber. In this way it is possible to avoid the incorporation of carbon (carbon contamination) in the growing film.

- 2) For the solar cell realization, depending on the light absorption properties of the layers, several microns of material are needed, therefore in order to avoid long growth processes, the gas sources should have adequate vapour pressure, in particular they should be suitable to reach growth rate in the range 2-10  $\mu\text{m/h}$ .
- 3) According to the literature review, the growth temperature should be kept in the range 350-500°C, therefore the gas sources should present adequate decomposition in the considered temperature range.
- 4) Commercially available, easy-to-buy precursors have to be preferred for an easier scale up of the industrial process.

### **5.3. MOVPE Growth of SiGe and SiGeSn by IBuGe, Si<sub>2</sub>H<sub>6</sub> and SnCl<sub>4</sub>.**

The IV elements growth has been carried out after depositing III-V compounds in the same growth chamber. In a first phase, SiGe and SiGeSn have been deposited just after III-V growth, without introducing any intermediate buffer or coating. Several SiGe layers have been preliminary grown at moderate temperature, around 600°C, with different gas phase composition and carrier gas. Then, SiGe deposition has been carried out by reducing the temperature to values lower than 500°C. Once SiGe deposition has been optimized, the study of SiGeSn growth took place.

#### **5.3.1. Preliminary SiGe deposition by IBuGe and Si<sub>2</sub>H<sub>6</sub>**

For SiGe growth, disilane Si<sub>2</sub>H<sub>6</sub> (diluted in H<sub>2</sub> with concentration of 1000 ppm and 10%) and IBuGe have been firstly selected. Disilane is a commercially available, easy-to-buy gas, that was already successfully used for SiGe growth at low temperature [103],[104]. IBuGe is metalorganic source, with a good vapour pressure (155 torr at 25°C), similar to that of TMGa and therefore, it should allow the deposition with a growth rate comparable with that obtained in III-V growth. Moreover it has been reported that IBuGe decomposes at 350°C [105], so it might be suitable for growing the ternary SiGeSn layer around 380-400°C. A possible drawback of using IBuGe is due to the fact that for the epitaxial germanium growth, good surface morphologies were obtained by introducing a moderate quantity of arsine in the growth chamber. Furthermore, the growth rate of epitaxial germanium was greatly reduced in the presence of arsine or TMGa (for T = 550°C, the growth rate dropped from 44 nm/min to 10 nm/min, with IBuGe partial pressure = 1.3 Pa and Arsine partial pressure of 0.018 Pa) [67]. Since arsenic is a N-type dopant for Ge, epitaxial germanium grown by IBuGe, in presence of arsine, is strongly N-type, making it difficult to obtain low p-type doped Ge layers. In spite of this critical factors, it was worthwhile to check the suitability of the IBuGe source at least for growing SiGeSn – N-type layers.

A calibration curve has been first identified, by linking the Si<sub>x</sub>Ge<sub>1-x</sub> solid phase composition determined by high resolution X ray diffraction (HR-XRD), with the gas phase composition  $\frac{P_{SiH_6}}{P_{SiH_6} + P_{IBuGe}}$ . In particular, the XRD peaks splitting (related to the SiGe solid composition), as function of the gas phase composition is reported in Figure 40.

By increasing the silicon content in the solid phase, the splitting between the SiGe XRD peak and the GaAs XRD substrate peak is reduced and becomes negative, indicating a lattice constant of the layer lower than the substrate. In order to get SiGe lattice matched to GaAs, a  $\text{Si}_2\text{H}_6$  gas phase composition a bit lower than 6% has to be selected. As a reference, the silicon content in the sample 460 and 506, grown with a gas phase composition of 9.74% has been evaluated by HR-XRD to be 2.85%. The  $\text{Si}_2\text{H}_6$  cracking efficiency does not seem influenced by the carrier gas, since all the data can be fit along the same straight line. At the deposition temperature of 620°C-640°C, the SiGe layers present mirror like morphologies, and high crystallographic quality, as showed by the interference fringes in the diffraction peak (see Figure 41). In order to confirm the possibility to use IBuGe for the growth of the SiGeSn ternary material, the temperature window has been reduced in the range 460°C-640°C. By keeping fixed the temperature at 460°C and the  $\text{Si}_2\text{H}_6$  partial pressure at 0.2 Pa, the IBuGe partial pressure has been changed between 1.9 Pa and 188 Pa and the corresponding variation of the growth rate measured (see Figure 42).

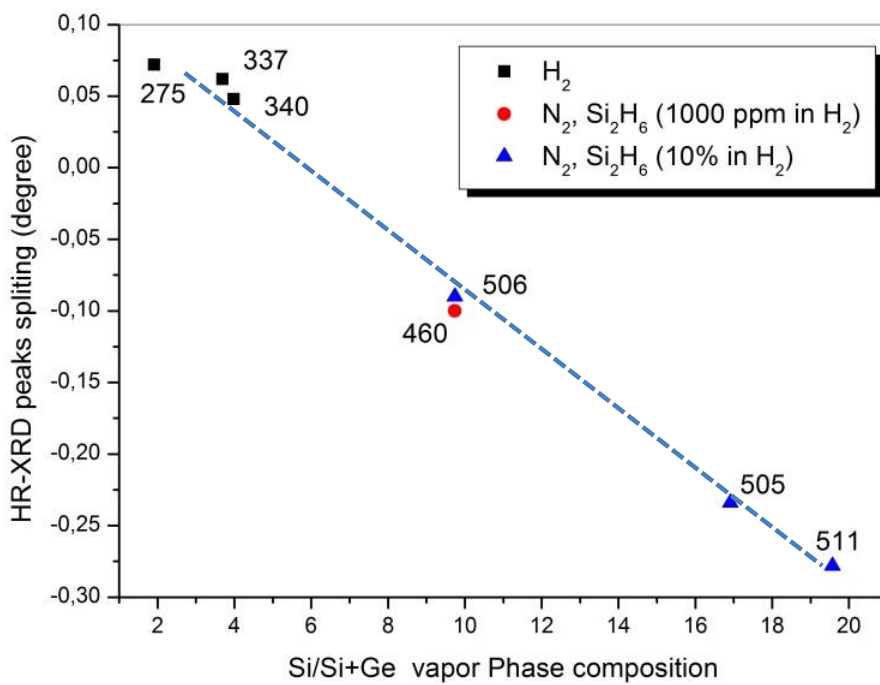


**Figure 40.** Splitting between the SiGe XRD peak and the GaAs XRD substrate peak versus gas phase composition, obtained from HRXRD  $2\theta-\omega$  curves. The samples have been deposited between 620°C-640°C, by using hydrogen ad nitrogen as carrier gas and disilane with different hydrogen dilution. The total gas flow was 12 l/min. The partial pressure of IBuGe and  $\text{Si}_2\text{H}_6$  have been changed between 1.9 Pa - 5.4 Pa and 0.1 Pa - 0.46 Pa, respectively.

The results of the experiments have been compared with the data reported by S.Wirths et al., for the growth of germanium [76]. Within the indicated temperature window, SiGe deposition proceeds in the kinetically limited regime. The activation energy for the “diluted” SiGe is 2.0 eV, against the 1.3 eV value reported for the Ge growth.

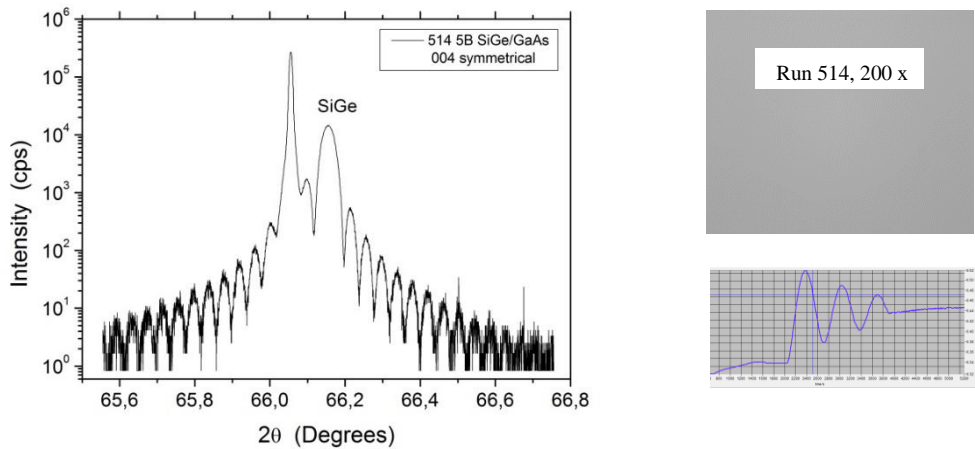


**Figure 41.** on the left,  $\omega$ - $2\theta$  curve acquired on SiGe grown on GaAs, sample 514, with the same composition of sample 460 or 506. On the right side, the surface morphology detected at the optical microscope and the reflectivity curve measured, at 950 nm, in-situ, during the deposition. T growth = 628°C.

Such a difference is neither due to the utilization of  $\text{Si}_2\text{H}_6$ , since the disilane phase composition is too low to justify such a growth rate difference (see later Figure 59 and Figure 60), nor due to the different carriers gas utilized, as nitrogen has been reported to favour the growth with respect to hydrogen [88].

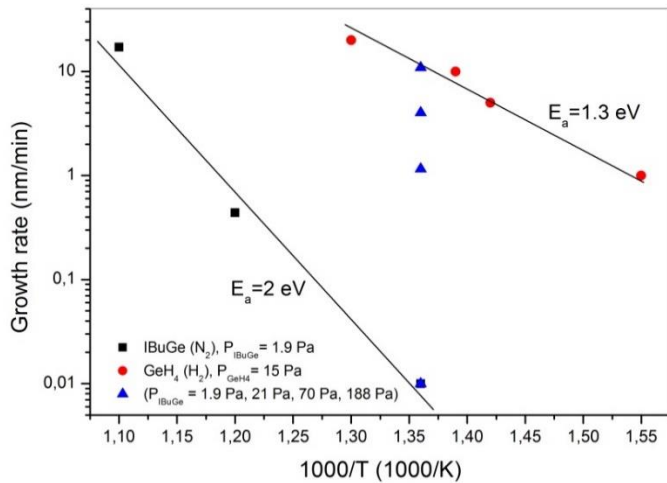


**Figure 42.** Comparison between the data reported in [76], related to the Ge growth by  $\text{GeH}_4$  (15 Pa) with hydrogen carrier gas (red circles) and those obtained by RSE on SiGe (triangles and squares). In the Arrhenius plot (black square) the IBuGe and  $\text{Si}_2\text{H}_6$  partial pressures were kept respectively at 1.9 Pa and 0.2 Pa. By keeping fixed the  $\text{Si}_2\text{H}_6$  partial pressure value, the IBUGe partial pressure was then increased (as indicated by the blue triangle) and the corresponding growth rate variation measured. Total carrier flow = 12 l/min.

The higher activation energy found for SiGe growth could be attributed to the lower cracking efficiency of IBuGe with respect to  $\text{GeH}_4$ . However, in literature,  $\text{GeH}_4$  decomposition is reported to take place at higher activation energy than IBuGe, even if data are dispersed in a wide range of values. For example, in [106] and [107] an activation energy of 41.2 kcal/mole and 42 kcal/mole are

respectively reported considering GeH<sub>4</sub> decomposition on Ge. A lower activation energy, 29.97 kcal/mol, has been reported in [76]. An activation energy of 39.7 kcal/mole is reported in [108] for a GeH<sub>4</sub> decomposition when Ge is grown on GaAs. These values should be compared with the activation energy of 27.4 kcal/mole (1.18 eV) determined for homoepitaxial Ge on Ge with IBuGe [109].

Two other factors could explain the lower growth rate of SiGe grown by IBuGe with respect to Ge grown by GeH<sub>4</sub>, namely, the “As carry over” and the dependence of the growth rate from the precursor partial pressure.

As a matter of fact, all the SiGe runs have been performed after several III-V growths, therefore we need to take into account the possible blocking role of As in saturating the surface sites, as reported in [89] for the growth of GeSn in presence of As. A strong change in the growth regime was also observed by R.Jakimin et al., in the growth of epitaxial Germanium by IBuGe as a function of the doping level of the samples [67]. In order to eliminate any possible penalization in the growth rate due to As “carry over”, in the next paragraph the growth procedure of depositing coating layers has been applied.

The dependence of the activation energy from the gas precursor partial pressure, as shown in [104], can also be considered: as matter of fact, in this work the activation energy for SiGe growth was determined by using a partial pressure of IBuGe of 1.9 Pa, while the data of S.Wirths reported in Figure 42 were obtained with a partial pressure of germane equal to 15 Pa. Indeed, by looking at Figure 42, SiGe growth rate has been changed by two order of magnitude, from 0.01 nm/min to 1 nm/min, when IBuGe partial pressure has been increased form 1.9 Pa to 21 Pa. However, by always referring to Figure 42, at the temperature of 460°C, even by considering SiGe deposited with a IBuGe partial pressure of 21 Pa, its growth rate remains one order of magnitude lower the Ge growth rate. SiGe growth rate becomes comparable with Ge growth rate, when IBuGe partial pressure is raised to 188 Pa, an order of magnitude higher than the GeH<sub>4</sub> partial pressure used for Ge growth. Therefore, we can rule out the effect of the precursor partial pressure and come to the conclusion that the main factor responsible for reduction in the SiGe growth rate is the “As carry over”.

### 5.3.2. SiGe deposition optimization by IBuGe and Si<sub>2</sub>H<sub>6</sub>

In order to increase the utilization efficiency of IBuGe, the growth rate has been maximised by reducing the parasitic deposition. In this way, the possible sources of contamination has also been minimized. In particular, owing to possible depletion of the gas phase at the ceiling of the growth chamber, the SiGe growth rate has been analysed as a function of the ceiling temperature (see Figure 43). The growth rate increases by increasing the ceiling temperature and the highest SiGe growth rate was obtained at the deposition temperature of 620°C, with a ceiling temperature > 190 °C. A similar behaviour was also observed at lower deposition temperature (540°C), however, in this case, a growth rate plateau was not identified, as it was not possible to increase the ceiling temperature over 180°C. This problem was more severe once the deposition temperature was lowered to 460°C: in this case the maximum attainable ceiling temperature was 113 °C. In order to

minimize the parasitic deposition on the ceiling, a new configuration of the ceiling was then conceived. Since the ceiling is cooled trough a N<sub>2</sub>/H<sub>2</sub> mixture by the top plate of the reactor chamber, a better thermal decoupling was accomplished by increasing the gap between the ceiling surface and the top plate (indicated by the arrow in Figure 43). For a medium and large ceiling gaps, temperatures of 150°C and 190°C could be obtained, respectively, bringing the ceiling temperature into the required range for maximizing the growth rate at low deposition temperature.

The parasitic deposition on the ceiling has also been investigated by changing the gas line through which IBuGe source is injected in the growth chamber, that is, IBuGe has been injected from the top or from the bottom of the hydride lines (see Figure 44). As expected, in order to maximize the growth rate, IBuGe should be injected from the bottom hydride line, this allows decreasing the parasitic deposition on the ceiling and therefore the depletion of the mother gas phase. Eventually the SiGe composition uniformity has been evaluated along the wafer radius, as showed in Figure 45. It is possible to point out a slight shift of the epilayer peak to higher diffraction degrees, as well as a higher FWHM, indicating, respectively, a silicon richer composition and a lower thickness going towards the edge of the wafer. The higher Si incorporation is due to a 5°C higher temperature on the edge with respect to the center. The lower growth rate in the edge has been ascribed to the presence of H<sub>2</sub> in the DGFR, as explained later in chapter 5.4.3.1.

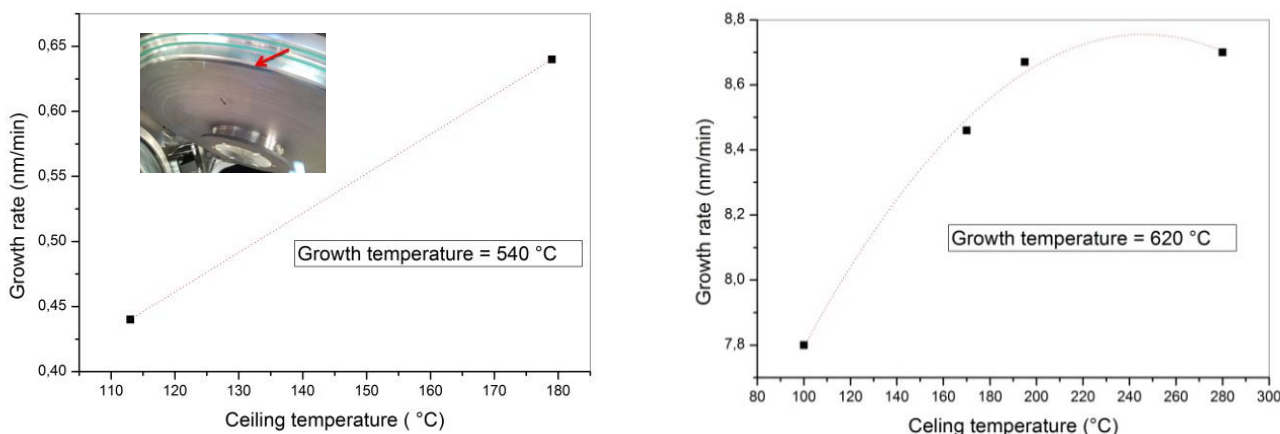


**Figure 43. Influence of the ceiling temperature on the SiGe growth rate, at different deposition temperature, as indicated in the figure. IBuGe and Si<sub>2</sub>H<sub>6</sub> partial pressures are 1.9 Pa and 0.20 Pa respectively. The dotted lines are added just to help the reading. A picture of the ceiling of the growth chamber is also included in the inset.**

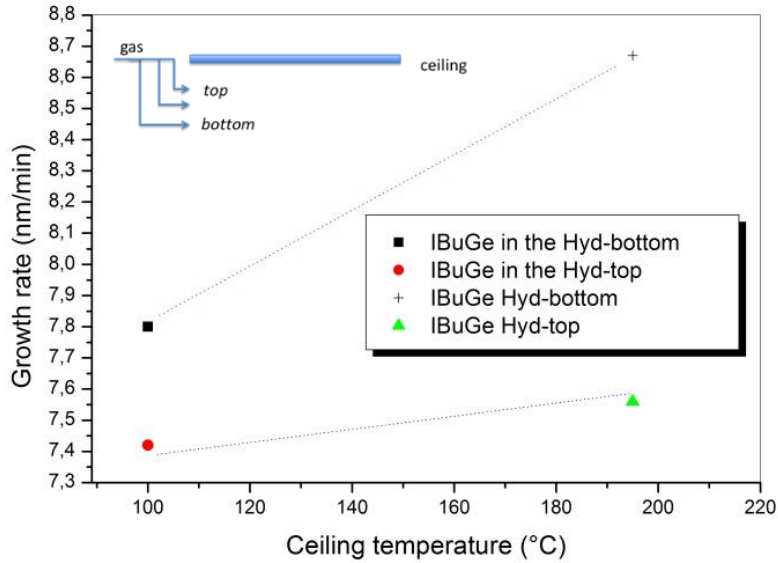


**Figure 44.** SiGe Growth rate as a function of the IBuGe line injection and ceiling temperature. IBuGe is injected into the bottom or in the top hydride lines as indicated in the inset.

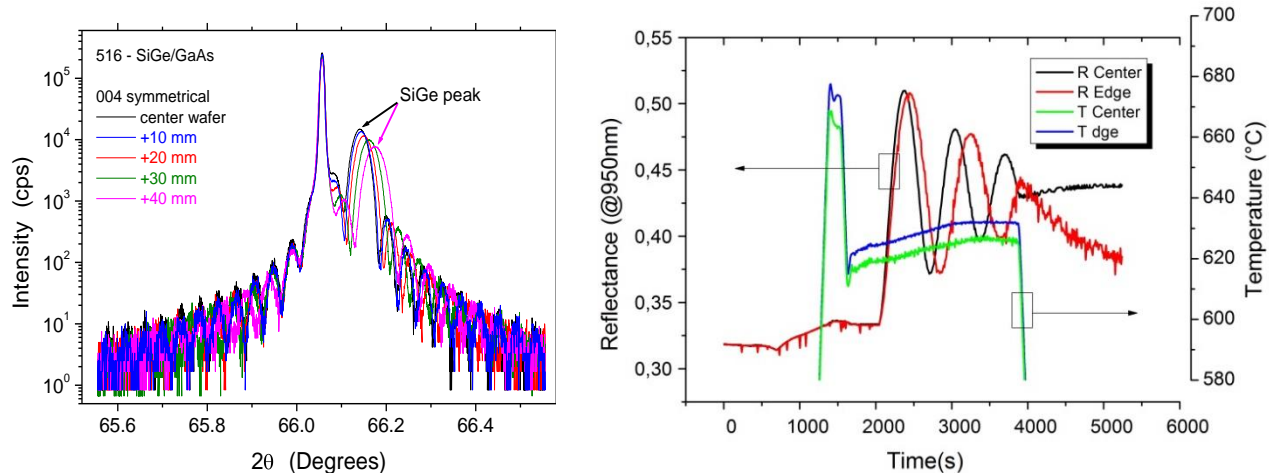


**Figure 45.** On the left, comparison among the  $\omega$ -2θ curves along the 004 symmetrical reflection acquired for the SiGe runs as a function of the position on the wafer; on the right reflectance and temperature measured on the center and edge of the wafer.

### 5.3.3. SiGeSn deposition by IBuGe, Si<sub>2</sub>H<sub>6</sub> and SnCl<sub>4</sub>.

By adding SnCl<sub>4</sub> to disilane and IBuGe and by keeping the temperature at 460°C, the study of SiGeSn MOVPE deposition was started. SnCl<sub>4</sub> is cheaper and easier to be purchased with respect to SnD<sub>4</sub>, that was utilized in the starting experiment on SiGeSn,. This source was also selected because was successfully utilized for the GeSn growth [110]. SiGeSn has been firstly deposited on GaAs (100) toward <110> and Ge (100) 6°off toward <111> substrates by keeping a small pressure of

arsine ( $P_{AsH_3} = 4$  Pa) over the wafers. These first SiGeSn runs have been carried out after six IV elements coating runs from the last III-V deposition. It is worthwhile pointing out that it is the first time the SiGeSn layers have been grown by MOVPE by using  $Si_2H_6$ , IBuGe and  $SnCl_4$ . The SiGeSn samples have been deposited by keeping the silicon gas phase composition in the range 5.95% - 9.88 %, near the value used for the samples of SiGe 506, 508, 516, (9.74%), whose XRD characterization results have been shown in Figure 40. The IBuGe and the  $SnCl_4$  partial pressures were kept fixed to 71 Pa and 1.2 Pa respectively, while  $Si_2H_6$  partial pressure was changed from 4.5 Pa to 7.9 Pa. The SiGeSn HR-XRD characterization results are reported in Figure 46.

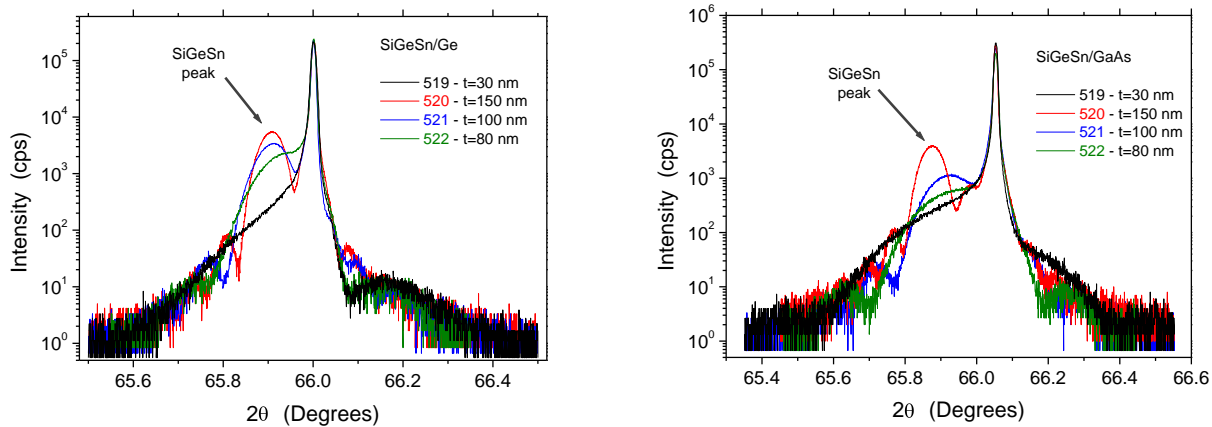


**Figure 46. HR-XRD  $\omega$ - $2\theta$  curves acquired on (004) symmetric related to SiGeSn samples grown, with different thickness, on GaAs and Ge substrates. XRD peaks are measured at the center of the wafers.  $P_{IBuGe} = 71$  Pa,  $P_{SnCl_4} = 1.2$  Pa,  $P_{Si_2H_6}$  (519) = 4.5 Pa,  $P_{Si_2H_6}$  (520) = 7 Pa,  $P_{Si_2H_6}$  (521) = 7 Pa,  $P_{Si_2H_6}$  (522) = 7.9 Pa.**

Tin incorporation in the SiGe matrix brings the epilayer XRD peak from the right to the left of the substrate XRD peak. Even by thinking that Sn can just reduce the silicon incorporation, in the worst case, this should finally produce an XRD layer peak overlapped to the Ge/GaAs XRD substrate peaks, while the layer peak is clearly on the left side of the Ge/GaAs peaks. Therefore, it can be concluded that the shift of the XRD SiGe peak on to the left side of the Ge (GaAs) substrate XRD peak is surely due to Sn incorporation in SiGe. The incorporation of Sn and Si in SiGeSn has thus an opposite effect: Sn increases, while Si decreases the value of the lattice constant. As expected, by increasing the film thickness, the SiGeSn diffraction peak intensity increases, while its position is almost unvaried in the center of the wafer, indicating no change in the average lattice parameter with different thickness. For the samples grown on the GaAs substrate, an apparent shift of the SiGeSn XRD peak towards the left side is found by increasing the thickness from 100 nm to 150 nm (sample 521 and 520 respectively), while no XRD shift is shown for the SiGeSn grown on Ge. This difference could be explained by assuming that for the samples grown on the GaAs substrate the XRD measurements have not been taken exactly in the same wafer central position. In fact, as shown in Figure 47, there is a SiGeSn composition non-uniformity along the wafer radius.

ADVANCEMENT ON THE MOVPE TECHNOLOGY TO EXPAND BAND GAP ENGINEERING POSSIBILITIES WITH  
THE COMBINED GROWTH OF III-V AND GROUP-IV MATERIALS

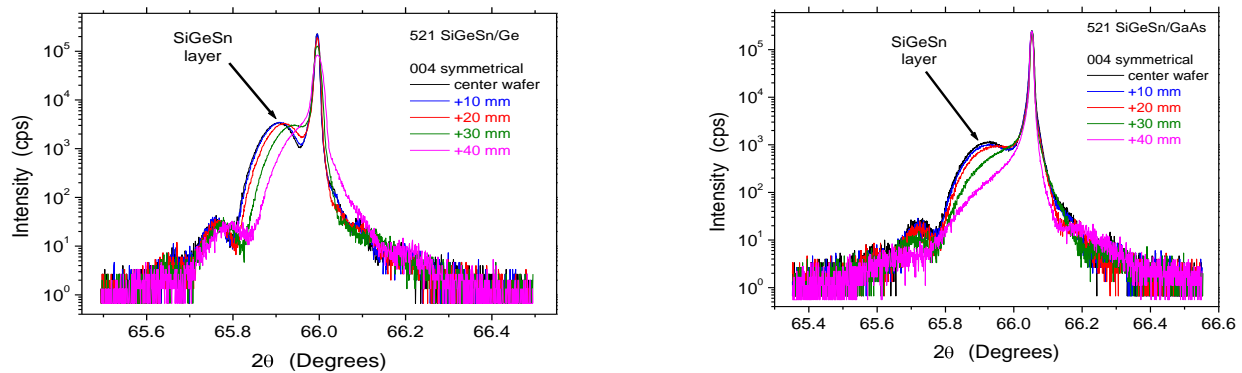


**Figure 47.** Comparison between the  $\omega$ – $2\theta$  curves along the 004 symmetrical reflection, acquired for the samples grown on Ge substrate (left) and GaAs substrate (right) as a function of the position on the wafer (left).

As already pointed out for the SiGe growth, also in the case of SiGeSn deposition there is a slight shift of the epilayer XRD peak towards higher diffraction degrees by going from the center to the edge of the wafer. The composition non-uniformity along the wafer radius determined for SiGe and SiGeSn has been compared (see Figure 48).

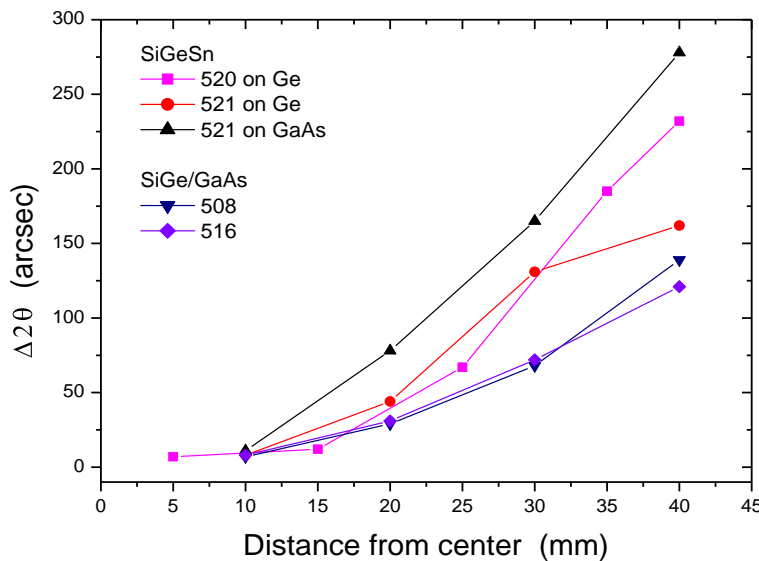


**Figure 48.** Separation between the layer and substrate XRD peak as a function of the distance from wafer center for SiGe and SiGeSn samples.

The Figure 48 shows that, the composition non-uniformity along the wafer radius is more pronounced for SiGeSn with respect to SiGe. This could mean either a higher radial non uniform incorporation of Si in SiGeSn layer with respect to SiGe or that both Si and Sn distributions are not uniform along the wafer radius. In the first case, this would mean that Sn influences Si

incorporation and that  $\text{SnCl}_4$  is anyway not uniformly distributed along the wafer radius. If both Si and Sn distributions are not uniform along the wafer radius, by considering that Sn (Si) incorporation brings the XRD SiGeSn peak on the left (right) of the XRD substrate peak we could conclude that, at the same time, Si increases and Sn decreases going from the center towards the wafer edge.

These data suggest that in order to improve the composition uniformity along the wafer radius, the Si, Ge ad Sn sources should be injected in the growth chamber independently, each one with dedicated gas line and mass flow controller.

The result of the SIMS characterization carried out on the SiGeSn/GaAs sample 520 is reported in Figure 49. The same result has been obtained for the SiGeSn sample grown on Ge substrate.

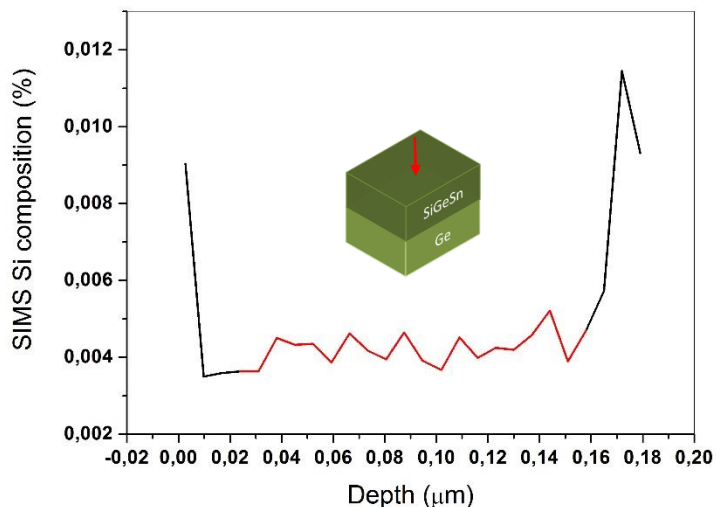


**Figure 49. SiGeSn/GaAs 520 SIMS in-depth profile of Si composition. The red line indicates the Si concentration in SiGeSn excluding the surface and the interface with the substrate. SiGeSn was grown with IBuGe,  $\text{Si}_2\text{H}_6$  and  $\text{SnCl}_4$  partial pressure respectively equal to 71 Pa, 7 Pa and 1.2 Pa.  $\text{Si}_2\text{H}_6$  gas phase composition = 8.8 %.**

The SIMS characterization shows that silicon incorporation in SiGeSn grown at 460°C with a  $\text{Si}_2\text{H}_6$  gas phase composition of 8.8 % is around 0.5%. This low value is reasonable, if compared with the silicon content of 2.85% determined in the samples 460 and 506, grown at 620°C with a gas phase composition of 9.74%. In fact, a much lower  $\text{Si}_2\text{H}_6$  decomposition is expected lowering the growth temperature from 620°C to 460°C.

The SiGeSn growth rate has been determined by fitting the in-situ reflectance measurements (see Figure 50) carried out on SiGeSn layers grown on a GaAs substrates. The determined value of 3 nm/min is a bit lower than the growth rate of SiGe (4 nm/min), that was grown at the same growth temperature of 460°C, with the same IBuGe partial pressure of (70 Pa) and with a lower  $\text{Si}_2\text{H}_6$  partial pressure (0.2 Pa in SiGe instead of 7 Pa used for SiGeSn) (see Figure 42.) According to [94], the lower growth rate of SiGeSn could be due to the higher partial pressure value of  $\text{Si}_2\text{H}_6$  used for SiGeSn with respect to the value used for SiGe.

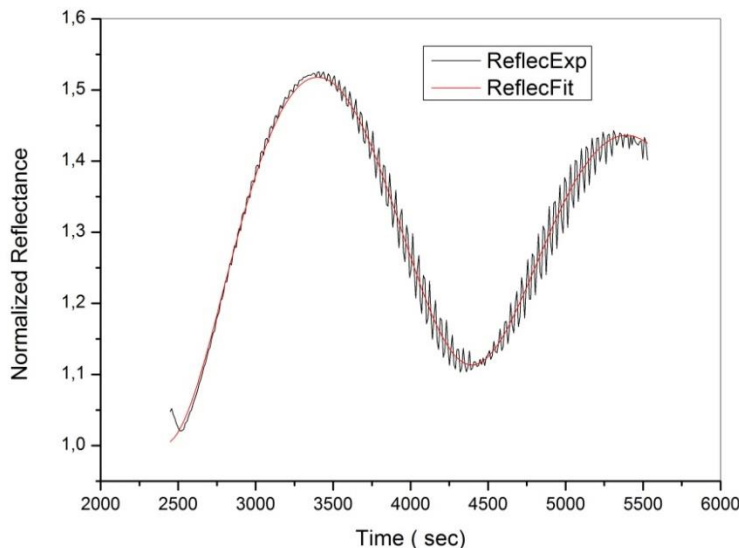


**Figure 50.** Reflectance at 905 nm measured during the deposition of the sample SiGeSn/GaAs 520 and related fitting.

Despite Ge and GaAs substrates have similar lattice constant and therefore SiGeSn is expected to find similar strain condition when grown on GaAs and on Ge, very different surface morphologies have been detected in the two cases. The morphology and structural analysis has been assessed by scanning electron microscope (SEM), angle annular dark field transmission electron microscopy (TEM HAADF), selected area diffraction (SAED), Pattern and energy dispersive X-ray analysis (EDX).

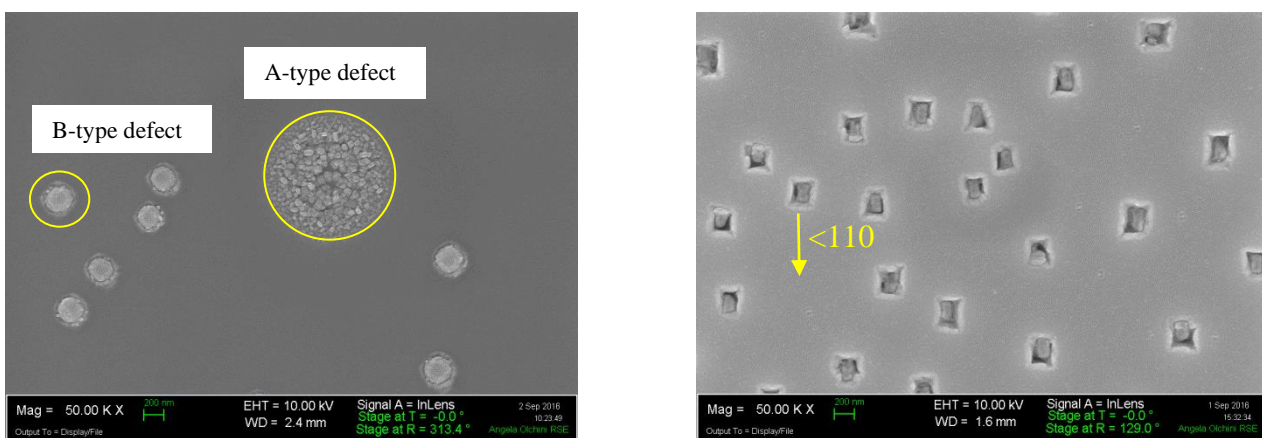


**Figure 51.** Top view SEM images of the sample SiGeSn /Ge 520 on the left, and of the sample SiGeSn/GaAs 522, on the right.

The SEM images reported in Figure 51 allow classifying the different morphological defects. In particular, two kinds of defects have been identified on SiGeSn samples grown on Ge: i) “A-type” round-shaped defects, of about 1.5  $\mu\text{m}$  diameter, including an agglomerate of nanocrystals, ii) “B-

type”, round-shaped defects, about 350 nm in size, with a homogenous structure. TEM HAADF and EDX analysis of the “A-type” defect are shown in Figure 52.

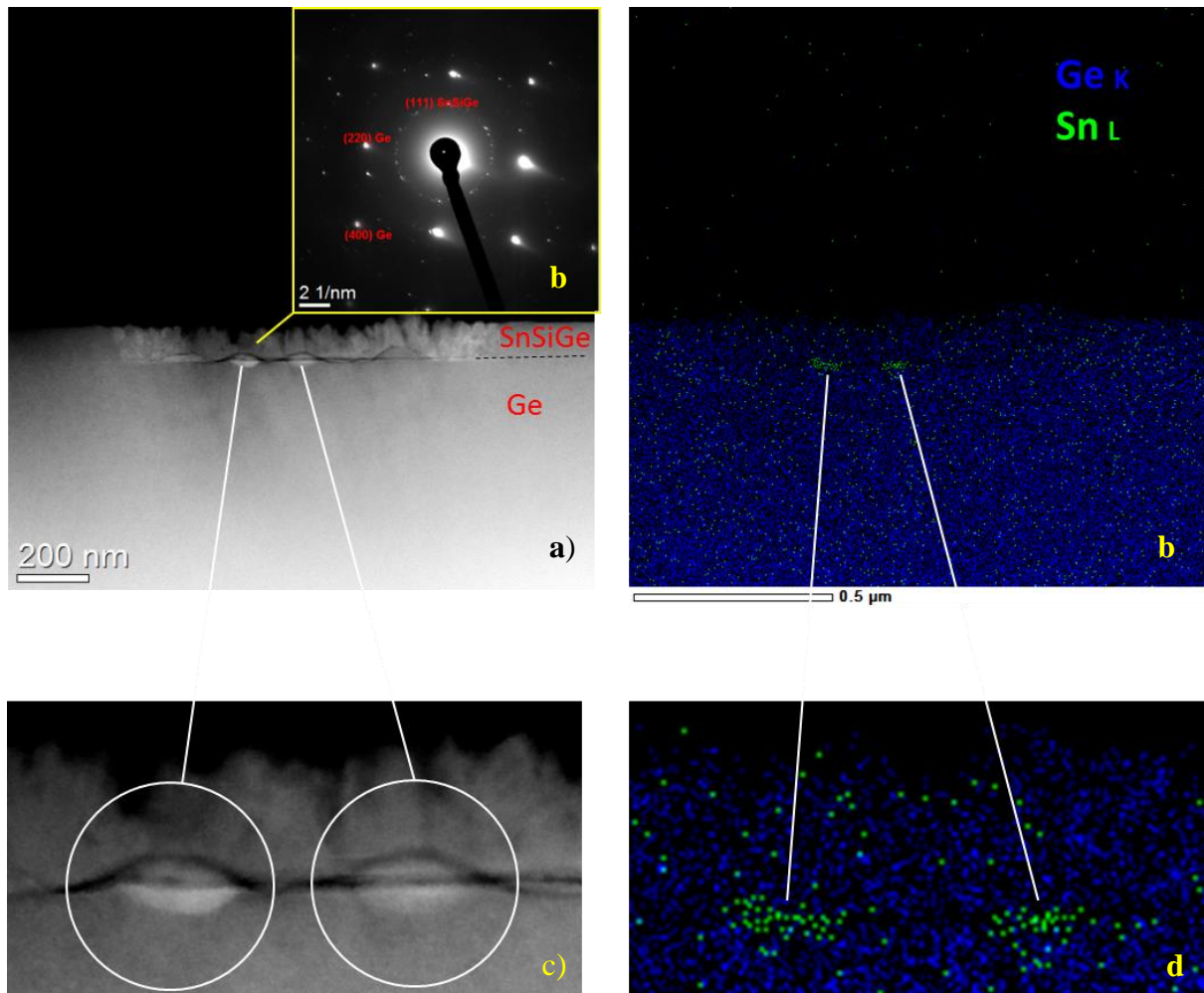


**Figure 52.** Structural analysis of the SiGeSn/Ge “A-type” defect: a) and c) TEM HAADF cross section (100), (Z contrast image: brighter areas= higher atomic number), b) Selected Area Diffraction (SAED) Pattern , d) EDX map.

The SAED Pattern carried out on the “A-type” defect shows that random oriented nanocrystals are present. At the base of the defect, Sn rich regions are identified by EDX analysis. It is possible to conclude that tin precipitates during the deposition and probably causes the loss of the epitaxy.

Owing to the relatively high deposition temperature (460 °C), tin precipitation could be expected, however, as shown later, tin precipitation has not been observed on GaAs substrate. The origin of tin precipitation will be clarified in the next paragraphs. For the “B-type” defect, TEM HAADF shows homogenous bright areas, while the SAED pattern allows assessing that the defect consists of SiGeSn protrusions, whose edges have structural defects, but the orientation of the matrix is preserved (see Figure 53).

“Craters like” defects have been detected on SiGeSn samples grown on GaAs, with their horizontal side parallel to the substrate flat, that is, perpendicular to the direction <110>.

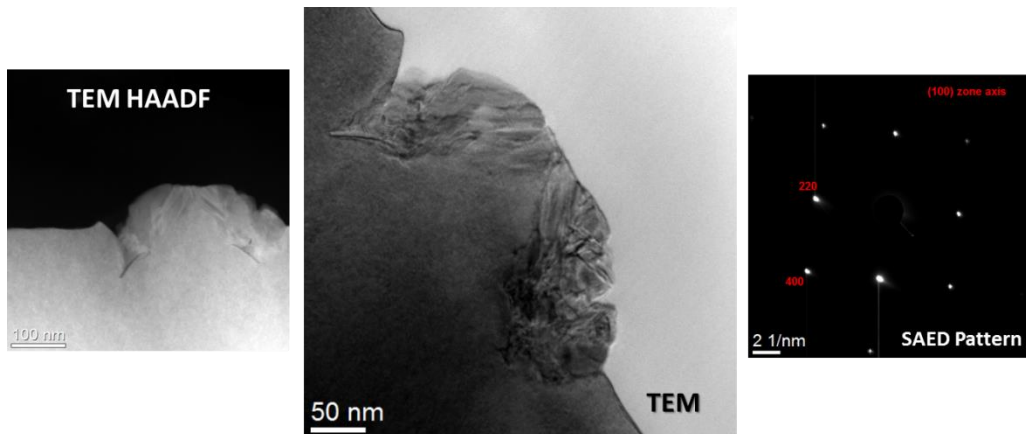


**Figure 53.** TEM HAADF, TEM cross section (100) and SAED Pattern of the SiGeSn/Ge “B-type” defect.

A TEM HAADF image and the EDX map of the “crater like” defect is reported in Figure 54.

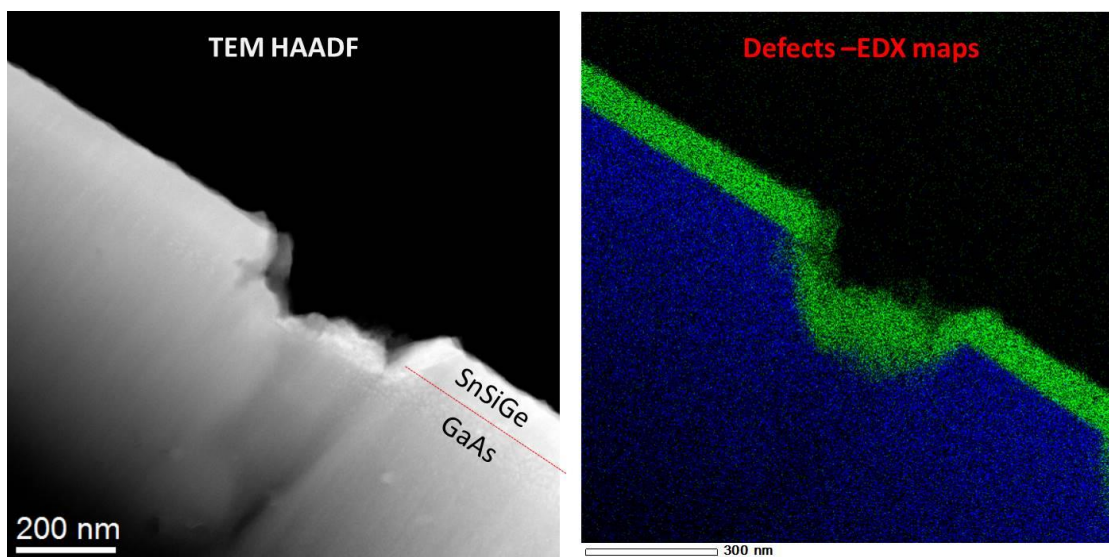


**Figure 54.** Structural analysis of the SiGeSn/GaAs “crater like”: TEM HAADF image and EDX map.

Tin precipitation is absent and SiGeSn film fills in the craters. The growth of SiGeSn on GaAs seems disturbed by the formation of etch pits that could be attributed to HCl etching action [111], since this acid is likely to be produced in the gas phase through the chemical reactions involving IBuGe, Si<sub>2</sub>H<sub>6</sub> and SnCl<sub>4</sub>.

However, HCl vapour should etch Ge substrate as well [112], while SiGeSn morphology on the Ge substrate does not show the “etch pit” found in the deposition on GaAs substrates.

As both substrates have been baked before deposition in nitrogen at around 660°C, the thermal treatment without arsine atmosphere could have been responsible for the GaAs surface decomposition and then of the V grooves formation where the deposition of SiGeSn later took place.

The TEM analysis reported in Figure 55 show that the SnSiGe film is completely twinned along the edge-‘craters’, probably due to the different step high found in the  $<100>$  and  $<10\bar{1}>$  directions as similarly found in [113].

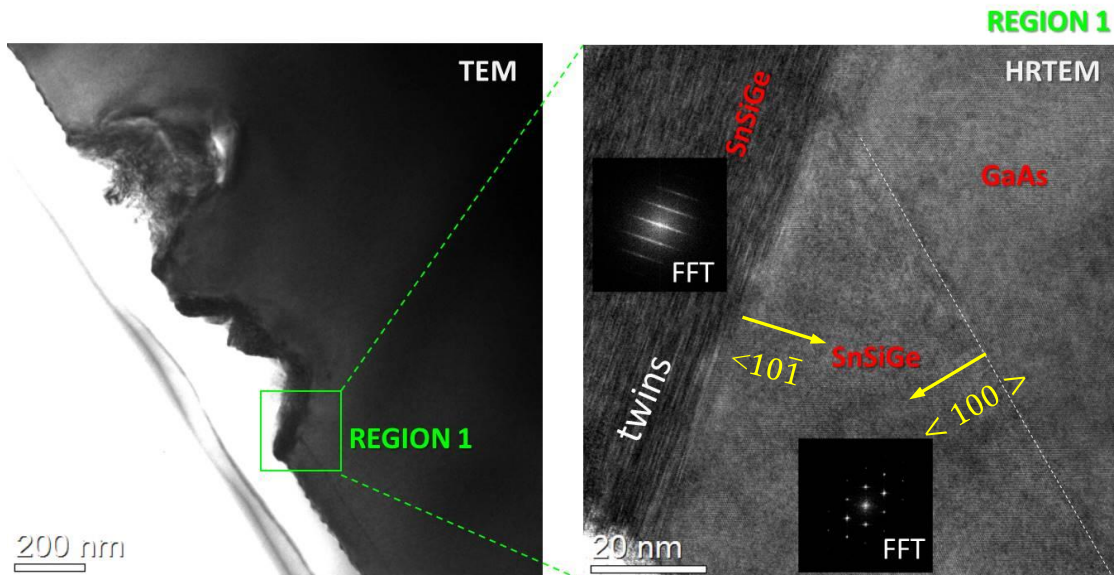


**Figure 55. TEM high resolution analysis of the SiGeSn/GaAs “crater like” defect.**

It is worthwhile to point out that Sn precipitation has been observed only when SiGeSn is deposited on Ge substrate, while no Sn precipitation has been detected when SiGeSn is deposited on GaAs substrate. This result could be related to the role of the As that has been investigated in [89] and it has been in depth studied in the experimental work hereafter presented.

#### **5.4. MOVPE Growth of Ge, SiGe and SiGeSn with $\text{GeH}_4$ , $\text{Si}_2\text{H}_6$ and $\text{SnCl}_4$**

SiGeSn has then been performed by replacing IBuGe with GeH<sub>4</sub>. Most of the experiments have been carried out by using GeH<sub>4</sub> 10% diluted in H<sub>2</sub>.

A few runs have also been performed by GeH<sub>4</sub> 10% diluted in N<sub>2</sub>.

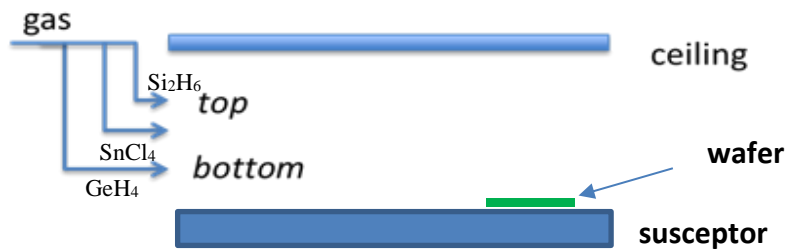


**Figure 56.** Gas distribution scheme of  $\text{Si}_2\text{H}_6$ ,  $\text{SnCl}_4$  and  $\text{GeH}_4$  within the MOVPE growth chamber. The three sources are injected into three different gas lines and the flow in each line can be adjusted independently from the others.

Preliminary runs of Ge and SiGe have been carried out before starting the study of SiGeSn deposition. In order to improve the composition uniformity, Ge, Si and Sn precursors have been injected in the growth chamber by separate gas lines. In particular,  $\text{Si}_2\text{H}_6$  was injected in the top hyd line,  $\text{GeH}_4$  on the bot hyd line, while  $\text{SnCl}_4$  in the MO line, as schematically indicated in Figure 56.

With the aim of eliminating the growth rate penalization owing to “As carry over”, the growth procedure of depositing on the graphite elements of the MOVPE growth chamber several “coating runs” constituted of IV elements materials has been applied. An average of 1  $\mu\text{m}$  deposition for each coating run has been carried out. After the coating run depositions, the layer under investigation has been grown and the related growth rate measured.

#### 5.4.1. MOVPE Growth of Ge with $\text{GeH}_4$

An in-depth Ge deposition analysis has been carried out, on 4- and 6-inch Germanium wafers (100) 6° off towards <111>. In the attempt to minimize the evaporation of the III-V contaminants from the graphite parts of the growth chamber, the growth temperature has been set up in the range 475–500°C. In Table 6, Ge growth rate has been evaluated as a function of several growth parameters, including the number of coating runs.

**Table 6.** Ge Growth rate obtained on 4- and 6-inch wafers as a function of growth parameters and of the number of IV-based materials coating runs.

N Run	T growth (K)	Total flow (l/min)	GeH4 partial pressure (Pa)	Wafer diameter (inch)	N. of coating runs of IV-based materials after the last III-V growth	Growth rate in the wafer center (nm/min)
S0	773	20.5	5.5	4	1	16
S1	773	21	15	4	2	99
S2	773	20.7	61	6	3	111
S3	773	20.5	22	6	4	100
S4	745	22	20	6	5	91
S5	750	18	25	6	6	119
S6	773	21.6	21	6	9	100

By referring to samples S0 and S1 reported in Table 6, it is worthwhile to point out a 6 times increase in the growth rate for a 3 times increase in GeH<sub>4</sub> partial pressure. This anomalous increase of the growth rate can be correlated to the “As carry over” reduction obtained by applying a couple of coating runs. This hypothesis has been confirmed by the results exposed in the following.

Ge growth rate values related to several depositions extracted from Table 6, performed with similar GeH<sub>4</sub> partial pressure (from 15 Pa to 25 Pa), as a function of the deposition temperature and of the coating runs number are shown in Figure 2.

It can be assessed that after already one IV elements coating run, Ge growth rate becomes mainly influenced by the MOVPE reactor geometry (which allows obtaining high germane utilization efficiency in comparison with reference data) and by other growth conditions, like the use of N<sub>2</sub> as carrier gas instead of H<sub>2</sub>, which further improves the growth rate.

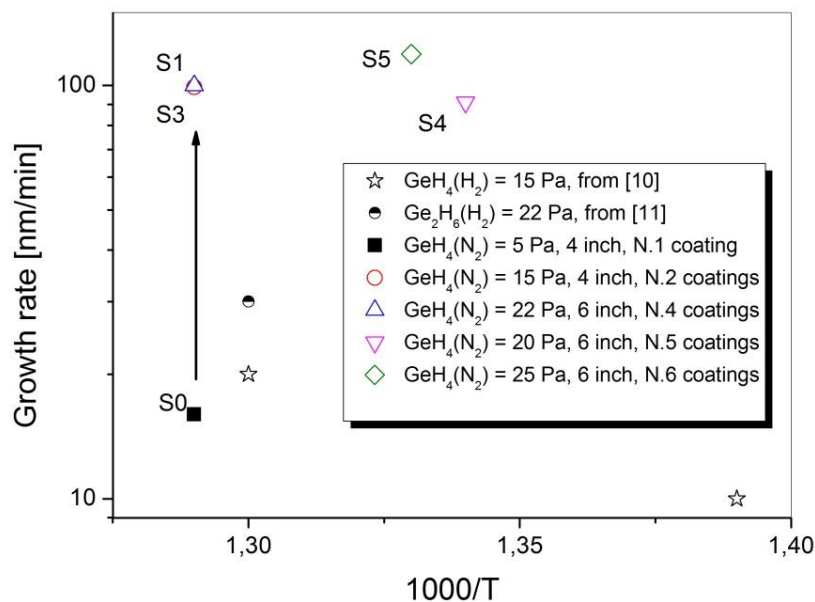


**Figure 57.** Comparison between Ge growth rate data obtained in this work, by using GeH<sub>4</sub> and N<sub>2</sub> as carrier gas, in a III-V contaminated MOVPE reactor (see Table 6 ) and those reported in ref [76] and [114] where Ge has been grown respectively by GeH<sub>4</sub> and by Ge<sub>2</sub>H<sub>6</sub>, with H<sub>2</sub> as carrier gas.

From sample S1 on, the “As growth blocking role” seems irrelevant, as the growth rate can be easily controlled and optimized, for example, by changing the total flow, the precursors partial pressure, or the growth temperature, as shown by comparing the runs S4, S5 and S6.

By comparing the runs S4 and S5 carried out at similar growth temperature, it is evident a 30 % growth rate increase obtained with a 22% total carrier flow decrease and a 25% Ge partial pressure increase. In kinetically controlled regime, the chemical reactions are strongly temperature dependent, therefore, by decreasing the total carrier flow, an increase of the precursor contact time with the hot wafers is achieved, this, in turn, increases the precursor cracking efficiency and then

the growth rate, by assuming the peak of the deposition rate over the wafer zone (see Figure 59). By comparing run S4 with run S6, it is eventually possible to check the influence of the growth temperature on the growth rate. The total carrier flow and GeH<sub>4</sub> partial pressure are almost kept at the same value in both runs, therefore the higher growth temperature of run S6 is clearly responsible of the higher growth rate, as expected to find in a kinetically limited regime.

#### 5.4.2. MOVPE Growth of SiGe with GeH<sub>4</sub> and Si<sub>2</sub>H<sub>6</sub>

After Ge depositions, several SiGe runs have been performed. This SiGe depositions series, therefore, benefit of several previous Ge coating runs. In Figure 58, the relationship between Si<sub>x</sub>Ge<sub>1-x</sub> solid phase composition,  $x$ , and gas phase composition,  $\frac{P_{Si_2H_6}}{P_{Si_2H_6} + P_{GeH_4}}$ , determined on 4 inch and 6 inch Ge wafers, is depicted.

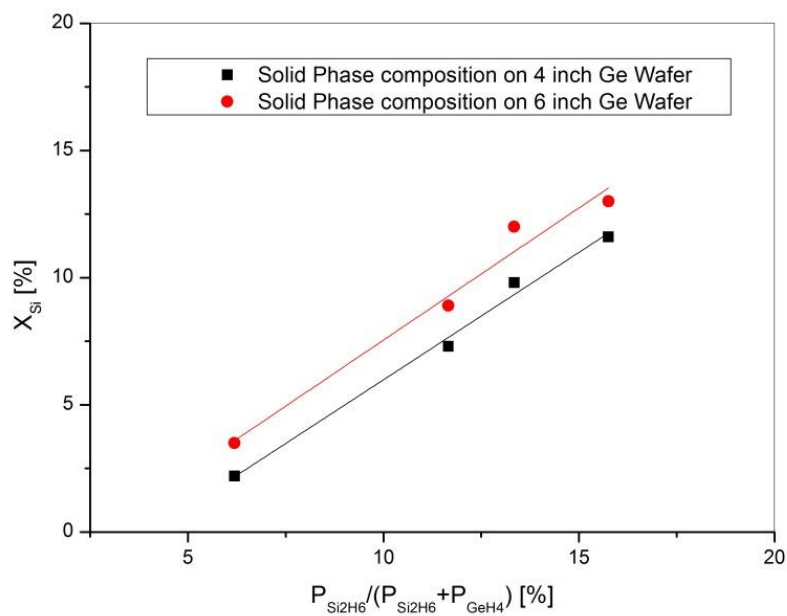


**Figure 58.** Relationship between the solid phase composition of Si<sub>x</sub>Ge<sub>1-x</sub> (measured at the center of the sample) and the Si<sub>2</sub>H<sub>6</sub> gas phase composition, in relation to the type of wafer used. The growth temperature on 4 inch and 6-inch G wafers is respectively of 475°C and 485°C. Total carrier flow = 25 l/min. The partial pressure of GeH<sub>4</sub> has been maintained at the value of 17.75 Pa, while Si<sub>2</sub>H<sub>6</sub> partial pressure has been changed assuming the following values: 1.17 Pa, 2.34 Pa, 2.73 Pa and 3.32 Pa.

The higher Si solid phase composition measured on 6 inch wafer with respect to the one measured on 4 inch wafer is due to the higher growth temperature (10°C) set on the former, obtained by properly regulating the DGFR mixture underneath the graphite satellites. The Si/Ge ratio in SiGe is higher at higher temperature for two reasons: i) Si<sub>2</sub>H<sub>6</sub> has a higher activation energy than GeH<sub>4</sub>, 1.56 eV vs 0.61 eV, respectively (Si-H bond energy is stronger than Ge-H bond energy) [103],

therefore, a higher fraction of Si atoms is made available in gas phase (and then in solid phase) with respect to Ge atoms, for the same temperature increment, ii) the binding energy of silicon is higher than germanium [115], thus at higher temperature, Ge atoms desorption is higher than Si atoms desorption.

It is possible to write the following relationship which allows calculating the incorporation efficiency ( $J$ ) of Si in  $\text{Si}_x\text{Ge}_{1-x}$ :

$$\frac{x}{1-x} = J \frac{P_{\text{Si}2\text{H}6}}{P_{\text{GeH}4}} \quad 5.1$$

By setting the gas phase composition:

$$x_g = \frac{P_{\text{Si}2\text{H}6}}{P_{\text{GeH}4} + P_{\text{Si}2\text{H}6}} \quad 5.2$$

It holds:

$$x = \frac{Jx_g}{(1-x_g) + jx_g} \quad 5.3$$

The Eq.5.3 fits the experimental data reported in Figure 58, obtained on the 6 inch Ge wafer, with  $J=0.8$ .

In Figure 59, SiGe growth rate as a function of the total carrier flow is depicted. The higher the total carrier flow, the lower the growth rate owing to the reduced contact time of the precursors with the hot wafer. Figure 59 also includes a further growth rate point extracted from Figure 42, in particular taken from the sample grown at 460°C, with around 1% of  $\text{Si}_2\text{H}_6$  gas phase composition, 21 Pa of IBuGe partial pressure and 12 l/min of total carrier gas flow.

The results of the experiments have been compared with the data reported by S.Wirths at al., for the growth of germanium [76]. Within the indicated temperature window, SiGe deposition proceeds in the kinetically limited regime. The activation energy for the “diluted” SiGe is 2.0 eV, against the 1.3 eV value reported for the Ge growth.

The arrow reported in Figure 59 shows the increment in the growth rate obtained on SiGe deposited with  $\text{GeH}_4$ , after several coating runs. The growth rate value is two order of magnitude higher than the growth rate of SiGe grown by IBuGe, whose deposition was penalized by the “As carry-over”. This result confirms that the procedure of using coating runs or proper buffer layers before Ge or SiGe deposition is effective in eliminating the “As carry-over” produced by the previous III-V runs.

We have to point out that, for a fair growth rate comparison, it is important to compare samples grown with comparable  $\text{Si}_2\text{H}_6$  gas phase composition and growth temperature. As reported in Figure 60, the higher the  $\text{Si}_2\text{H}_6$  partial pressure, by keeping constant the germane partial pressure, the lower is the growth rate

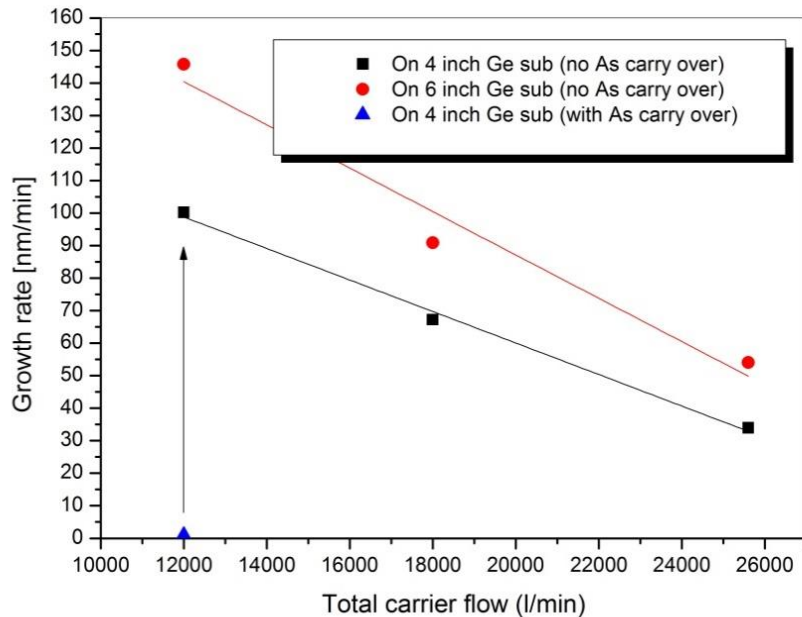


**Figure 59.** Growth rate of SiGe with  $\text{Si}_2\text{H}_6$  gas phase composition equal to 6.2%, after several coating runs, as a function of the total carrier flow. Growth temperature on 4 inch and 6 inch wafer, respectively of 475°C and 485°C A further growth rate data (1 nm/min) extracted from Figure 42 is included. See text for explanation.

The results obtained in Figure 60 can be explained by assuming a growth rate limited by the surface passivation of hydrogen atoms coming from  $\text{Si}_2\text{H}_6$  cracking [116].

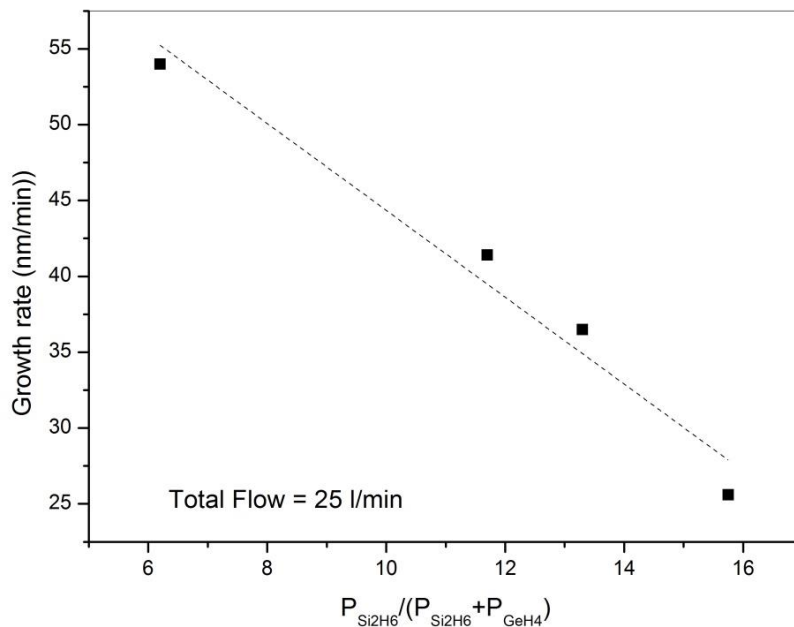


**Figure 60.** Growth rate versus SiGe gas phase composition measured on 6 inch Ge wafers. T growth = 485°C.

A growth rate decrease as function of Si<sub>2</sub>H<sub>6</sub> partial pressure has also been reported by S. Wirths in SiGeSn growth [87]. Since in the previous growth rate comparison the higher growth rate has been obtained with an higher Si<sub>2</sub>H<sub>6</sub> gas phase composition, the reported conclusion is still valid. As far as the growth temperatures are concerned, it is true that the lower growth rate has been obtained on the sample grown at lower temperature (460°C instead of 475°C), however, according to Figure 42, an increment of 15 °C can justify a growth rate increase from 1 nm/min to 2 nm/min (which is still much lower than 100 nm/min) therefore, the previous conclusion is again confirmed.

#### 5.4.3. MOVPE Growth of SiGeSn with GeH<sub>4</sub>, Si<sub>2</sub>H<sub>6</sub> and SnCl<sub>4</sub>

In Table 7 the growth parameters and composition results on SiGeSn depositions on Ge substrates are reported. For sake of completeness, in Table 7, SiGeSn samples 520 and 521, grown by IBuGe, reported in chapter 5.3.3 are also reported and renamed as S1 and S2.

The new deposition series starts from sample S3, which took place after forty MOVPE coating runs of (Ge)Si from the last III-V run. Therefore, the MOVPE reactor was less contaminated by As with respect to the previous, S1 and S2 SiGeSn samples (that took place only after six IV elements coating runs). From run S3 to run S7 only SiGeSn depositions have been performed. The run S8 has been carried out in a clean reactor without As carry-over. The run S10 has been performed after eight Ge coating runs from the last III-V deposition. Then for this last run, the reactor chamber presented an As carry-over comparable with the carry-over that was present in the growth of sample S1 and S2.

##### 5.4.3.1. SiGeSn XRD analysis

In Table 7, all the SiGeSn samples have been grown lattice matched on Ge or very near to the lattice matching condition. as shown, for example, in Figure 61.

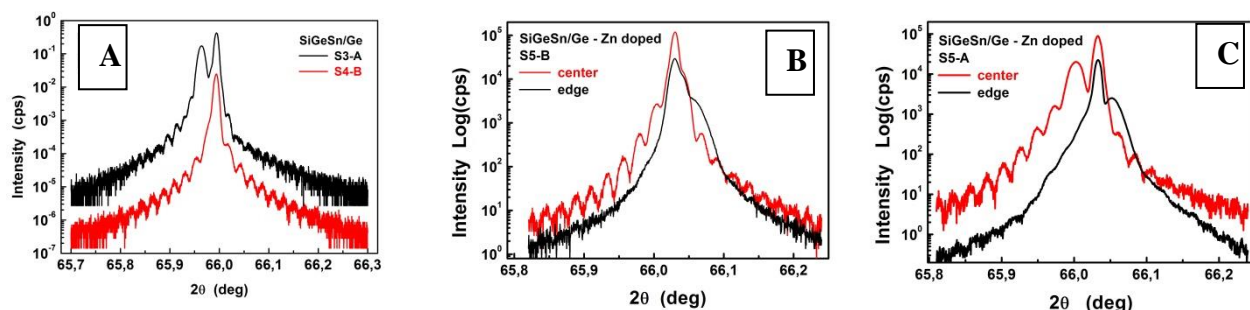


**Figure 61. HRXRD  $\omega$ – $2\theta$  curves measured:** A) in the center of the 4 inch wafer S4-B and of the 6 inch wafer S3-A, B) in the centre and in the edge of the 4 inch wafer S5-B, C) in the centre and in the edge of the 6 inch wafer S5-A.

ADVANCEMENT ON THE MOVPE TECHNOLOGY TO EXPAND BAND GAP ENGINEERING POSSIBILITIES WITH  
THE COMBINED GROWTH OF III-V AND GROUP-IV MATERIALS

**Table 7. Growth rate and composition results on MOVPE SiGeSn deposition in a III-V contaminated reactor**

MOCVD runs	T <sub>growth</sub> (°C)	P <sub>par</sub> IBuGe /GeH <sub>4</sub> (Pa)	Zn dopant	SnCl <sub>4</sub> gas phase comp. (%)	Si <sub>2</sub> H <sub>6</sub> gas phase comp. (%)	GR (nm/m in)	Si from SIMS (%)	Sn XRD sim. (%)	Notes
S1 and S2	460	71(*)	No	1.5	8.8	3	0.5	<0.5	AsH <sub>3</sub> during deposition
S3-B	475	37.8	No	3	13.7	-	-	-	Rough morphology
S3-A	486	37.8	No	3	13.7	5	<2	-	6 inches
S4-A	486	37.8	No	2.9	13.7	-	1.6	0.5-0.6	6 inches
S4-B	490	37.8	No	2.9	13.7	5.2	-	-	-
S5-B	489	37.8	Yes	3	13.7	7.4	2	0.6	Thickness 665 nm
S5-A	491	37.8	Yes	3	13.7	7.4	3	0.7	6 inches
S6	487	37.8	Yes	3	13.7	-	-	-	-
S7-B	490	39	Yes	7.7	36.7	13.4	3	0.9	Thickness 1610 nm
S7-A	500	39	Yes	7.7	36.7	-	-	-	Sn precipitation, 6 inches
S8	487	37.8	Yes	3	13.7	-	-	-	Sn precipitation, deposition in clean growth chamber
S9	487	37.8	Yes	3	13.7	-	-	-	After GaAs/Ge coating
S10	480	37.5	Yes	7.7	36.7	5.5	2	0.55	N <sub>2</sub> Diluting gas in GeH <sub>4</sub>

(\*) The value refers to the IBuGe partial pressure. All runs are on 4 inch wafers, if not otherwise stated in the notes. All runs have been performed with a total carrier gas flow of 12 l/min.

In general, in the center of the samples, HRXRD analysis shows intense interference fringes around the main peak. On the edge of the samples, interference fringes are not observed, showing the presence of stronger compositional gradient at the interface between SiGeSn and Ge substrate. By analysing the HRXRD peaks separation, on 4-inch wafers, a composition non-uniformity better than 1% has been estimated, this value increases to around 3% on 6-inch wafers. The composition non uniformity can be mainly attributed to the non-uniform distribution of Si, as shown by SIMS results depicted in Figure 62, related to the sample S5-A.

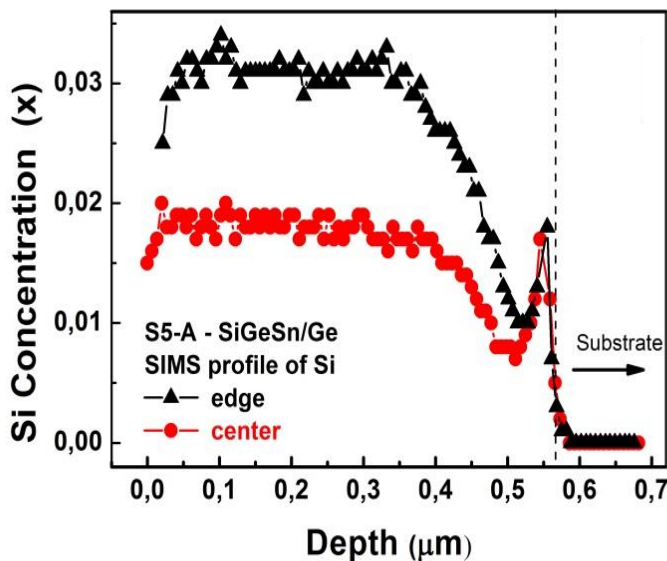


**Figure 62.** Silicon concentration measured by SIMS at the center and at the edge of the 6-inch wafer (S5-A). The sample has been grown with  $\text{Si}_2\text{H}_6$  and  $\text{SnCl}_4$  partial pressure of 6.25 Pa and 1.3 Pa, respectively. The spikes at the  $\text{SiGeSn}/\text{Ge}$  interface are due to a measurement artifact.

Since the deposition on 4 and 6 inch wafers took place in the same MOVPE run, the different uniformity obtained on the two wafers is a limitation imposed by the kinetic growth regime: the gas sources change their residence time as long as they proceed horizontally over the wafer surface, therefore the efficiency of the chemical reaction cannot be uniform along the wafer radius, producing a variation of the thickness and of the layer composition. In principle, a better uniformity can also be obtained on 6-inch wafers by modifying the growth parameters that were optimized for the growth over 4-inch wafers. In particular, in the kinetic regime, a proper temperature gradient imposed over the wafer should help in improving the deposition uniformity.

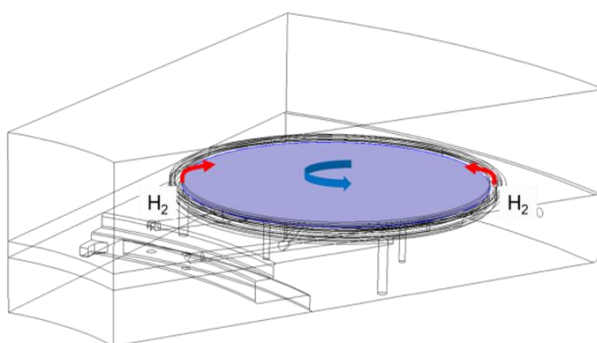


**Figure 63.** Mechanism through which  $\text{H}_2$  from the gas foil rotation is adsorbed on wafer surface and reduces the growth rate on the wafer border. Experiments carried out on Ge showed a thickness non uniformity even of 100% on 6-inch wafer when  $\text{H}_2$  was used in the gas foil rotation.

For this purpose, the MOVPE reactor was set up with a special design of the gas foil rotation, which allowed changing underneath the wafer, in the centre and in the edge, the mixture of hydrogen and nitrogen. Unfortunately at the low temperature necessary for  $\text{SiGe}(\text{Sn})$  growth, the use of hydrogen

in the gas foil rotation has a drawback: as in the case of Si, it passivates the Ge surface and blocks the growth [117], therefore the growth rate at the wafer edge is strongly reduced (see Figure 63). The same growth rate decrease at the edge has been measured on Ge and SiGe growth.

In this case, the use of the special design of the gas foil rotation brings an advantage in the modulation of the temperature over the wafer radius. However, at the same time, a certain reduction of the wafer yield, owing to the reduction of the growth rate at the wafer edge, has to be expected. Alternatively, in order to improve the composition uniformity on 6-inch wafers, the total gas flow can be increased, by accepting a reduction in the precursor's utilization efficiency.

Also the sample S10, grown with  $\text{GeH}_4$  diluted in  $\text{N}_2$  showed an excellent crystal quality clearly evidenced by the high contrast interference fringes in the  $\omega$ - $2\theta$  curve (see Figure 64).

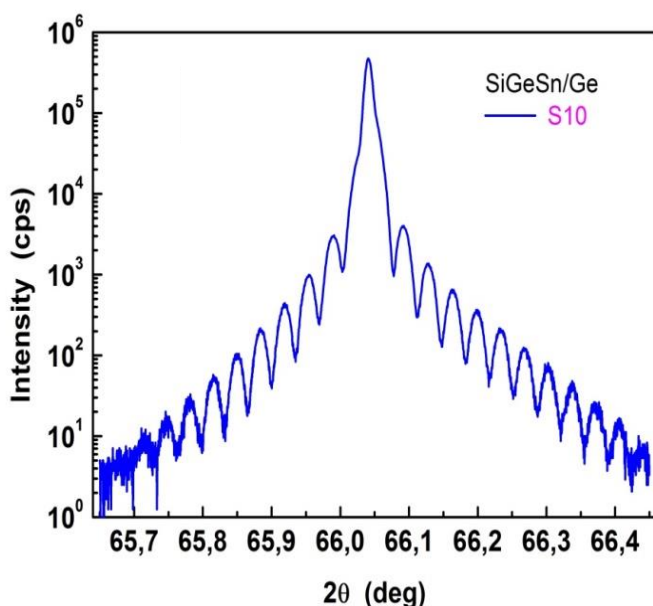


**Figure 64.**  $\omega$ - $2\theta$  curve of S10, showing high contrast interference fringes, demonstrating excellent crystal quality.

#### 5.4.3.2. *Si incorporation in SiGeSn*

If we compare the HRXRD measurements reported in Figure 47, related to sample S2 and in Figure 61B, related to sample S5-B, we may infer that the increment of the deposition temperature from run S2 to run S5-B could have favoured a better composition uniformity along the wafer radius. The shift of the HRXRD peak to higher  $2\theta$  angle, could be due in principle to a higher Si concentration or/and to a lower Sn concentration in SiGeSn, as Si (Sn) incorporation have been reported to increase (decrease) by increasing the growth temperature. However, since Si incorporation exponentially increases with the growth temperature, with an activation energy higher than Sn [118], we are brought to conclude that the distribution of silicon is the main responsible of the worse composition uniformity found on sample S1-S2, in analogy on what has been found for the

sample S5-A and confirmed by SIMS measurements reported in Figure 62. It is worthwhile to point out that the temperature difference between the center and the edge of the sample S5-A was just 2°C, with the edge being at higher temperature. In the kinetic regime, the role of temperature is thus of primary importance concerning the Si<sub>2</sub>H<sub>6</sub> decomposition and the related Si incorporation in SiGeSn. The variation of the Si distribution coefficient (i.e the ratio between the Si in the solid phase and Si<sub>2</sub>H<sub>6</sub> gas phase composition) with the growth temperature has been analysed by considering the samples S1-S2, S4-A and S5-B grown, respectively at 460 °C, 486 °C and 489 °C. The incorporation of Si in kinetic regime is thermally activated following an exponential law, thus we can also write:

$$\frac{x_s}{x_g} = A * e^{-\frac{E_a}{KT}} \quad 5.4$$

Where  $\frac{x_s}{x_g}$  is the ratio between the fraction of Si in the solid phase and Si<sub>2</sub>H<sub>6</sub> gas phase composition,  $E_a$ =activation energy [eV],  
 $K$ = Boltzmann constant = $8.333*10^{-5}$  [eV],  
 $T$  = absolute temperature [K].

By plotting Eq.5.4 we can get the activation energy as reported in Figure 65.

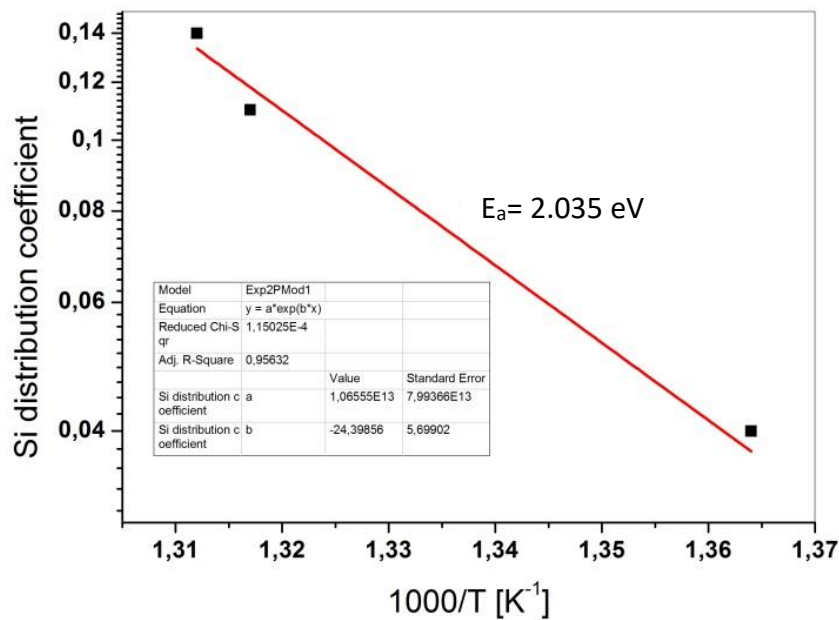


**Figure 65. Silicon distribution coefficient versus temperature. The slope multiplied by  $K*1000$  allows getting  $E_a$ .**

The activation energy value for the incorporation of Si in SiGeSn is higher than the value reported in [103] for Si incorporation in SiGe (2 eV vs 1.56 eV). Therefore, it seems that the incorporation of Si is reduced in presence of SnCl<sub>4</sub>. This hypothesis is confirmed by observing that Si distribution coefficient drops from 0.14 in run S5-B to 0.08 in the run S7-B, despite both MOVPE runs have

been carried out at almost the same temperature ( $489\text{ }^{\circ}\text{C}$  and  $490\text{ }^{\circ}\text{C}$ , respectively), but in which a different amount of  $\text{Si}_2\text{H}_6$  and  $\text{SnCl}_4$  precursors has been used. In run S7-B the quantities of both precursors have been increased with respect to run S5-B. It results that, the higher the  $\text{SnCl}_4$  gas phase composition, the more difficult it is to incorporate Si in the  $\text{SiGeSn}$  layer. The competition between  $\text{Si}_2\text{H}_6$  and  $\text{SnCl}_4$  along with the kinetic growth regime introduce a loss of linearity between the gas phase and the solid composition, which can be inferred by comparing again runs S5-B and S7-B. Between the two runs, the  $\text{Si}_2\text{H}_6$  and  $\text{SnCl}_4$  gas phase compositions have been both increased by a factor approximatively equal to 2.6, however, Si and Sn solid composition have increased only of 50% (Si increased from 2% to 3% and tin from 0.6% to 0.9%).

#### 5.4.3.3. *$\text{SiGeSn}$ morphology*

The surface morphology of  $\text{SiGeSn}$  grown in a III-V contaminated growth chamber has been observed to be strongly temperature dependent, as well as influenced by the level of arsenic As carry-over in the growth chamber and by the growth rate (see Figure 66).

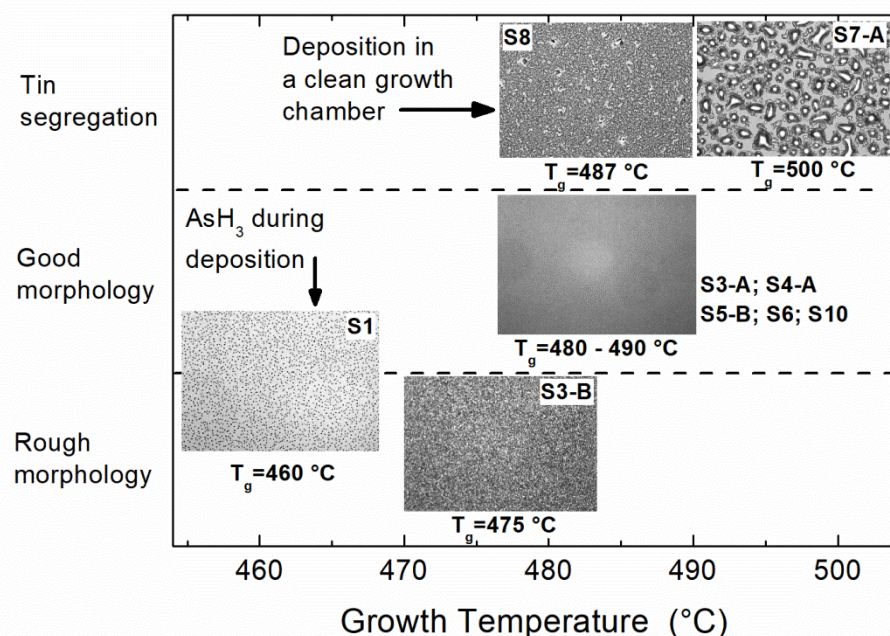


**Figure 66.** Morphology diagram for  $\text{SiGeSn}$  growth with  $\text{GeH}_4$  or  $\text{IBuGe}$  in a III-V contaminated reactor, if not otherwise stated. Images taken at optical microscope with 500x magnification.

At temperatures around  $475\text{ }^{\circ}\text{C}$ , the  $\text{SiGeSn}$  surface becomes rough, while at temperature around  $500\text{ }^{\circ}\text{C}$ , strong Sn segregation appears. Morphology can improve at temperature lower than  $475\text{ }^{\circ}\text{C}$ , as in the case of S1, grown at  $460\text{ }^{\circ}\text{C}$ , if arsine  $\text{AsH}_3$  is injected in the growth chamber during the run, showing the role of As in preventing the morphology deterioration, as better described later.

Perhaps, the more remarkable result is that in the temperature range 480°C-490°C, Sn segregation free samples have been obtained.

A more in-depth morphology analysis carried out by AFM shows, however, that SiGeSn layers grown in the temperature window 480 °C – 490 °C present defects, at different concentration and size, which look like etch pits, correlated with the Sn content in the samples

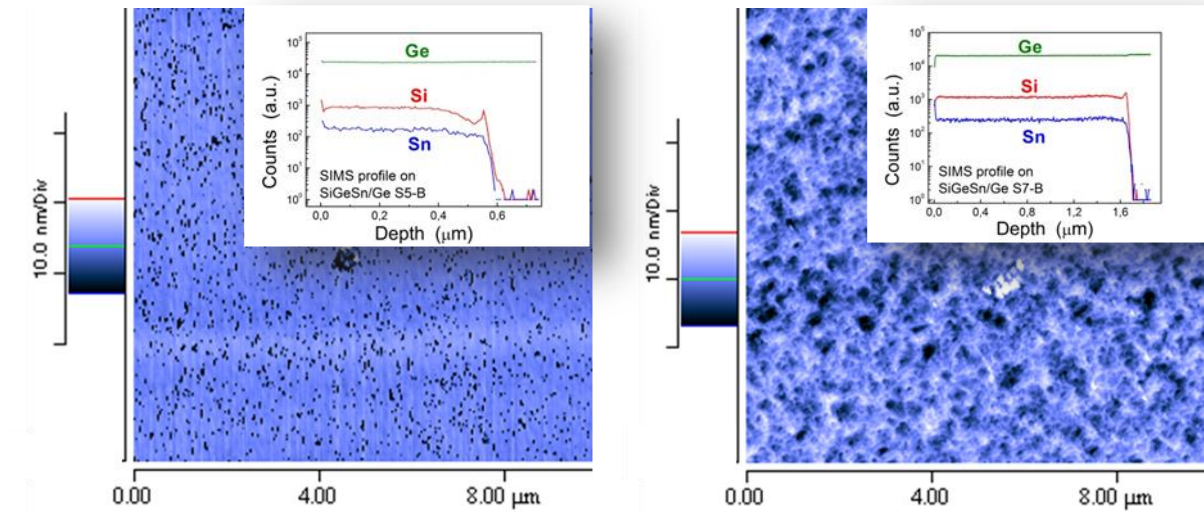


**Figure 67.** AFM images of sample S5-B (left) containing 0.6% of Sn and S7-B (right) containing 0.9% of Sn. In the insets the corresponding SIMS profiles of the Ge, Si and Sn elements

The presence of holes on the SiGeSn surface was also observed by Lupien et al [80] and it was attributed to bulk diffusion of Sn and its evaporation from the surface. Etch pit defects have also been observed on SiGe owing to Ge evaporation from the surface [119]. Since SIMS characterization showed almost constant Sn concentration along the thickness (see Figure 67), Sn could evaporate from SiGeSn surface during the cooling phase of the MOVPE growth run. A sample with a higher Sn content should therefore present a more pronounced evaporation phenomenon and an increase in the “porosity” of the surface. This behaviour is observed and shown by AFM images of samples S5-B and S7-B (see Figure 67). TEM cross section analysis carried out on sample S7-B evidences a defect free and sharp interface between Ge and SiGeSn and that the pores are indeed confined on the surface, presenting different size, especially along the growth axes (see Figure 68).

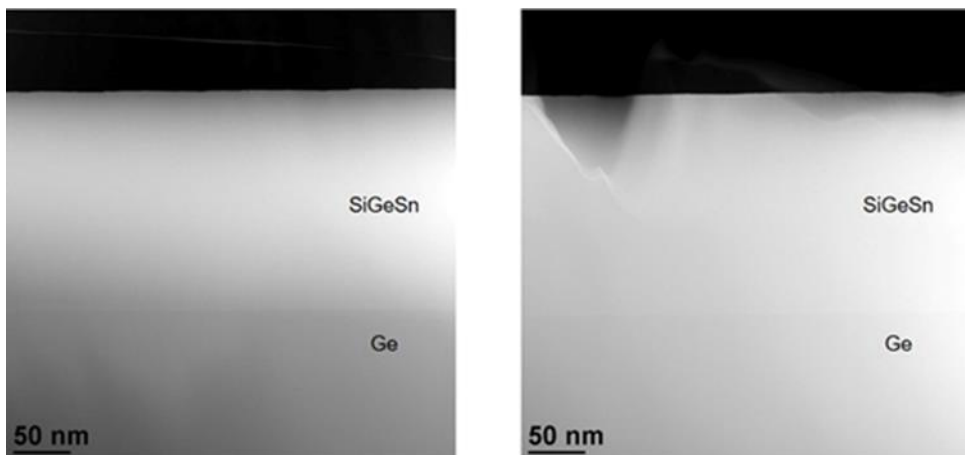


**Figure 68.** Cross section HAADF-STEM images of sample S7-B taken at different regions. The image on the right shows differently sized holes at the surface, as evidenced by AFM in Figure 67.

It seems therefore that such a defect could be avoided by protecting the SiGeSn layer before the MOVPE run cooling stage.

#### **5.4.3.4. *A theory on the role of the bond length of adatoms in inhibiting tin segregation***

Most of the published results on SiGeSn deposition stress the importance of decreasing the growth temperature to values lower than 350 °C in order to avoid Sn precipitation or segregation (see, for example [120], [24] and [121]). More recently a detailed analysis of the influence of SiGeSn morphology as a function of temperature has been reported by R. Khazaka et al [118]. However, one important finding of the experiments shown in Figure 66 is the possibility to get SiGeSn tin-precipitation free even at temperatures around 490 °C. Interestingly, it will be shown that this possibility is linked to the presence of As in the growth chamber, owing to the previous III-V runs. The presence of As in the growth chamber has been indirectly ascertained by measuring the incorporated As in the SiGeSn samples by SIMS as shown in Figure 69.

The inhibiting role of arsenic As for Sn precipitation/segregation was already reported by Nupur Bhargava et al., who introduced arsine AsH<sub>3</sub> during SiGeSn runs [89]. The authors considered the role of As as a surfactant which can suppress the islanding and/or Sn segregation. Hereafter a specific surface-driven mechanism is proposed to explain the experimental results. If we consider that the driving force for segregation is the energy gain obtained when Sn incorporated in the crystal exchanges its position with a Ge adatom on the surface, we can also argue that the presence of As adatoms on the surface could disfavour this process.

By considering that the bond length increases from Ge-Ge (242 pm) to Ge-As (247 pm), the exchange process would then be inhibited, because the compressive strain value reached with Sn segregated on the surface with As adatoms could be higher than that generated with Sn incorporated in the SiGeSn crystal

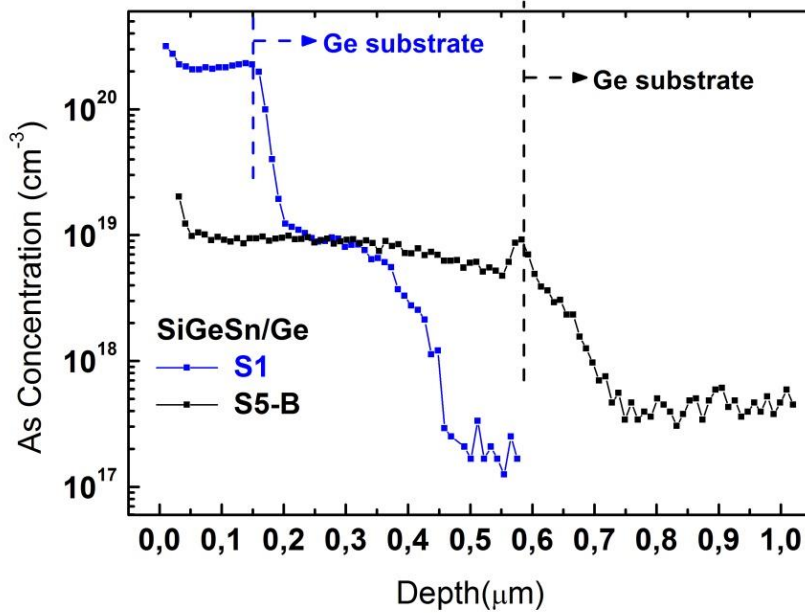


**Figure 69.** SIMS profile of As in SiGeSn samples S1 and S5-B, deposited in a MOVPE growth chamber with a different As carry-over.

Kasper showed that, for low Sn adatom coverage, the Sn surface adatom concentration,  $C_{Sn}^s$ , is linearly linked to the Sn bulk concentration,  $C_{Sn}^b$ , through the segregation length,  $\Delta_s$  [122]:

$$C_{Sn}^s = \Delta_s C_{Sn}^b \quad 5.5$$

Therefore, if we assume that the presence of As adatoms is equivalent to a decrease of the segregation length, since this length is strongly temperature-dependent, and in particular, it decreases by decreasing the temperature (see again [122]), we can conclude that the presence of As adatoms on the Ge surface has the same effect of decreasing the growth temperature.

This stress surface-driven mechanism seems to explain well why it is possible to grow SiGeSn layer Sn segregation free even at temperatures up to 490 °C. Some assessment on the theory has then been carried out. If the bond length of adatoms determines the inhibiting role for Sn precipitation, the use of phosphine (PH<sub>3</sub>) instead of arsine AsH<sub>3</sub> would not be effective, since the bond length of Ge-P is 230 pm. As a matter of fact, when PH<sub>3</sub> is used during SiGeSn growth, Sn segregation is still observed. According to this theory, the use of Sb-based precursors could be more effective than AsH<sub>3</sub>, since the Ge-Sb bond length is higher (266 pm) than the Ge-As bond length. However, since both As and Sb give n-type polarity to SiGeSn, other precursors would have to be searched to get p-type SiGeSn tin precipitation free. Zn could be a p-type dopant for Ge, however, Zn-Ge bond length is 238.38 pm, and again by using DEZn during SiGeSn growth, Sn segregation is still observed. A possible solution could be the use of cyclopentadienylmagnesium (Cp<sub>2</sub>Mg), (C<sub>5</sub>H<sub>5</sub>)<sub>2</sub>Mg, since Mg is a group II element and the bond length of Ge-Mg is 271.9 pm.

It could be speculated that the absence of Sn segregation could be due to the low Sn incorporation measured in the samples, as Sn concentration lower than Sn solid solubility has been measured by

SIMS. However, this hypothesis is contradicted by the fact that when SiGeSn samples are grown at temperatures around 490°C, without As adatoms, i.e. in an arsenic free growth chamber, Sn segregation takes place. The proof of the concept is reported in Figure 70. SiGeSn has been first grown in a clean growth chamber (run S8), that is, with susceptor, satellites and ceiling that did not see any deposition. Then SiGeSn deposition has been repeated (run S9), by keeping unchanged the precursor partial pressures and temperature (controlled in-situ), by preliminary depositing a Ge/GaAs coating run. GaAs was deposited to make available in the growth chamber a source of As atoms, Ge deposition over GaAs was carried out in order to reduce/control the arsenic As in the growth environment. The drastic variation of morphologies of runs S8 and S9 and the segregation of tin Sn only in the sample S8, indicate that an accurate control of the arsenic in the MOVPE growth chamber is indeed of paramount importance to avoid tin precipitation or segregation at the considered deposition temperature.

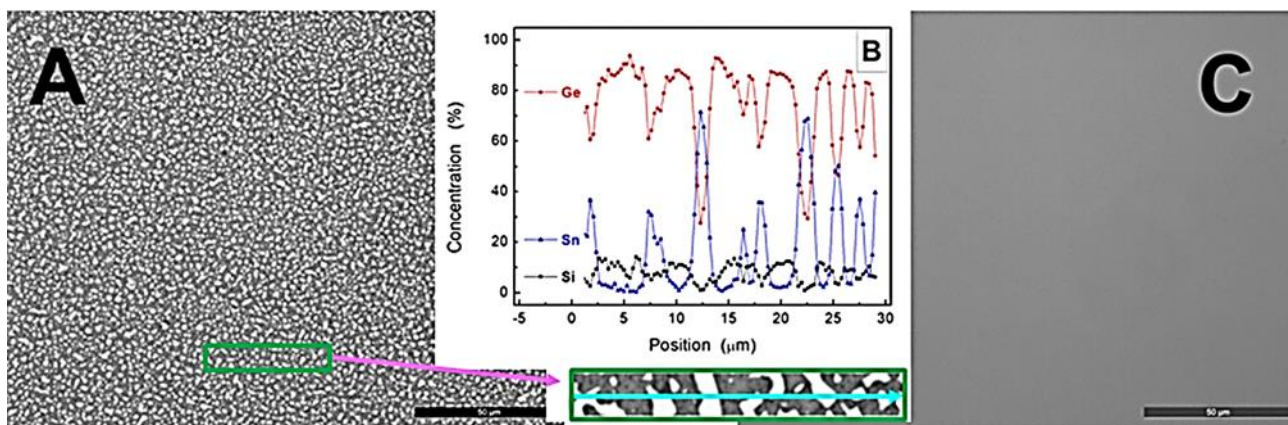


**Figure 70.** Optical microscope images of the morphology of SiGeSn deposited in A) a growth chamber with a clean susceptor and satellites (run S8); C) after GaAs and Ge coating on the susceptor and satellites (run S9). For both MOVPE runs the same growth temperature and gas phase composition have been utilized; B) EDX line scan to assess Sn segregation, carried out on the region of the sample S8 depicted by the SEM image. Sn segregation is absent on sample S9.

It has been assessed that the morphology deterioration takes place from the beginning of SiGeSn deposition. Several samples have been analysed (see Figure 71), also to rule out any possible influence of temperature, growth rate or strain on Sn segregation.

By referring to Figure 71, we can observe that in spite samples S9 and S13 have been deposited at different growth temperature, there is no reflectance deterioration during the deposition. This confirms that the morphology deterioration is not due to any temperature fluctuation, at least in the considered temperature range. On the other hand, in all samples grown in an As-free environment, as soon as the run starts, there is an abrupt change in the reflectivity and a gradual increase of the surface temperature (not a temperature fluctuation but a precise temperature trend, see sample S8, S11 and S12). Since during the deposition, the process temperature has been kept constant, the surface temperature change has to be ascribed to a change in the surface status, as shown by the reflectance signal change. This change of the reflectivity (and of the refractive index) is likely to be due to the start of Sn segregation process.

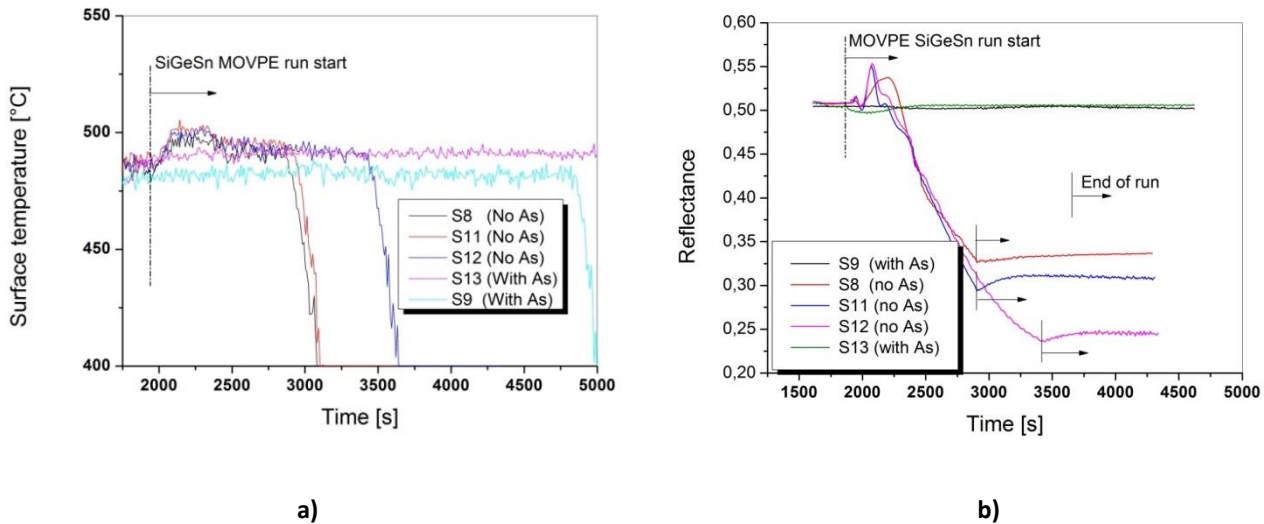


**Figure 71.** Surface temperature a) and reflectance b) measured in-situ during different SiGeSn depositions, carried out in As free or in As contaminated MOVPE growth chamber, as indicated in the legend.

Sn can be incorporated in the crystal or can remain on the surface, depending on what is more energetically favourable. When there is not As adsorbed, it seems that Sn “prefers” to stay at the surface. Then, the layer morphology starts soon deteriorating, as shown by the sharp decrease of the reflectance value. On the other hand, for the samples S9 and S13, grown in As contaminated environment, it is not energetically favourable for Sn segregate at the surface, so Sn has two choices: i) either it stays in the bulk, or ii) it evaporates, (see Figure 72).

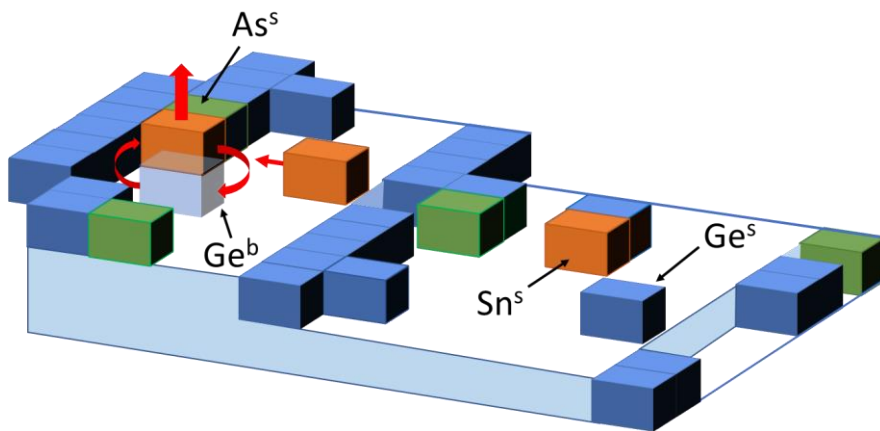


**Figure 72.** Schematic of the surface stress driven phenomenon which avoids Sn segregation. When As atoms are adsorbed on the Ge surface, Sn adsorbed atoms can either replace Ge atoms in the bulk or evaporate.

Therefore, in As contaminated chamber, there is no morphology deterioration, SiGeSn reflectance remains constant for all the run duration, as SiGeSn has a composition very similar to Ge and therefore the refractive index of the two materials are very similar.

It is not therefore surprising that the quality of the grown layers suffered of some structural defects, despite the Sn compositions shown in Table 7 were near to the equilibrium content and therefore these layers were thermodynamically stable. There is no apparent contradiction, because according to the presented theory, the morphology deterioration is not due to an excess of Sn with respect to the equilibrium value but it is rather related to the surface growth mechanism which develops at the beginning of deposition.

Since the samples considered in the comparison have been grown within the same temperature range, with very similar precursor partial pressure, we can rule out any growth rate dependence on Sn segregation. Eventually, as lattice matched samples have been considered, we can also rule out any role of dislocation in Sn incorporation and segregation. Therefore, the observed morphology changes are indeed due to the presence/absence of As in the growth environment.

While other possible pathways to suppress Sn segregation could be considered to explain the experimental results, like, for example, the interaction between the adsorbed As with Sn precursor, if the surface stress-driven mechanism proposed in this thesis were confirmed by the test with  $(C_5H_5)_2Mg$ , this would allow reaching the considerable achievement of producing both p-type and n-type SiGeSn Sn-segregation free at relatively high temperature.

#### 5.4.3.5. *Role of the growth rate in inhibiting tin segregation in SiGeSn*

As anticipated in chapter 5.4.3.3 also the growth rate plays an important role in the determination of the SiGeSn surface morphology. N. Taoka et al. found significant Sn migration and desorption in 200 nm thick SiGeSn samples grown at 350 °C, with a Sn concentration which doubled during the growth process; they concluded that the amount of Sn segregated atoms increases by increasing the thickness [86]. However as shown by SIMS analysis reported in Figure 67, in this study we can point out only a small increase in the Sn concentration in the first 200 nm of SiGeSn deposition, followed by a stable Sn concentration all over the run duration. Moreover, there is no increase of Sn migration by growing thicker samples, in particular passing from run S5-B, 665 nm thick, to run S7-B, 1.61 μm thick. Therefore, what did hinder Sn migration during the SiGeSn growth, in spite SiGeSn samples of this work were much thicker than the samples considered in [86] and were grown with a temperature 140 °C higher?

A possible explanation for the encountered differences could be found by considering the higher growth rate and the lower Sn concentration utilized to deposit the samples S5-B and S7-B: 7.4 nm/min for the run S5-B and 13.4 nm/min for the run S7-B vs 1.6 nm/min utilized by N. Taoka, while Sn was around 1% in samples S5-B and S7-B vs 4.5% in Taoka samples. Of course, the Sn segregation process becomes more and more important as much as we overcome the Sn equilibrium concentration allowed in SiGeSn. However, also J. Margetis et al. reported a quite homogenous Sn distribution throughout the epilayer of GeSn samples even with 7% of Sn in the alloy, deposited at temperature < 450 °C with a growth rate higher than 20 nm/min [110]. Therefore, we are induced to conclude that the growth rate is a key parameter to contrast Sn migration and this could explain why

in spite of the utilization of arsine during the growth, tin precipitation has been observed in run S1, which was carried out at 460 °C but with a growth rate much lower than the sample S5-B (3 nm/min, vs 7.4 nm/min, respectively).

#### 5.4.3.6. *Role of DeZn in increasing SiGeSn growth rate*

Despite Zn is not effective in inhibiting Sn segregation, on the other hand, the use of DEZn helps increasing the growth rate, as shown by comparing the growth rate measured on samples S4-B and S5-A, where for the latter sample, DEZn, with a molar fraction of  $7.8 \times 10^{-6}$ , was introduced in the growth chamber during SiGeSn deposition (see Table 7). The duration of the SiGeSn MOVPE runs have been respectively 120 min and 90 min as shown in Figure 73. SEM cross section has been carried out in order to measure the sample thickness, resulting in a thickness of 621 nm for the sample S4-B and of 649 nm for the sample S5-A. Since runs S4-B and S5-A have been carried out at the same temperature, we can argue that DEZn was responsible for the 38% increase in SiGeSn growth rate. The growth rate increase can be explained by considering the molecule structure of DEZn and its pyrolysis products (see Figure 74). The ethyl groups of the DEZn molecule decompose and methyl radicals CH<sub>3</sub> are formed. They can react with H<sub>2</sub> which comes from the pyrolysis reactions of Si<sub>2</sub>H<sub>6</sub> and GeH<sub>4</sub> and form methane (CH<sub>4</sub>). The methane is then transported to the exit of the growth chamber by the carrier gas.

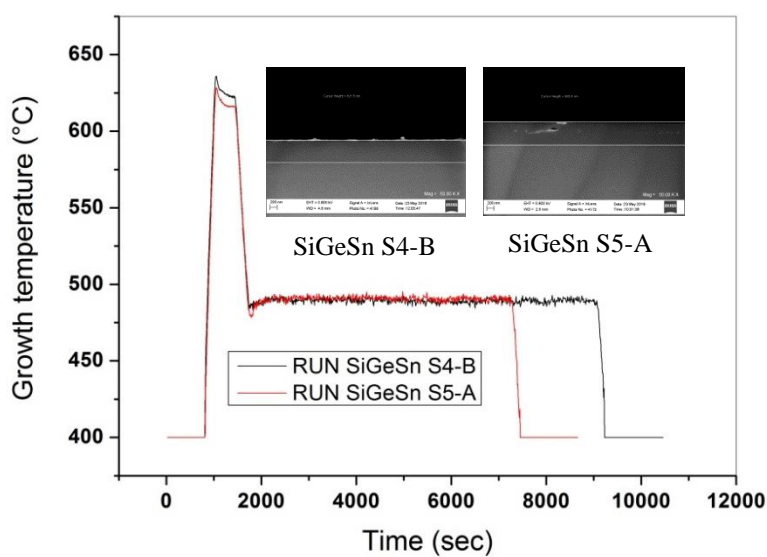


**Figure 73.** Temperature profile and run duration of the MOVPE SiGeSn run S4-B and S5-A. SEM cross sections of the samples are depicted.

This process reduces the concentration of hydrogen atoms which are adsorbed on the surface of the film and are known to hinder the growth process, consequently, there is an increase of the deposition rate. Another possible and complementary explanation could be linked to the reduction of gaseous HCl formed at the growing surface owing to the reaction among SnCl<sub>4</sub>, Si<sub>2</sub>H<sub>6</sub> and GeH<sub>4</sub>. HCl, in fact, is known to be an etchant for group IV elements [112],[123].

Cl atoms, instead of reacting with hydrogen, could react with the methyl radicals and form methyl chloride, Cl-CH<sub>3</sub>, which could also be evacuated by the carrier gas. This chemical process by reducing the HCl etch of the growing surface allows increasing the growth rate.

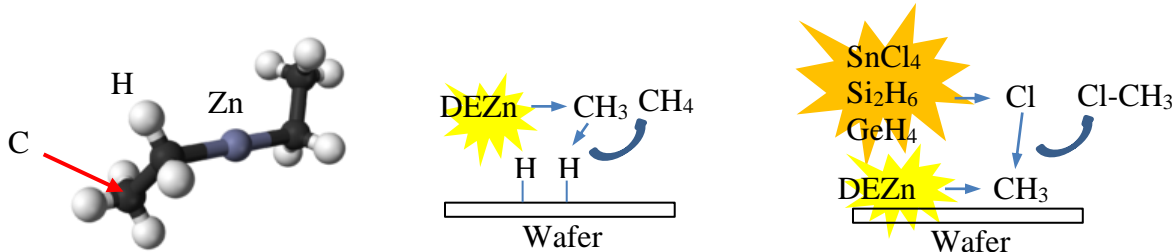


**Figure 74.** On the left, the molecular structure of DEZn: Zn atom is bonded to two ethyl groups, formed by two carbon atoms bonded to five hydrogen atoms. In the center and in the right, the possible mechanisms explaining the growth rate increase when DeZn is used during SuGeSn deoposition.

If the presence of ethyl radicals is the key factor which allows increasing the growth rate, we could also think to replace DEZn with other metalorganic, like, for example, DEGa.

#### 5.4.3.7. *Optical properties of SiGeSn*

The complex dielectric function of sample SiGeSn S5-B (Si = 1% and Sn = 0.6%) has been determined by Ellipsometry and compared to the Germanium one; the best-fit procedure to the experimental spectra with the semiconductor parametric model by WVASE® software gives refractive index and absorption coefficient spectra shown in Figure 75.

The overall SiGeSn spectra have a similar critical point (CP) structure with respect to Ge, with increased CP broadening and a slight blue shift of the E<sub>0</sub> direct bandgap (0.86 eV vs 0.79 eV). An indirect absorption edge should be extrapolated at about 0.62 eV (E<sub>g</sub>); likely owing to the high As incorporation, the absorption coefficient of the SiGeSn sample presents a broad Urbach band tail, and the absorption becomes higher than for Ge below the direct bandgap. It is known that a shrinkage of the bandgap occurs when the impurity concentration is particularly high [124]. Thus a bandgap narrowing effect is expected for the highly As doped SiGeSn, due to the emerging of the impurity band formed by the overlapped impurity states.

For comparison D. Phoebe-Pearce et al.[93] reported E<sub>0</sub> at 0.87 eV for SiGeSn film with similar composition (3% Si, 0.8% Sn); calculations from linear interpolation formulas [125] for the present composition (2% Si, 0.6% Sn) give 0.83 eV to 0.68 eV bandgaps at  $\Gamma$  and L valleys, respectively. The low bandgap of SiGeSn is also due to the diluted nature of SiGeSn layers. In order to get higher bandgap and make the material suitable to be used as a third junction in a four-junction solar cell, an increase of Sn and Si incorporation will have to be accomplished.

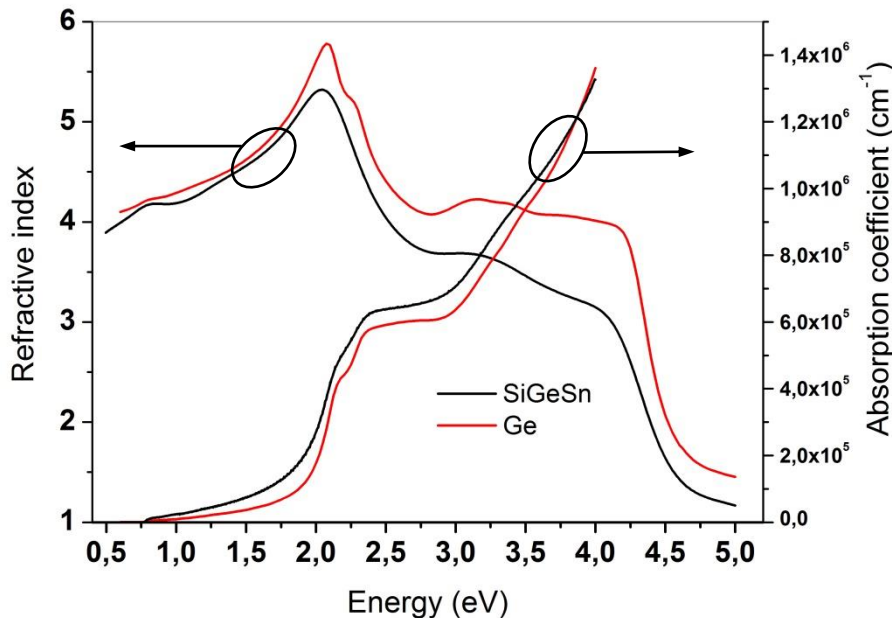


**Figure 75.** Absorption coefficient and refractive index spectra of SiGeSn sample S5-B and bulk Ge.

### 5.5. *Study of the cross-influence between III-V and IV elements deposited in the same MOVPE growth chamber*

As already introduced, the deposition III-V and group IV-based semiconductors inside the same MOVPE growth chamber has been so far hindered by the cross influence between groups IV and III-V elements. There are two main issues to be tackled in order to advance the realization of III-V and group IV-based monolithic architectures in the same MOVPE growth apparatus: i) to control the As “carry-over”, so that the growth of IV-based materials can be carried out without a growth rate penalization, and ii) to adopt proper growth conditions in order to reduce cross doping, so that the conductivities of both III-V and IV-based semiconductors can be modulated. A further issue still to be investigated is whether the cross influence between groups IV and III-V elements can also affect the morphology of III-V and IV-based semiconductors.

After performing the MOVPE hardware change already introduced in chapter 5.1.1, proper growth condition have been searched to face the elencated issues.

In order to reduce the unwanted doping in IV (III-V)-based semiconductors, the growth procedure of depositing on the graphite elements of the MOVPE growth chamber several “coating runs” constituted of IV (III-V) elements materials has been first applied. An average of 1  $\mu\text{m}$  deposition for each coating run has to be considered. After the coating run depositions, the layer under investigation has been grown, the morphology analyzed, the related growth rate and dopant incorporation measured. The possibility to replace some parts of the MOVPE growth chamber over which the deposition takes place has also been evaluated. In particular, the susceptor, the graphite

satellites, the ceiling and the quartz plate have been replaced. The graphite ring, usually operating at lower temperature than the other growth chamber parts, has not been replaced.

### 5.5.1. Control of As carry over and back ground carrier concentration in Ge

In Table 8, the growth rate of Ge deposited on Ge 4 and 6 inch substrates, in a III-V contaminated MOVPE reactor, as a function of several growth parameters, along with the number of IV elements coating runs, is reported. The Ge growth rate related to MOVPE depositions extracted from Table 8 performed with similar germane partial pressure (from 15 Pa to 25 Pa), as a function of the deposition temperature and of the coating runs number is shown in Figure 76.

**Table 8. Ge Growth rate obtained on 4- and 6-inch wafers as a function of growth parameters and of the number of IV-based materials coating runs.**

N Run	T growth (K)	Total flow (l/min)	GeH <sub>4</sub> partial pressure (Pa)	Wafer diameter (inch)	N. of coating runs of IV-based materials after the last III-V growth	Growth rate in the wafer center (nm/min)
S0	773	20.5	5.5	4	1	16
S1	773	21	15	4	2	99
S2	773	20.7	61	6	3	111
S3	773	20.5	22	6	4	100
S4	745	22	20	6	5	91
S5	750	18	25	6	6	119
S6	773	21.6	21	6	9	100
<b>Replacement of growth chamber reactor parts</b>						
S7	748	18	25	4	1	-
S8	748	18	25	4	12	-
S9	748	18	25/2.2	4	13	117
S10	753	18	25	4	21	126 (*)
S11	723	18	25	4	22	(*)
S12	723	18	25	4	24	(*)
S13	748	18	24	4	25	(*)

Note: All the runs have been performed with nitrogen as carrier gas and germane diluted in hydrogen, if not otherwise stated. The growth rate has been measured in the center of the samples. (\*) GeH<sub>4</sub> diluted in N<sub>2</sub>.

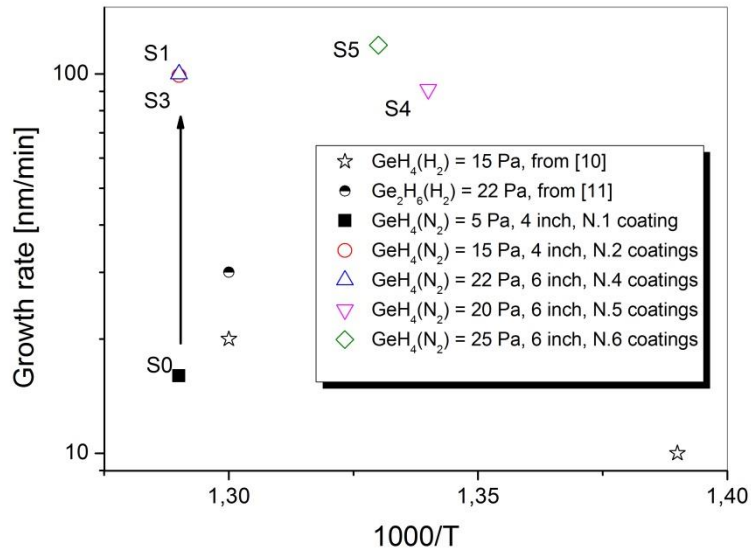


**Figure 76.** Comparison between Ge growth rate data obtained in this work, by using GeH<sub>4</sub> and N<sub>2</sub> as carrier gas, in a III-V contaminated MOVPE reactor (see Table 8) and those reported in ref [76] and [114], where Ge has been grown respectively by GeH<sub>4</sub> and by Ge<sub>2</sub>H<sub>6</sub>, with H<sub>2</sub> as carrier gas.

It can be pointed out that few IV-based material coating runs are enough to obtain high growth rate, as compared with the values reported in literature (see [76] and [113]) related to samples grown at similar temperatures and precursor partial pressure. After already one IV elements coating run, Ge growth rate becomes mainly influenced by the MOVPE reactor geometry (which allows obtaining high germane utilization efficiency) and by other growth conditions, like the use of N<sub>2</sub> as carrier gas instead of H<sub>2</sub>, which improves the growth rate [88].

At this stage, the “As growth blocking role” seems irrelevant, as the growth rate can be easily controlled and optimized, for example, by comparing the runs S4 and S5 where the total flow and the precursors partial pressure have been changed. The evolution of the background carrier concentration related to the samples S1, S2, S4, S7, S8 and S10, nominally undoped, has been measured by electrochemical capacitance-voltage measurements (see Figure 77). In sample S1, a carrier concentration around 10<sup>20</sup>cm<sup>-3</sup>, (likely due to the incorporation of arsenic, see SIMS analysis reported in Figure 82) has been measured at the beginning of the run. This value is reduced to 1-2\*10<sup>18</sup>cm<sup>-3</sup> after 2 μm thick Ge deposition. During Ge growth, the level of contamination is reduced, as germanium is deposited, with different efficiency, on all the growth chamber surfaces (susceptor and ceiling, etc) from which the previous deposited arsenic can evaporate. From sample S1 to sample S4, the carrier concentration drops at the end of the run from 2\*10<sup>18</sup> cm<sup>-3</sup> to 3\*10<sup>17</sup>cm<sup>-3</sup>.

After replacing the susceptor, ceiling, quarts plate and graphite satellites, a significant arsenic contamination is still present at the beginning of run S7, probably due to the residual evaporation of arsenic from the graphite ring, however, this contamination is reduced to 4\*10<sup>16</sup> cm<sup>-3</sup> after 3.5 μm thick Ge deposition

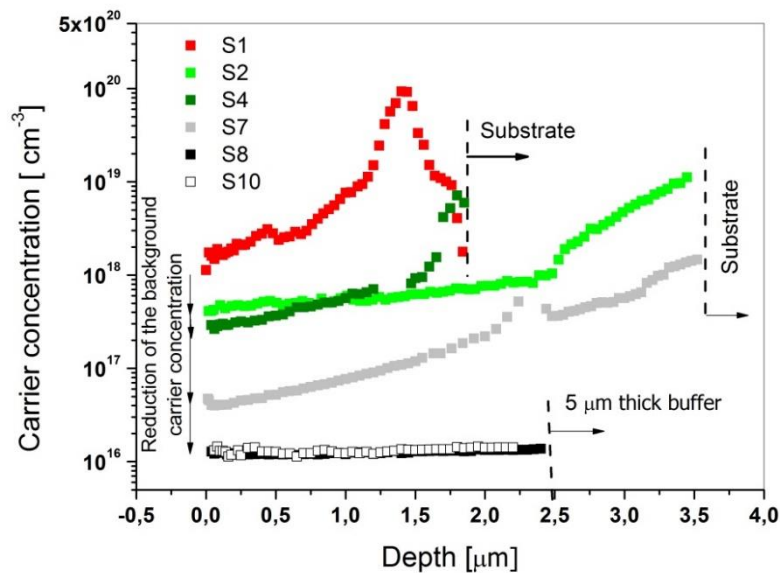


**Figure 77.** ECV n-type carrier concentration in Ge samples grown in a III-V contaminated MOVPE reactor after different Ge and SiGeSn coating deposition. Refer to Table 8

The contamination further decreases to  $1 \times 10^{16} \text{ cm}^{-3}$  in run S8, after a Ge deposition 7.5-8  $\mu\text{m}$  thick. This carrier background value has remained constant even after several further coating runs, as shown by looking at the carrier profile measured in the sample S10 (performed after further 21 coating runs of Ge and SiGeSn layers). It is worthwhile to point out that the background “contamination” is also related to the growth rate, as shown in Figure 78. The first part of S9 has been carried out at high growth rate (117 nm/min), while the second part, with a growth rate one order of magnitude lower (10 nm/min). The back ground carrier concentration increases from  $6 \times 10^{15} \text{ cm}^{-3}$  to  $4.5 \times 10^{16} \text{ cm}^{-3}$  by switching from high to low growth rate.

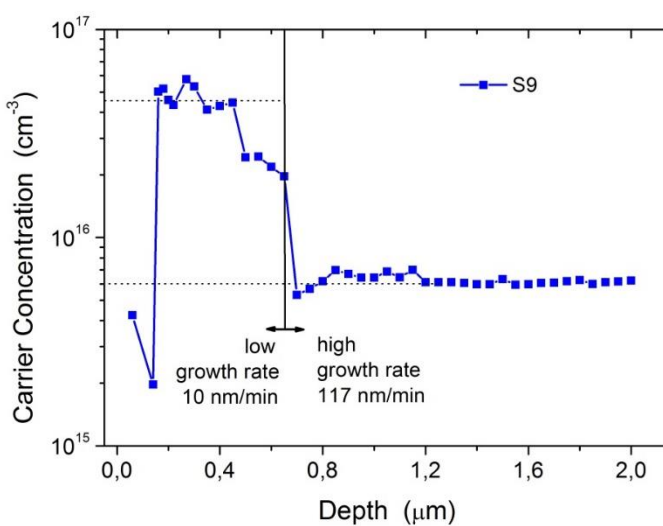


**Figure 78.** Variation of the N-type carrier concentration in sample S9, measured by ECV, as a function of the growth rate. The drop in carrier concentration registered near the surface could be a measurement artefact or it could be explained by the evaporation of the contaminant during the cool down phase of the MOVPE run.

This result can be explained by considering that by increasing the growth rate, the contaminants which are present in the MOVPE growth chamber become much more diluted during the deposition of the material.

Since the growth rate plays an important role in decreasing the back ground carrier concentration, a growth rate optimization has been obtained by a proper selection of diluting gas of the hydrides precursors. By comparing the growth rate values reported in Table 8 for samples S5 and S10, it is possible to point out an increase the growth rate by 6%, without varying the growth temperature (and keeping constant the total carrier flow and the germane partial pressure), just by replacing germane diluted in hydrogen with germane diluted in nitrogen.

Remarkably, by controlling the As carry over, i.e. by reducing the As incorporation in the layers, it is possible to switch Ge conductivity polarity from n-type to p-type as shown in Figure 79.

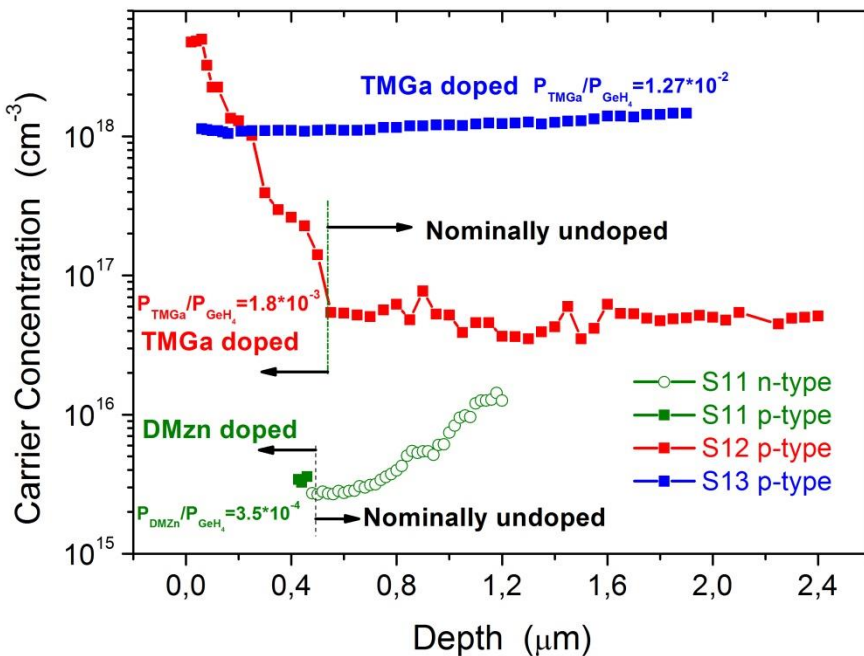


**Figure 79.** N-type and p-type carrier concentration in Ge samples S11, S12 and S13 measured by ECV. The first part of sample S11 (S12) is grown nominally undoped, the last part of the layer is grown by injecting in the MOVPE growth chamber a DMZn (TMGa) molar fraction equal to  $3.5 \cdot 10^{-4}$  ( $1.8 \cdot 10^{-3}$ ). Sample S13 has been grown by injecting a constant TMGa molar fraction equal to  $1.27 \cdot 10^{-2}$ .

The first part of sample S11 has been grown nominally un-doped, then, by injecting in the growth chamber DEZn, with a molar fraction of  $3.5 \cdot 10^{-4}$ , the last part of the sample shows a p-type conductivity, with a carrier concentration around  $2-3 \cdot 10^{15} \text{ cm}^{-3}$ . On sample S12, DEZn has been replaced with TMGa and the dopant molar fraction has been increased to  $1.8 \cdot 10^{-3}$ . Eventually, sample S13 has been deposited with a constant TMGa molar fraction of  $1.27 \cdot 10^{-2}$ . The related ECV characterization shows a constant p-type carrier profile, with a concentration around  $1 \cdot 10^{18} \text{ cm}^{-3}$ . It is worth noting that the doping level of sample S13 is lower than the peak doping level of sample S12, despite a higher input TMGa molar fraction has been utilized for the former sample. This

apparent contradiction is due to the higher growth temperature utilized in the deposition of sample S13 (25°C higher than the one set for the growth of sample S12, see Table 8). The TMGa molar fraction decreases as the temperature increases, because GeH<sub>4</sub> activation energy is higher than TMGa activation energy (41-42 kcal/mole versus 35.4 kcal/mole, respectively). This means that the effective TMGa molar fraction was actually lower in the sample S13 than in the sample S12.

The carrier concentration results related to runs S11, S12 and S13 show that to a large extent it is possible to modulate the p-type doping in Ge even when the IV element semiconductor is deposited in a reactor which is also utilized for III-V growth.

### 5.5.2. Back ground carrier concentration in SiGeSn

For the study of the back ground carrier concentration in SiGeSn, refer to Table 9. SiGe(Sn) depositions, from sample S14 to sample S17, have also been carried out in a III-V contaminated reactor and after several IV-based coating runs.

**Table 9. SiGe(Sn) growth rate obtained on Ge wafers as a function of the growth parameters and of the IV elements coating runs number.**

N Run	T growth (K)	Total flow (l/min)	GeH <sub>4</sub> partial pressure (Pa)	Si <sub>2</sub> H <sub>6</sub> partial pressure (Pa)	SnCl <sub>4</sub> partial pressure (Pa)	N. of coating runs of IV-based materials after the last III-V growth	Growth rate (nm/min)
S14 (SiGe)	748	12	37.9	2.5	NA	33	100
S15 (SiGeSn)	756	12	37.9	6.25	1.34	39	7
S16 (SiGeSn/Ge)	756	12/18	37.9/ 37.9	6.25/0	1.34/0	43	-
Replacement of growth chamber reactor parts							
S17 (SiGeSn)	756	12	37.9	8.12	1.7	1	-

Note: All the runs have been performed with nitrogen as carrier gas and germane diluted in hydrogen, if not otherwise stated. The growth rate has been measured in the center of the samples.

The growth rate of run S14 (SiGe), coherently with the results presented in the previous chapter, is comparable with that obtained on Ge epitaxial samples, even if a higher GeH<sub>4</sub> partial pressure has been utilized. It is worthwhile to point out that an increment in GeH<sub>4</sub> partial pressure is required to compensate the growth rate decrease caused by the injection of Si<sub>2</sub>H<sub>6</sub> in the growth chamber (see Figure 80).

A carrier concentration peak value as high as  $4 \times 10^{19} \text{ cm}^{-3}$  has been measured by EVC on sample S14, deposited after 33 coatings runs (see Figure 81). This value is four times higher than the value measured on sample S4, which was deposited only after five coating runs (see Figure 77). In order to understand the reason behind this result, the IV elements coating runs performed till the sample S14 has been analysed. I came to the conclusion that the background carrier concentration peak value measured in sample S14 could be correlated to the three SiGeSn coating runs sequentially deposited just before the run S14. During SiGeSn growth, in fact, HCl can be formed in the growth chamber by the decomposition products of SnCl<sub>4</sub> and hydrides (Si<sub>2</sub>H<sub>6</sub> and GeH<sub>4</sub>).

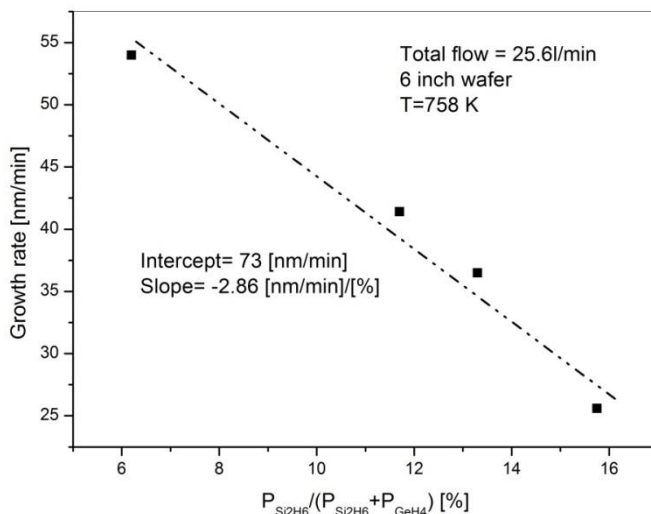


Figure 80. SiGe growth rate as a function of Si<sub>2</sub>H<sub>6</sub> composition in the gas phase.

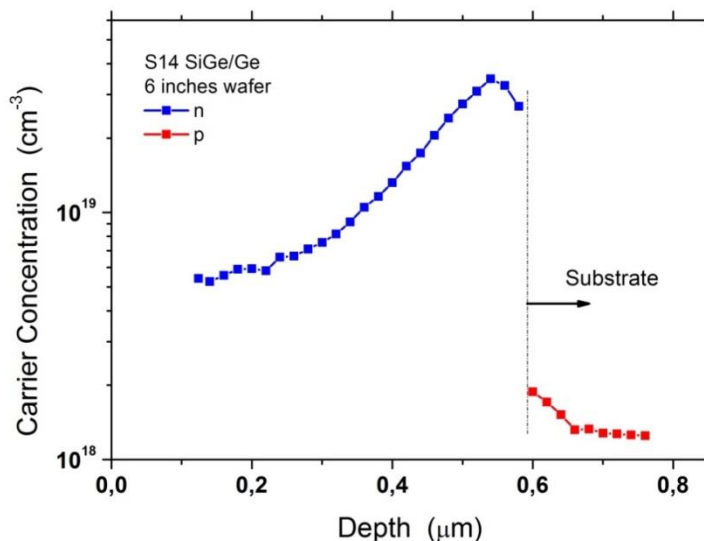
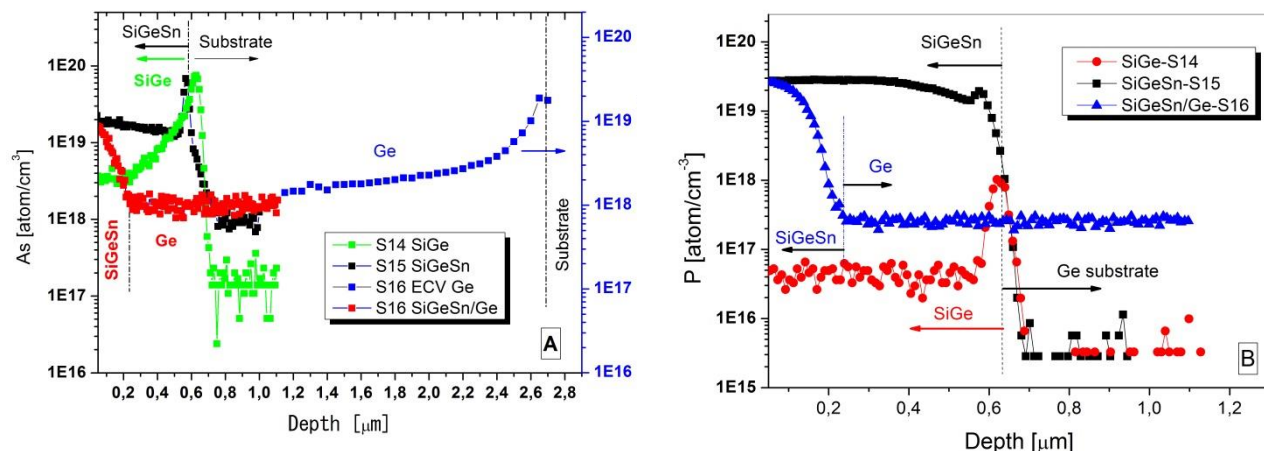


Figure 81. ECV carrier profile measured on the sample S14.

Since HCl is recognized as an etchant for Ge and SiGe [112], during SiGeSn deposition, Ge and SiGe coatings already deposited on the reactor graphite parts could be subjected to chemical etching and, as a consequence, possible evaporation paths for the previous deposited As could be generated.

The presence of a high arsenic concentration in the sample S14 and in the subsequent samples (S15 and S16) has been assessed by SIMS, as shown in Figure 82 A.

Indeed, in all samples a high As incorporation is measured at the beginning of the MOVPE deposition. Since SiGe growth rate is one order of magnitude higher than the SiGeSn growth rate (see Table 9), the As contaminant can be highly diluted in SiGe and its concentration strongly decreases during the SiGe growth, while it remains almost constant in the case of SiGeSn growth



**Figure 82.** SIMS profile of As (A) and P (B) in samples S14, S15 and S16. The As profile of sample S15 has been stopped around 1.1  $\mu\text{m}$  depth. Subsequently, the carrier concentration profile has been measured by ECV.

. The effect of the growth rate on As incorporation is also evidenced on sample S16, composed of a first Ge buffer layer and of a subsequent SiGeSn layer. For this sample, owing to the high thickness, the results of SIMS and ECV measurements are joined in order to show both As and the carrier profile along the sample depth (see Figure 82 A). Like SiGe, Ge deposition takes place at high growth rate, therefore the ECV measurement shows a rapid decrease in the carrier concentration during the deposition. On the contrary, on SiGeSn, SIMS measurement shows that As concentration first sharply decreases and then rises to values as high as  $10^{19} \text{ cm}^{-3}$ .

All these data lead to the following conclusions: i) in a III-V contaminated MOVPE growth chamber, during SiGeSn deposition a considerable amount of arsenic can be re-released from the MOVPE reactor walls and can be incorporated in SiGeSn and subsequent layers, ii) the As contamination can be reduced during the deposition by growing the group IV compounds at high growth rate, around 100 nm/min, while it remains at level around  $10^{19} \text{ cm}^{-3}$  when the growth rate is one order of magnitude lower (10 nm/min).

At this point, it becomes interesting to analyse the reason of the growth rate reduction from run S14 (SiGe) to run S15 (SiGeSn), despite both MOVPE runs have been carried out with the same  $\text{GeV}_4$  partial pressure. Neither the higher  $\text{Si}_2\text{H}_6$  partial pressure utilized in run S15 with respect to run S14, nor the “As growth blocking role” can explain the reduction in growth rate. In fact, referring to the data shown in Figure 80, an increase of  $\text{Si}_2\text{H}_6$  partial pressure from 2.5 Pa to 6.25 Pa can only explain a 20% decrease in the growth rate. Furthermore, the same starting As contamination has

been measured in SiGe and SiGeSn (see Figure 82 A). This means that As “carry-over” have saturated SiGe and SiGeSn surface sites in the same way. The low growth rate of SiGeSn can still be understood by considering the etching action on Ge and SiGe produced by HCl, as formed by the decomposition products of SnCl<sub>4</sub>, Si<sub>2</sub>H<sub>6</sub> and GeH<sub>4</sub>. The contrasting actions between the deposition rate and the etching rate has also been observed in GeSn growth by GeH<sub>4</sub> and SnCl<sub>4</sub> [126].

In order to reduce the weight of the etching action, a higher germane partial pressure could be used. For example, S.Wirths at al., have shown that it is possible to reach SiGeSn growth rates as high as 125 nm/min with a Ge<sub>2</sub>H<sub>6</sub> partial pressure of 120 Pa (a value four time higher than the GeH<sub>4</sub> partial pressure used to grow the samples of this study) [87]. Therefore, in principle, by increasing SiGeSn growth rate it should be possible to reduce the As background concentration near the value obtained in Ge and SiGe.

However, there is a further difficulty in controlling SiGeSn conductivity, due to the presence of impurities in SnCl<sub>4</sub> precursor. This is evidenced by SIMS analysis related to P incorporation in the samples S14, S15 and S16 as shown in Figure 82 B. It can be pointed out that in run S14 (SiGe) and in the first part of run S16 (Ge growth), where SnCl<sub>4</sub> is not used, a P concentration, respectively, around  $4 \times 10^{16}$  cm<sup>-3</sup> and  $3 \times 10^{17}$  cm<sup>-3</sup> has been measured, instead, during the growth of SiGeSn (S15), P concentration increases to  $3 \times 10^{19}$  cm<sup>-3</sup>.

Thus, we can conclude that by using SnCl<sub>4</sub>, a considerable amount of P is introduced in the growth chamber. Like As, P introduces electrons in IV-based compounds and therefore it influences the material’s conductivity. The P contamination of the growth chamber produced by SnCl<sub>4</sub> allows explaining the higher P concentration measured in Ge, in run S16, than in SiGe, in run S14. Ge deposition, in fact, has been carried out after SiGeSn growth (S15).

During SiGeSn deposition, P is introduced in the growth chamber, can be deposited on the MOVPE reactor walls and then subsequently be released and be incorporated in Ge during the growth. Therefore, for controlling SiGeSn conductivity, regardless the contamination introduced from the previous III-V deposition, it is important to reduce the amount of P contained in SnCl<sub>4</sub>, or to consider alternative precursors, like, for example, TESn (Triethyltin) as, reported for the growth of GeSn [127].

### 5.5.3. Back ground carrier concentration in III-V compounds

I did not observe any III-Vs growth rate change owing to the previous IV elements growth. Therefore, I have focused the investigation on how to control the III-Vs conductivity, trying to reduce to acceptable levels the IV elements contamination in III-Vs. The III-Vs structures analyzed are reported in Table 10.

ADVANCEMENT ON THE MOVPE TECHNOLOGY TO EXPAND BAND GAP ENGINEERING POSSIBILITIES WITH  
THE COMBINED GROWTH OF III-V AND GROUP-IV MATERIALS

**Table 10.** Growth condition related to III-Vs deposition in a MOVPE growth chamber contaminated by IV elements.

N Run	T growth (K)	Total flow (l/min)	Growth rate (nm/min)	N. of coating runs of III-Vs after the last IV-based growth	Substrate
S18 (AlAs/GaAs DBR)	888	12	40/40	1	GaAs
S19 (AlAs/GaAs DBR)	888	12	40/40	8	GaAs
S20 (InGaP/InGaAs/ InGaP)	773/903/903	12	11/200/9.1	20	Ge and GaAs
S21 (InGaAs/InGaAs/ InGaP)	773/903/903	12	66/200/9.1	31	Ge
S22 (GaAs/AGaAs/ GaAs)	764	12	-/28.3/-	1 (*)	Ge and GaAs

Note: (\*) after SiGeSn deposition

MOVPE runs S18 and S19 are related to AlAs/GaAs distributed Bragg reflector (DBR) structures, whose period has been repeated 15 times. These samples have been deposited in mass transport regime ( $T_{growth} = 888$  K) after one and eight III-V coating runs, respectively

In Figure 83, SIMS concentrations of Ge, Si and Sn, measured along the thickness of the samples S18 and S19 are depicted.

The incorporation of Ge, Si and Sn is different in AlAs and GaAs, therefore, along the DBR structure thickness, the concentration of these atoms oscillates. After one coating run, the maximum group IV elements concentration in the III-V Bragg test structure is around  $5 \times 10^{17}$  cm<sup>-3</sup>. After eight coating runs (with an equivalent deposition of 8 μm thick III-Vs), the maximum background contamination is reduced to values lower than  $2 \times 10^{17}$  cm<sup>-3</sup>. This value is more than half of the previously reported value measured in GaAs ( $4.6 \times 10^{17}$  cm<sup>-3</sup>), in a Si-Ge MOVPE contaminated growth chamber, after a 10 μm thick coating run [128].

In order to further reduce IV elements incorporation in III-Vs, the influence of the growth temperature on the background carrier concentration has been assessed. The evaporation of the contaminants from the MOVPE reactor walls is tightly related to the growth temperature and, in particular, by decreasing the growth temperature, the background IV elements concentration in III-V semiconductors is expected to be reduced.

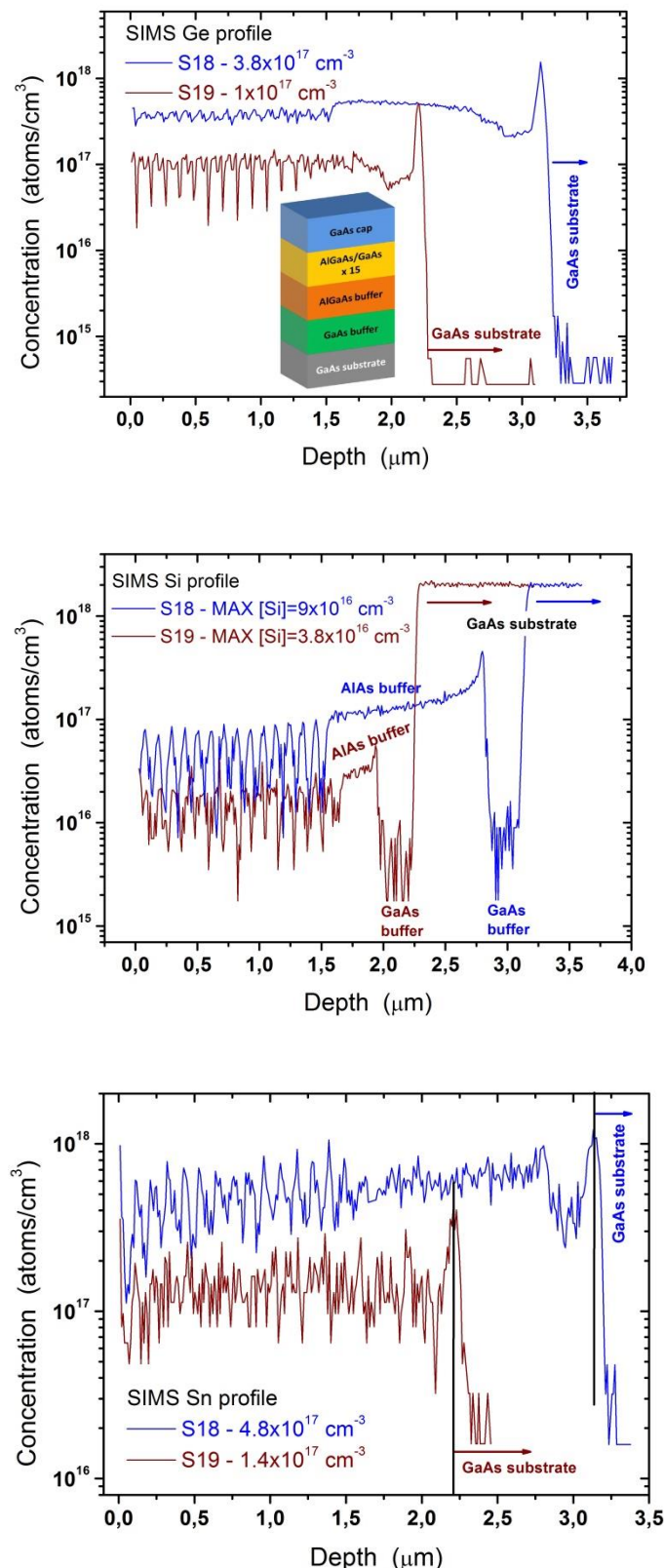


**Figure 83.**SIMS profile of: Ge, Si and Sn in samples S18 (deposited after one III-V coating run) and S19 (deposited after eight III-V coating runs). In the inset, the DBR structure is shown.

Two test structures have been investigated: i) InGaP/InGaAs/InGaP/Ge(GaAs) structure (S20), in which the bottom InGaP and InGaAs layers have been deposited at 903 K, while InGaP top layer has been deposited at lower temperature (773 K), ii) structure S21, where the growth process of run S20 concerning the InGaP and InGaAs bottom layers has been replicated, while the InGaP top layer has been replaced by the InGaAs one. For both samples, the IV elements concentration has been indirectly measured by ECV, as shown in Figure 84. It is worthwhile to point out that the MOVPE deposition of sample S20 and S21 have been carried out after 20 and 32 III-V coating runs, respectively.

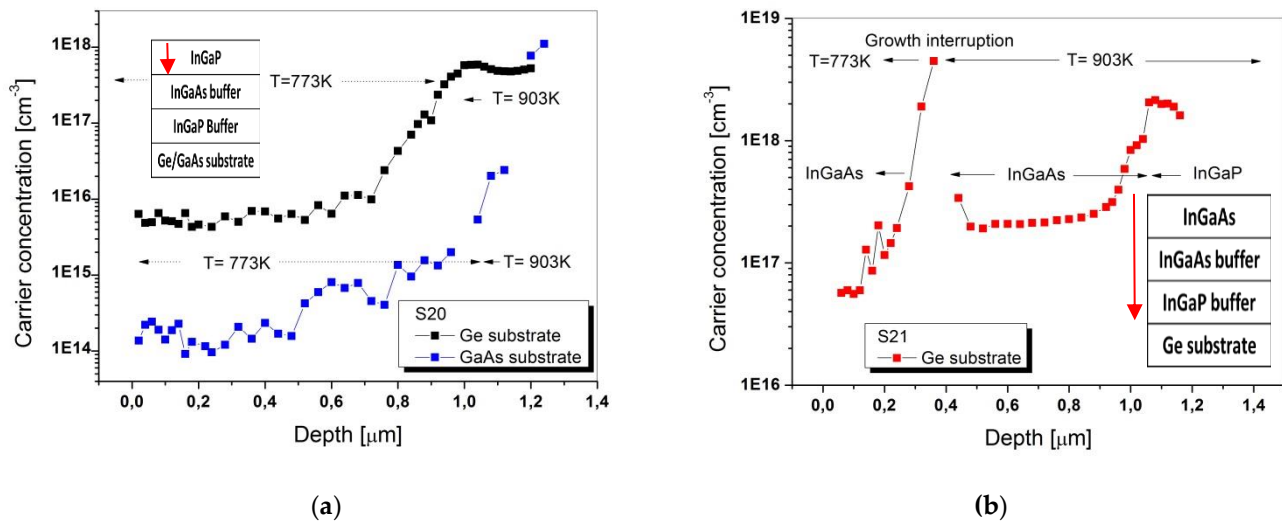


**Figure 84.** ECV Profile on: (a) sample S20 and (b) on sample S21 In the insets, the structures investigated are depicted. The arrows indicate the etching depth.

On sample S20, a starting background carrier concentration near  $1 \times 10^{18} \text{ cm}^{-3}$  has been measured when the material is grown at 903 K on Ge substrate. After depositing 1  $\mu\text{m}$  of InGaP at 773 K, the background carrier concentration is reduced to  $6 \times 10^{15} \text{ cm}^{-3}$ , a value around three order of magnitude lower than the value measured by E. Welser, in InGaP layers grown in a Ge-contaminated MOVPE growth chamber [27]. This comparison confirms the key role of the growth temperature for decreasing the incorporation of IV elements contaminants in III-Vs. By growing InGaP on a GaAs substrate, the carrier concentration can be further reduced by an order of magnitude, down to  $3 \times 10^{14} \text{ cm}^{-3}$ . By using a GaAs substrate, in fact, the Ge auto-doping and Ge solid state diffusion that take place during the InGaP growth on a Ge substrate can be both suppressed [129].

A strong decrease in the background carrier concentration owing to the reduction of the growth temperature has also been measured on sample S21 (see Figure 84 B). During InGaP nucleation, which takes place at 903 K, the starting carrier concentration level is as high as  $2 \times 10^{18} \text{ cm}^{-3}$ . During the InGaAs deposition carried out with a growth rate twenty-four times higher than the InGaP one, the level of contamination is reduced to  $2 \times 10^{17} \text{ cm}^{-3}$ . As soon as the growth is stopped, before the temperature ramping, there is an accumulation of contaminants on the sample surface. Eventually, after the growth of 0.4  $\mu\text{m}$  InGaAs at 773 K, the carrier concentration sharply decreases to  $6 \times 10^{16} \text{ cm}^{-3}$ . This value is still higher than the value measured in the top InGaP layer of sample S20,

because the top InGaAs layer of sample S21 has been deposited with a thickness which is more than half of the InGaP one.

It is interesting to compare the background carrier concentration measured at the end of InGaAs layer grown at higher temperature on the sample S21 with the IV elements atoms concentration measured by SIMS on sample S19 (see Figure 84 B and Figure 83). These values are almost equal, showing that after 8  $\mu\text{m}$  thick III-V coating deposition, the subsequent III-V coatings are not effective in further reducing the background carrier concentration.

Therefore, it can be concluded that in a IV elements contaminated reactor, it is possible to reduce under  $1*10^{16} \text{ cm}^{-3}$  the residual IV elements contamination in III-Vs compounds, by depositing a 8  $\mu\text{m}$  thick buffer and then by reducing the growth temperature to value around 500 °C.

#### 5.5.4. Morphological aspects

The effect of the cross influence between group IV and III-V elements on the morphology and crystal structure of III-V and IV-based semiconductors has been assessed. As shown in Figure 85,



**Figure 85. Optical microscope characterization of sample S12. Magnification 500 X. The surface is featureless.**

Ge surface morphology does not degrade when Ge is grown in a III-V contaminated MOVPE reactor. The surface morphologies of Ge layers are excellent and the best ones have been obtained when Ge is doped with Gallium (sample S12). Similar morphological results have been obtained for SiGe. On the other hands, as already shown S5.4.3.4, SiGeSn morphology has been found strongly dependent on the level of As contamination in the MOVPE growth chamber.

Concerning III-Vs semiconductors, it has been found that when they are deposited in a IV elements contaminated MOVPE growth chamber their morphology changes as a function of the substrate type and orientation. On sample S20, for example, the top InGaP layer, deposited at low temperature, presents a featureless morphology on GaAs substrate and different oriented defects on Ge substrate (see Figure 86).



**Figure 86.** Run S20 InGaP morphology on (a) on Ge substrate and (b) on GaAs substrate. Magnification 500 X.

Regardless of the growth temperature, III-V's morphology on Ge substrate strongly degrades in Sn-contaminated MOVPE growth chamber, eventually leading to a polycrystalline material. For example, the structural characterization of a AlGaAs/GaAs/AlGaAs hetero-structure, deposited on Ge and GaAs substrates in a Sn-contaminated MOVPE growth chamber is depicted in Figure 87.

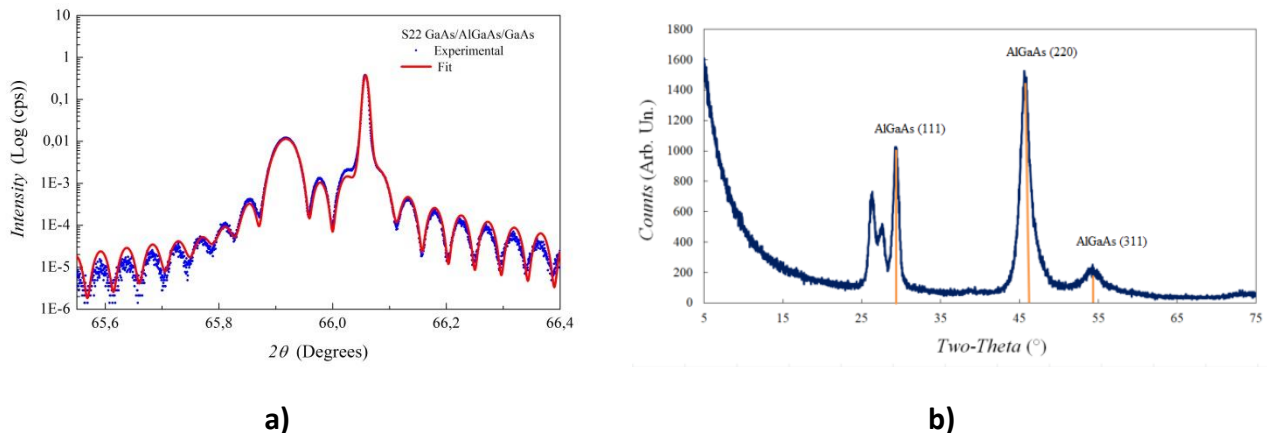


**Figure 87.** GaAs/AlGaAs/GaAs XRD and GIXRD characterization, (a) XRD characterization on GaAs substrate, the intense interference fringes are an index of the sharpness of the interfaces i.e. of their low roughness morphology, (b) GIXRD characterization on Ge substrate, showing the polycrystalline nature of the deposited layer.

The results reported in Figure 87 could be explained by assuming that during the heating phase of the MOVPE run, Sn evaporates from the reactor walls and can be adsorbed on the substrate surface at different concentrations according to the substrate orientation. In particular the Ge (100) 6° off towards <111> orientation has more steps and kinks, where Sn can be adsorbed, than GaAs (100), 2° off towards <110> orientation. If Sn adsorbed somehow disturbs the atoms incorporation in the crystal, the epitaxial growth could be prejudiced on substrates whose orientation favours Sn adsorption. In order to confirm this hypothesis and exclude the influence of the chemical nature of the substrate, further experiments will have to be performed by considering the deposition of III-Vs on Ge substrates with the same orientation of the GaAs ones.

## 6. Towards the realization of all MOVPE grown 4J InGaP/InGaAs/SiGeSn/Ge solar cells

*To investigate the photovoltaic behaviour of SiGeSn, deposited in a III-V contaminated growth chamber, a single-junction GaAs/InGaP/SiGeSn/Ge functional device has been manufactured and characterized by external quantum efficiency (EQE) and current-voltage measurements. The experimental data have been fitted confirming the higher absorption coefficient of SiGeSn with respect to Ge, as measured by Ellipsometry in chapter 5. By applying the new mathematical approach developed in chapter 3, I perform several simulations in order to evaluate the potential of the InGaP/InGaAs/SiGeSn/Ge MJ solar cells. For the first time the performance of thin quadruple junction (QJ) InGaP/InGaAs/SiGeSn/Ge solar cells, in two (2T) and three terminal (3T) configurations are compared. Efficiency values up to 45.1% and 44.9%, respectively, have been simulated at 1000 X concentration, by considering the MJ limited by the InGaAs sub-cell. Finally, it is estimated that the QJ InGaP/InGaAs/SiGeSn/Ge solar cell has the potential to reach efficiencies over 50% by assuming proper antireflective coatings.*

### 6.1. Realization and characterization of GaAs(n-type)/InGaP(n-type)/SiGeSn(n-type)/Ge(p-type) heterojunction.

During the collaborative European project CPV Match, a preliminary integration of SiGeSn with III-Vs has been accomplished by manufacturing a GaAs(n-type)/InGaP(n-type)/SiGeSn(n-type)/Ge(p-type) heterojunction. In this preliminary test, SiGeSn has been grown in a III-V contaminated reactor, while the deposition of subsequent InGaP and GaAs layers have been accomplished with the collaboration of another partner who carried out the deposition by using another MOVPE growth apparatus. The main purpose of this experiment was to investigate the photovoltaic behaviour of SiGeSn deposited at the same growth condition of sample S5-B (i.e in a As contaminated reactor), whose optical properties were already investigated in chapter 5.4.3.7. Over SiGeSn, a InGaP layer, 65 nm thick, has been further deposited in the attempt to passivate the SiGeSn emitter. Eventually a GaAs layer, 0.4  $\mu\text{m}$  thick, has been grown on top of the structure in order to improve the ohmic contact. In order to simplify the manufacturing process, this cap layer has not been removed from the front side of the device, so it also behaves like a light filter. The cell structure has been finally coated with a  $\text{SiO}_2/\text{Ta}_2\text{O}_5$  stack. For the front and back contacts, Ti/Au/Ag/Au and Zn/Au/Ag/Au have been deposited with a total thickness of 4  $\mu\text{m}$  and 2  $\mu\text{m}$ , respectively. A sketch of the SiGeSn/Ge based device and a SEM cross section of the MOVPE structure are depicted in Figure 88.

The SiGeSn/Ge based device has been characterized by external quantum efficiency (EQE) and current-voltage (IV) measurement, the later characterization was carried out from 1 sun to 173 suns, under AM1.5D spectrum.

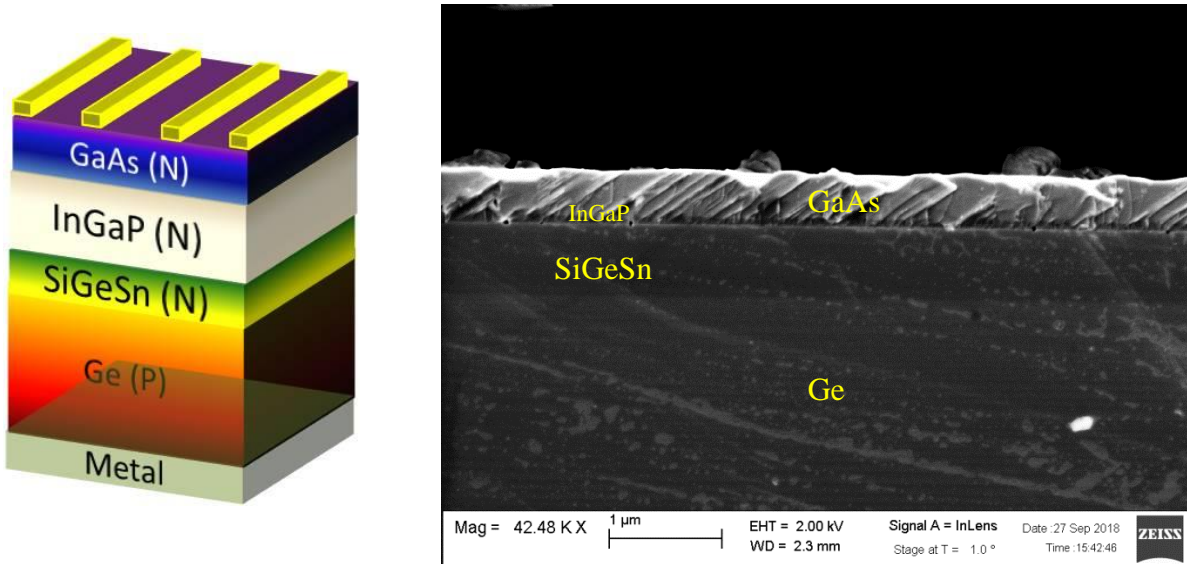


**Figure 88.** On the left, a schematic representation of the SiGeSn/Ge based device; on the right, the SEM cross view of the MOVPE structure (metals deposition are not included as realized by e-beam evaporation).

EQE and IV data have also been fitted to extract some solar cells parameters. For the simulation of EQE, the scattering matrix method and the simplified solution of the continuity equation, as developed in chapter 1, have been applied.

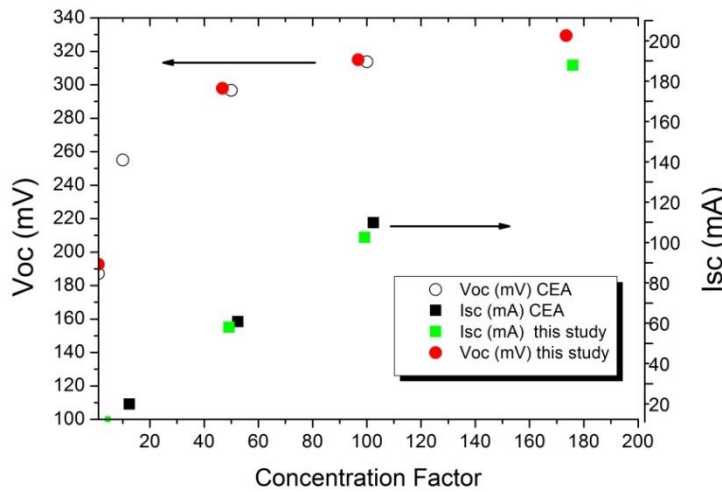
Only SiGeSn and Ge have been considered as active PV layers. In fact, at the interface between SiGeSn and InGaP an energy band discontinuity is formed so that the minority carriers generated in GaAs cannot be collected at the junction (see Figure 90). On the other hand, the carrier generation in InGaP can be considered negligible, owing to GaAs absorption. The simulated EQE data are in good agreement with the experimental ones, if we consider the following approximations: i) for the optical properties of InGaP and GaAs layers, literature data have been used, ii) in the reflectance modelling, the surface and interfaces have been considered optically flat, while the cell surface was somewhat rough (as shown in Figure 88) and light scattering was produced.

The IV curve data at different concentration value are reported in Table 11.

A Round-Robin campaign has been carried out on the electrical parameters measured at different concentration factor [130] in order to confirm the experimental data, as reported in Figure 89

**Table 11. SiGeSn/Ge based device IV data measured under AM1.5 D spectrum at different concentration level.**

	IV Characterization AM1.5D			
Suns	1	47,1	90,7	173,4
Voc (V)	0,197	0,294	0,312	0,327
Jsc (mA)	1,040	49,002	94,323	180,390
Jsc/X (mA)	1,040	1,040	1,040	1,040
FF	0,620	0,673	0,659	0,618

**Figure 89. Voc and Isc data from the IV measurements performed, on the SiGeSn/Ge based device, in this study and at CEA for sake of comparison. The device shows good linearity.**

The IV curve at 50 suns has then been successfully simulated by using the EQE data and a triple diode model (see 6.1 and Figure 91), whose pre-exponential terms, for the diffusion ( $J_0$ ), recombination ( $J_{rec}$ ) and tunnelling ( $J_{tun}$ ) current density, along with the series ( $R_s$ ) and shunt ( $R_{sh}$ ) resistance assumed, respectively, the following values:  $J_0=6.7 \times 10^{-6} \text{ A/cm}^2$ ,  $J_{rec}=1.53 \times 10^{-7} \text{ A/cm}^2$ ,  $J_{tun}=2.5 \times 10^{-5} \text{ A/cm}^2$ ,  $R_s=0.15 \Omega$  and  $R_{sh}=1100 \Omega$ .

$$I = J_{ph} \cdot A_{att} - J_{01} \cdot A_{tot} \left( e^{\frac{q(V+I \cdot R_s)}{KT}} - 1 \right) - J_{02} \cdot A_{tot} \left( e^{\frac{q(V+I \cdot R_s)}{2KT}} - 1 \right) - J_{03} \\ \cdot A_{tot} \left( e^{B(V+I \cdot R_s)} \right) - \frac{V + I \cdot R_s}{R_{sh}} \quad 6.1$$

Apart the usual terms and those already introduced:

$A_{att}$  = PV active area =  $0.0521 \text{ cm}^2$

$A_{tot}$  = total device area =  $0.0712 \text{ cm}^2$

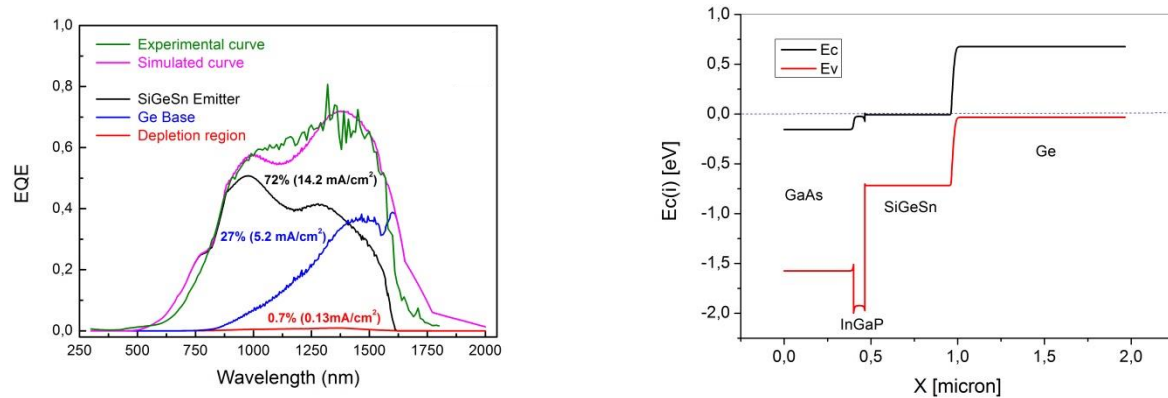


**Figure 90. a)** EQE data and simulated curve. The contribution the overall current produced by each layer has been calculated by integrating the simulated EQE with AM1.5D spectrum (the surface recombination velocity between InGaP and SiGeSn is  $10^5$  cm/sec); **b)** energy band diagram of the GaAs/InGaP/SiGeSn/Ge heterojunction. The holes generated in GaAs have to overcome a barrier of about 0.48 eV to be transferred in the SiGeSn emitter, this means that these carriers cannot reach the junction.

B = exponential coefficient term of the tunnelling current =  $\frac{8\pi}{3h} \sqrt{\frac{m^*\epsilon}{N_d}} = 26.2$  (value introduced for the best fit of the experimental data)

Where:

$h$  = Plank constant,

$m^*$  = effective mass

$\epsilon$  = dielectric constant

$N_d$  = donor atoms concentration =  $10^{19}$  cm<sup>-3</sup> ( measured by ECV)

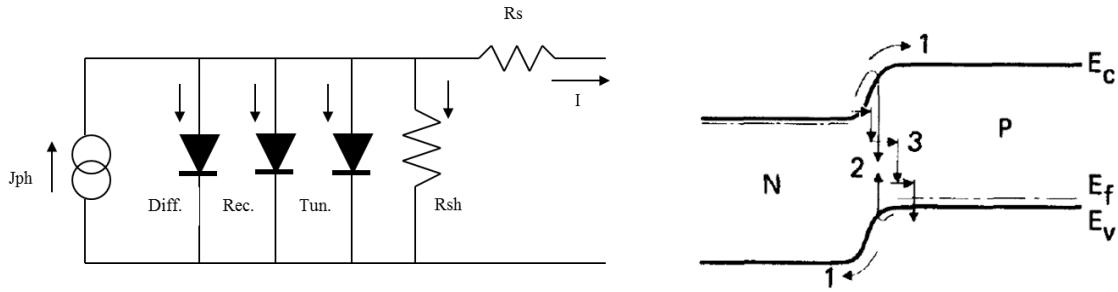


**Figure 91.** On the left, the equivalent electrical scheme of the triple diode model; on the right, the band diagram of the junction in which the three recombination mechanisms that contribute to the dark current are depicted (from[35]).

Considering the short circuit current measured at 50 X and the PV active area, a one sun short circuit current density ( $J_{sc}$ ) of 19.5 mA/cm<sup>2</sup> has been calculated. This value is mainly limited by the high value of the surface recombination velocity between SiGeSn and InGaP, whose value, extracted from the EQE simulation, resulted to be  $>10^5$  cm<sup>2</sup>.

The open circuit voltage ( $V_{oc}$ ) is limited both by the low bandgap of SiGeSn and by the high surface recombination velocity.

In order to bring the SiGeSn cell closer to a realistic condition in which SiGeSn behaves like a bottom cell in InGaP/GaAs/SiGeSn MJ structure, the measured EQE, as reported in Figure 89 a), has been cut for all the wavelength  $< 970\text{nm}$ .

The short circuit current density has been re-calculated (13.4 mA/cm<sup>2</sup>) and then difference  $W_{oc}=E_g/q-V_{oc}$  (by considering an  $E_g$  of 0.62 eV as extracted from the ellipsometry data reported in chapter 5.4.3.7) has been obtained. The one sun  $V_{oc}$  has been re-calculated by assuming a single diode model with a pure diffusion process. Therefore, the quantity  $(KT/q) \log(19.5/13.4) = 9.37\text{ mV}$ , has been subtracted to the originally one sun value (197 mV, as reported in Table 11), where K=Boltzmann constant, T=absolute temperature, q= electron charge.

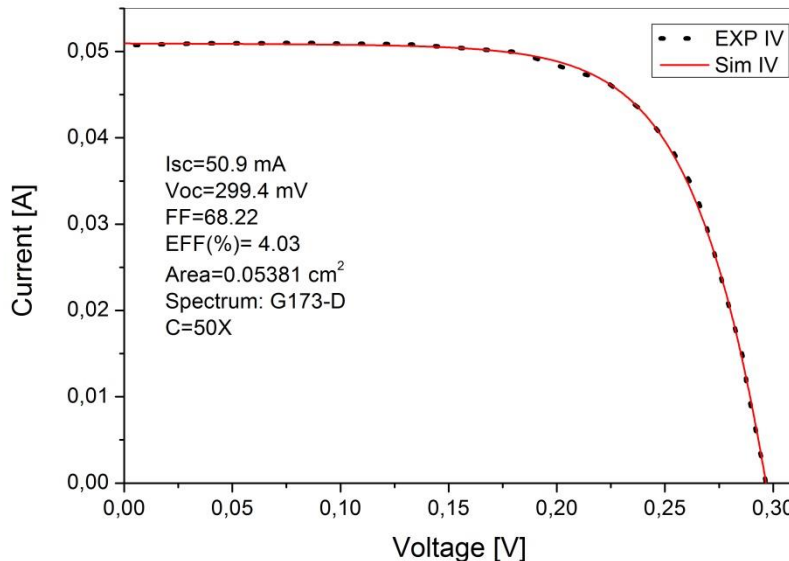


**Figure 92.** IV curve obtained under AM1.5D spectrum at 50x concentration and simulated data of the GaAs/InGaP/SiGeSn/Ge heterojunction. The Area reported in the inset correspond to the designated area of the solar cells.

The calculated  $W_{oc}$  is 0.432 V. This value is quite similar to the value presented by Ge [131], as we could expect for dilute SiGeSn, and remarkable lower than the value that can be calculated from [30] (0.72V), related to 1eV SiGeSn single junction.

We could wonder: what could be the one sun short circuit density value of SiGeSn/Ge heterojunction integrated in a MJ structure, if instead of considering a SiGeSn with  $E_g$  of 0.62 eV we could consider the material with  $E_g = 1\text{ eV}$ ? A new simulation has then been performed by assuming: i) to introduce the same cell parameters utilised to simulate the EQE, as reported in Figure 89 a), apart the surface recombination velocity between InGaP and SiGeSn which has been reduced to  $10^3\text{ cm/sec}$ , ii) to cut the EQE for all wavelength  $> 1240\text{ nm}$ , and iii) to deposit over the SiGeSn/Ge heterojunction and InGaP layer, a 3.5 um thick GaAs layer in order to simulate the absorption of a realistic GaAs middle cell.

By integrating the simulated EQE (see Figure 93) with the AM1.5D spectrum, a one sun short circuit current density of  $15.95 \text{ mA/cm}^2$  has been obtained. Since very efficient 4J solar cells (EFF >47%) require short circuit current density of  $15 \text{ mA/cm}^2$  [132], the performed simulation shows that the quality of the SiGeSn MOVPE grown is already sufficient to be integrated in MJ structure, considering that further main efforts will have to be addressed to increase the  $E_g$  and reduce the surface recombination velocity between InGaP and SiGeSn. The importance of decreasing the surface recombination velocity between InGaP and SiGeSn has been further ascertained with the following simulations.

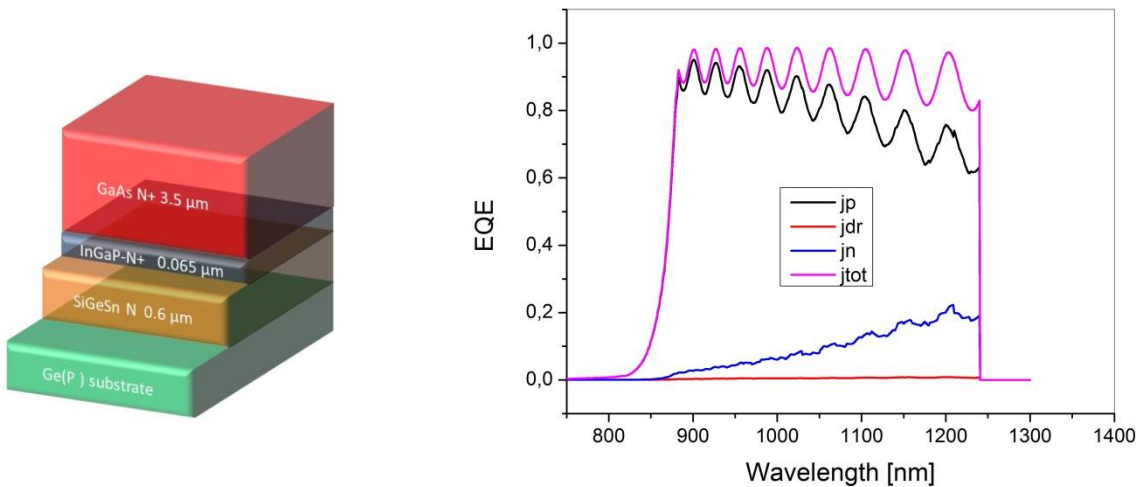


**Figure 93. SiGeSn/He HJ structure and related EQE simulation by assuming a surface recombination velocity at the interface between SiGeSn and InGaP =  $10^3 \text{ cm/sec}$ .**

Considering again the SiGeSn/Ge heterojunction with a  $0.4 \mu\text{m}$  thick GaAs layer, SiGeSn has been replaced by a Ge emitter, by keeping the emitter thickness unchanged ( $0.6 \mu\text{m}$  thick) and the EQE simulated (see Figure 94 a). By comparing Figure 90 a) with Figure 94 a), it is evident that a lower absorption takes place in the emitter when Ge is used instead of SiGeSn: the emitter contribution to the short circuit current reaches 72% when SiGeSn is used, while it drops to 47%, when Ge replaces SiGeSn.

It is interesting to point out that simulating the Ge emitter case, an EQE with a max around 0.8, instead of 0.7, has been obtained. This is due to the combined effects of a reduced absorption in the emitter and of a high recombination velocity at the interface between the emitter and the InGaP. By replacing SiGeSn with Ge, while keeping the same value for the surface recombination velocity, we can generate more carriers in the base, where we have less non-radiative recombination and consequently, we can get higher EQE values.

The higher absorption coefficient of SiGeSn with respect to Ge could be fully exploited once the recombination velocity at the interface SiGeSn/InGaP could be reduced, for example, to  $10^2 \text{ cm/sec}$ . In this case, the contribution of the emitter to the short circuit current is calculated to rise to 82% (see Figure 94 b) and the cell efficiency would be boosted from 4% to 7%. It is worthwhile to point out that, by keeping unchanged the surface recombination velocity at  $10^2 \text{ cm/sec}$  and by using a Ge homojunction instead of a SiGeSn/Ge heterojunction, the EQE simulation shows that a Ge emitter

thickness three times higher than a SiGeSn one would be required in order to get the same emitter contribution in the short circuit current (see Figure 95).

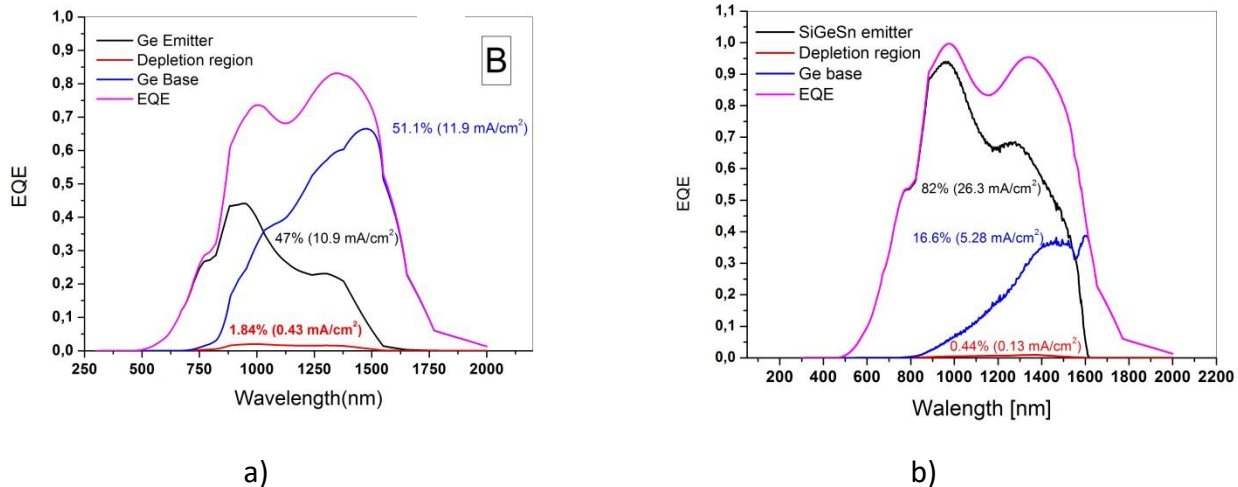


**Figure 94.** EQE simulations: a) EQE simulation of a GaAs(n-type)/InGaP(n-type)/Ge(n-type)/Ge(p-type) PV structure, with a Ge(n-type) layer with the same thickness of the SiGeSn emitter (the surface recombination velocity between InGaP and Ge has been fixed to  $10^5$  cm/sec); b) EQE simulation of a GaAs(n-type)/InGaP(n-type)/SiGeSn(n-type)/Ge(p-type) PV structure, in which the surface recombination velocity between InGaP and SiGeSn has been reduced to  $10^2$  cm/sec.

Owing to the remarkably higher absorption coefficient of SiGeSn with respect to Ge, the dilute SiGeSn considered in this study could be exploited both in TPV and space applications. In particular, since in a triple junction InGaP/InGaAs/Ge structure, Ge has shown poor resistance to proton radiation, especially in the case of low-energy protons (0.7 MeV) [133], SiGeSn could allow realizing devices more radiation resistant than Ge, owing the possibility to generate the same current with thinner layers.

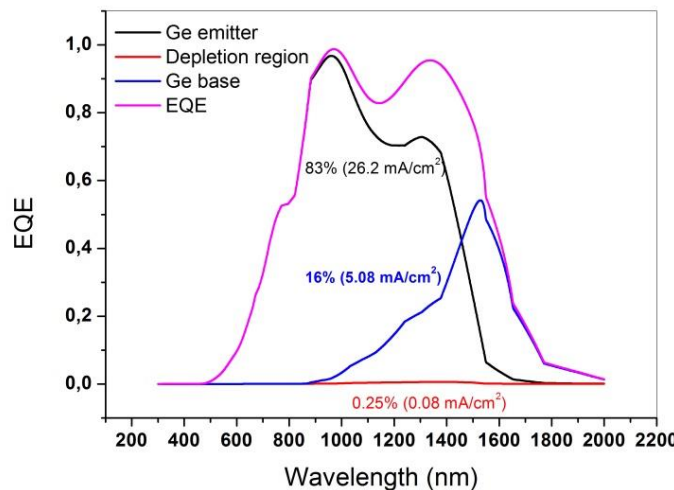


**Figure 95.** EQE simulation of a GaAs(n-type)/InGaP(n-type)/Ge(n-type)/Ge(p-type) PV structure, with a Ge emitter layer 1.85  $\mu\text{m}$  thick (the surface recombination velocity between InGaP and Ge has been fixed to  $10^2$  cm/sec).

## 6.2. Efficiency prediction of InGaP/InGaAs/SiGeSn/Ge solar cells in two and three terminal configurations

A first reference investigation on the performances of four junction solar cell by using InGaP, GaAs, Ge and a 1 eV semiconductor (as a third junction) was performed by Sarah R. Kurtz, D. Myers and J. M. Olson [20]. Ideal efficiencies were determined by assuming: i) no recombination at the front and back surfaces, ii) no losses from grid shadowing, series resistance and shunt resistance, iii) a single diode model, iv) Ge substrate 150  $\mu\text{m}$  thick. For such four-junction solar cell, under terrestrial concentrator condition, the cited Authors calculated a conversion efficiency over 50%. While electron/holes mobility and lifetime values were indicated for InGaP, GaAs and Ge, no cell parameters were reported for the 1 eV semiconductor.

Assuming terrestrial concentrator condition and by considering GaInNAs for the third junction with 1 eV  $E_g$ , J.F. Geisz and D.J. Friedman predicted for the 4J structure a 51% conversion efficiency value [134]. More recently [28], Tom Wilson et al, calculated an efficiency value of 48%, for a InGaP/InGaAs/SiGeSn/Ge four junction solar cell. In this case, even if no cell parameters were reported, 4% contact shading losses were indicated in the calculation (the reported I-V curve showed series resistance effects even if no mention was done concerning this loss mechanism).

In this chapter a more detailed investigation on the performances of InGaP/InGaAs/SiGeSn/Ge four junction solar cell is carried out by using the optical data of SiGeSn investigated in chapter 2.3.4.3.7.

The single diode model, no losses from shunt resistance and good electrical performing tunnel diodes (TDs) are the only assumptions still maintained, while the 4J cell performances have been calculated by considering realistic cell parameters (see Table 12). Even if in this study high surface recombination velocity have been extracted from EQA data concerning the SiGeSn/InGaP interface, it is believed that a realist value of  $10^3 \text{ cm/sec}$  can be achieved, by further optimising the growth condition. In order to simulate a SiGeSn layer with 1 eV  $E_g$  threshold, the absorption coefficient data on SiGeSn reported in chapter 2.3.4.3.7 has been used imposing a threshold absorption at 1240 nm. Since the absorption coefficient has been observed to decrease as a function of the energy gap [93], this assumption/simplification could bring to over evaluate the photovoltaic current generated in SiGeSn.

Furthermore, in the simulation, the tunnel diodes (TD) layers optical absorption, series resistance effect and a grid shadowing of 4% have been included, also considering the removal of the Ge substrate to boost the cell's voltage.

Eventually, since for a MJ solar cell that includes IV and III-V elements grown in the same MOVPE chamber, the realization of an “efficient” tunnel diode between the third and four junction can be problematic, as it will be discussed later, the simulated quantum efficiencies and the I-V curves have been calculated for a InGaP/InGaAs/SiGeSn/Ge four junction solar cell both in two and three terminal configuration.

Concerning the solar cell parameters the following further assumptions have been adopted: i), owing to the 97% amount of Ge in the ternary alloy, the mobility and lifetime values of SiGeSn have been assumed equal to those of Ge, ii) owing to the 1% amount of In in InGaAs, the mobility,

lifetime and absorption coefficient values of the III-V ternary material have been assumed equal to those of the binary GaAs. For the calculation of the voltage, however, the true InGaAs  $E_g$  has been considered.

The solar cell's parameter considered for InGaP, InGaAs, SiGeSn and Ge are summarized in Table 12.

**Table 12. Parameters assumed in the performance evaluation of 4J- InGaP/InGaAs/SiGeSn/Ge solar cells. The considered lifetimes are compared with the purely radiative lifetimes.**

Cell/parameters	$\tau_p/\tau_{rad}$ [s]	$\mu_p$ [cm <sup>2</sup> /(V*s)]	$S_p$ [cm/s]	$\tau_n/\tau_{rad}$ [s]	$\mu_n$ [cm <sup>2</sup> /(V*s)]	$S_n$ [cm/s]
Top-InGaP	$1*10^{-9}$ / $5*10^{-9}$	80	$1.3 *10^3$	$1 *10^{-8}$ / $1* 10^{-7}$	1745	$10^3$
Middle-(Al)InGaAs	$8*10^{-10}$ / $1.1*10^{-9}$	116	$10^3$	$1* 10^{-9}$ / $3.4 10^{-9}$	2950	$10^3$
Intermediate SiGeSn	$1*10^{-7}$ / $1.5*10^{-6}$	200	$10^3$	$3*10^{-6}$ / $1.5 10^{-5}$	1000	$10^3$
Bottom-Ge (2T)	$1*10^{-7}$ / $1.5*10^{-6}$	209	$10^3$	$3*10^{-6}$ / $1.5 10^{-5}$	1009	$10^3$
Bottom-Ge (3T)	$1*10^{-5}$ / $1.5*10^{-4}$	800				

For the Ge bottom cell, the cell's parameters are different for the two terminal (2T) and for the three terminal (3T) QJ, as the polarity of the junction is inverted, and different doping levels are used. The selected parameters values have been extrapolated from the data reported in [135], [136], [137] and [138]. The radiative lifetime,  $\tau_{rad}$ , has been calculated according to the following simplified relationship:

$$\tau = \frac{1}{\beta N} \quad 6.2$$

Where:  $\beta$  is the B-B recombination coefficient [cm<sup>3</sup>/s], N= doping level [cm<sup>-3</sup>] and by considering  $\beta_{Ge} = 6.4 10^{-14}$  cm<sup>3</sup>/s;  $\beta_{GaAs} = 7.2 10^{-10}$  cm<sup>3</sup>/s;  $\beta_{InGaP} = 1 10^{-10}$  cm<sup>3</sup>/s [136].

The structures of the two and three terminal 4J devices are reported in Figure 96. The two terminal QJ includes an AlGaAs buffer and (In)GaAs bottom tunnel diode (TD). The two terminal QJ is challenging because of the cross-contamination problem. In fact, if the (In)GaAs layers are kept very thin to avoid limiting the current of the bottom cell, it is possible to foresee that the residual contamination present in the growth chamber after the IV elements deposition, could cause a

polarity inversion in the (In)GaAs-P side of the TD. A strategy to avoid the polarity inversion could be the utilization of thick and high energy gap buffer, however the bottom TD must also survive to the thermal MOVPE load due to the deposition of the upper layers. These growth problematics make it really challenging to realize a bottom tunnel diode with a peak current value higher than the cell's short circuit current value when the cell operates at high concentration.

These questions justify the proposal of a three terminal QJ, which allows eliminating the bottom TD, and therefore, from the growth's point of view, it presents an easier and more robust QJ structure. Furthermore, the current matching is only required for the first, second and third junction, as the fourth junction can be independently contacted. For the three terminal device, however, we have to consider the following drawbacks: i) it presents a bit more complicated post-growth manufacturing process, ii) as the grid contacts are interdigitated, the grid pitch has to be larger than the case of the two terminal device, this, in turn, can introduce series resistance problem, iii). the "double" grid introduces a higher shadowing.

It is then interesting to evaluate and compare the possible performances of the QJ in two terminal (2T) and three terminal (3T) configurations. The utilized grid mask for the two and three terminal devices are reported in Figure 97. In Table 13, the series resistance calculations are reported, according to following formula [139]:

$$R = \frac{R_{sh} a^2}{12} + \frac{R_m a b^2}{3t} + \frac{R_c}{S} \quad 6.3$$

where:

$R_{sh}$  = InGaP or Ge emitter sheet resistance (window's contribution not considered);

$R_c$  = contact resistance;

$R_m$  = sheet resistance of the metal =  $\rho_m/w$ ,  $\rho_m$  and  $w$  respectively resistivity and thickness of the metal;

$a$  = grid pitch;

$t$  = grid width;

$b$  = average grid length;

$S = t/a$  = grid shadowing factor.

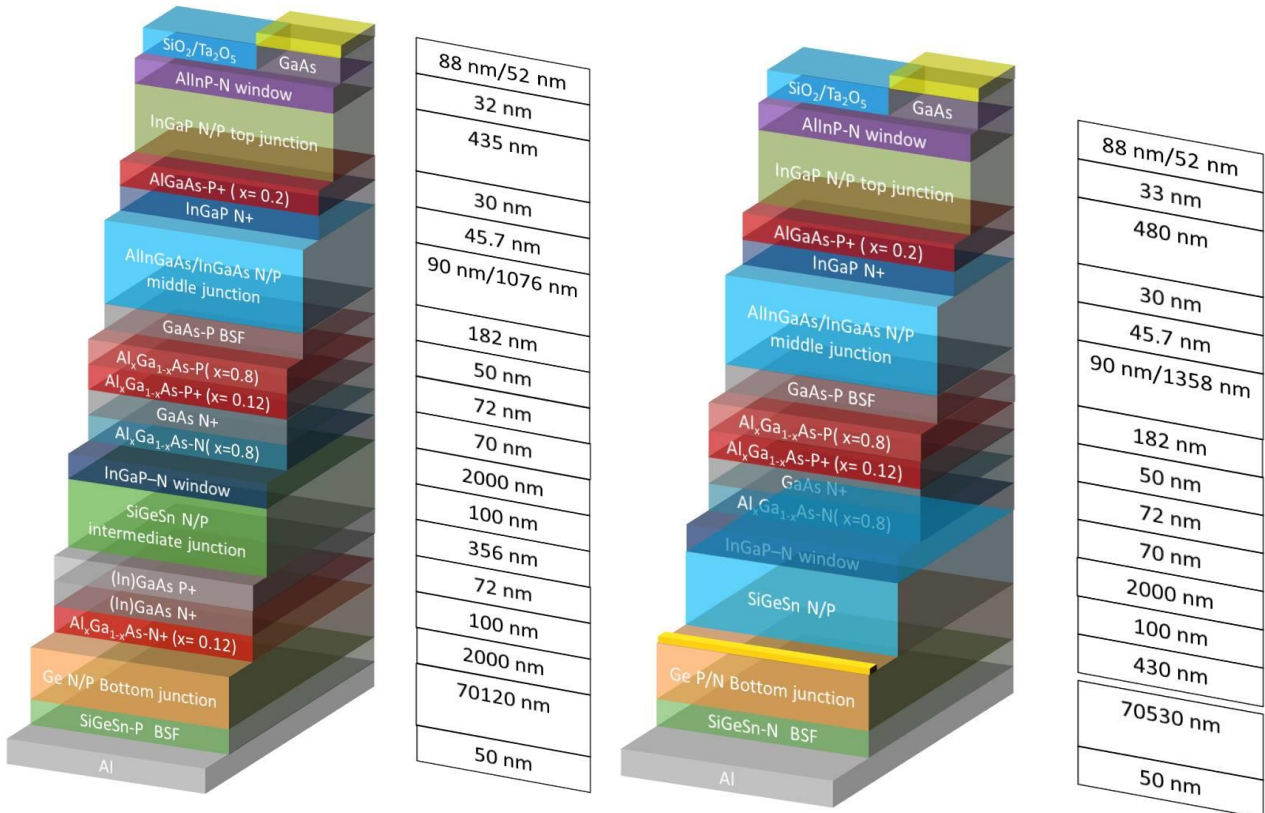


**Figure 96.** Structures of the 2T (left) and 3T (right) InGaP/InGaAs/SiGeSn/Ge four junction solar cells. The substrate has been removed in both structures.

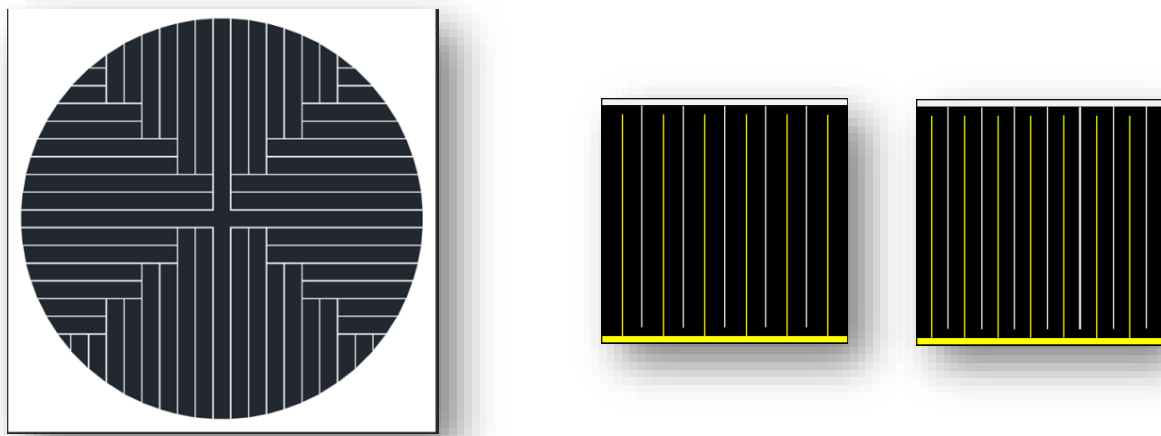


**Figure 97.** On the left, the metallic grid utilized for the 2T device with a grid pitch of 100  $\mu\text{m}$ ; on the right, the metallic grid utilized for the 3T device, with a grid pitch of 160  $\mu\text{m}$  and 120  $\mu\text{m}$ .

**Table 13. Grid main parameters and series resistance calculation according to Eq.6.3.**

	<b>2T QJ</b> <b>Cell dimension: 2.4 mm x 2.4 mm</b>	<b>3T QJ</b> <b>Cell dimension: 1 mm x 1mm</b>
a [μm]	100	160/120
b [μm]	680	900
S (t/a)	0.05	0.05
R <sub>s</sub> [Ω]	0.46	(3J) 1.48 /0.92 (bottom J) 0.52/ 0.38

Note: R<sub>sh(InGaP)</sub>= 1950 Ω/sq ; R<sub>sh(Ge)</sub>= 78 Ω/sq ; R<sub>m</sub> = 0.08 Ω ; R<sub>c</sub>= 5\*10<sup>-6</sup> Ω cm<sup>2</sup>.

For the 3T device the series resistance contribution has been calculated separately for the three-junction connected in series (top, middle, intermediate) and for the bottom junction, considering two different grid design with 160 μm and 120 μm pitch. Figure 98 shows the EQE of the InGaP/InGaAs/SiGeSn/Ge 2T QJ cell, while, in Figure 99 the related I-V curves are depicted with and without the grid mask. The effect of the series resistance is shown in Figure 100. It is worthwhile to point out that the efficiency values have been calculated by assuming a conventional SiO<sub>2</sub>/Ta<sub>2</sub>O<sub>5</sub> antireflective coating, which shows a non-ideal reflectivity curve in the wavelength range 900-nm-1600 nm.

With respect to an ideal QJ operating at 500 sun, a “realistic” 2T four junction InGaP/InGaAs/SiGeSn/Ge solar cell presents an efficiency value 2.4 points lower (47.6% instead of 50%). The calculated performances are also lower than those reported by Tom Wilson et al. [28] under AM1.5D illumination at 1000 sun concentration and considering a 4% grid shadowing. The one-sun current density and efficiency values calculated in [28] and here are respectively: 13.9 mA/cm<sup>2</sup> against 12.5 mA/cm<sup>2</sup> and 48% against 45 %. (see Figure 99 and Figure 100).

It has to point out that in [28] a MgF<sub>2</sub>/ZnS dual planar-layer anti-reflection coating was considered. Therefore, the lower current value calculated in this work can be mainly attributed to the utilization of a SiO<sub>2</sub>/Ta<sub>2</sub>O<sub>5</sub> coating instead of the MgF<sub>2</sub>/ZnS one. Indeed, the SiO<sub>2</sub>/Ta<sub>2</sub>O<sub>5</sub> planar coating used in these simulations does not show optimized reflectance values in the wavelength range where the SiGeSn and Ge sub cells are active (see Figure 98). This condition forces to limit the thickness of the InGaP and InGaAs junctions and then to collect a lower overall current.

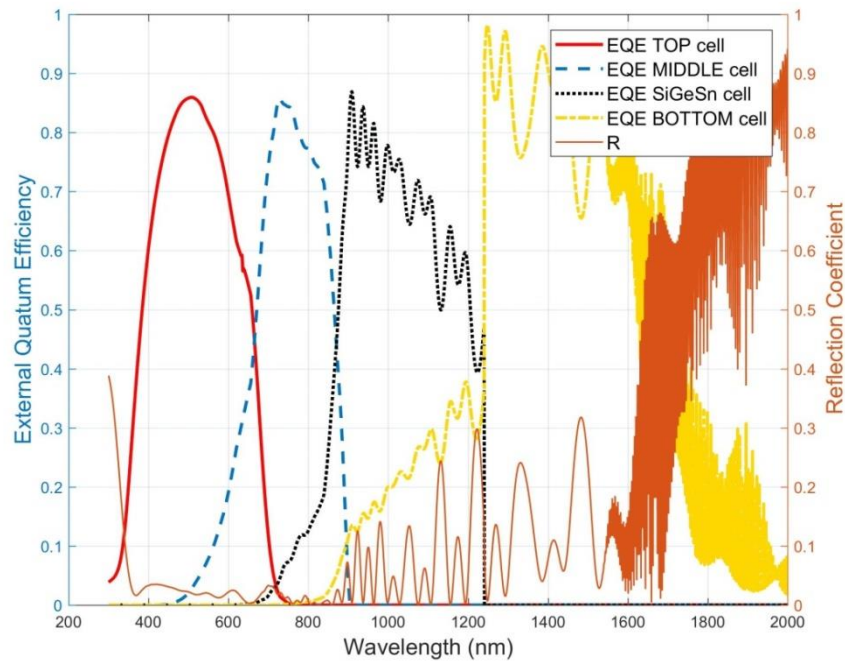


**Figure 98.** Simulated EQE and reflection coefficient of a InGaP/InGaAs/SiGeSn/Ge four junction solar cell in a two-terminal configuration. Ge thickness = 70  $\mu\text{m}$ .

The calculated voltage by Tom Wilson et al., was around 4.2 V against 4.05 V reported in this study. Such a difference can be due to several factors: different doping levels, difference in the surface recombination velocities, different layers thickness and bus bar area. Nevertheless, these simulations show that efficiency values higher than 45% can likely be obtained from a “realistic” 2T InGaP/InGaAs/SiGeSn/Ge QJ solar cell, keeping in mind that proper growth condition and cell’s structure have to be selected for avoiding the IV elements contamination in the bottom III-V based TD and for controlling atoms interdiffusion.

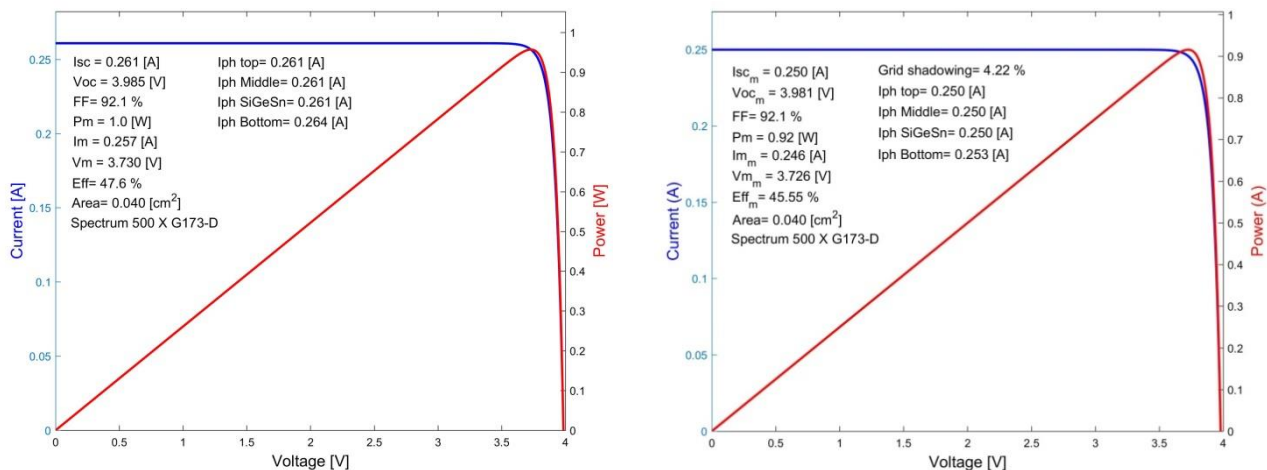


**Figure 99.** IV curves of the InGaP/InGaAs/SiGeSn/Ge solar cells without (left) and with (right) the grid mask. The one sun current density is reduced from 13.05 mA/cm<sup>2</sup> to 12.5 mA/cm<sup>2</sup> owing to the grid mask. The QJ is top limited.

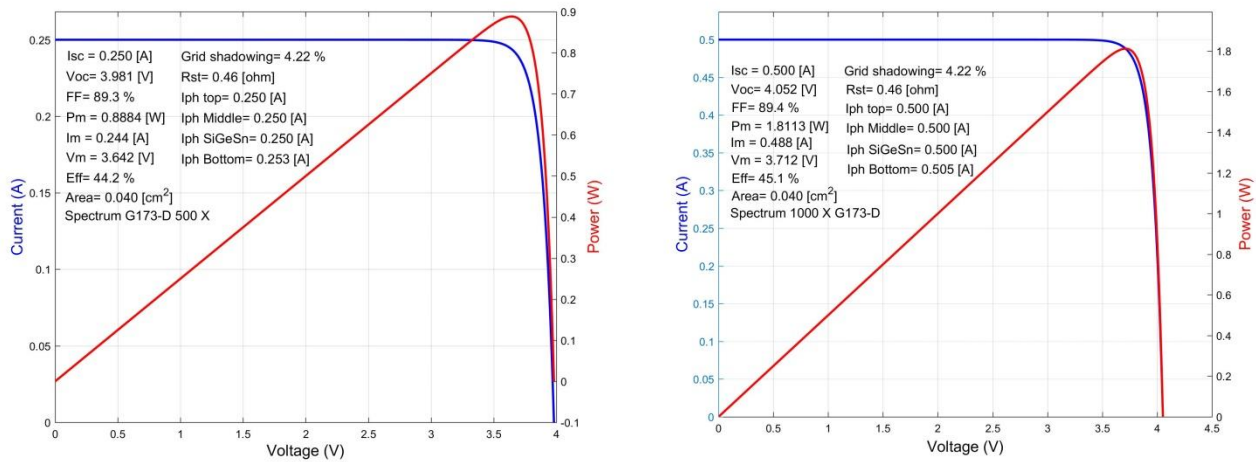


**Figure 100.** IV curves of the InGaP/InGaAs/SiGeSn/Ge 2T solar cell with the grid mask, also considering the series resistance as shown in Table 13, at 500 X (left) and 1000 X (right). The QJ is middle limited.

The results of the simulations concerning the 3T QJ are reported in Figure 101 and Figure 102.

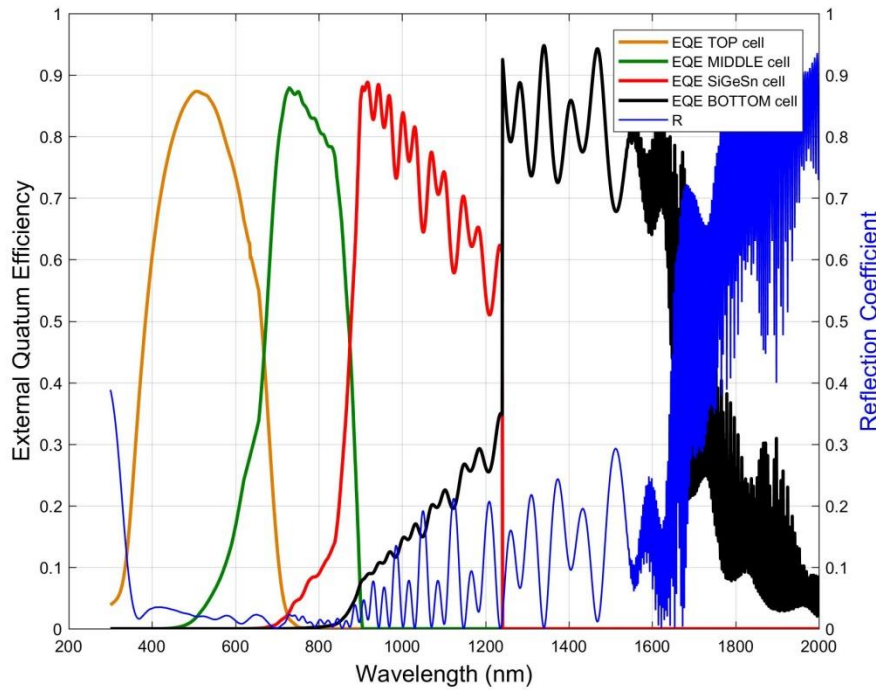


**Figure 101.** Simulated EQE and reflection coefficient of a InGaP/InGaAs/SiGeSn/Ge four junction solar cell in a 3T configuration. Ge thickness = 70  $\mu\text{m}$ .

At 1000 X, the efficiency is 44.9% with a grid shadowing of 4.17% and 44.5% with a grid shadowing of 5.3%. These values are slightly lower than the value obtained for the QJ in the two terminal configuration, because of the series resistance losses which penalise the FF value. It is worthwhile to mention that the efficiency value could increase to 45.5% and 45.1% with a grid

shadowing of 4.17% and 5.3% respectively, only by assuming for the Ge and the SiGeSn cells a surface recombination value at the base/ BSF interface equal to  $10^2$  cm/sec instead of the assumed value of  $10^3$  cm/sec.

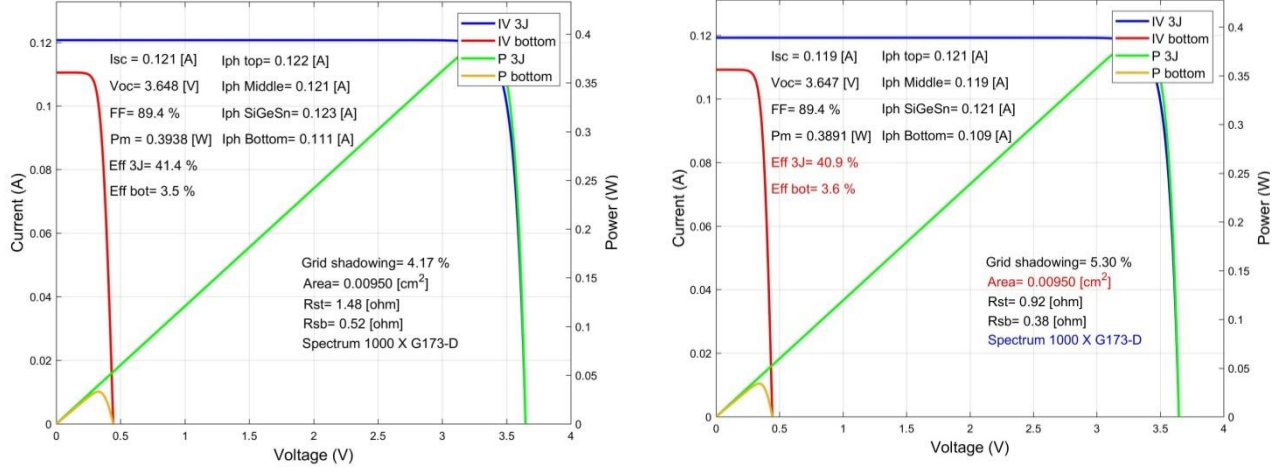


**Figure 102. IV curves of the InGaP/InGaAs/SiGeSn/Ge solar cell in a 3T configuration, with the grid mask and also considering the series resistance, considering the two-grid design, left): 160  $\mu\text{m}$  pitch, right) 120  $\mu\text{m}$  pitch.**

It is straightforward to check that by assuming the same MgF<sub>2</sub>/ZnS coating, in order to reach the same current density measured by [28] and preserving the high fill factor value obtained in our simulation (by considering an InGaAs limited QJ cell), our calculation would show an efficiency value potentially over 50%, in agreement with the simulation reported by Sarah R. Kurtz and by J.F. Geisz at a on QJ cells with a 1eV E<sub>g</sub> third junction. Overcoming the 50% efficiency threshold is of course a major goal for present-day research on MJ solar cells.

## CONCLUSIONS AND PERSPECTIVES

## 7. Conclusions and perspectives

Global warming and climate change are universally accepted as being the major challenges facing humankind. Presently, a pervasive utilization of renewable energy sources (RES) must be deployed as a solution to mitigate the human impact on climate and for building up a sustainable power generation system. Among the RES so far developed over recent decades, namely bioenergy, geothermal, hydropower, solar and wind, the solar solution is by far the most abundant, and it is available everywhere.

The photovoltaic technology, in particular, is one of the most valuable solutions to exploit solar energy and since its starting match in the 50s, it has been rapidly grown. The future development of PV is nowadays a core component of the integrated national energy and climate plan that EU Member States need to establish to meet the Union's binding target of at least 32% renewable energy generation by 2030.

Such a target will be easier and faster reached by developing more efficient PV technologies. Among the most promising ones, the concentrating photovoltaic (CPV) technology is expected to play a key role in this race, as already it represents the most efficient solution in the variegated PV panorama.

The core of the CPV technology is the multi-junction (MJ) solar cell, that with its ability of absorbing most of the solar spectrum without compromising the device voltage, has reached conversion efficiency over 45% and it still offers the possibility of fixing new targets towards 50%.

For producing high efficiency next generation MJ solar cells, new accurate and fast computation methods should be developed, as well as, new growth approaches that can allow expanding the band gap engineering possibilities by reducing the manufacturing costs.

For fulfilling the above requirements, this thesis addressed the research in two directions:

- 1) a theoretical study on a more efficient computation method for the MJ solar cell modelling,
- 2) a feasibility experimental study to combine III-V and IV elements in a new MOVPE growth monolithic approach, in view of realizing high-efficiency and low cost InGaP/InGaAs/SiGeSn/Ge quadruple junction solar cells.

With the aim to preserve the simplicity of the Hovel model and, at the same time, to offer the accuracy of the TMM without suffering of its numerical instability, a new mathematical approach has been implemented, based on SMM and a simplified generation function.

The key assumption utilized to simplify the generation function has been related to the possibility to neglect the interference of counter propagating waves that are indeed negligible with respect to the positive and negative radiation flux components.

In this way it has been possible to get sufficiently accurate analytical solutions of the continuity equation in the quasi-neutral regions of the sub-cells of the MJ device, getting a very good trade-off between computing time and accuracy.

## CONCLUSIONS AND PERSPECTIVES

In order to expand the band gap engineering possibilities while reducing the manufacturing cost, an in depth growth analysis has been addressed to advance in the deposition of III-V and IV elements in the same Metalorganic Vapour Phase Epitaxy (MOVPE) growth chamber, trying to overcome the problems that hindered so far this approach.

The experimental work has been articulated on two main research lines: i) the study of diluted SiGeSn deposition in a III-V contaminated MOVPE reactor ii) the study of the cross influence between groups IV and III-V elements.

Several aspects of the MOVPE SiGeSn growth have been investigated bringing to the deposition, high crystalline quality SiGeSn layers lattice matched to Ge, with FWHM of the XRD diffraction peaks as low as 48 arcsec and with an excellent composition uniformity of 1% on 4 inch wafers.

New insights have been evidenced on the SiGeSn MOVPE growth as summarised in Table 14.

The more relevant result of the experimental work is the possibility to get SiGeSn layers - Sn segregation free - even at temperatures up to 490°C, exploiting the As contamination of the growth chamber produced by the previous III-V runs, allowing to keep active the in-situ temperature wafer control during the MOVPE growth.

Arsenic adatoms on SiGeSn surface seem to play a role similar to Si atoms incorporated in SiGeSn: they both facilitate Sn incorporation in the SiGeSn matrix, the former by controlling the exchange process between Ge and Sn atoms on the surface and bulk, the latter by decreasing the compressive strain in the SiGeSn matrix [140]. The new theory proposed on the bond length of adatoms for inhibiting Sn precipitation allows predicting that Mg adatoms could also be effective to deposit SiGeSn - tin segregation free - at relatively high temperature, with a p-type polarity. In this way the switching between As and Mg doping could allow depositing SiGeSn P/N junction tin segregation free.

An interesting consequence of the proposed theory is that it also allows explaining the formation of structural defects even in samples in which Sn is near to the equilibrium content. The morphology deterioration, in fact, are not caused by samples not thermodynamically stable but rather by a surface growth mechanism that develops at the beginning of SiGeSn deposition.

Concerning the cross influence between III-V and IV elements, it has been studied its effect on the growth rate, background doping and layers morphology.

It is shown that the IV elements growth rate penalization due to As “carry over” can be eliminated by depositing proper coating runs, while the background doping level can be drastically reduced to values as low as  $3 \times 10^{14}$  in III-Vs and around  $10^{15} \text{ cm}^{-3}$  in Ge and SiGe semiconductors, by reducing the growth temperature (around 500°C), setting adequate growth rate (around 100 nm/min, for IV elements based materials) and including thick buffer layers.

On the other hand, SiGeSn growth has been found limited by the etching action produced by HCl, as formed by the decomposition products of  $\text{SnCl}_4$ ,  $\text{Si}_2\text{H}_6$  and  $\text{GeH}_4$ .

**Table 14. Advances in SiGeSn MOVPE growth**

Issues	New insights
Sn segregation/precipitation in SiGeSn	SiGeSn layers, tin segregation free have been obtained in the temperature range, 480-490°C, by depositing SiGeSn at growth rate values > 7 nm/min and by exploiting the arsenic carry-over (i.e. the presence of As adatoms). A new theory on the bond length of adatoms in determining the inhibiting role for Sn precipitation is proposed.
Control of SiGeSn composition in kinetic growth regime	Si <sub>2</sub> H <sub>6</sub> is the gas source more influenced by the growth temperature compared to GeH <sub>4</sub> and SnCl <sub>4</sub> , therefore, the control of wafer temperature profile is of primary importance concerning Si <sub>2</sub> H <sub>6</sub> decomposition and Si incorporation uniformity
Precursor competition	There is a competition between Si <sub>2</sub> H <sub>6</sub> and SnCl <sub>4</sub> which makes it necessary to inject more Si <sub>2</sub> H <sub>6</sub> to incorporate Si in SiGeSn, as SnCl <sub>4</sub> partial pressure is increased;
SiGeSn growth rate	The use of DEZn is helpful in increasing the SiGeSn growth rate, up to 40%, as DEZn decomposition produces CH <sub>3</sub> radicals which can either reduce the hydrogen or HCl at the wafer surface.

The etching action produced by HCl produces two negative effects, that hinder the reduction of the group V elements contamination in this ternary material:

- 1) it decreases the SiGeSn growth rate (one order of magnitude with respect to SiGe grown at the same GeH<sub>4</sub> partial pressure),
- 2) it removes the Ge and SiGe coatings already deposited on the reactor graphite parts, thus opening possible evaporation paths for the previous deposited As.

Moreover, we have assessed that the SnCl<sub>4</sub> precursor utilized in the SiGeSn growth transfers a considerable amount of P in the reactor chamber; therefore, regardless the contamination due to the previous III-V deposition, a reduction of the amount of P impurities in the SnCl<sub>4</sub> has to be addressed in order to reduce to acceptable level the background carrier concentration in SiGeSn.

Concerning the morphology aspects, this study shows that at low temperature, around 500°C, Ge and SiGe morphologies do not degrade when the IV elements semiconductors are grown in a III-V-contaminated MOVPE growth chamber. On the other hands, critical morphology aspects have been identified for SiGeSn, as already indicated, depending of the As contamination level of the MOVPE growth chamber and in III-Vs, when the deposition takes place in Sn-contaminated MOVPE growth chamber. III-Vs morphologies, in particular, are influenced by the substrate type and orientation: no morphology issues have been observed when the III-V deposition takes place on GaAs (100), 2° off towards <110> substrate, while morphology degradation takes place when the III-V deposition is carried out over Ge (100) 6° off towards <111> substrates.

## CONCLUSIONS AND PERSPECTIVES

It is worthwhile to point out that the MOVPE developing work, in particular addressed to improve SiGeSn growth uniformity and to control the parasitic deposition and cross doping when III-V and IV elements are grown in the same growth environment, has also required an important re-design of the MOVPE growth chamber. Several hardware changes have been introduced, as summarized in Figure 103.

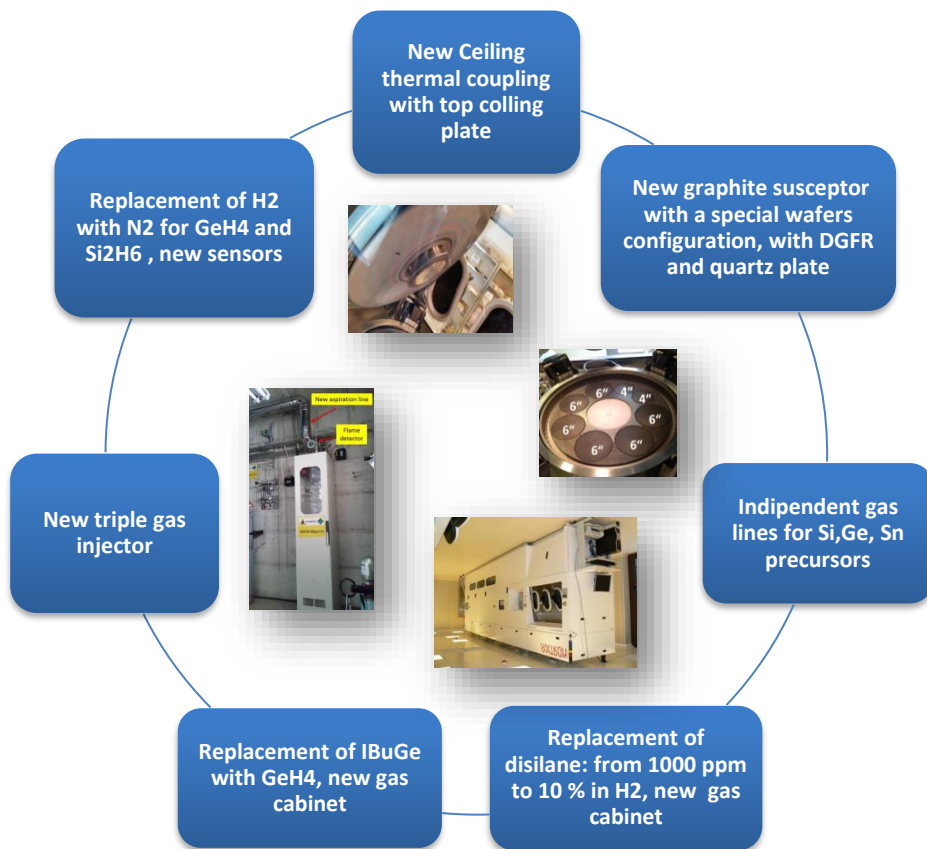


**Figure 103. Summary of the hardware modification introduced in the MOVPE reactor in order to improve the SiGeSn growth and the control of the III-V and IV element cross influence**

Some preliminary results have been produced at the device level. In order to study the SiGeSn PV behaviour, a first InGaP/SiGeSn/Ge heterojunction filtered by a 0.4 µm thick GaAs cap layer has been manufactured and characterized by EQE and IV. The latter characterization was carried out from 1 sun to 173 suns, under AM1.5D spectrum.

An EQE value of about 70% has been measured, while the device reaches 4% efficiency under G173-D spectrum, at 50x concentration. The EQE simulations, carried out by considering the measured refractive index and absorption coefficient of the SiGeSn layer, show that the bulk quality of the SiGeSn-n-type layers, MOVPE grown, are already sufficient to be integrated in triple junction structures, replacing Ge bottom cells.

## CONCLUSIONS AND PERSPECTIVES

An interesting output of this study is the remarkably high absorption coefficient determined for SiGeSn with respect to Ge. This result suggests that by using diluted SiGeSn we could realize thinner TPV devices or more radiation resistance solar cells than Ge ones.

For an assessment of the potential of the InGaP/InGaAs/SiGeSn/Ge solar cell technology, several simulations have been finally carried out, by using the SMM implemented in chapter 3 and the optical properties of SiGeSn measured and reported in chapter 5.

The PV performances have been evaluated for a InGaP/InGaAs/SiGeSn/Ge four junction solar cell both in two (2T) and three terminal (3T) configurations, at 1000 X concentration.

The computed efficiencies, by assuming that both 2T and 3T QJs are limited by the middle cells, are respectively 45.1% and 44.9%. The very near efficiency values indicate that the 3T QJ is an alternative solution to the 2T QJ, in case it will be difficult to realize “efficient” tunnel diodes between the third and four junctions.

The reported efficiencies values are a bit lower than those reported in the literature for analogous devices, however, it has been estimated that the QJ InGaP/InGaAs/SiGeSn/Ge solar cell has the potential to reach efficiencies over 50% by assuming proper antireflective coatings and recombination velocities of  $10^3$  cm/s for the SiGeSn sub-cell. Reaching the 50% efficiency threshold is of course a major goal for present-day research on MJ solar cells.

In summary, this thesis work has allowed advancing in the deposition of III-V and IV elements in the same Metalorganic Vapour Phase Epitaxy (MOVPE) growth chamber, in view of their monolithic integration, facing several problems that hindered so far this approach.

In particular, the achievements reported in this study show that, while for the final integration of SiGeSn in III-V based MJ solar cells, further SiGeSn MOVPE growth optimizations are necessary, the realization of III-V and Ge (or SiGe) based monolithic MJ architectures in the same MOVPE growth apparatus, by using commercial precursors, can already be feasible.

This conclusion allows opening new prospective and addresses the next development steps on the MJ solar cell technology based on the combination of III-V and IV elements.

The possibility to integrate III-V with Ge or SiGe opens the path for realizing *four junction solar cells partially segmented* [141], i.e. in which the two lower junctions can be made of the same material, both of Ge or of SiGe, and are vertically monolithically grown under a dual junction III-V stack. The design of such a device was theoretically presented in the early 2000, by Daniel J.Aiken [142] so far never realized, owing to the cross influence between III-V and IV elements.

An InGaP/InGaAs/Ge/Ge MJ structure has the advantage to exploit the current in excess that would be produced by a Ge bottom cell under a InGaP/GaAs stack. Preliminary simulations show that the proposed four junction solar cell should allow improving the InGaP/InGaAs/Ge solar cell efficiency of 1.5 absolute point, as a results of an increment in the solar cell voltage and of a small penalization in the current that would be produced with respect to the triple junction solar cell.

The realization of a InGaP/InGaAs/Ge/Ge MJ structure - all MOVPE grown- would be an important test bench to control the atom inter-diffusion that could compromise the MJ device functioning.

While the cross contamination from the vapour phase has been reduced to acceptable levels, the next challenge to be faced in order to realize a high efficient MJ device will be the control of the IV elements diffusion in III-V adjacent layers and vice versa. The solution to this problem is expected to be the utilization of proper designed cell structures.

For this purpose, two promising MJ structures are, for example, proposed in Figure 104. They concern 3T QJ devices in which the bottom junction has a p/n polarity and the subsequent junctions have n/p polarities. Such structures are expected to be suitable for controlling the atom inter-diffusion, since in Figure 104 a) all the adjacent III-V and IV layers have n-type polarity, while in Figure 104 b) there is only one InGaP(p) layer sandwiched between two SiGe(p)layers. The InGaP(p) layer has been included with a double function: 1) it can be used as a stop etch layer, 2) it can work as a minority carrier “mirror” for both the SiGe layers.

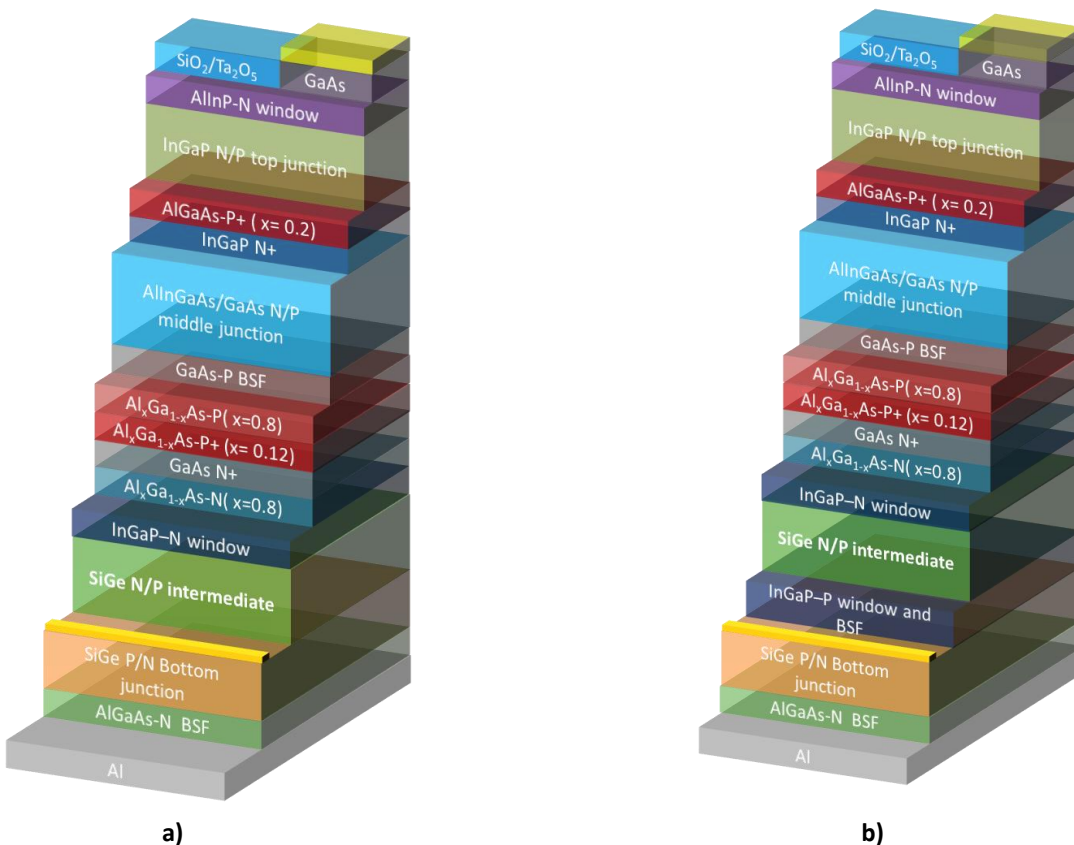


**Figure 104. Four junctions partial segmented InGaP/GaAs/SiGe/SiGe solar cells. Both structures can grow on a GaAs substrate that can be subsequently removed. The MJ structure depicted in b) has an added InGaP interlayer, sandwiched between the two SiGe sub cells, with respect to the MJ structure depicted in a). This layer has been included to improve the cell manufacturing and enhance the cell performances.**

Of course, these solutions will be less efficient than a III-V based 4-junction solar cell in which 1eV SiGeSn is included as a third junction, however, the realization of InGaP/InGaAs/(Si)Ge/(Si)Ge 4-junction solar cells, with efficiency around 40%, can be thought as

## CONCLUSIONS AND PERSPECTIVES

the first proof-of-the-concept of the monolithic integration IV and III-V elements in a fully-MOVPE-grown MJ solar cell, and for this reason, it will constitute a very important intermediate step.

As the final aim is the integration of SiGeSn in III-V based MJ solar cells, the next important achievements to be reached on the MOVPE SiGeSn growth for this purpose, have been summarized in Table 15.

The main challenges still to be faced are: i) the increase of Sn and Si incorporation in the ternary material to around respectively 2% and 8% to achieve an energy gap around 0.9 eV , ii) the realization of SiGeSn p-type layers at relatively high temperature, iii) the reduction of the carrier background concentration in SiGeSn.

**Table 15. Next achievements for SiGeSn MOVPE growth**

Achievement	Objective
Obtain SiGeSn layers - Sn segregation free - still keeping the growth temperature >400 °C, with Si and Sn concentration respectively of 8% and 2%	Increase E <sub>g</sub> from 0.62 eV top 0.9 eV
Obtain SiGeSn layers - Sn segregation free - still keeping the growth temperature >400 °C, with p-type polarity, by testing (C <sub>5</sub> H <sub>5</sub> ) <sub>2</sub> Mg	Realize SiGeSn P/N junction at relative high temperature
Reduce SiGeSn surface porosity due to the presence of etch pit like defects, correlated with the Sn content in the samples.	Decrease the surface recombination velocity to 10 <sup>2</sup> -10 <sup>3</sup> cm/sec
Increase the GeH <sub>4</sub> partial pressure in order to increase SiGeSn growth rate from 7 nm/min to 100 nm/min	Reduce the SiGeSn background contamination to the levels reached in Ge and SiGe
Procurement of new SnCl <sub>4</sub> sources with higher purity grade	Reduce P contamination in SiGeSn < 10 <sup>16</sup> cm <sup>-3</sup>
Growth of III-V in a Sn contaminate MOVPE growth chamber on Ge substrate with orientation (100), 2° off towards <110> substrate	Assess whether the morphology degradation observed on III-Vs deposited in a Sn contaminated MOVPE growth chamber is related to the chemical nature of the substrate or to its orientation

In prospective, in view of a further reduction of the MJ solar cell cost, the results presented in this thesis open the possibility for a monolithic integration of IIIVs and Si by using the same MOVPE deposition system, possibly simplifying the manufacturing steps nowadays necessary with the wafer bonding or by the mechanical stacking approaches.

As a final conclusion, it is worthwhile to come back to the computation carried out in the introduction of this thesis, in which I demonstrated that by covering an average regional area of 15 km<sup>2</sup> even with 10% efficient PV systems we could produce, an energy equal to the Italy annual

## CONCLUSIONS AND PERSPECTIVES

imported energy. The results of this work and related simulations show that MJ cell technology based on III-V and IV elements has the potential to achieve efficiency above 45%. By assuming to use CPV modules with optics having an optical efficiency of 80%, we could get 36% efficient CPV modules and 30% efficient PV systems. This means that the average regional area needed to generate an energy equal to the Italy annual imported energy would be three time less than previously calculated, i.e. just 5 km<sup>2</sup>. This area would correspond to only 0.02% of the Emilia Romagna area.

This conclusion motivates the future MJ cell development efforts necessary to transfer the results of this work in a highly efficient CPV technology for realising a decarbonised power sector and a more sustainable energy supply in our Country.

## Bibliography

- [1] International Energy Agency, World Energy Outlook, (2017) 17. <https://doi.org/10.1787/20725302>.
- [2] I.E. Agency, Key World Energy Statistics, (2016).
- [3] IEA, Key World Energy Statistics, (2017).
- [4] IEA Key, Key World Energy Statistics 2020, Int. Energy Agency. 33 (2020) 4649. [https://webstore.iea.org/download/direct/4035%0Ahttp://data.iea.org/payment/products/103-world-energy-statistics-and-balances-2018-edition-coming-soon.aspx%0Ahttps://www.oecd-ilibrary.org/energy/key-world-energy-statistics-2020\\_295f00f5-en](https://webstore.iea.org/download/direct/4035%0Ahttp://data.iea.org/payment/products/103-world-energy-statistics-and-balances-2018-edition-coming-soon.aspx%0Ahttps://www.oecd-ilibrary.org/energy/key-world-energy-statistics-2020_295f00f5-en).
- [5] World Energy Council [WEC], World Energy Resources: Solar 2016, World Energy Counc. (2016) 6. [https://doi.org/https://www.worldenergy.org/wp-content/uploads/2013/10/WER\\_2013\\_8\\_Solar\\_revised.pdf](https://doi.org/https://www.worldenergy.org/wp-content/uploads/2013/10/WER_2013_8_Solar_revised.pdf).
- [6] S.P. Philipps, A.W. Bett, K. Horowitz, S. Kurtz, Current Status of Concentrator Photovoltaic (CPV) Technology, Natl. Renew. Energy Lab. (2015) 1–25. <https://doi.org/http://www.ise.fraunhofer.de/en/publications/veroeffentlichungen-pdf-dateien-en/studien-und-konzeptpapiere/current-status-of-concentrator-photovoltaic-cpv-technology.pdf>.
- [7] W.H. Press, Theoretical maximum for energy from direct and diffuse sunlight, Nature. 264 (1976) 734–735. <https://doi.org/10.1038/264734a0>.
- [8] and M.U. IYoshiya ABIKO, Rui MIKAMI, Kazushi IYATANI, Shinji TANURA, Kaiji SUGIYAMA, Evaluation of Concentrator Photovoltaic System Power Plant, Environ. Energy, SEI Tech. Rev. No.86. (2018) 100–105.
- [9] V.M. Emelyanov, E.S. Aranova, M. V Nakhimovich, M.Z. Shvarts, Output Energy Predictions for Hybrid Concentrator III-V / Planar Thin-Film Modules, in: CPV14, n.d.
- [10] U.C. Berkeley, Electronic Thesis and Dissertations Thermodynamics , Entropy , Information and the Efficiency of Solar Cells By Zeev R . Abrams A dissertation submitted in partial satisfaction of the requirements for the degree of Doctor of Philosophy in Applied Science , (2012).
- [11] G. Siefer, A.W. Bett, Analysis of temperature coefficients for III-V multi-junction concentrator cells, Prog. Photovoltaics Res. Appl. 22 (2014) 515–524. <https://doi.org/10.1002/pip.2285>.
- [12] G.F. Nemet, Beyond the learning curve: factors influencing cost reductions in photovoltaics, Energy Policy. 34 (2006) 3218–3232. <https://doi.org/10.1016/j.enpol.2005.06.020>.
- [13] L.L. Kazmerski, Conversion efficiencies of the best research solar cells worldwide from 1976 through 2017 for various photovoltaic technologies, Natl. Renew. Energy Lab. (NREL), Golden, CO. (2017). <https://www.nrel.gov/pv/assets/images/efficiency-chart.png>.
- [14] J.F. Geisz, R.M. France, K.L. Schulte, M.A. Steiner, A.G. Norman, H.L. Guthrey, M.R. Young, T. Song, T. Moriarty, Six-junction III–V solar cells with 47.1% conversion efficiency under 143 Suns concentration, Nat. Energy. (2020). <https://doi.org/10.1038/s41560-020-0598-5>.

## BIBLIOGRAPHY

- [15] J.F. Geisz, M.A. Steiner, N. Jain, K.L. Schulte, R.M. France, W.E. McMahon, E.E. Perl, D.J. Friedman, Building a Six-Junction Inverted Metamorphic Concentrator Solar Cell, *IEEE J. Photovoltaics.* 8 (2018) 626–632. <https://doi.org/10.1109/JPHOTOV.2017.2778567>.
- [16] M. of the T.W.G. TWG, SET-Plan TWP PV Implementation Plan Final Draft, (2017) 1–32. [https://setis.ec.europa.eu/system/files/set\\_plan\\_pv\\_implementation\\_plan.pdf](https://setis.ec.europa.eu/system/files/set_plan_pv_implementation_plan.pdf).
- [17] R. Cariou, J. Benick, P. Beutel, N. Razek, C. Flotgen, M. Hermle, D. Lackner, S.W. Glunz, A.W. Bett, M. Wimplinger, F. Dimroth, Monolithic Two-Terminal III-V//Si Triple-Junction Solar Cells with 30.2% Efficiency under 1-Sun AM1.5g, *IEEE J. Photovoltaics.* 7 (2017) 367–373. <https://doi.org/10.1109/JPHOTOV.2016.2629840>.
- [18] S. Essig, C. Alleb , T. Remo, J.F. Geisz, M.A. Steiner, K. Horowitz, L. Barraud, J.S. Ward, M. Schnabel, A. Descoeuilles, D.L. Young, M. Woodhouse, M. Despeisse, C. Ballif, A. Tamboli, Raising the one-sun conversion efficiency of III-V/Si solar cells to 32.8% for two junctions and 35.9% for three junctions, *Nat. Energy.* 2 (2017). <https://doi.org/10.1038/nenergy.2017.144>.
- [19] V.R. D’Costa, Y.Y. Fang, J. Tolle, J. Kouvettakis, J. Men ndez, Tunable optical gap at a fixed lattice constant in group-IV semiconductor alloys, *Phys. Rev. Lett.* 102 (2009). <https://doi.org/10.1103/PhysRevLett.102.107403>.
- [20] S.R. Kurtz, D. Myers, J.M. Olson, Projected performance of three- and four-junction devices using GaAs and GaInP, in: *Conf. Rec. IEEE Photovolt. Spec. Conf., 1997:* pp. 875–878. <https://doi.org/10.1109/PVSC.1997.654226>.
- [21] B.R. Conley, H. Naseem, G. Sun, P. Sharps, S.Q. Yu, High efficiency MJ solar cells and TPV using SiGeSn materials, in: *Conf. Rec. IEEE Photovolt. Spec. Conf., 2012.* <https://doi.org/10.1109/PVSC.2012.6317814>.
- [22] J. Taraci, J. Tolle, J. Kouvettakis, M.R. McCartney, D.J. Smith, J. Menendez, M.A. Santana, Simple chemical routes to diamond-cubic germanium-tin alloys, *Appl. Phys. Lett.* 78 (2001) 3607–3609. <https://doi.org/10.1063/1.1376156>.
- [23] M. Bauer, J. Taraci, J. Tolle, A.V.G. Chizmeshya, S. Zollner, D.J. Smith, J. Menendez, C. Hu, J. Kouvettakis, Ge-Sn semiconductors for band-gap and lattice engineering, *Appl. Phys. Lett.* 81 (2002) 2992–2994. <https://doi.org/10.1063/1.1515133>.
- [24] J. Kouvettakis, J. Menendez, A.V.G. Chizmeshya, TIN-BASED GROUP IV SEMICONDUCTORS: New Platforms for Opto- and Microelectronics on Silicon, *Annu. Rev. Mater. Res.* 36 (2006) 497–554. <https://doi.org/10.1146/annurev.matsci.36.090804.095159>.
- [25] Y.Y. Fang, J. Xie, J. Tolle, R. Roucka, V.R. D’Costa, A.V.G. Chizmeshya, J. Menendez, J. Kouvettakis, Molecular-based synthetic approach to new group IV materials for high-efficiency, low-cost solar cells and si-based optoelectronics, *J. Am. Chem. Soc.* 130 (2008) 16095–16102. <https://doi.org/10.1021/ja806636c>.
- [26] J. Kouvettakis, J. Mathews, R. Roucka, A.V.G. Chizmeshya, J. Tolle, J. Menendez, Practical materials chemistry approaches for tuning optical and structural properties of group IV semiconductors and prototype photonic devices, *IEEE Photonics J.* 2 (2010) 924–941. <https://doi.org/10.1109/JPHOT.2010.2081357>.
- [27] E. Welser, W. Guter, A. Wekkeli, F. Dimroth, Memory effect of Ge in III-V semiconductors,

## BIBLIOGRAPHY

- J. Cryst. Growth. 310 (2008) 4799–4802. <https://doi.org/10.1016/j.jcrysgro.2008.08.037>.
- [28] T. Wilson, T. Thomas, M. Führer, N.J. Ekins-Daukes, R. Roucka, A. Clark, A. Johnson, R. Hoffman, D. Begarney, Single and multi-junction solar cells utilizing a 1.0 eV SiGeSn junction, in: AIP Conf. Proc., 2016. <https://doi.org/10.1063/1.4962096>.
- [29] P. Cano, I. Lombardero, I. Rey-Stolle, A. Johnson, R. Hoffman, Multijunction solar cells incorporating group IV SiGeSn alloys, in: 2017 Spanish Conf. Electron Devices, CDE 2017, 2017. <https://doi.org/10.1109/CDE.2017.7905233>.
- [30] R. Roucka, A. Clark, T. Wilson, T. Thomas, M. Führer, N. Ekins-Daukes, A. Johnson, R. Hoffman, D. Begarney, Demonstrating Dilute-Tin Alloy SiGeSn for Use in Multijunction Photovoltaics: Single- and Multijunction Solar Cells with a 1.0-eV SiGeSn Junction, IEEE J. Photovoltaics. (2016). <https://doi.org/10.1109/JPHOTOV.2016.2559785>.
- [31] P. Wurfel, U. Wurfel, Physics of solar cells : from basic principles to advanced concepts, Phys. Textb. (2009) xii, 244 p. <https://doi.org/10.1109/PhysRev.109.603>.
- [32] L. Esaki, New phenomenon in narrow germanium p-n junctions [3], Phys. Rev. 109 (1958) 603–604. <https://doi.org/10.1103/PhysRev.109.603>.
- [33] Z.Q. Li, Y.G. Xiao, M. Lestrade, Z.M.S. Li, 2D-simulation of inverted metamorphic GaInP/GaAs/GaInAs triple junction solar cell, in: Conf. Rec. IEEE Photovolt. Spec. Conf., 2008. <https://doi.org/10.1109/PVSC.2008.4922475>.
- [34] A. Bozzola, M. Liscidini, L.C. Andreani, Broadband light trapping with disordered photonic structures in thin-film silicon solar cells, Prog. Photovoltaics Res. Appl. 22 (2014) 1237–1244. <https://doi.org/10.1002/pip.2385>.
- [35] Harold. J. Hovel, Semiconductors and semimetals: Solar cells, Academic Press Inc, London, 1975.
- [36] B. Harbecke, Coherent and Incoherent Reflection and Transmission of Multilayer Structures, Appl. Phys. B. 39 (1986) 165–170. <https://doi.org/10.1007/BF00697414>.
- [37] Z. KNITTL, Optics of thin films, 1976. <https://doi.org/10.1007/s13398-014-0173-7.2>.
- [38] K. Ohta, H. Ishida, Matrix formalism for calculation of electric field intensity of light in stratified multilayered films., Appl. Opt. 29 (1990) 1952–9. <https://doi.org/10.1364/AO.29.001952>.
- [39] S.R. Kurtz, J.M. Olson, D.J. Friedman, J.F. Geisz, K.A. Bertness, A.E. Kibbler, Passivation of Interfaces in High-Efficiency Photovoltaic Devices, MRS Proc. 573 (1999) 95. <https://doi.org/10.1557/PROC-573-95>.
- [40] G. Letay, M. Breselge, a. W. Bett, Calculating the generation function of III-V solar cells, 3rd World Conf. OnPhotovoltaic Energy Conversion, 2003. Proc. 1 (2003) 741–744.
- [41] E. Centurioni, Generalized matrix method for calculation of internal light energy flux in mixed coherent and incoherent multilayers, Appl. Opt. 44 (2005) 7532. <https://doi.org/10.1364/AO.44.007532>.
- [42] I. Bhattacharya, Florida State University Libraries Design and Modeling of Very High-Efficiency Multijunction Solar Cells, (2013).

## BIBLIOGRAPHY

- [43] L.A.A. Pettersson, L.S. Roman, O. Inganäs, Modeling photocurrent action spectra of photovoltaic devices based on organic thin films, *J. Appl. Phys.* 86 (1999) 487–496. <https://doi.org/10.1063/1.370757>.
- [44] R. Brendel, M. Hirsch, R. Plieninger, J.H. Werner, Quantum Efficiency Analysis of Thin-Layer Silicon Solar Cells, *IEEE Trans. Electron Devices*. 43 (1996) 1104–1113.
- [45] M.P. Lumb, C.G. Bailey, J.G.J. Adams, G. Hillier, F. Tuminello, V.C. Elarde, R.J. Walters, Extending the 1-d hovel model for coherent and incoherent back reflections in homojunction solar cells, *IEEE J. Quantum Electron.* 49 (2013) 462–470. <https://doi.org/10.1109/JQE.2013.2252148>.
- [46] O. Deparis, Poynting vector in transfer-matrix formalism for the calculation of light absorption profile in stratified isotropic optical media, *Opt. Lett.* 36 (2011) 3960. <https://doi.org/10.1364/OL.36.003960>.
- [47] A.J. Yuffa, J.A. Scales, Object-oriented electrodynamic S-matrix code with modern applications, *J. Comput. Phys.* 231 (2012) 4823–4835. <https://doi.org/10.1016/j.jcp.2012.03.018>.
- [48] M.N. and S.Y. N.Shigyo, H.Tanimoto, Minority Carrier Mobility Model for Device Simulation, *Solid. State. Electron.* 33 (1990) 727–731.
- [49] G. Létay, M. Hermle, A.W. Bett, Simulating single-junction GaAs solar cells including photon recycling, *Prog. Photovoltaics Res. Appl.* 14 (2006) 683–696. <https://doi.org/10.1002/pip.699>.
- [50] S.M. Sze, K.N. Kwok, *Physics of Semiconductor Devices*, 2007. <https://doi.org/10.1049/ep.1970.0039>.
- [51] E.F. Schubert, *Light-Emitting Diodes* - 2nd Edition, 2006. <https://doi.org/10.2277/0521865387>.
- [52] M.A. Steiner, J.F. Geisz, I. García, D.J. Friedman, A. Duda, S.R. Kurtz, Optical enhancement of the open-circuit voltage in high quality GaAs solar cells, *J. Appl. Phys.* 113 (2013). <https://doi.org/10.1063/1.4798267>.
- [53] D.J. Friedman, J.F. Geisz, M.A. Steiner, Effect of luminescent coupling on the optimal design of multijunction solar cells, *IEEE J. Photovoltaics*. 4 (2014) 986–990. <https://doi.org/10.1109/JPHOTOV.2014.2308722>.
- [54] O.D. Miller, E. Yablonovitch, S.R. Kurtz, Strong internal and external fluorescence as solar cell approach the SQ efficiency limit, *IEEE J. Photovoltaics*. 2 (2012) 303–311. <https://doi.org/10.1109/JPHOTOV.2012.2198434>.
- [55] E. O. Göbel, K. Ploog, Fabrication and optical properties of semiconductor quantum wells and superlattices, *Prog. Quantum Electron.* 14 (1990) 289–356. [https://doi.org/10.1016/0079-6727\(90\)90001-E](https://doi.org/10.1016/0079-6727(90)90001-E).
- [56] J.H. van der Merwe, Misfit Dislocation Generation in Epitaxial Layers, *Crit. Rev. Solid State Mater. Sci.* (1991). <https://doi.org/10.1080/10408439108243751>.
- [57] R.A. Soref, C.H. Perry, Predicted band gap of the new semiconductor SiGeSn, *J. Appl. Phys.* 69 (1991) 539–541. <https://doi.org/10.1063/1.347704>.

## BIBLIOGRAPHY

- [58] B.R. Conley, H. Naseem, G. Sun, P. Sharps, S.Q. Yu, High efficiency MJ solar cells and TPV using SiGeSn materials, *Conf. Rec. IEEE Photovolt. Spec. Conf.* (2012) 1189–1192. <https://doi.org/10.1109/PVSC.2012.6317814>.
- [59] J. Kouveticakis, V.R.D. Costa, Y. Fang, J. Tolle, A.V.G. Chizmeshya, J. Xie, J. Menéndez, Independently tunable electronic and structural parameters in ternary Group IV semiconductors for optoelectronic applications, *Sci. Technol.* (2008) 4–8.
- [60] J. Xie, J. Tolle, V.R. D’Costa, A.V.G. Chizmeshya, J. Menéndez, J. Kouveticakis, Direct integration of active  $\text{Ge}_{1-x}(\text{Si}_4\text{Sn})_x$  semiconductors on  $\text{Si}(100)$ , *Appl. Phys. Lett.* 95 (2009) 181909. <https://doi.org/10.1063/1.3242002>.
- [61] L.S. Cells, S. Optoelectronics, Y. Fang, J. Xie, J. Tolle, R. Roucka, V.R.D. Costa, A.V.G. Chizmeshya, J. Menendez, J. Kouveticakis, Molecular-Based Synthetic Approach to New Group IV Materials for Molecular-Based Synthetic Approach to New Group IV Materials for High-Efficiency , Low-Cost Solar Cells and, (2008) 16095–16102.
- [62] R. Fischer, H. Morkoç, D.A. Neumann, H. Zabel, C. Choi, N. Otsuka, M. Longerbone, L.P. Erickson, Material properties of high-quality gaas epitaxial layers grown on si substrates, *J. Appl. Phys.* (1986). <https://doi.org/10.1063/1.337253>.
- [63] W. Efficiency, S. Essig, M.A. Steiner, C. Alleb, J.F. Geisz, B. Paviet-salomon, S. Ward, A. Descoedres, V. Lasalvia, L. Barraud, N. Badel, A. Faes, J. Levrat, M. Despeisse, C. Ballif, P. Stradins, D.L. Young, Realization of GaInP / Si Dual-Junction Solar Cells, *IEEE J. Photovoltaics.* 6 (2016) 1012–1019. <https://doi.org/10.1109/JPHOTOV.2016.2549746>.
- [64] R. Beeler, J. Mathews, C. Weng, J. Tolle, R. Roucka, A.V.G. Chizmeshya, R. Juday, S. Bagchi, J. Menndez, J. Kouveticakis, Comparative study of InGaAs integration on bulk Ge and virtual Ge/Si(1 0 0) substrates for low-cost photovoltaic applications, *Sol. Energy Mater. Sol. Cells.* 94 (2010) 2362–2370. <https://doi.org/10.1016/j.solmat.2010.08.016>.
- [65] A.H. Soeriyadi, L. Wang, B. Conrad, M. Diaz, X. Zhao, D. Li, A. Lochtefeld, A. Barnett, I. Perez-wurfl, A Direct Method Of Analysing The Current Matching Condition In A Multi-Junction Solar Cell, in: 31st Eur. Photovolt. Sol. Energy Conf. Exhib., 2015: pp. 1456–1460.
- [66] M. Dubey, K.A. Jones, D.W. Eckart, L.M. Casas, R.L. Pfeffer, M. Dubey, K.A. Jones, D.W. Eckart, L.M. Casas, R.L. Pfeffer, Growth of single crystal Ge films on GaAs and InGaP and highly oriented Au films on Ge, *Appl. Phys. Lett.* 2697 (1994).
- [67] R. Jakomin, G. Beaudoin, N. Gogneau, B. Lamare, L. Largeau, O. Mauguin, I. Sagnes, P and n-type germanium layers grown using iso-butyl germane in a III-V metal-organic vapor phase epitaxy reactor, *Thin Solid Films.* 519 (2011) 4186–4191. <https://doi.org/10.1016/j.tsf.2011.02.019>.
- [68] Y. Kim, K. Kim, C.Z. Kim, S.H. Jung, H.K. Kang, W.K. Park, J. Lee, Highly efficient epitaxial Ge solar cells grown on GaAs (001) substrates by MOCVD using isobutylgermane, *Sol. Energy Mater. Sol. Cells.* 166 (2017) 127–131. <https://doi.org/10.1016/j.solmat.2017.03.015>.
- [69] G. Timò, N. Armani, G. Abagnale, B. Schineller, Advancement in the MOVPE technology to increase the process yield and expand the band gap engineering possibilities, in: 2014 IEEE 40th Photovolt. Spec. Conf. PVSC 2014, 2014: pp. 554–558. <https://doi.org/10.1109/PVSC.2014.6924981>.

## BIBLIOGRAPHY

- [70] G. Timò, G. Abagnale, N. Armani, E. Malvisi, G. Carbi, F. Farina, B. Schineller, Novel approaches to MOVPE material deposition for high efficiency Multijunction Solar Cells, in: Cryst. Res. Technol., 2014: pp. 606–613. <https://doi.org/10.1002/crat.201300448>.
- [71] R. Jia, T. Zhu, V. Bulović, E.A. Fitzgerald, Luminescence of III-IV-V thin film alloys grown by metalorganic chemical vapor deposition, J. Appl. Phys. 123 (2018). <https://doi.org/10.1063/1.5016443>.
- [72] Robert DeHoff, Thermodynamics in material science, 2nd ed., CRC PRESS, 2006.
- [73] A.V.. C. and J. Kouvettakis, Practical Strategies for Tuning Optical, Structural and Thermal Properties in Group IV Ternary Semiconductors, ECS Trans. 33 (2010) 717–728.
- [74] J. Xie, A.V.G. Chizmeshya, J. Tolle, V.R. Dcosta, J. Menendez, J. Kouvettakis, Synthesis, stability range, and fundamental properties of Si-Ge-Sn semiconductors grown directly on Si(100) and Ge(100) platforms, Chem. Mater. 22 (2010) 3779–3789. <https://doi.org/10.1021/cm100915q>.
- [75] B. Vincent, F. Gencarelli, H. Bender, C. Merckling, B. Douhard, D.H. Petersen, O. Hansen, H.H. Henrichsen, J. Meersschaut, W. Vandervorst, M. Heyns, R. Loo, M. Caymax, Undoped and in-situ B doped GeSn epitaxial growth on Ge by atmospheric pressure-chemical vapor deposition, Appl. Phys. Lett. 99 (2011) 15–17. <https://doi.org/10.1063/1.3645620>.
- [76] S. Wirths, D. Buca, G. Mussler, A.T. Tiedemann, B. Hollander, P. Bernardy, T. Stoica, D. Grutzmacher, S. Mantl, Reduced Pressure CVD Growth of Ge and Ge<sub>1-x</sub>Sn<sub>x</sub> Alloys, ECS J. Solid State Sci. Technol. 2 (2013) N99–N102. <https://doi.org/10.1149/2.006305jss>.
- [77] P. Aella, C. Cook, J. Tolle, S. Zollner, A.V.G. Chizmeshya, J. Kouvettakis, Optical and structural properties of Si<sub>x</sub>Sn<sub>y</sub>Ge<sub>1-x-y</sub> alloys, Appl. Phys. Lett. 84 (2004) 888–890. <https://doi.org/10.1063/1.1645324>.
- [78] Y.Y. Fang, J. Tolle, A.V.G. Chizmeshya, J. Kouvettakis, V.R. D'Costa, J. Menendez, Practical B and P doping via Six Sn<sub>y</sub> Ge<sub>1-x-y-z</sub> Mzquaternaries lattice matched to Ge: Structural, electrical, and strain behavior, Appl. Phys. Lett. 95 (2009) 2–5. <https://doi.org/10.1063/1.3204456>.
- [79] B. Alharthi, J. Margetis, H. Tran, S. Al-kabi, W. Dou, S.A. Ghetmiri, A. Mosleh, J. Tolle, W. Du, M. Mortazavi, B. Li, H. Naseem, S.-Q. Yu, Study of material and optical properties of Si<sub>x</sub>Ge<sub>1-x-y</sub>Sn<sub>y</sub> alloys for Si-based optoelectronic device applications, Opt. Mater. Express. 7 (2017) 3517. <https://doi.org/10.1364/ome.7.003517>.
- [80] J.-H. Fournier-Lupien, D. Chagnon, P. Levesque, A.A. AlMutairi, S. Wirths, E. Pippel, G. Mussler, J.-M. Hartmann, S. Mantl, D. Buca, O. Moutanabbir, In Situ Studies of Germanium-Tin and Silicon-Germanium-Tin Thermal Stability, ECS Trans. 64 (2014) 903–911. <https://doi.org/10.1149/06406.0903ecst>.
- [81] V.R. D'Costa, Y.Y. Fang, J. Tolle, J. Kouvettakis, J. Menéndez, Ternary GeSiSn alloys: New opportunities for strain and band gap engineering using group-IV semiconductors, Thin Solid Films. 518 (2010) 2531–2537. <https://doi.org/10.1016/j.tsf.2009.09.149>.
- [82] B. Alharthi, A. Mosleh, J. Margetis, S. Al-Kabi, S.A. Ghetmiri, H. Tran, W. Du, M. Benamara, M. Mortazavi, J. Tolle, H.A. Naseem, S.-Q. Yu, CVD growth and characterization of Si<sub>x</sub>Ge<sub>1-x-y</sub>Sn<sub>y</sub> alloys for high efficiency multi-junction solar cells, Conf. Rec. IEEE Photovolt. Spec. Conf. 2016-Novem

## BIBLIOGRAPHY

- (2016) 5–9. <https://doi.org/10.1109/PVSC.2016.7750166>.
- [83] P. Moontragoon, Band structure calculation of Si-Ge-Sn binary and ternary alloys , nanostructures and devices, (2009).
  - [84] R. Soref, Direct-bandgap compositions of the CSiGeSn group-IV alloy, Opt. Mater. Express. 4 (2014) 836–842. <https://doi.org/10.1364/OME.4.000836>.
  - [85] C. Weng, J. Kouvettakis, A.V.G. Chizmeshya, A novel predictive model for formation enthalpies of Si and Ge hydrides with propane- and butane-like structures, J. Comput. Chem. 32 (2011) 835–853. <https://doi.org/10.1002/jcc.21662>.
  - [86] N. Taoka, T. Asano, T. Yamaha, T. Terashima, O. Nakatsuka, I. Costina, P. Zaumseil, G. Capellini, S. Zaima, T. Schroeder, Non-uniform depth distributions of Sn concentration induced by Sn migration and desorption during GeSnSi layer formation, Appl. Phys. Lett. 106 (2015) 0–5. <https://doi.org/10.1063/1.4908121>.
  - [87] S. Wirths, D. Buca, Z. Ikonic, P. Harrison, A.T. Tiedemann, B. Holländer, T. Stoica, G. Mussler, U. Breuer, J.M. Hartmann, D. Grützmacher, S. Mantl, SiGeSn growth studies using reduced pressure chemical vapor deposition towards optoelectronic applications, Thin Solid Films. 557 (2014) 183–187. <https://doi.org/10.1016/j.tsf.2013.10.078>.
  - [88] P. Meunier-Beillard, M. Caymax, K. Van Nieuwenhuysen, G. Doumen, B. Brijs, M. Hopstaken, L. Geenen, W. Vandervorst, N<sub>2</sub> as carrier gas: An alternative to H<sub>2</sub> for enhanced epitaxy of Si, SiGe and SiGe:C, Appl. Surf. Sci. 224 (2004) 31–35. <https://doi.org/10.1016/j.apsusc.2003.08.088>.
  - [89] J.M. and J.T. Nupur Bhargava, As doping of Si – Ge – Sn epitaxial semiconductor materials on a commercial CVD reactor, Semicond. Sci. Technol. 32 (2017).
  - [90] R. Soref, Silicon-based silicon – germanium – tin heterostructure photonics, Philos. Trans. Ropyal Soc. <http://rst> (2015).
  - [91] R.T. Beeler, D.J. Smith, J. Kouvettakis, J. Menéndez, GeSiSn photodiodes with 1 eV optical gaps grown on Si(100) and Ge(100) platforms, IEEE J. Photovoltaics. 2 (2012) 434–440. <https://doi.org/10.1109/JPHOTOV.2012.2206568>.
  - [92] R. Roucka, A. Clark, B. Landini, Si-Ge-Sn alloys with 1.0 eV gap for CPV multijunction solar cells, AIP Conf. Proc. 1679 (2015) 0–7. <https://doi.org/10.1063/1.4931519>.
  - [93] N.E.-D. Phoebe Pearce, Tom Wilson, Andrew Johnson, III-V Multi-Junction Solar Cells Utilising Group IV SiGeSn Alloys as a 1.0 eV Component Sub-Cell, in: 33rd Eur. Photovolt. Sol. Energy Conf. Exhib., 2017: pp. 1248–1252. <https://doi.org/10.15713/ins.mmj.3>.
  - [94] N. von den Driesch, D. Stange, S. Wirths, D. Rainko, I. Povstugar, A. Savenko, U. Breuer, R. Geiger, H. Sigg, Z. Ikonic, J.M. Hartmann, D. Grützmacher, S. Mantl, D. Buca, SiGeSn Ternaries for Efficient Group IV Heterostructure Light Emitters, Small. 13 (2017) 1–9. <https://doi.org/10.1002/smll.201603321>.
  - [95] A. Ulyanenkov, Novel methods and universal software for HRXRD, XRR and GISAXS data interpretation, Appl. Surf. Sci. 253 (2006) 106–111. <https://doi.org/10.1016/j.apsusc.2006.05.099>.
  - [96] P.M. Frijlink, A new versatile, large size MOVPE reactor, J. Cryst. Growth. (1988).

## BIBLIOGRAPHY

- [https://doi.org/10.1016/0022-0248\(88\)90529-5.](https://doi.org/10.1016/0022-0248(88)90529-5)
- [97] D. Brien, M. Dauelsberg, K. Christiansen, J. Hofeldt, M. Deufel, M. Heuken, Modelling and simulation of MOVPE of GaAs-based compound semiconductors in production scale Planetary Reactors, *J. Cryst. Growth.* 303 (2007) 330–333. <https://doi.org/10.1016/j.jcrysgro.2006.11.319>.
- [98] M.L.H. Anthony C Jones, Chemical Vapour Deposition: Precursors, Processes and Applications, 2008. <https://doi.org/https://doi.org/10.1039/9781847558794>.
- [99] T.F.Kuech, Metal Organic Vapor Phase Epitaxy of Compound Semiconductors, *Mater. Sci. Reports.* 2 (1987) 1–50. [https://doi.org/10.1007/978-3-662-07064-2\\_8](https://doi.org/10.1007/978-3-662-07064-2_8).
- [100] G.B. Stringfellow, A critical appraisal of growth mechanisms in MOVPE, *J. Cryst. Growth.* 68 (1984) 111–122. [https://doi.org/10.1016/0022-0248\(84\)90405-6](https://doi.org/10.1016/0022-0248(84)90405-6).
- [101] M. Dauelsberg, M. Deufel, M. Reinhold, G. Strauch, T. Begunde, Equipment and Process Simulation of Compound Semiconductor MOCVD in the Production Scale Multiwafer Planetary Reactor, in: *Simul. Semicond. Process. Devices* 2001, 2001. [https://doi.org/10.1007/978-3-7091-6244-6\\_28](https://doi.org/10.1007/978-3-7091-6244-6_28).
- [102] H.M. Manasevit, W.I. Simpson, The Use of Metal-Organics in the Preparation of Semiconductor Materials I. Epitaxial Gallium-V Compounds, *J. Electrochem. Soc.* 116 (1969) 1725–1732. <https://doi.org/10.1149/1.2411685>.
- [103] A. Salemi, Low Temperature Epitaxy Growth and Kinetic Modeling of SiGe for BiCMOS Application, KTH Master Thesis. (2011).
- [104] S. Wirths, D. Buca, A.T. Tiedemann, P. Bernardy, B. Holländer, T. Stoica, G. Mussler, U. Breuer, S. Mantl, Low temperature RPCVD epitaxial growth of Si<sub>1-x</sub>Gex using Si<sub>2</sub>H<sub>6</sub> and Ge<sub>2</sub>H<sub>6</sub>, *Solid. State. Electron.* 83 (2013) 2–9. <https://doi.org/10.1016/j.sse.2013.01.032>.
- [105] D. V. Shenai, R.L. DiCarlo, M.B. Power, A. Amamchyan, R.J. Goyette, E. Woelk, Safer alternative liquid germanium precursors for relaxed graded SiGe layers and strained silicon by MOVPE, *J. Cryst. Growth.* 298 (2007) 172–175. <https://doi.org/10.1016/j.jcrysgro.2006.10.194>.
- [106] K. Tamari, The thermal decomposition of germane. I. Kinetics, *J. Phys. Chem.* 59 (1955) 801–805. <https://doi.org/10.1021/j150531a001>.
- [107] J.M. Hartmann, J. Aubin, J.P. Barnes, A benchmark of germane and digermane for the low temperature growth of intrinsic and heavily in-situ boron-doped SiGe, *ECS Trans.* 75 (2016) 281–293. <https://doi.org/10.1149/07508.0281ecst>.
- [108] C.-B. Cha, I.-S, Lim, J.-Y., Shin, I.-C., Park, The Characteristics of Arsenic in the CVD Growth of GE on GaAs(100), in: World Conf. 2nd, Photovolt. Sol. Energy Convers., 1998: pp. 3658–3662.
- [109] M. Bosi, G. Attolini, M. Calicchio, C. Ferrari, C. Frigeri, E. Gombia, A. Motta, F. Rossi, Homoepitaxial growth of germanium for photovoltaic and thermophotovoltaic applications, *J. Cryst. Growth.* 318 (2011) 341–344. <https://doi.org/10.1016/j.jcrysgro.2010.10.112>.
- [110] J. Margetis, S.A. Ghetmiri, W. Du, B.R. Conley, A. Mosleh, R.A. Soref, G. Sun, L. Domulevicz, H.A. Naseem, S.Q. Yu, J. Tolle, Growth and characterization of epitaxial Ge<sub>1-x</sub>

## BIBLIOGRAPHY

- Sn<sub>x</sub> alloys and heterostructures using a commercial CVD system, *ECS Trans.* 64 (2014) 711–720. <https://doi.org/10.1149/06406.0711ecst>.
- [111] S. Iida, S.I. Hirose, Vapor Etching of GaAs Single Crystals with HCl Gas, *Japanese J. Appl. Physics, Part 1 Regul. Pap. Short Notes Rev. Pap.* 4 (1965) 1025–1026.
- [112] Y. Bogumilowicz, J.M. Hartmann, R. Truche, Y. Campidelli, G. Rolland, T. Billon, Chemical vapour etching of Si, SiGe and Ge with HCl; applications to the formation of thin relaxed SiGe buffers and to the revelation of threading dislocations, *Semicond. Sci. Technol.* 20 (2005) 127–134. <https://doi.org/10.1088/0268-1242/20/2/004>.
- [113] P.R. Pukite, P.I. Cohen, Multilayer step formation after As adsorption on Si (100): Nucleation of GaAs on vicinal Si, *Appl. Phys. Lett.* (1987). <https://doi.org/10.1063/1.97733>.
- [114] F. Gencarelli, B. Vincent, L. Souriau, O. Richard, W. Vandervorst, R. Loo, M. Caymax, M. Heyns, Low-temperature Ge and GeSn chemical vapor deposition using Ge<sub>2</sub>H<sub>6</sub>, *Thin Solid Films.* 520 (2012) 3211–3215. <https://doi.org/10.1016/j.tsf.2011.10.119>.
- [115] M. Tada, J.H. Park, J.R. Jain, K.C. Saraswat, Low-temperature, low-pressure chemical vapor deposition and solid phase crystallization of silicon-germanium films, *J. Electrochem. Soc.* 156 (2009) 23–27. <https://doi.org/10.1149/1.3008009>.
- [116] M. Liehr, C.M. Greenlieff, S.R. Kasi, M. Offenberg, Kinetics of silicon epitaxy using SiH<sub>4</sub> in a rapid thermal chemical vapor deposition reactor, *Appl. Phys. Lett.* 56 (1990) 629–631. <https://doi.org/10.1063/1.102719>.
- [117] S.M. Gates, S.K. Kulkarni, Hydrogen coverage during Si growth from SiH<sub>4</sub> and Si 2H<sub>6</sub>, *Appl. Phys. Lett.* 60 (1992) 53–55. <https://doi.org/10.1063/1.107371>.
- [118] R. Khazaka, E. Nolot, J. Aubin, J.M. Hartmann, Growth and characterization of SiGeSn pseudomorphic layers on 200 mm Ge virtual substrates, *Semicond. Sci. Technol.* 33 (2018) 124011. <https://doi.org/10.1088/1361-6641/aaea32>.
- [119] Z. Zhang, J.S. Pan, J. Zhang, E.S. Tok, Kinetics of Ge diffusion, desorption and pit formation dynamics during annealing of Si<sub>0.8</sub>Ge<sub>0.2</sub>/Si(001) virtual substrates, *Phys. Chem. Chem. Phys.* 12 (2010) 7171–7183. <https://doi.org/10.1039/b927274g>.
- [120] M. Bauer, C. Ritter, P.A. Crozier, J. Ren, J. Menendez, G. Wolf, J. Kouvetsakis, Synthesis of ternary SiGeSn semiconductors on Si(100) via Sn<sub>x</sub>Ge<sub>1-x</sub> buffer layers, *Appl. Phys. Lett.* 83 (2003) 2163–2165. <https://doi.org/10.1063/1.1606104>.
- [121] C. Xu, R.T. Beeler, L. Jiang, J.D. Gallagher, R. Favaro, J. Menéndez, J. Kouvetsakis, Synthesis and optical properties of Sn-rich Ge<sub>1-x</sub>-ySixSn<sub>y</sub> materials and devices, *Thin Solid Films.* 557 (2014) 177–182. <https://doi.org/10.1016/j.tsf.2013.08.043>.
- [122] E. Kasper, J. Werner, M. Oehme, S. Escoubas, N. Burle, J. Schulze, Growth of silicon based germanium tin alloys, *Thin Solid Films.* 520 (2012) 3195–3200. <https://doi.org/10.1016/j.tsf.2011.10.114>.
- [123] A. Mosleh, M.A. Alher, L.C. Cousar, W. Du, S.A. Ghetmiri, T. Pham, J.M. Grant, G. Sun, R.A. Soref, B. Li, H.A. Naseem, S.Q. Yu, Direct growth of Ge 1-x Sn x films on Si using a cold-wall ultra-high vacuum chemical-vapor-deposition system, *Front. Mater.* 2 (2015) 1–7. <https://doi.org/10.3389/fmats.2015.00030>.

## BIBLIOGRAPHY

- [124] Jacques I. Pankove, Optical Processes in semiconductors, London, 1971.
- [125] J. Vanjaria, A.C. Arjunan, T. Salagaj, G.S. Tompa, H. Yang, T. Houghton, H. Yu, Growth of SiGeSn Thin Films Using Simplified PECVD Reactor towards NIR Sensor Devices, *ECS J. Solid State Sci. Technol.* 9 (2020) 074001. <https://doi.org/10.1149/2162-8777/abaeb2>.
- [126] J. Margetis, A. Mosleh, S. Al-Kabi, S.A. Ghetmiri, W. Du, W. Dou, M. Benamara, B. Li, M. Mortazavi, H.A. Naseem, S.Q. Yu, J. Tolle, Study of low-defect and strain-relaxed GeSn growth via reduced pressure CVD in H<sub>2</sub> and N<sub>2</sub> carrier gas, *J. Cryst. Growth.* 463 (2017) 128–133. <https://doi.org/10.1016/j.jcrysgro.2017.01.041>.
- [127] E.C.S. Transactions, Ge<sub>1-x</sub>Sn<sub>x</sub> Epitaxial Growth on Ge Substrate by MOCVD, *ECS Meet. Abstr.* (2014) 6–11. <https://doi.org/10.1149/ma2014-02/35/1828>.
- [128] G. Timò, G. Abagnale, N. Armani, E. Malvisi, G. Carbi, F. Farina, B. Schineller, Novel approaches to MOVPE material deposition for high efficiency Multijunction Solar Cells, *Cryst. Res. Technol.* 49 (2014) 606–613. <https://doi.org/10.1002/crat.201300448>.
- [129] L. Barrutia, E. Barrigón, I. García, I. Rey-Stolle, C. Algora, Effect of Ge autodoping during III-V MOVPE growth on Ge substrates, *J. Cryst. Growth.* 475 (2017) 378–383. <https://doi.org/10.1016/j.jcrysgro.2017.06.022>.
- [130] F.A. G.Timò, G.Abagnale, M.Calicchio, M.Cornelli, N.Armani, F. Trespidi, E.Malvisi, E.Achilli, G.S. and R.C. B. Schineller, NEW RESULTS ON SiGeSn MOVPE GROWN FOR MULTI-JUNCTION SOLAR CELLS, in: 36th Eur. Photovolt. Sol. Energy Conf. Exhib., 2019: pp. 699–703.
- [131] L. Barrutia, I. García, E. Barrigón, M. Ochoa, C. Algora, I. Rey-Stolle, Impact of the III-V/Ge nucleation routine on the performance of high efficiency multijunction solar cells, *Sol. Energy Mater. Sol. Cells.* 207 (2020). <https://doi.org/10.1016/j.solmat.2019.110355>.
- [132] M.J. Hossain, B. Tiwari, I. Bhattacharya, Novel High Efficiency Quadruple Junction Solar Cell with Current Matching and Quantum Efficiency Simulations, *ArXiv.* (2019) 100–107.
- [133] R. Campesato, C. Baur, M. Casale, M. Gervasi, E. Gombia, E. Greco, A. Kingma, P.G. Rancoita, D. Rozza, M. Tacconi, NIEL DOSE and DLTS Analyses on Triple and Single Junction solar cells irradiated with electrons and protons, in: 2018 IEEE 7th World Conf. Photovolt. Energy Conversion, WCPEC 2018 - A Jt. Conf. 45th IEEE PVSC, 28th PVSEC 34th EU PVSEC, 2018. <https://doi.org/10.1109/PVSC.2018.8548237>.
- [134] J.F. Geisz, D.J. Friedman, III-N-V semiconductors for solar photovoltaic applications, *Semicond. Sci. Technol.* 17 (2002) 769–777. <https://doi.org/10.1088/0268-1242/17/8/305>.
- [135] M. Levinshtein, S. Rumyantsev, M. Shur, Volume 1 Si, Ge, C (Diamond), GaAs, GaP, GaSb, InAs, InP, InSb, in: *Handb. Ser. Semicond. Parameters*, 1996.
- [136] M. Levinshtein, S. Rumyantsev, M. Shur, *Handbook Series on Semiconductor Parameters*. volume 2, 1996. <https://doi.org/10.1142/2046-vol2>.
- [137] D. Elfiky, M. Yamaguchi, T. Sasaki, T. Takamoto, C. Morioka, M. Imaizumi, T. Ohshima, S.I. Sato, M. Elnawawy, T. Eldesoky, A. Ghitas, Theoretical optimization of base doping concentration for radiation resistance of InGaP subcells of InGaP/GaAs/Ge based on minority-carrier lifetime, *Jpn. J. Appl. Phys.* 49 (2010). <https://doi.org/10.1143/JJAP.49.121201>.

## BIBLIOGRAPHY

- [138] Hojun Yoon, K.M. Edmondson, G.S. Kinsey, R.R. King, P. Hebert, R.K. Ahrenkiel, B.T. Cavicchi, N.H. Karam, Minority carrier lifetime and radiation damage coefficients of germanium, (2005) 842–845. <https://doi.org/10.1109/pvsc.2005.1488264>.
- [139] W. Liu, Y. Li, J. Chen, Y. Chen, X. Wang, F. Yang, Optimization of grid design for solar cells, *J. Semicond.* 31 (2010) 3–6. <https://doi.org/10.1088/1674-4926/31/1/014006>.
- [140] Y. Shimura, T. Asano, T. Yamaha, M. Fukuda, W. Takeuchi, O. Nakatsuka, S. Zaima, EXAFS study of local structure contributing to Sn stability in Si<sub>y</sub>Ge<sub>1-y</sub>-zSn<sub>z</sub>, *Mater. Sci. Semicond. Process.* 70 (2017) 133–138. <https://doi.org/10.1016/j.mssp.2016.11.013>.
- [141] C.E. Valdivia, K. Hinzer, Segmented Multi-Junction Solar Cells: A New Opportunity for Cell Design Optimization, *Conf. Rec. IEEE Photovolt. Spec. Conf.* (2019) 45–48. <https://doi.org/10.1109/PVSC40753.2019.8980689>.
- [142] D.J. Aiken, InGaP/GaAs/Ge multi-junction solar cell efficiency improvements using epitaxial germanium, in: *Conf. Rec. IEEE Photovolt. Spec. Conf.*, 2000. <https://doi.org/10.1109/PVSC.2000.916053>.

## APPENDIX 1

## Appendix 1. Determination of the electric field at the beginning of each layer by applying TMM and SMM

As demonstrated in chapter 3.1, the Poynting vector changes along the layer thickness following a generalized Lambert-Beer law. The Lambert-Beer law can then be applied for the determination of the electric field at the beginning of a layer, starting from the electric field at the end of the layer. However, we can get the electric field at the beginning of a layer also by applying the TMM, by considering a different coordinate system. In order to determine the complex amplitudes of the forward and backward waves at the beginning of each layer, it is possible to apply the procedure followed in the chapter 2.4, by considering the geometrical representation of Figure 105.

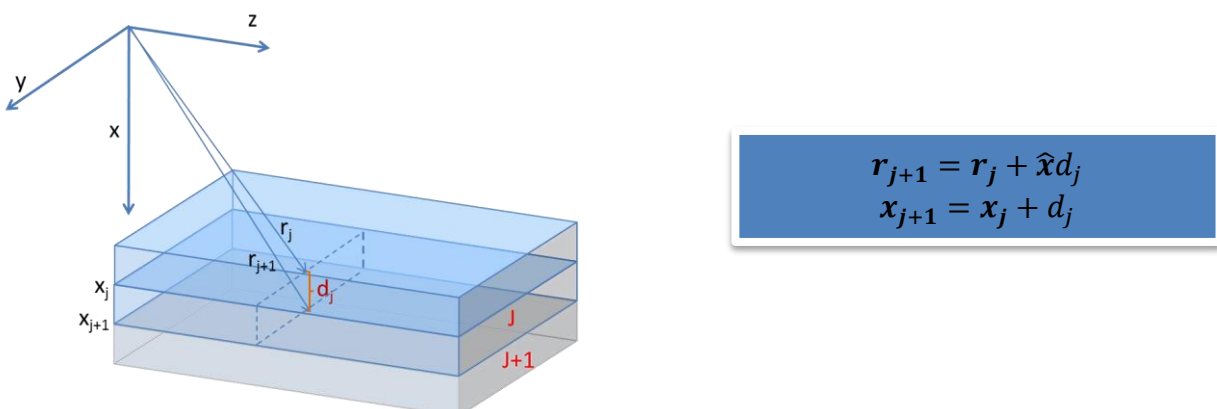


**Figure 105.** Geometrical representation of the interface between layer  $j$  and  $j+1$ . The coordinate  $x_j$  identifies the beginning of the layer  $j$ .

In particular, by considering the boundary conditions for TM mode (Eq.2.56 and Eq.2.59) and for TE mode (Eq.2.112 and Eq.2.116) at the interface  $x_{j+1}$  and the coordinate system depicted in Figure 105, the generic (for TM and TE modes) characteristic layer matrix  $T_j$  becomes:

$$T_j = \frac{1}{2\beta_{j+1}} \begin{bmatrix} \Psi_j^+(\beta_{j+1} + \beta_j) & \Psi_j^-(\beta_{j+1} - \beta_j) \\ \Psi_j^+(\beta_{j+1} - \beta_j) & \Psi_j^-(\beta_{j+1} + \beta_j) \end{bmatrix} \quad 0.1$$

Where, the complex coefficient  $\beta_j$  are given by Eq.2.61 or Eq.2.117 for TM and TE mode, respectively.

Therefore, it holds:

$$\begin{bmatrix} F_{j+1}^+ \\ F_{j+1}^- \end{bmatrix} = T_j \begin{bmatrix} F_j^+ \\ F_j^- \end{bmatrix} \quad 0.2$$

As already claimed, also the matrix  $T_j$  can be expressed as a product of an “interface” and “propagation” matrix, which describe the reflection of the electric field at the interface  $j+1, j$  and the propagation of the electric field inside the layer  $j$ :

## APPENDIX 1

$$T_j = \underbrace{\frac{\beta_{j+1} + \beta_j}{2\beta_{j+1}} \begin{bmatrix} 1 & \frac{\beta_{j+1} - \beta_j}{\beta_{j+1} + \beta_j} \\ \frac{\beta_{j+1} - \beta_j}{\beta_{j+1} + \beta_j} & 1 \end{bmatrix}}_{\text{interface}} \underbrace{\begin{bmatrix} \Psi_j^+ & 0 \\ 0 & \Psi_j^- \end{bmatrix}}_{\text{Propagation}} \quad 0.3$$

Where:

$$\frac{\beta_{j+1} + \beta_j}{2\beta_{j+1}} \begin{bmatrix} 1 & \frac{\beta_{j+1} - \beta_j}{\beta_{j+1} + \beta_j} \\ \frac{\beta_{j+1} - \beta_j}{\beta_{j+1} + \beta_j} & 1 \end{bmatrix} = \frac{1}{t_{j+1,j}} \begin{bmatrix} 1 & r_{j+1,j} \\ r_{j+1,j} & 1 \end{bmatrix} \quad 0.4$$

$t_{j+1,j}$  and  $r_{j+1,j}$ , are, respectively, the Fresnel transmission and reflection coefficients.

Comparing, for example, Eq.2.74 with Eq.0.4, it can be verified that:

$$r_{j,j+1} = -r_{j+1,j} \quad \text{and} \quad t_{j+1,j} = t_{j,j+1} \frac{w_j}{w_{j+1}}$$

From Eq.0.2 :

$$\begin{bmatrix} \mathcal{F}_N^+ \\ \mathcal{F}_N^- \end{bmatrix} = T_{N-1} \dots \dots T_0 \begin{bmatrix} \mathcal{F}_0^+ \\ \mathcal{F}_0^- \end{bmatrix} \quad 0.5$$

Since  $\mathcal{F}_N^- = 0$ , we get:

$$\begin{bmatrix} \mathcal{F}_N^+ \\ 0 \end{bmatrix} = \begin{bmatrix} T_{11} & T_{12} \\ T_{21} & T_{22} \end{bmatrix} \begin{bmatrix} \mathcal{F}_0^+ \\ \mathcal{F}_0^- \end{bmatrix} \quad 0.6$$

Therefore:

$$\mathcal{F}_N^+ = T_{11}\mathcal{F}_0^+ + T_{12}\mathcal{F}_0^- ; \quad \mathcal{F}_0^- = -\frac{T_{21}}{T_{22}}\mathcal{F}_0^+ \quad 0.7$$

Eq.0.7 allows determining the reflection coefficient:

$$R_{TM} = \frac{\langle \tilde{S}_0(x_0) \rangle_{TM,TE}^-}{\langle \tilde{S}_0(x_0) \rangle_{TE,TE}^+} = \frac{|\mathcal{F}_0^-|^2}{|\mathcal{F}_0^+|^2} = \frac{|T_{21}|^2}{|T_{22}|^2} \quad 0.8$$

By knowing  $\mathcal{F}_0^+$  and  $\mathcal{F}_0^-$ , it is possible from Eq.0.2, to determine all the  $\mathcal{F}_j^+$  and  $\mathcal{F}_j^-$ , for  $j=1\dots N-1$

The matrix elements of the generic scattering matrix become:

$$S_j(1,1) = \frac{(\beta_j - \beta_{j-1})(\psi_{j-1}^+)^2 + (\beta_j + \beta_{j-1})S_{j-1}(1,1)}{(\beta_j + \beta_{j-1})(\psi_{j-1}^+)^2 + (\beta_j - \beta_{j-1})S_{j-1}(1,1)} \quad 0.9$$

Getting  $S_{j-1}(1,1)$  from  $S_j(1,1)$ :

$$S_{j-1}(1,1) = \frac{(\psi_{j-1}^+)^2 [(\beta_j + \beta_{j-1}) S_j(1,1) - (\beta_j - \beta_{j-1})]}{[(\beta_j + \beta_{j-1}) - S_j(1,1)(\beta_j - \beta_{j-1})]} \quad 0.10$$

For  $J=N$ , recalling that  $S_N(1,1) = 0$ , it follows:

$$S_{N-1}(1,1) = \frac{(\beta_{N-1} - \beta_N)}{(\beta_{N-1} + \beta_N)} (\psi_{N-1}^+)^2 \quad 0.11$$

$$S_j(2,1) = \frac{2\beta_j \psi_{j-1}^+ S_{j-1}(2,1)}{(\beta_j - \beta_{j-1}) S_{j-1}(1,1) + (\beta_j + \beta_{j-1})(\psi_{j-1}^+)^2} \quad 0.12$$

Getting  $S_{j-1}(2,1)$  from  $S_j(2,1)$ :

$$S_{j-1}(2,1) = \frac{S_j(2,1) [(\beta_j - \beta_{j-1}) S_{j-1}(1,1) + (\beta_j + \beta_{j-1})(\psi_{j-1}^+)^2]}{2\beta_j \psi_{j-1}^+} \quad 0.13$$

For  $J=N$ , recalling that  $S_N(2,1) = 1$  and by considering Eq.0.11, it follows:

$$S_{N-1}(2,1) = \frac{2\beta_{N-1}}{\beta_N + \beta_{N-1}} \psi_{N-1}^+ \quad 0.14$$

The remaining calculation scheme reported in Figure 15 can be applied.

A precaution has to be considered regarding the scattering matrix elements  $S_{N-1}(1,1)$  and  $S_{N-1}(2,1)$ , from which all the others  $S_j(1,1)$  and  $S_j(2,1)$  elements can be determined. It can be pointed out from Eq.0.11 and Eq.0.14 that the matrix elements contain the term  $\psi_{N-1}^+$ . In all cases where the  $N-1$  layer is thick (one important case is that where the  $N-1$  layer is the thinned substrate), the propagation function  $\psi_{N-1}^+$  can assume a value near to zero for low wavelength values (where the extinction coefficient is larger) and it comes that the range of wavelength where  $\psi_{N-1}^+$  is near zero becomes larger as the thickness of this layer increases. As a consequence, the near zero value in  $\psi_{N-1}^+$  propagates in the calculation of the  $S_j(1,1)$  or  $S_j(2,1)$  elements. At the end of the computation process, we could find a drastic cut off the reflectance and therefore, of the top cell EQE, in the low wavelength region. This means that a proper set up of the software code utilized for the calculation of the scattering matrix elements is necessary to avoid that any *underflow* condition could bring to a wrong evaluation of the top cells current.

## LIST OF PUBLICATIONS

---

## List of publications promoted by the thesis

The thesis is based on the following published papers in conferences and scientific journals.

### PUBLICATIONS

Simon P. Philipps, Mathieu Baudrit, Karla Hillerich, Valentine Moreau, Rolando Parmesani, Eduardo Román, Gabriel Sala, Bernd Schineller, **Gianluca Timò** and Andreas W. Bett, “CPVMatch - Concentrating Photovoltaic Modules Using Advanced Technologies and Cells for Highest Efficiencies”, Proceeding of the 32nd European PV Solar Energy Conference and Exibition, 20-24 June , 2016, Munich , Germany, DOI: 10.4229/EUPVSEC20162016-4CV.1.4.

**Gianluca Timò** and Lucio Andreani,” *Simulation of the performances of multijunction solar cells with improved voltage by transfer and scattering matrix methods*”, Proceedings of 44th IEEE Photovoltaic Specialists Conference, June 25-30, Washington DC, USA, 2017. DOI: 10.1109/PVSC.2017.8521506.

**Gianluca Timò**, Giovanni Abagnale, Nicola Armani, Marco Calicchio and Bernd Schineller, “*MOVPE SiGeSn development for the next generation four junction solar cells*”, AIP Conference Proceedings 2012, 040011 (2018); <https://doi.org/10.1063/1.5053519>

**G. Timò**, G. Abagnale, M. Calicchio, M. Cornelli, N. Armani, F. Trespidi, E. Malvisi, E. Achilli, F. Annoni, B. Schineller, G. Siefer, R. Couderc, “*New Results on SiGeSn MOVPE Grown for Multi-Junction Solar Cells*”, Proceedings of the 36th EU PVSEC 2018, 7 - 11 September 2020, Lisbon DOI: 10.4229/EUPVSEC20192019-3BV.1.57

**Gianluca Timò**, Alessio Martinelli, Lucio Claudio Andreani,” *A new theoretical approach for the performance simulation of multijunction solar cells*”, Prog. Photovoltaics Res. Appl., no. October 2019, pp. 1–16, 2020. <https://doi.org/10.1002/pip.3225>

**Gianluca Timò**, Marco Calicchio, Giovanni Abagnale, Nicola Armani, Elisabetta Achilli, Marina Cornelli, Filippo Annoni, Nicola Castagnetti, Maddalena Patrini, Lucio Claudio Andreani, Lucia Nasi and Bernd Schineller, “*Results on MOVPE SiGeSn deposition for the monolithic integration of III-V and IV elements in multi-junction solar cells*”, Solar Energy Materials & Solar Cells 224 (2021) 111016.

**Gianluca Timò**, Marco Calicchio, Giovanni Abagnale, Nicola Armani, Elisabetta Achilli, Marina Cornelli, Filippo Annoni, Bernd Schineller and Lucio Claudio Andreani, “*Study of the cross-influence between III-V and IV elements deposited in the same MOVPE growth chamber*”, Materials 2021, Volume 14, Issue 5, 1066

.



There are different kind of scientists and researchers: those who have an insatiable curiosity for how the world works and applications are not of interest, others whose activity is driven by military applications, others who push ahead the technological innovation independently on the impact it can have on the society and eventually others who consider that at the base of theirs scientific breakthroughs there must be a vision of the society, and, in particular, the aim to meets the mankind needs in a sustainable way.

I have always been attracted by this last category of researchers and I will be very pleased if this thesis will contribute to their work in the construction of a more sustainable society.